ABSTRACT

Title of Dissertation:	ACTIVE GALACTIC NUCLEUS FEEDBACK IN GIANTS AND DWARFS
	Weizhe Liu Doctor of Philosophy, 2022
Dissertation Directed by:	Professor Sylvain Veilleux Department of Astronomy

Feedback from Active Galactic Nucleus (AGN) may play a critical role in the coevolution of galaxies and supermassive black holes (SMBH). Specifically, AGN feedback may quench star formation, suppress baryon-to-dark matter mass ratio, shape galaxy morphology, impact the circumgalactic (CGM)/intergalactic medium (IGM), and regulate SMBH accretion. One of the most important forms of AGN feedback is powerful, quasar/AGN-driven outflows. However, the physical details of these outflows, including their driving mechanism and spatial extent, are still not well constrained. In addition, while these outflows are believed to be effective in massive galaxies, their impact on dwarf galaxies ($M_\star \lesssim 10^{9.5}$ $M_\odot$) remains largely unknown. To answer these open questions, my thesis focuses on AGN feedback via quasar/AGN-driven outflows in both ultraluminous infrared galaxies (ULIRGs) and dwarf galaxies with four projects.

In the first half of my thesis, I examine the outflows in nearby ULIRGs with two objectives: In Chapter 2, I present a dedicated investigation of the highly ionized, likely pc-scale quasar/AGN winds in a sample of 21 nearby ULIRGs through *HST*/COS far-ultraviolet (FUV) spectroscopy.

Blueshifted Lyα emission is prevalent in the sample, which is probably closely related to the outflowing gas and AGN activity in these objects. Additionally, the Lyα escape fractions tend to be slightly larger in objects with stronger AGN and larger outflow velocities. Highly ionized O VI and N V outflows are detected in a coherently selected, AGN-dominated ULIRG sample for the first time. Together with the results from a matched quasar sample, these outflows show higher incidence rates and larger EW and velocities in X-ray weak sources and sources with high X-ray absorbing column densities, implying that these outflows are radiatively-driven. In Chapter 3, I describe a deep, *Chandra* imaging spectroscopy study of the nearby ULIRG Mrk 273. The data have revealed a $\sim$40 kpc$\times$40 kpc X-ray nebula, which is relatively hot and has a super-solar α/Fe abundance ratio. This nebula is most likely heated and metal-enriched by outflows over time. Additionally, the existence of a dual AGN is strongly suggested by the data, and extended 1–3 keV emission are detected, likely related to the AGN photoionized gas and/or outflowing gas.

In the second half of my thesis, I turn to look at the AGN-driven outflows in dwarf galaxies: In Chapter 4, I report the results from a dedicated optical integral field spectroscopic study of a sample of eight dwarf galaxies with known AGN and suspected outflows. Fast, kpc-scale outflows are detected in seven of them. The outflows show 50-percentile (median) velocity of up to $\sim$240 km s^{-1} and 80-percentile line width reaching $\sim$1200 km s^{-1}, in clear contrast with the more quiescent kinematics of the host gas and stellar components. The kinematics and energetics of these outflows suggest that they are primarily driven by the AGN. A small but non-negligible portion of the outflowing material likely escapes the main body of the host galaxy and contributes to the enrichment of the circumgalactic medium. The impact of these outflows on their dwarf host galaxies is similar to those taking place in the more luminous AGN with massive hosts in the low-redshift universe. In Chapter 5, I discuss the results from a pilot *HST*/COS spectroscopy program to examine three objects studied in Chapter 4. Blueshifted absorption features tracing fast outflows are detected in two of the three objects. For object J0954+47, the outflow is detected in multiple ions and is much faster than those in star-forming galaxies with similar star formation rates. The outflow velocity exceeds the escape velocity of this system, suggesting that a large fraction of the outflowing gas may escape. The outflow carries significant amount of mass, momentum and kinetic energy, which may transport material out of the galaxy more efficiently than the gas consumption by star formation. The ratio of kinetic energy outflow rate to AGN luminosity of this outflow is at least comparable to the expectation from simulations of AGN feedback.

Finally, in Chapter 6, I summarize the main results of the whole thesis, and briefly highlight several future works that may lead to a more comprehensive understanding of AGN feedback in ULIRGs and dwarf galaxies.

ACTIVE GALACTIC NUCLEUS FEEDBACK IN GIANTS AND DWARFS

by

Weizhe Liu

Dissertation submitted to the Faculty of the Graduate School of the
University of Maryland, College Park in partial fulfillment
of the requirements for the degree of
Doctor of Philosophy
2022

Advisory Committee:
- Professor Sylvain Veilleux, Chair/Advisor
- Professor Alberto D. Bolatto
- Professor James F. Drake
- Professor Richard Mushotzky
- Professor David S. N. Rupke

Preface

The research presented in Chapter 2 has been accepted for publication, the research presented in Chapters 3 and 4 have been previously published, and the research presented in Chapter 5 will be submitted to Academic Journal this year.

Chapter 2 is presented with only minimal modification since accepted for publication in The Astrophysical Journal as "Galactic Winds across the Gas-Rich Merger Sequence II. Lyman Alpha Emission and Highly Ionized O VI and N V Outflows in Ultraluminous Infrared Galaxies" [Liu et al., 2022]. The authors are Weizhe Liu, Sylvain Veilleux, David S. N. Rupke, Todd M. Tripp, Frederick Hamann, and Crystal Martin.

Chapter 3 is presented with only minimal modification since publication in The Astrophysical Journal as "Elliptical Galaxy in the Making: The Dual Active Galactic Nuclei and Metal-enriched Halo of Mrk 273" [Liu et al., 2019]. The authors are Weizhe Liu, Sylvain Veilleux, Kazushi Iwasawa, David S. N. Rupke, Stacy Teng, Vivian U, Francesco Tombesi, David Sanders, Claire E. Max, and Marcio Meléndez.

Chapter 4 is presented with only minimal modification since publication in The Astrophysical Journal as "Integral-Field Spectroscopy of Fast Outflows in Dwarf Galaxies with AGN" [Liu et al., 2020]. The authors are Weizhe Liu, Sylvain Veilleux, Gabriela Canalizo, David S. N. Rupke, Christina M. Manzano-King, Thomas Bohn, and Vivian U.

Chapter 5 is going to be submitted to The Astrophysical Journal as "Fast Outflows and Strong He II Emission in Dwarf Galaxies with AGN" (Liu 2022b, in prep.).

Dedication

To my mother, my youngest auntie, and my fiancee.

Acknowledgments

First and foremost, I owe a big thank you to my advisor, Prof. Sylvain Veilleux for being such a great guide along the way. He always encourages me to pursue my own research interest and independence, while directing me to challenging science projects, sparkling science findings and brilliant science ideas that really open my eye. He helps me set goals to get things done and keep me on track when I feel lost or distracted half-way. I truly appreciate his sage suggestions and constructive comments during our delightful weekly meetings. Without him, I can never start this exciting adventure.

I would also thank my close collaborators Prof. David Rupke and Prof. Gabriela Canalizo. Dave and Gaby always give great suggestions and comments and I really enjoy the enlightening discussion with both of them. I can never thank them more for their support to my postdoc applications. I am fortunate to build my software and tools based on Dave's wonderful software. Gaby has kindly offered me access to the Keck/KCWI data that really blow my mind away, and my visits to Keck Observatory and UC Riverside were more than spectacular.

I thank Prof. Richard Mushotzky for all those great conversations about cutting-edge science and technologies, new science envisions, anecdotes and life stories. It has been really relaxing just sitting in his office for casual chats. I also benefit a lot from those inspiring side projects, which I blame myself for not pushing through. I will always cherish the kind help from Prof. Alberto Bolatto on the preparation of ALMA proposal and on all other problems I ran into. I thank both of them for giving inspiring suggestions during committee meetings, after which I always get refreshed and motivated, well prepared to continue with my research. I would also like to extend my gratitude to Prof. James Drake who agreed to serve on my thesis defense committee as Dean's representative.

I truly appreciate the great help from all my other collaborators, including Prof. Kazushi Iwasawa, Dr. Stacy Teng, Dr. Vivian U, Prof. Francesco Tombesi, Prof. David Sanders, Prof. Claire E. Max, Dr. Marcio Meléndez, Dr. Christina M. Manzano-King, Dr. Thomas Bohn, Prof. Todd Trip, Prof. Fred Hamann, Prof. Crystal Martin, Prof. Nadia L. Zakamska, Dr. Dominika Wylezalek, Dr. Andrey Vayner, Dr. Caroline Bertemes, and Mr. Yuzo Ishikawa.

I would like to thank my dearest friends, Jialu, Peizhi, Da Chengzi and Shi Yu and all other friends, who help me survive the graduate school. Thanks all of them, especially Jialu and Peizhi, for sharing their curiosity, humor, courage, and wisdom towards science and life with me. I can never forget those laughters, songs, delicious food and road trips. I even cherish the "harsh criticism" Jialu has poured onto me (which are sometimes not well grounded I must say).

I am grateful to all my other classmates, Carrie, Chongchong, Elizabeth, Laura, and I'd like to thank Pradip and Robyn for their kind help on my research projects. Many thanks to my fellow graduate students Thomas, Drew, Tomás, Milena, Becca, Alex, Dana, Amy, Guangwei, Julian, Sergio, Sara, Qian, Ginny, and many others.

I want to thank Prof. Drake Deming, Prof. Andrew Harris, Prof. Coleman Miller, Prof. Derek Richardson, and Prof. Massimo Ricotti for their wonderful classes, and all other faculty for their kindness and help. I am also grateful to all the administrative staff in the department. The whole department has always been warm and welcome, and I truly appreciate all the friendly faces, wonderful conversations, inspiring discussions, and kind help from everyone.

I also want to thank Prof. Lei Hao and Prof. Qiusheng Gu, who introduced me to the wonderful world of astronomy research, and my gratitude should definitely be extended to all my great teachers along the way.

I owe my deepest gratitude to the three greatest ladies in my life - my mother, my youngest auntie or "Yaoyi", and my fiancee. I am so fortunate and humbled to be surrounded by their love all the time.

My mother has set up a great role model for me, for both work and life. Without her sacrifice, her dedication, and her selfless love, I can never chase my dream freely. She always respects my decision, and also guides me when I am confused or hesitant. Without her, my life will never start. Without her, I can never be myself.

"Yaoyi" has taught me countless life wisdom. She is always warm and considerate, and has always been there for me, especially when I was rebelling or grumpy. Without my "Yaoyi", my life would never be as pleasant. I would even miss the most spectacular cuisines in my life.

I can never express enough gratitude to my fiancee, Huan. She is always kind, supportive and lovable. She always stands by my side and walks me through the dark time. Even our occasional disagreements turn out to be my precious. I cannot be more lucky to get to share my life with her.

I can of course never forget the endless love and support from all my family members, without whom I can never come this far.

Thank you, to all the people who have made this thesis possible and because of whom this journey will be a priceless memory forever!

Table of Contents

Preface ii

Foreword iii

Dedication iii

Acknowledgements iv

Table of Contents vii

List of Tables xi

List of Figures xiii

List of Abbreviations xvii

Chapter 1: Introduction 1
- 1.1 Coevolution between Supermassive Black Holes and Galaxies 1
- 1.2 AGN Feedback in a Nutshell 3
- 1.3 Quasar-mode AGN Feedback 4
- 1.4 Quasar-driven Outflows in Ultraluminous Infrared Galaxies (Chapter 2 & 3) . . . 7
  - 1.4.1 How Are Quasar-driven Outflows Launched? (Chapter 2) 7
  - 1.4.2 How Far Can Quasar-driven Outflows Reach? (Chapter 3) 9
- 1.5 AGN Feedback in the Dwarf Galaxy Regime? (Chapter 4 & 5) 10
- 1.6 Thesis Outline 12

Chapter 2: Lyman Alpha Emission and Highly Ionized O VI and N V Outflows in Ultraluminous Infrared Galaxies 14
- 2.1 Introduction 14
- 2.2 HST and Ancillary Data on the ULIRGs 17
  - 2.2.1 HST/COS G130M Observations of ULIRGs 19
  - 2.2.2 HST/COS Data Reduction 21
  - 2.2.3 Ancillary Data and Measurements 22
- 2.3 Results from the HST Data Analysis 25
  - 2.3.1 Lyα Emission 26
  - 2.3.2 Continuum Luminosity at 1125 Å 39
  - 2.3.3 FUV Absorption Features 39

2.4 Origin of the Lyα Emission . . . 48
2.4.1 Effect of the AGN . . . 51
2.4.2 Effect of the Outflow . . . 53
2.4.3 Effect of Dust . . . 57
2.4.4 Overall Trends . . . 61
2.5 O VI and N V Absorbers in the ULIRGs . . . 62
2.5.1 Origin of the O VI and N V Absorbers . . . 62
2.5.2 Location and Energetics of the Outflows . . . 64
2.6 O VI and N V Absorbers in the Combined ULIRG + Quasar Sample . . . 66
2.6.1 Overall Incidence Rates and Regressions . . . 67
2.6.2 Dependence on the X-ray Properties . . . 70
2.6.3 Radiation Pressure as the Most Plausible Wind-Driving Mechanism . . . 75
2.6.4 The Effects of Stochasticity of AGN-Outflow Activity . . . 77
2.7 Summary . . . 78

Chapter 3: Elliptical Galaxy in the Making: The Dual Active Galactic Nuclei and Metal-enriched Halo of Mrk 273 . . . 82
3.1 Introduction . . . 82
3.2 Observation and Data Reduction . . . 86
3.2.1 Chandra Observations . . . 86
3.2.2 Ancillary Datasets . . . 87
3.3 Results . . . 88
3.3.1 Overview of the Chandra Data . . . 88
3.3.2 Nuclear Region (Region 1) . . . 92
3.3.3 Host Galaxy Region (Region 2) . . . 109
3.3.4 Ionization Cones and Outflow . . . 111
3.3.5 Southern Nebula (Region 3) . . . 115
3.3.6 NE-extended Nebula (Region 4) . . . 121
3.4 Discussion . . . 122
3.4.1 Origin of the Southern Nebula . . . 122
3.4.2 X-ray Nebulae at Different Merger Stages . . . 129
3.4.3 The α/Fe ratios in (U)LIRGs and Early-type Galaxies . . . 130
3.5 Conclusions . . . 131

Chapter 4: Integral Field Spectroscopy of Fast Outflows in Dwarf Galaxies with AGN . . . 134
4.1 Introduction . . . 134
4.2 Sample, Observations, & Data Reduction . . . 137
4.2.1 Sample . . . 137
4.2.2 Observations . . . 138
4.2.3 Data Reduction . . . 141
4.3 Analysis . . . 143
4.3.1 Voronoi Binning . . . 143
4.3.2 Spectral Fits . . . 144
4.3.3 Non-Parametric Measurements of the Emission Line Profiles . . . 147
4.3.4 AGN Luminosities . . . 148

4.3.5 Upper Limits on the Star Formation Rates 149
4.4 Outflows Detected in the Sample 150
4.4.1 Gas Kinematics across Our Sample 154
4.4.2 Spatial Extents of the Outflows 158
4.4.3 Outflow Ionization: AGN or Shocks? 161
4.4.4 Electron Densities of the Outflows 169
4.4.5 Dust Extinction of the Outflows 170
4.4.6 Comparison with the Keck/LRIS Data 170
4.5 Discussion 172
4.5.1 Energetics of the Outflows 172
4.5.2 Comparison with More Luminous AGN 178
4.5.3 What Drives these Outflows: AGN or Starbursts? 182
4.5.4 Does the Outflowing Gas Escape the Galaxies? 185
4.6 Conclusions 187

Chapter 5: Fast UV Outflows and Strong He II Emission in Dwarf Galaxies with AGN 191
5.1 Introduction 191
5.2 HST and Ancillary Data 193
5.2.1 HST/COS Observations 193
5.2.2 Data Reduction and Ancillary Data 194
5.3 Outflows Traced by Blueshifted Absorption Features 196
5.3.1 Detection and Characterization of Outflows 196
5.3.2 The Outflow in J0954+47 200
5.4 He II λ1640 Emission 207
5.4.1 Detection and Basic Properties 207
5.4.2 Blueshifted He II λ1640 Emission Tracing Highly-ionized Outflow in J1009+26? 210
5.5 Summary 211

Chapter 6: Summary and Future Work 213
6.1 AGN Feedback in ULIRGs 213
6.1.1 Summary 213
6.1.2 Future Work 214
6.2 AGN Feedback in Dwarf Galaxies 216
6.2.1 Summary 216
6.2.2 Future Work 217

Appendix A: Appendix for Chapter 2 219
A.1 Notes on Individual Objects 219

Appendix B: Appendix for Chapter 3 222
B.1 Spectral Analysis of Mrk 273x 222

Appendix C: Appendix for Chapter 4 224
C.1 Results on Individual Objects 224

C.1.1 J0100−01 224
C.1.2 J0811+23 232
C.1.3 J0840+18 232
C.1.4 J0842+03 235
C.1.5 J0906+56 242
C.1.6 J0954+47 250
C.1.7 J1005+12 254
C.1.8 J1009+26 258

Appendix D: Appendix for Chapter 5 264
D.1 AGN Luminosity and SFR of J0954+47 264
D.2 Full G160M Spectra of Our Objects 265

Appendix E: Facilities and Software 269
E.1 Facilities 269
E.2 Softwares 269

List of Tables

2.1 Basic Properties of the ULIRGs in the Sample 18
2.1 Basic Properties of the ULIRGs in the Sample 20
2.2 Summary of the HST/COS G130M Observations 21
2.3 Lyα Measurements 30
2.3 Lyα Measurements 32
2.4 Optical Spectroscopic Measurements 36
2.4 Optical Spectroscopic Measurements 38
2.5 Properties of the O VI and N V Absorption Features 42
2.5 Properties of the O VI and N V Absorption Features 44
2.6 Correlation Tests with the Lyα Properties 50
2.6 Correlation Tests with the Lyα Properties 51
2.7 Estimated Outflow Energetics for O VI and N V Absorptions 63
2.8 Incidence Rates of O VI and N V Absorbers in the Combined ULIRG + Quasar Sample 69
2.8 Incidence Rates of O VI and N V Absorbers in the Combined ULIRG + Quasar Sample 70
2.9 Regression Analysis on the O VI and N V Absorbers in the Combined ULIRG+Quasar Sample 73
2.9 Regression Analysis on the O VI and N V Absorbers in the Combined ULIRG+Quasar Sample 75

3.1 Summary of Counts in the Data Sets 94
3.2 Results from Fits of the Individual SW and NE Nuclei 102
3.3 Comparison among the Physical Properties of the Thermal Gas Component in Different Regions 110
3.4 Properties of the X-ray Nebulae within the three (U)LIRGs 130

4.1 Properties of the Targets 138
4.2 Summary of Observations 139
4.3 Kinematic Properties of the Targets 152
4.3 Kinematic Properties of the Targets 153
4.3 Kinematic Properties of the Targets 155
4.4 Energetics of the Outflows 177
4.5 Outflow Escape Fractions 186

5.1 Properties of the Targets 195
5.2 Properties of the Outflows 201

List of Figures

1.1 The M_{BH}-σ relation for galaxies with dynamical measurements. 2
1.2 A summary of major observational evidence for AGN feedback. 4
1.3 Neutral gas outflow in the nearby quasar/ULIRG Mrk 231. 8
1.4 Suppression of stellar mass to dark matter halo mass ratio due to AGN feedback. 11

2.1 The X-ray to optical spectral index α_{OX} versus the X-ray to FUV spectral index $\alpha_{UV,X}$ for the quasars in Paper I. 24
2.2 Lyα profiles of the 14 objects with clear Lyα emission and the one with a potential detection F07599. 28
2.3 Example of a line profile illustrating the various non-parametric kinematic parameters. 29
2.4 Comparison of Lyα profiles with [O III] λ5007 emission lines. 31
2.5 Comparison of Lyα profiles with Hα emission lines. 33
2.6 Best fits to the O VI $\lambda\lambda$1032, 1038 and N V $\lambda\lambda$1238, 1243 absorption features detected. 47
2.7 The Lyα EWs for the ULIRGs versus AGN luminosities and AGN fractions. . . . 52
2.8 The 80-percentile velocities v_{80} of Lyα for the ULIRGs versus AGN luminosities and AGN fractions. 52
2.9 The Lyα escape fractions for the ULIRGs versus AGN luminosities and AGN fractions. 53
2.10 Comparisons of the kinematic properties derived from Lyα and [O III] λ5007. . . 54
2.11 The Lyα EWs (left) and Lyα escape fractions as functions of the 80-percentile velocities v_{80} of [O III] λ5007 emission lines. 56
2.12 Comparison between the Lyα and Na I D $\lambda\lambda$5890, 5896 profiles for sources F05189, F11119 and Mrk 231 57
2.13 Lyα escape fractions as a function of the color excess $E(B-V)$. 58
2.14 f_{esc}(Lyα) as a function of $E(B-V)$ from a simple model reflecting the effect of mixing two ionized gas clouds. 59
2.15 Velocity-integrated EWs, W_{eq}, depth-weighted velocities, v_{wtavg} and depth-weighted velocity dispersions, σ_{rms} for absorption features 74
2.16 Same as Fig. 2.15 but as function of the logarithm of the X-ray absorbing column densities N_H(X-ray). 74

3.1 Merged and smoothed X-ray images from all observations. 89

3.2 Adaptively smoothed images from all combined observations. 90
3.3 The different spatial regions used for the analyses. 91
3.4 Image of the Nuclear Region in the 4-6 keV band, with sector annuli used to extract the radial profiles from the image. 93
3.5 The spectral extraction regions for the SW and NE nuclei. 94
3.6 The original spectra of the SW nucleus. 95
3.7 Best fit for the spectra of SW nucleus. 96
3.8 The original spectra of the NE nucleus. 99
3.9 Best fit for the spectra of NE nucleus. 99
3.10 Pseudo slits on the Nuclear Region. 103
3.11 Spectra across the Nuclear Region. 104
3.12 Best fit of the Nuclear Region. 104
3.13 Best fit of the Host Galaxy Region. 111
3.14 Analyses of Region 2. 112
3.15 1-3 keV to 0.4-1 keV flux ratio map. 112
3.16 Best fit to the Southern Nebula 117
3.17 The probability contours of the Si (Ne,Mg) and Fe abundances for the Southern Nebula. 118
3.18 Image of Mg XI 1.34 keV emission. 120
3.19 Spectra from Si-bright region and Mg-bright region. 121
3.20 Best fit of the NE-extended Nebula. 122
3.21 Comparison of the nebula emission from (U)LIRGs and those from other galaxies with similar stellar mass. 128

4.1 Examples of fits to the [O III] $\lambda\lambda$4959, 5007 line profiles. 143
4.2 Examples of fits to the [O III] $\lambda\lambda$4959, 5007 line profiles. 144
4.3 Example of a line profile illustrating the various non-parametric kinematic parameters. 147
4.5 Same as Fig. 4.4 but for line width W_{80} (in units of km s^{-1}). 157
4.6 [O III]/Hβ vs [S II]/Hα for the C2 and C1 components of J0842+03. 162
4.7 Same as Fig. 4.6 but for the C3 (black) and C2 (gray) components of J0906+56. 162
4.8 [S II]/Hα ratios versus gas velocity dispersions for the outflow components in J0842+03 (top) and J0906+56 (bottom) based on the GMOS data. 162
4.9 [O II]/[O III] vs [O III]/Hβ for the outflow components of all seven targets. 163
4.10 [O III]/Hβ ratios versus gas velocity dispersions for the outflowing gas in all seven targets. 164
4.11 [O III] λ5007 line widths W_{80} vs [O III] λ5007 luminosities for the seven targets with detected outflows. 179
4.12 Ratios of the kinetic energy outflow rates to the AGN bolometric luminosities as a function of the AGN bolometric luminosties and H-band absolute magnitudes . 180

5.1 The fit to the C IV absorption feature in J0906+56. 198
5.2 The C II λ1335, Si IV λ1394, Si II λ1526, and C IV λ1550 absorption features in J0954+47. 199

5.3 Phase plot showing the ionization solutions for the entire outflow and the high-v outflow of J0954+47. 200
5.4 Outflow velocity (v_{50}) as function of star formation rate and circular velocity. . . 208
5.5 **Left:** Ratio of kinetic energy outflow rate to AGN luminosity as a function of AGN luminosity for J0954+47. **Right:** Momentum outflow rate versus expected momentum injection rate from the star formation activity for J0954+47. 209
5.6 He II λ1640 emission line profile compared with C IV λ1550, He II λ4686 and [O III] λ5007 emission line profiles, respectively. 210

B.1 The spectra and best fit model for Mrk 273x. 223

C.1 Voronoi-binned maps of the [O III] λ5007 flux and kinematics in J0100−01. . . . 225
C.2 Maps of the stellar median velocity and velocity dispersion in J0100−01. 226
C.3 Top panel: Radial profiles of the [O III] λ5007 fluxes from the two velocity components of J0100−01; Bottom panel: C2/C1 flux ratios on a logarithmic scale as a function of distance from the spaxel with peak emission line flux. 227
C.4 Same as Fig. C.1 but for J0811+23, where a single Gaussian component is sufficient to fit the [O III] λ5007 line profiles. 230
C.5 Same as Fig. C.2 but for J0811+23. 231
C.6 Same as the top panel of Fig. C.3 but for J0811+23. 231
C.7 Same as Fig. C.4 but for J0840+18, where a single Gaussian component is sufficient to fit the [O III] λ5007 line profiles. This is the only object in our sample without a clear sign of outflow. 233
C.8 Same as Fig. C.5 but for J0840+18. 233
C.9 Same as Fig. C.6 but for J0840+18. 234
C.10 Same as Fig. C.1 but for the GMOS data (left) and KCWI data (right) of J0842+03. 236
C.11 Same as Fig. C.2 but for J0842+03. 237
C.12 Same as Fig. C.3 but for the GMOS data (left) and KCWI data (right) of J0842+03. 238
C.13 Emission line diagnosis for the C1 component of J0842+03. 239
C.14 Same as Fig. C.13 but for the component C2. 240
C.15 Same as Fig. C.10 but for the GMOS data (left) and KCWI data (right) of J0906+56, where three velocity components C1, C2, and C3 are needed to adequately fit the emission-line profiles. 243
C.16 Same as Fig. C.2 but for J0906+56. 244
C.17 Same as Fig. C.3 but for the GMOS data (left) and KCWI data (right) of J0906+56. 244
C.18 Emission line diagnosis for the sum of the host component C1 + outflow component C2 of J0906+56. 245
C.19 Same as Fig. C.18 but for the outflow component C3. 246
C.20 Same as Fig. C.1 but for J0954+47 based on the KCWI data. 251
C.21 Same as Fig. C.2 but for J0954+47. 252
C.22 Same as Fig. C.3 but for J0954+47. 253
C.23 Same as Fig. C.1 but for J1005+12. 255
C.24 Same as Fig. C.2 but for J1005+12. 256

C.25 Same as Fig. C.3 but for J1005+12. Contrary to Fig. C.3, the data points of C1 and C2 components beyond the maximal spatial extent of the C3 component are shown instead. 257
C.26 Same as Fig. C.1 but for J1009+26. 261
C.27 Same as Fig. C.2 but for J1009+26. 262
C.28 Same as Fig. C.3 but for J1009+26. 263

D.1 Full G160M spectrum for J0906+56. The expected locations of strong transitions at the systemic velocity are marked in red dashed lines. The expected locations of strong z=0 foreground absorption features are marked in blue dashed lines. . . . 266
D.2 Same as Fig. D.1 but for J0954+47. 267
D.3 Same as Fig. D.1 but for J1009+26. 268

List of Abbreviations

AO	Adaptive Optics
AGN	Active Galactic Nucleus
BAL	Broad Absorption Line
COS	Cosmic Origin Spectrograph
CGM	Circumgalactic Medium
DESI	Dark Energy Spectroscopic Instrument
eROSITA	the extended ROentgen Survey with an Imaging Telescope Array
EW	Equivalent Width
FUV	Far-Ultraviolet
HST	Hubble Space Telescope
IFS	Integral Field Spectroscopy
IGM	Intergalactic Medium
ISM	Interstellar Medium
JWST	James Webb Space Telescop
KCWI	Keck Cosmic Web Imager
MUSE	Multi Unit Spectroscopic Explorer
NAL	Narrow Absorption Line
NIRSPEC	Near Infrared Spectrograph
NSA	NASA Sloan Atlas
PFS	Prime Focus Spectrograph
QSO	Quasi-stellar Object
SDSS	Sloan Digital Sky Survey
SMBH	Supermassive Black Hole
UFO	Ultra-Fast Outflow
ULIRG	Ultraluminous Infrared Galaxy
VLA	Karl G. Jansky Very Large Array
VLT	Very Large Telescope
WA	Warm Absorber
XRISM	X-Ray Imaging and Spectroscopy Mission

Chapter 1: Introduction

1.1 Coevolution between Supermassive Black Holes and Galaxies

During the 1950s–1980s, it was heavily debated what powers a class of exceptionally luminous extragalactic objects now known as Quasar/active galactic nuclei (AGN) [e.g. Baade and Minkowski, 1954, Burbidge et al., 1963, Matthews and Sandage, 1963, Rees, 1984]. The prevailing idea was that the energy comes from the accretion of matter onto supermassive black holes (SMBHs) residing within the nuclei of galaxies, which is now widely accepted by the community. Contrary to the impression left by the "supermassive" in its name, a SMBH is, in fact, tiny when compared to the host galaxy, with a typical BH-to-host mass ratio of $\sim$0.1%. The sphere-of-influence radius of a SMBH is $GM_{BH}/\sigma^2 \simeq 1$ to 100 pc (M_{BH} is the black hole mass, and σ is the stellar velocity dispersion of the host galaxy), in comparison the typical size of the dark matter halo of a galaxy is on the order of several hundred kpc. Therefore, it is more than surprising that a relatively tight correlation exists between the mass of the SMBH and the velocity dispersion of the galaxy or classic bulge [M_{BH}-σ relation; e.g. Fig. 1.1; Ferrarese and Merritt, 2000, Gebhardt et al., 2000, Gültekin et al., 2009, Kormendy and Ho, 2013b]. Apparently, the SMBH and the galaxy know each other well, but how?

One important mechanism for a SMBH to affect the host galaxy is through AGN feedback. The accretion onto SMBH releases a large portion of the potential energy, which is more than

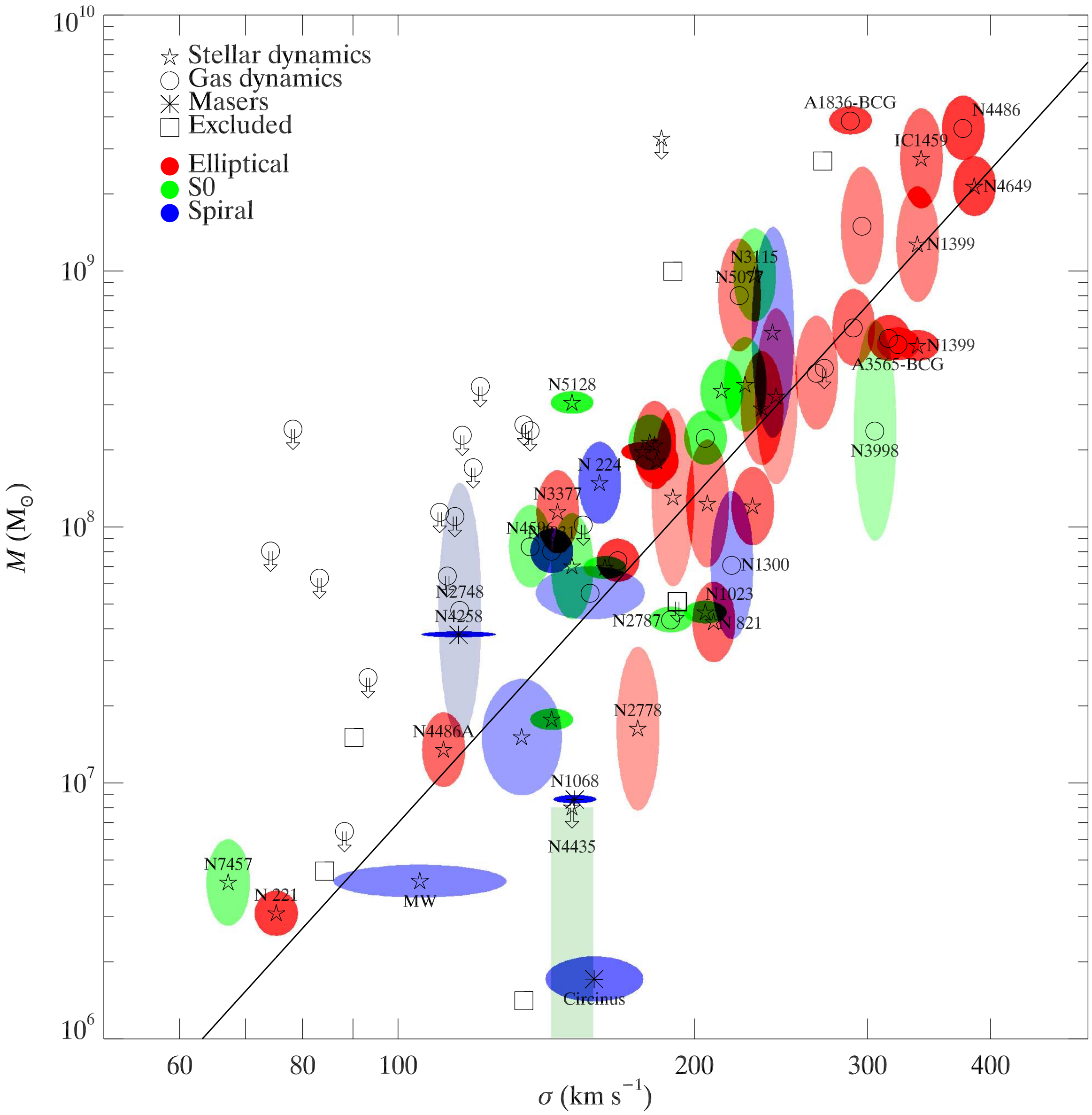

Figure 1.1: The M_{BH}-σ relation for galaxies with dynamical measurements. The best-fit relation is shown in black line: $M_{BH} = 10^{8.12} M_\odot (\sigma/200\ km\ s^{-1})^{4.24}$. The method of BH mass measurement is indicated by symbol: stellar dynamical (pentagrams), gas dynamical (circles), masers (asterisks). Arrows indicate 3σ upper limits on BH mass. For clarity, error boxes are plotted only for upper limits that are close to or below the best-fit relation. The Hubble type of the host galaxy is indicated by the color of the error ellipse: elliptical (red), S0 (green), and spiral (blue). The saturation of the colors in the error ellipses or boxes is inversely proportional to the area of the ellipse or box. Sources shown in squares are not included in the fit. The mass uncertainty for NGC 4258 has been plotted much larger than its actual value so that it will show on this plot. Image credit: Gültekin et al. [2009].

enough to unbind the galaxy if the energy is well coupled to the galaxy. The binding energy of a galaxy is on the order of $E_{gal} \simeq M_{gas}\sigma^2$, where M_{gal} is the mass of the galaxy and σ is the velocity dispersion of it. The typical black hole mass to galaxy mass ratio, M_{BH}/M_{gas} is observed to be $\sim 1.4 \times 10^{-3}$ [Gebhardt et al., 2000, Merritt and Ferrarese, 2001, Häring and Rix, 2004] and σ of galaxies are in general <400 km s^{-1}. The energy released by the accretion onto a black hole is $E_{BH} = 0.1 M_{BH} c^2$, assuming a typical radiative efficiency of 10%. Therefore, E_{BH}/E_{gal} is $M_{gas}/M_{BH}(c/\sigma)^2 \gtrsim 80$. If a portion of the energy released by the accretion is coupled to the material within the galaxy, then the AGN can impact the host galaxy significantly. Such process is broadly termed as AGN feedback.

1.2 AGN Feedback in a Nutshell

Broadly speaking, AGN feedback may be effective in (i) quenching the star formation [e.g. Zubovas and King, 2012], (ii) suppressing the baryon-to-dark matter mass ratio at the higher mass end [e.g. Croton et al., 2006], (iii) shaping galaxy morphology [e.g. Dubois et al., 2016], (iv) impacting the circum/intergalactic medium CGM/IGM][e.g. Tumlinson et al., 2017], and (v) regulating supermassive black hole (SMBH) accretion [Hopkins et al., 2016, Volonteri et al., 2016]. From observations, evidence of AGN feedback have been accumulating (see Fig. 1.2 for a list of major observational evidence of AGN feedback). In (semi)analytic models and modern numerical simulations, AGN feedback has been modeled carefully to reproduce the physical properties of massive galaxies we see today [e.g. Silk and Rees, 1998, Di Matteo et al., 2005, Hopkins et al., 2006, Sijacki et al., 2007, Somerville et al., 2008, Booth and Schaye, 2009, Schaye et al., 2015, Weinberger et al., 2017, Nelson et al., 2019].

Evidence	Quality
High-velocity broad absorption lines in quasars	Strong
Strong winds in AGN	Strong
1,000 km s^{-1} galactic outflows	Strong
Bubbles and ripples in brightest cluster galaxies	Strong
Giant radio galaxies	Strong
Lack of high star-formation rate in cool cluster cores	Indirect
M–σ relation	Indirect
Red and dead galaxies	Indirect
Lack of high lambda, moderate N_H, quasars	Indirect
Steep L–T relation in low T clusters and groups	Indirect

Figure 1.2: A summary of major observational evidence for AGN feedback. Image credit: Fabian [2012]

Two major modes of AGN feedback have been explored extensively in past and current studies: The first mode is the quasar-mode or radiative mode, where a luminous quasar drives a fast and energetic galactic outflow that either expel the gas out of the galaxy and/or heat the gas within the galaxy to suppress the star formation within the system. The second mode is the radio-mode or maintenance mode, where the radio jets launched by the AGN heat the hot gas in the intra-cluster medium (ICM), intra-group medium (IGM) or the interstellar medium (ISM) of massive galaxies and prevent the hot gas from cooling and eventually forming new stars.

1.3 Quasar-mode AGN Feedback

The quasar-mode/radiative-mode feedback though quasar/AGN-driven outflows is the focus of this thesis.

A simple calculation assuming momentum balance suggests that quasar-mode feedback may lead to the observed form of the M_{BH}-σ relation where approximately $M_{BH} \propto \sigma^4$. As pointed out by Silk and Rees [1998, and references therein], the Eddington luminosity of a SMBH is $L_{Edd} = 4\pi G M_{BH} m_p c/\sigma_T$, where the spherically-symmetric accretion onto the SMBH under gravity is balanced by the radiation pressure. Here G is the Gravitational constant, M_{BH} is the mass of the SMBH, m_p is the proton mass, c is the speed of light, and σ_T is the cross-section of Thomson scattering. Imagining that the radiation pressure (L_{Edd}/c) from an Eddington-limited quasar has swept the gas, of mass $M_{gas} = fM_{gal}$, all the way to the edge of the galaxy (which is in principle a galaxy-wide outflow), then the balance between the outward radiation force and the inward one due to gravity gives

$$\frac{4\pi G M_{BH} m_p}{\sigma_T} = \frac{L_{Edd}}{c} = \frac{G M_{gal} M_{gas}}{r^2} = \frac{f G M_{gal}^2}{r^2} = \frac{fG}{r^2}(\frac{2\sigma^2 r}{G})^2 \tag{1.1}$$

So $M_{BH} = \frac{f\sigma_T}{\pi G^2 m_p}\sigma^4$ where σ is the velocity dispersion of the galaxy, M_{gal} is the mass of the galaxy, M_{gas} is the mass of the swept gas which is a fraction, f, of M_{gal}. For the last equality above, the galaxy is assumed to be isothermal with a radius r.

Evidence of quasar-mode feedback has been accumulating rapidly over the past decades. Energetic AGN-driven outflows are observed in low-redshift quasars and Seyfert galaxies [e.g. Veilleux, 1991, Crenshaw and Kraemer, 2000, Crenshaw et al., 2010, Liu et al., 2013b, Zakamska and Greene, 2014, Wylezalek et al., 2020], luminous quasars at the peak of cosmic star formation [e.g. Harrison et al., 2012, Carniani et al., 2015, Zakamska et al., 2016b, Bischetti et al., 2017, Brusa et al., 2018], and all the way to z$\gtrsim$ 6 quasars at the end of reionization era [e.g. Maiolino et al., 2012, Bischetti et al., 2019, 2022]. Such outflows are observed to range from the <kpc, fast quasar-wind traced by ultra-frast outflows (UFO) and warm absorbers [WA; e.g. Tombesi et al., 2010, 2015, Nardini et al., 2015, King and Pounds, 2015], and broad absorption lines (BAL) and

narrow absorption lines [NAL; e.g. Hamann et al., 1997b, 2002, Trump et al., 2006, Arav et al., 2008, Knigge et al., 2008, Hamann et al., 2011, Gibson et al., 2009, Allen et al., 2011] to kpc-scale galactic winds in ionized [e.g. Liu et al., 2013a,b, Harrison et al., 2014, Westmoquette et al., 2013, Ramos Almeida et al., 2019], neutral [e.g. Rupke and Veilleux, 2011, 2013a,b, 2015, Morganti et al., 2016, Rupke et al., 2017] and molecular phases [e.g. Veilleux et al., 2013a, González-Alfonso et al., 2014, Cicone et al., 2014, Feruglio et al., 2015, Aalto et al., 2015, Veilleux et al., 2017, 2020], likely blending seamlessly with the circumgalactic medium [CGM; e.g. Tumlinson et al., 2017].

Despite the decades of effort devoted by the community, the physical details and effectiveness of quasar-mode feedback is still under debate. For example, the driving mechanism of the quasar wind is still unsettled [e.g. Zubovas and King, 2014, Faucher-Giguère and Quataert, 2012, Richings and Faucher-Giguère, 2018a,b, Ishibashi et al., 2018]; the impact from quasar-driven outflows on the interstellar medium of galaxies may be limited [Husemann et al., 2013, 2016, Karouzos et al., 2016, Villar-Martín et al., 2016, Bae et al., 2017]; the CGM may be "vulnerable" to quasar-driven outflows [e.g. Veilleux et al., 2014, Tumlinson et al., 2017, Liu et al., 2019]; the existence of quasar-mode feedback in the first generation of massive galaxies is controversial [e.g. Novak et al., 2020]. We are still lack of a comprehensive understanding of quasar-mode feedback (and more broadly, AGN feedback).

1.4 Quasar-driven Outflows in Ultraluminous Infrared Galaxies (Chapter 2 & 3)

In the local universe, AGN-dominated ultraluminous infrared galaxies (ULIRGs; they are defined as galaxies with total infrared luminosity $L_{IR} \geq 1 \times 10^{12} L_{\odot}$, and they are giant systems with mass $\simeq$ 1–3 M_*) are arguably the best laboratories to examine AGN feedback in the form of quasar-driven outflow. In a popular galaxy evolution model, the merging of two gas-rich star-forming galaxies will lead to an early type galaxies with little star formation. In this process, there is a ULIRG phase in the late merging stage where strong AGN feedback via outflows driven by the quasars (likely buried in dust) will expel the gas outflow of the system or heat the gas within it, so that the star formation will be largely quenched, leaving the galaxy "red and dead" [e.g. Sanders et al., 1988, Hopkins et al., 2006].

Energetic, kpc-scale outflows are indeed frequently observed in such systems in ionized, neutral and molecular phases [e.g. Fig. 1.3; Rupke et al., 2005a,b,c, Sturm et al., 2011, Veilleux et al., 2013a, Spoon et al., 2013, González-Alfonso et al., 2014, Feruglio et al., 2015, Aalto et al., 2015, Stone et al., 2016], suggesting effective, on-going quasar-mode feedback. However, the properties of both the nuclear, <kpc portion and the large-scale, $\gtrsim$10 kpc portion of such quasar-driven outflows are largely unknown. As a result, two critical questions remain unanswered:

1.4.1 How Are Quasar-driven Outflows Launched? (Chapter 2)

A complete picture of AGN feedback in ULIRGs relies crucially on the knowledge of how the accretion energy released is coupled to the ambient gas near the quasar/AGN and drives the

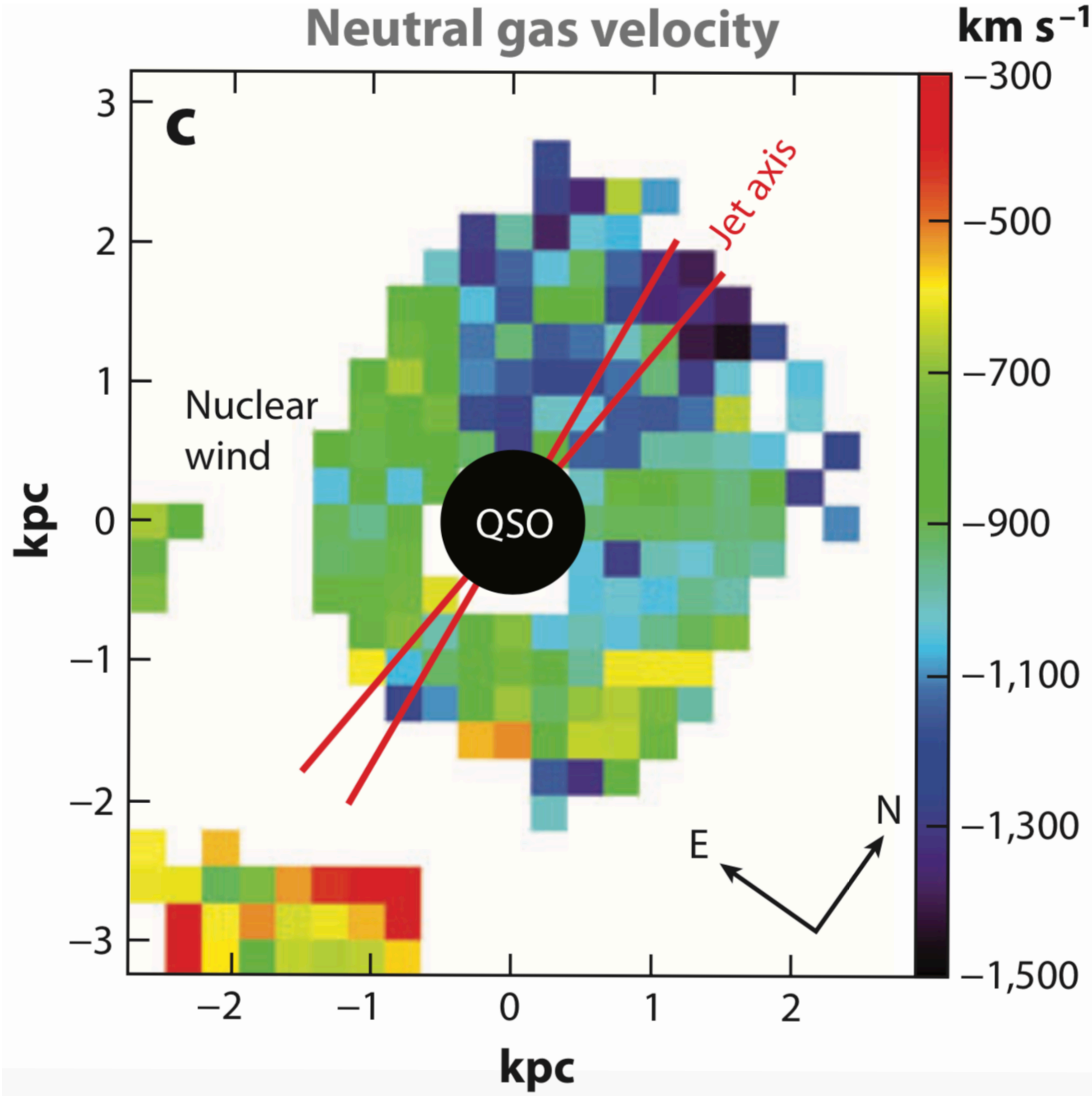

Figure 1.3: Neutral gas outflow in the nearby quasar/ULIRG Mrk 231. The colored map shows the spatially resolved velocity field of the Na I D absorption line from Rupke and Veilleux [2011], which traces outflow extending from the nucleus up to 2–3 kpc in all directions (as projected in the plane of the sky).. The central QSO is masked by the black filled circle, and the radio jet axis is indicated by the red solid lines. Image credit: Rupke and Veilleux [2011].

outflow outwards. It is the nuclear (<kpc) outflows that may be used to decide how those powerful quasar/AGN winds are launched. For example, in a popular blast-wave model for quasar-mode feedback, a fast, nuclear, hot wind shocks the surrounding ISM, which then eventually cools to reform the molecular gas after having acquired a significant fraction of the kinetic energy of the initial hot wind [e.g. Faucher-Giguère and Quataert, 2012, Richings and Faucher-Giguère, 2018a,b]. The detection of the nuclear, warm-hot (T $\sim 10^{5.5}$ K; most likely traced by O VI $\lambda\lambda$1032, 1038, N V $\lambda\lambda$1238, 1243, and perhaps traced by Lyα) outflow phase associated with the cooling shocked ISM is critical to confirm this scenario.

In ULIRGs, the nuclear region is usually heavily obscured. The nuclear outflows cannot be observed easily and has thus not been examined systematically with a coherent sample. As a result, it is not entirely clear how the dust enshrouded quasars/AGN drive the observed kpc-scale outflows in these systems. To shed new light on this issue, in Chapter 2, I present a dedicated investigation of the blueshifted Lyα emission likely closely related to the outflow and the highly ionized, <kpc scale, O VI $\lambda\lambda$1032, 1038 and N V $\lambda\lambda$1238, 1243 outflows in a sample of nearby AGN-dominated ULIRGs through *HST*/COS far-ultraviolet (FUV) spectroscopy.

1.4.2 How Far Can Quasar-driven Outflows Reach? (Chapter 3)

The ultimate spatial extent of the outflows in ULIRGs is also not well constrained. Detecting outflows on large spatial scale ($\gtrsim$ 10 kpc) is vital to determine how much gas may escape the system, which is a key evaluation for the effectiveness of AGN feedback. It will also reveal the amount of energy injected into the CGM and the amount of metals available to enrich it. There is an emerging scenario that the star formation activity within the galaxy is heavily affected by the properties of the CGM, the critical interface through which gas flows inwards from the ICM and flows outwards from the ISM [Tumlinson et al., 2017]. An investigation of the impact from outflows on CGM contributes to our understanding of the baryon cycle of galaxies and the rise-and-fall of star formation activities over time. The low surface brightness nature of the outflowing gas breaking out from the interstellar medium requires deep observations. To depict the fate of outflowing gas, in Chapter 3, I describe a case study of the giant, X-ray emitting gaseous halo around a nearby ULIRG with deep *Chandra* imaging spectroscopy. In addition, the deep X-ray data also reveal the dual AGN activity and hot, X-ray emitting gas on kpc-scale in this object.

1.5 AGN Feedback in the Dwarf Galaxy Regime? (Chapter 4 & 5)

So far, the discussion of AGN feedback in literature has mainly been confined to massive galaxies (e.g., see Fig. 1.4). Feedback from stellar processes, with stellar wind and supernovae as the two most popular mechanisms, are deemed important in the evolution of dwarf galaxies. The feasibility of AGN feedback in dwarf galaxies may be overlooked, which is resulted from at least two reasons: on the one hand, only a small fraction of dwarf galaxies are found to host AGN [See Greene et al., 2019, for a recent review], and on the other hand, stellar feedback seems adequate to explain many of the observed dwarf galaxy properties [see Heckman and Thompson, 2017, for a recent review]. Furthermore, while many modern cosmological simulations suggest no clear requirement of AGN feedback in dwarf galaxies, it is primarily stemed from the fact that no black holes, and thus no AGN are "formed" in low mass galaxies in such simulations. Nevertheless, a series of recent analytic evaluations emphasize the likely importance of AGN feedback in dwarf galaxies [e.g. Silk, 2017]. Dedicated simulations carefully putting AGN in

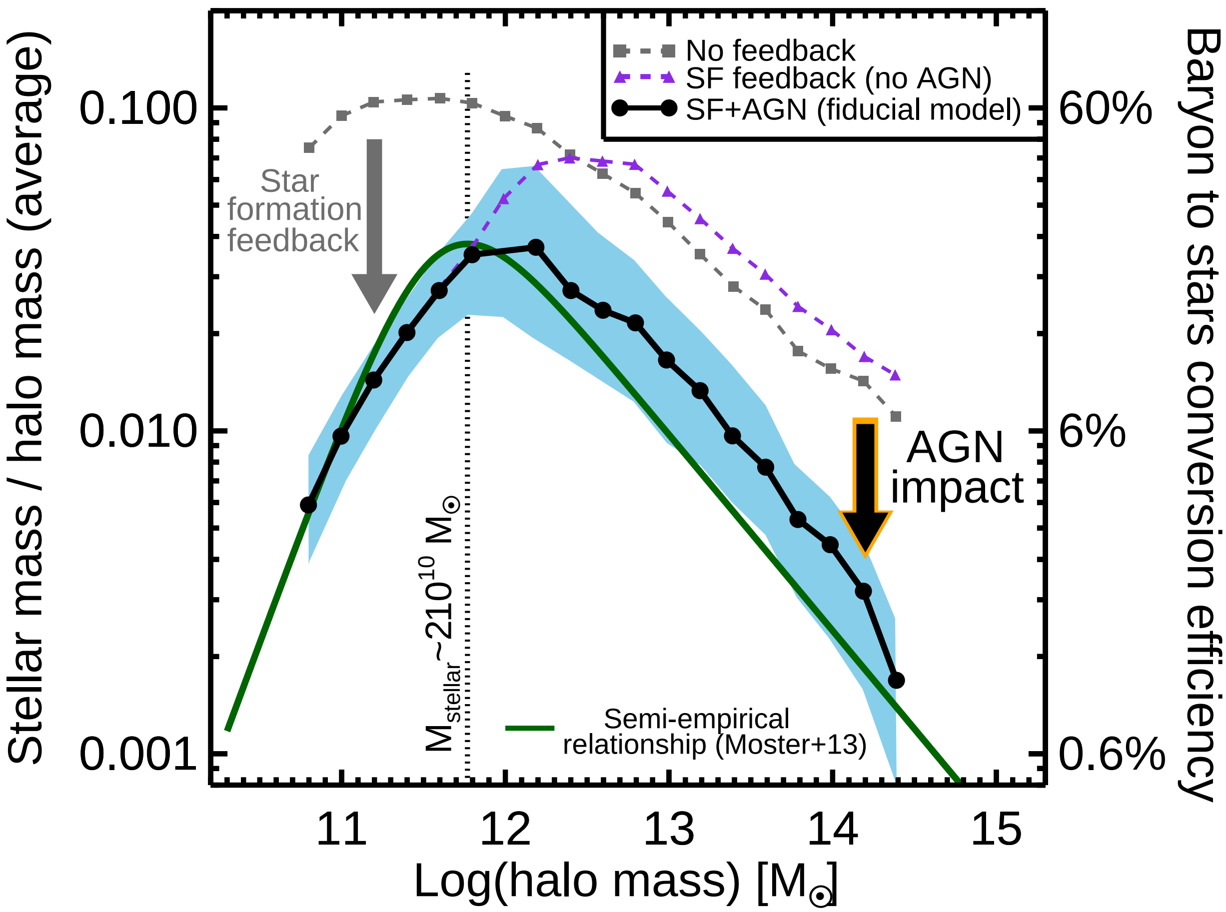

Figure 1.4: The stellar mass to dark matter halo mass ratio as a function of halo mass from three different runs of the simulation in Somerville et al. [2008] and from the semi-empirical relationship obtained in Moster et al. [2013]. The shaded region shows the 16th and 84th percentiles of the fiducial model that includes feedback from AGN and star formation (SF). The right y-axis shows the efficiency for turning baryons into stars ($M_{\rm stellar}/[f_b * M_{\rm halo}]$). In low mass haloes, the stellar feedback reduces the efficiency of converting baryons into stars. In massive haloes, AGN feedback is required in order to reduce the efficiency. Image credit: Harrison et al. [2018].

dwarf galaxies and considering their feedback do suggest tantalizing evidence for AGN feedback in those dwarf systems [e.g. Koudmani et al., 2019, 2020].

AGN do exist in dwarf galaxies, and the number of new discoveries keeps accumulating. In addition, recent studies have revealed increasing number of AGN in dwarf galaxies, and evidence exists that stellar feedback alone may not be able to reproduce certain properties of the present-day dwarf galaxies as expected [e.g. Garrison-Kimmel et al., 2013, McQuinn et al., 2019]. It is thus interesting to ask whether AGN feedback plays a role in the formation and evolution of dwarf galaxies. In Chapter 4 and Chapter 5, I present two pilot studies to explore this issue. In Chapter 4, I report a ground-based integral field spectroscopy survey (IFS) survey dedicated to examining the gas kinematics and dynamics in a sample of dwarf galaxies with AGN and suspected outflows. In Chapter 5, I describe an *HST*/COS FUV spectroscopy study of the absorption-feature traced outflows in three objects from the sample examined in Chapter 4.

1.6 Thesis Outline

Here I lay out again the three main questions addressed by this thesis:

- How are quasar-driven outflows launched in ULIRGs? *(Chapter 2)*
- How far can outflows reach in ULIRGs? *(Chapter 3)*
- Is there AGN Feedback in the dwarf galaxy regime? *(Chapter 4 and 5)*

The rest of the thesis is organized as follows. In Chapter 2, I present a dedicated investigation of the blueshifted Lyα emission and highly ionized O VI $\lambda\lambda$1032, 1038 and N V $\lambda\lambda$1238, 1243 outflows in a sample of nearby AGN-dominated ULIRGs through *HST*/COS FUV spectroscopy. In Chapter 3, I describe a case study of the giant, X-ray-emitting gaseous halo around a nearby ULIRG, as well as the dual AGN activity and hot ISM of the ULIRG, with deep *Chandra* imaging spectroscopy. In Chapter 4, I report a ground-based optical IFS survey dedicated to examining the gas kinematics and dynamics in a sample of dwarf galaxies with AGN and suspected outflows. In Chapter 5, I describe an *HST*/COS FUV spectroscopic study of the outflows and He II λ1640 emission lines in three objects from the sample examined in Chapter 4. Finally, in Chapter 6, I summarize the main conclusions of the whole thesis and lay out several paths forward.

Chapter 2: Lyman Alpha Emission and Highly Ionized O VI and N V Outflows in Ultraluminous Infrared Galaxies

2.1 Introduction

Major mergers of gas-rich galaxies, both near and far, are the paradise for magnificent starbursts and rapid growth of supermassive black holes. In the local universe, the majority of the ultraluminous infrared galaxies (ULIRGs) are mergers of gas-rich galaxies. The merger process drives the gas and dust to the central region of the system, fueling the (circum)nuclear starbursts and the rapid accretion of the supermassive black holes. As described by a popular evolution scenario, the merger system advances from the ULIRG phase to the dusty quasar phase, and then to a fully-exposed quasar phase, with the gas and dust either transformed into stars or expelled and/or heated by the galactic winds triggered by the quasar and starburst activities [e.g., Sanders et al., 1988, Veilleux et al., 2009b, Hickox and Alexander, 2018]. The ubiquity of galactic winds in local ULIRGs, dusty quasars, and luminous post-starburst galaxies supports this scenario. The observed winds extend over a large physical scale, from fast, nuclear winds on $\lesssim$pc scales all the way to galactic winds reaching $\gtrsim$10 kpc, blending smoothly with the circumgalactic medium [e.g., Martin, 2005, Rupke et al., 2005c, Martin, 2006, Tremonti et al., 2007, Martin and Bouché, 2009, Sturm et al., 2011, Rupke and Veilleux, 2013b, Veilleux et al., 2013c,b, Cicone et al., 2014, Veilleux et al., 2014, Tombesi et al., 2015, Rupke et al., 2017, Liu et al., 2019, Fluetsch et al., 2019, 2020, Lutz et al., 2020, Veilleux et al., 2020, for a review].

While the cooler, neutral and/or molecular phases on larger scale ($\gtrsim$kpc) often dominate the outflow energetics, it is the hotter, ionized phase of the wind that serves as the best probe for the driving mechanism of these winds. ULIRG F11119+3257, arguably the best example so far, possesses a massive, galactic scale (1–10 kpc) molecular and neutral-gas outflow apparently driven by the fast ($>$0.1 c), highly ionized (Fe XXV and Fe XXVI at $\sim$7 keV) nuclear wind [Tombesi et al., 2015, 2017, Veilleux et al., 2017]. While this result is intriguing, the faintness of the majority of ULIRGs at $\sim$ 7 keV, unlike many quasars, has impeded a statistically meaningful study of this phenomenon in most ULIRGs with current X-ray facilities.

The superb far-ultraviolet (FUV) sensitivity of the Cosmic Origins Spectrograph (COS) on the Hubble Space Telescope (HST) provides a powerful alternative tool for such study in the low-z universe. Rest-frame FUV spectroscopy has enabled a comprehensive study of the multi-phase nature of outflows, built upon the abundant spectral features arising from the high-ionization, low-ionization, and neutral phases of the outflowing gas [e.g., Chisholm et al., 2015, Tripp et al., 2011, Heckman et al., 2015, Hamann et al., 2019, Arav et al., 2020]. Up to now, only about a dozen ULIRGs have been studied with HST/COS data, but the results are fascinating. In Mrk 231, highly blueshifted Lyα emission (with respect to systemic velocity) is observed to coincide in velocity with the highly blueshifted absorption features tracing the fast outflow in this galaxy, suggesting an outflow-related origin for the Lyα emission [Veilleux et al., 2013c, 2016]. With a larger sample of 11 ULIRGs, Martin et al. [2015, hereafter M15] have shown that prominent, blueshifted Lyα emission down to -1000 km s^{-1} exists in about half of the objects, and they argued that the blueshifted Lyα emission originates from the clumps of gas condensing out of hot winds driven by the central starbursts [Thompson et al., 2016]. In addition, blueshifted absorption features from high-ionization species like O^{5+} and/or N^{4+} (114 and 77 eV are needed to produce these ions, respectively) and low-ionization species like Si^{+} and Fe^{+} are also detected in a few objects, providing unambiguous evidence of outflowing gas.

Despite the tantalizing evidence of FUV-detected outflows in the ULIRGs described above, the sample examined so far is small and incomplete, where AGN-dominated ULIRGs and matched quasars are largely missing. To address this issue, we have selected a more complete sample of ULIRGs and quasars to systematically study the gaseous environments along the merger sequence, from ULIRGs to quasars. In Veilleux et al. [2022] (hereafter Paper I), we presented the results from the first part of our study, focused on the highly-ionized gas outflows, traced by O VI $\lambda\lambda$1032, 1038 and N V $\lambda\lambda$1238, 1243 absorption features, in a sample of 33 local quasars. We found that the O VI and N V outflows are present in $\sim$61% of the sample, and the incidence rate and equivalent widths (EWs) of these highly ionized outflows are higher among X-ray weak or absorbed sources. Similarly, the flux-weighted outflow velocity dispersions are also the highest among the X-ray weakest sources. However, no significant correlation is visible between the flux-weighted outflow velocities/velocity dispersions and the other properties of the quasars and host galaxies.

In this paper, we report the results from an analysis of the Lyα emission and O VI and N V absorption features of the 21 ULIRGs in the sample [1], expanding on the results from Paper I by considering the combined ULIRG + quasar sample. In Sec. 2.2, we describe the HST/COS observations of the ULIRG sample, the reduction of the data sets, and the ancillary data from the

[1]While FUV studies analyze Si IV and C IV transitions along with the lines of O VI and N V, our spectra do not cover the Si IV and C IV doublets at the target redshifts.

literature. In Sec. 2.3, we present the analysis of the FUV spectra of the ULIRGs, focusing on Lyα emission in the first part and the O VI and N V absorption features in the second. In Sec. 2.4, we discuss the potential key factors that control the observed Lyα properties, and in Sec. 2.5, we examine the incidence rates and properties of the O VI and N V outflows. In Sec. 2.6, we search for trends between the O VI and/or N V outflow properties and the AGN/galaxy properties in the ULIRG+quasar sample. In Sec. 2.7, we summarize the main results of this paper. Throughout the paper, we adopt a ΛCDM cosmology with H_0 = 75 km s^{-1} Mpc^{-1}, $\Omega_{\rm m}$ = 0.3, and $\Omega_\Lambda = 0.7$.

2.2 HST and Ancillary Data on the ULIRGs

Table 2.1. Basic Properties of the ULIRGs in the Sample

Name	Short Name	z	$\log(\frac{L_{bol}}{L_\odot})$	Spectral Type	Merger Class	AGN Fraction	m_{FUV} (AB)	log(SX) [erg s^{-1}]	log(HX) [erg s^{-1}]	N_H(X-ray) [10^{22} cm^{-2}]	$\log(\lambda L_{1125})$	$\alpha_{UV,X}$
(1)	(2)	(3)	(4)	(5)	(6)	(7)	(8)	(9)	(10)	(11)	(12)	(13)
F01004−2237	F01004	0.117701[a]	12.36	HII	V	55	18.5	41.0	42.1	...	44.2	−3.0
QSO-B0157+001	Mrk 1014	0.16311[b]	12.70	S1	IVb	73^{+24}_{-27}	16.6	43.92±0.04	$43.83^{+0.11}_{-0.25}$	<0.009	45.3	−1.2
...	...	...	...	...	...	...	...	$44.00^{+0.04}_{-0.08}$	$43.86^{+0.04}_{-0.04}$	<0.009	...	...
F04103−2838	F04103	0.117464[b]	12.30	L	IVb	49	20.2	41.8	42.1	0.190	42.6	−1.4
F05189−2524	F05189	0.04288[c]	12.22	S2	IVb	71	19.1	43.4	43.4	7.83	42.8	−1.1
F07599+6508	F07599	0.1483[c]	12.58	S1	IVb	75	17.6	43.5	42.9	52.2	...	−2.5
F08572+3915:NW	F08572	0.0584[d]	12.22	L	IIIb	72	19.1	40.0	41.4	2.40	42.0	−3.4
F11119+3257	F11119	0.189[e]	12.64	S1	IVb	80	21.4	44.2	44.2	1.71	...	0.1
Z11598−0112	Z11598	0.150694[a]	12.49	S1	IVb	74	17.9	43.6	43.1	...	44.6	−0.9
F12072−0444	F12072	0.128360[a]	12.45	S2	IIIb	65	20.5	41.4	41.2	<0.01	42.9	−1.8
3C 273	3C 273	0.158339[b]	13.03	S1	IVb	95^{+5}_{-13}	13.3	$45.491^{+0.002}_{-0.002}$	$45.742^{+0.008}_{-0.008}$	<0.01	46.5	−0.9
...	...	...	...	...	...	...	...	$45.461^{+0.004}_{-0.004}$	$45.722^{+0.005}_{-0.006}$	<0.01	...	...
...	...	...	...	...	...	...	...	$45.591^{+0.002}_{-0.002}$	$45.820^{+0.004}_{-0.005}$	<0.01	...	...
...	...	...	...	...	...	...	...	$45.663^{+0.002}_{-0.001}$	$45.825^{+0.006}_{-0.006}$	<0.01	...	...
...	...	...	...	...	...	...	...	$45.461^{+0.003}_{-0.004}$	$45.67^{+0.01}_{-0.02}$	<0.01	...	...
...	...	...	...	...	...	...	...	$45.544^{+0.003}_{-0.003}$	$45.941^{+0.010}_{-0.007}$	<0.01	...	...

2.2.1 HST/COS G130M Observations of ULIRGs

Our sample is selected based on three criteria: (1) They are part of the 1-Jy sample of 118 local ULIRGs with z < 0.3 and $|b| > 30^{\circ}$ [hence modest Galactic extinctions; Kim and Sanders, 1998a]; (2) In order to address the role of AGN feedback in these systems, the ULIRGs have AGN signatures in the optical (AGN Type 1 or 2) or in the mid-infrared [Spitzer-derived AGN bolometric fraction $\gtrsim$40%; Veilleux et al., 2009b]. (3) They are the FUV-brightest ULIRGs of the 1-Jy sample with FUV magnitudes (AB) $m_{FUV} \lesssim 21$. These criteria result in a sample of 21 objects (Table 5.1): 15 of which were observed through the HST cycle 26 program (PID:15662; PI: Sylvain Veilleux), and the remaining 6 objects have archival COS G130M spectra of sufficient quality from three programs (PID: 12533, PI: C. Martin; PID: 12569, PI: S. Veilleux; PID: 12038: PI: J. Green). Among these 6 objects, QSO-B0157+001, 3C 273, and Mrk 231 were also studied in Paper I as they meet the criteria for QUEST quasars, and F01004−2237, Z11598−0112, and F12072−0444 were also studied in M15. In the following sections, we adopt the short names listed in Table 5.1 when referring to the objects in our sample.

The Cycle 26 HST/COS spectra presented in this paper were obtained in TIME-TAG mode through the PSA using the medium resolution FUV grating, G130M. Four focal plane offset positions were adopted to reduce the impact of fixed-pattern noise associated with the micro-channel plate. We got all four FP-POS settings for all targets, except for targets F04103, F14070, F21219, and F23233 with a central wavelength of 1291 Å. For these objects, we followed the COS2025 recommendations and used FP-POS = 3 and 4 to get equal exposures for segments A and B. The wavelength setting was adjusted according to the redshift of the target and was selected to optimize the number of strong lines that can be observed with G130M. At all but the

Table 2.1 (cont'd)

Name (1)	Short Name (2)	z (3)	$\log(\frac{L_{bol}}{L_\odot})$ (4)	Spectral Type (5)	Merger Class (6)	AGN Fraction (7)	m_{FUV} (AB) (8)	log(SX) [erg s^{-1}] (9)	log(HX) [erg s^{-1}] (10)	N_H(X-ray) [10^{22} cm^{-2}] (11)	$\log(\lambda L_{1125})$ (12)	$\alpha_{UV,X}$ (13)
Mrk 231	Mrk 231	0.0422[c]	12.61	S1	IVb	71^{+7}_{-7}	19.0	$42.13^{+0.01}_{-0.04}$	$42.58^{+0.01}_{-0.11}$	$9.5^{+2.3}_{-1.9}$	42.7	−1.3
...	...	...	...	...	...	...	...	...	...	$19.4^{+5.7}_{-4.4}$	...	...
F13218+0552	F13218	0.2047[c]	12.68	S1	V	83	19.4	42.2	42.7	0.17	43.8	−2.0
F13305−1739	F13305	0.148365[b]	12.27	S2	V	88	19.5	...	...	...	...	...
Mrk 273	Mrk 273	0.03778[b]	12.24	S2	IVb	46	18.6	42.7	43.0	41.3	42.0	−1.6
F14070+0525	F14070	0.26438[b]	12.84	S2	V	41	21.0	...	...	...	...	...
F15001+1433:E	F15001	0.162746[b]	12.51	S2	Tpl	43	20.3	...	...	...	...	...
F15250+3608	F15250	0.05515[b]	12.12	L	IVa	45	18.5	43.1	42.8	132	42.7	−2.3
F16156+0146:NW	F16156	0.132[e]	12.19	S2	IIIb	77	20.9	...	...	...	...	...
F21219−1757	F21219	0.1127[c]	12.17	S1	V	78	17.3	...	...	...	44.7	...
F23060+0505	F23060	0.173[e]	12.50	S2	IVb	75	20.2	...	...	...	...	...
F23233+2817	F23233	0.114009[b]	12.06	S2	Iso	72	20.9	...	...	...	41.0	...

Note. — Column (1): Name of the object; Column (2): Short names of the objects adopted in this paper; Column (3): Redshift. The label on the upper-right corner of each entry indicates the reference of the redshift. a: Based on the narrow optical emission lines from Martin et al. [2015]. b: The best redshift adopted by NASA/IPAC Extragalactic Database[2]. c: Based on the narrow optical emission lines from Rupke et al. [2017]. d: Based on the narrow optical emission lines From Rupke and Veilleux [2013a]. e: Based on the optical emission lines from Kim and Sanders [1998b]; Column (4): Log of bolometric luminosity in solar units based on. For ULIRGs, we assumed L_{bol}= 1.15 L_{IR} where L_{IR} is the 8-1000 μm infrared luminosity from Kim and Sanders [1998b]. For the QUEST quasars, we assumed L_{bol}= 7 L(5100Å) + L_{IR} based on Netzer et al. [2007]; Column (5): Optical spectral type from Veilleux et al. [1999]: S1 means Seyfert 1, S2 means Seyfert 2, L means LINER, HII means star-forming. Column (6): Interaction class from Veilleux+02: I–First approach, II–First contact, III(a/b)–Pre-merger (Wide binary/Close binary), IV(a/b)–Merger (Diffuse/Compact), V–Old Merger, Iso–Isolated, Tpl–triplet. Column (7): Fraction (in percentage) of the bolometric luminosity produced by the AGN, based on the mean values derived in Veilleux et al. [2009b]. The typical uncertainties are 10–15%. Column (8): FUV AB magnitudes from GALEX. Column (9): Soft (0.5–2 keV) X-ray luminosity. For X-ray related quantities (Column (9), (10), (11) and (13)), different rows = different observations dates. The references for these quantities are described in Sec. 2.2.3.2. The errors are omitted whenever they are not available from the literature or public data; Column (10) Hard (2–10 keV) X-ray luminosity; Column (11): The X-ray absorbing column density in units of 10^{22} cm^{-2}; Column (12): Monochromatic continuum luminosity at the rest-frame 1125 Å; Column (13): X-ray-to-UV index, $\alpha_{UV,X}$, as defined in Sec. 2.2.3.2.

Table 2.2. Summary of the HST/COS G130M Observations

Name (1)	PID (2)	PI (3)	Date (4)	R.A. (5)	Dec. (6)	Wavelength Coverage (7)	t_{exp} (8)
F01004	12533	C. Martin	2011-12-03	01 02 49.9631	−22 21 57.02	1137-1274/1292-1432	1716
Mrk 1014	12569	S. Veilleux	2012-01-25	01 59 50.250	+00 23 41.30	1154-1468	1961
F04103	15662	S. Veilleux	2020-01-23	12 19.413	-28 30 24.64	1137-1274/1292-1432	10798
F05189	15662	S. Veilleux	2019-07-18	05 21 01.388	-25 21 45.10	1069-1207/1223-1363	7802
F07599	15662	S. Veilleux	2019-02-21	04 30.487	+64 59 52.75	1173-1312/1328-1468	2148
F08572	15662	S. Veilleux	2019-10-17	00 25.281	+39 03 54.83	1069-1207/1223-1363	7906
F11119	15662	S. Veilleux	2020-01-20	14 38.908	+32 41 33.04	1173-1312/1328-1468	13537
Z11598	12533	C. Martin	2011-11-18	12 02 26.7505	−01 29 15.49	1154-1468	1304
F12072	12533	C. Martin	2013-01-24	12 09 45.1000	−05 01 13.20	1137-1448	1176
3C 273	12038	J. Green	2012-04-22	12 29 06.695	+02 03 08.66	1137-1408	4515
Mrk 231	12569	S. Veilleux	2011-10-15	12 56 14.111	+56 52 24.70	1154-1468	12851
F13218	15662	S. Veilleux	2020-05-21	24 19.897	+05 37 05.06	1069-1207/1223-1363	7742
F13305	15662	S. Veilleux	2019-12-17	33 16.529	−17 55 10.52	1173-1312/1328-1468	7776
Mrk 273	15662	S. Veilleux	2019-07-23	13 44 42.080	+55 53 12.99	1069-1207/1223-1363	4086
F14070	15662	S. Veilleux	2020-06-30	09 31.249	+05 11 31.45	1137-1274/1292-1432	13377
F15001	15662	S. Veilleux	2020-03-01	02 31.936	+14 21 35.15	1173-1312/1328-1468	10719
F15250	15662	S. Veilleux	2019-07-11	26 59.463	+35 58 37.47	1069-1207/1223-1363	4951
F16156	15662	S. Veilleux	2020-07-08	18 09.426	+01 39 21.66	1173-1312/1328-1468	13346
F21219	15662	S. Veilleux	2019-04-13	24 41.606	−17 44 45.52	1137-1274/1292-1432	2210
F23060	15662	S. Veilleux	2019-12-05	08 33.947	+05 21 29.95	1173-1312/1328-1468	10703
F23233	15662	S. Veilleux	2019-10-14,2020-01-2223	25 49.406	+28 34 20.84	1137-1274/1292-1432	13477

Note. — Column (1): Name of the object; Column (2): HST Program ID; Column (3): Principal Investigator; Column (4): Date of Observation; Column (5) & (6): J2000 coordinates; Column (7): Wavelength coverage of the observations in Å. The values are formatted as A/B segments or entire wavelength ranges; Column (8) Total exposure time in seconds.

highest redshifts (z $<$ 0.2), Lyα, the high-ionization lines from N V, and low-ionization lines from Si II λ1260 and Si III λ1206 fit within the wavelength coverage of the data. At the highest redshifts (z $\simeq$ 0.20-0.27), we lose N V and Lyα but gain Lyβ and O VI $\lambda\lambda$1032, 1038. The wavelength coverage for individual observations is summarized in Table 4.2.

2.2.2 HST/COS Data Reduction

Among the 6 objects with archival data, we retrieved the fully reduced spectra for 5 of them from the Hubble Legacy Spectrum Archive [Peeples et al., 2017], and obtained the fully reduced spectrum of F12072−0444 published in M15 from C. L. Martin. For the other 15 newly-observed objects presented in this paper, the raw data were processed and combined by the CAL-

COS pipeline v3.3.10. CALCOS corrects the data for instrumental effects, assigns a vacuum wavelength scale, and extracts flux-calibrated spectra. It applies a heliocentric correction to the final x1d files for each exposure, and combines the individual exposures to a single spectra when possible.

The COS aperture is filled with emission from geocoronal airglow, so the observed wavelengths of these lines are independent of target position in the PSA. By inspecting the velocity offsets of theoretical and observed wavelength of strong geocoronal lines, we can examine the potential systematic errors in the wavelength calibration. The measured velocity offsets are randomly distributed with absolute values < 30 km s^{-1}, and we take these measurements as typical errors of the wavelength calibration from the pipeline.

Finally, all spectra are corrected for foreground Galactic extinctions from Schlafly and Finkbeiner [2011] and the reddening curve with R_V =3.1 of Fitzpatrick [1999].

2.2.3 Ancillary Data and Measurements

2.2.3.1 General Physical Properties

For the bolometric luminosities of our sources, we adopt L$_{bol}$ $=$ 1.15 L$_{IR}$ where L$_{IR}$ is the 8-1000 μm infrared luminosity retrieved from Kim and Sanders [1998a], except for the three sources that are also QUEST quasars, which are quoted from Paper I where we assume L$_{bol}$= 7 L(5100Å) $+$ L$_{IR}$ based on Netzer et al. [2007]. The L(5100Å) is the continuum luminosity λL$_{\lambda}$ at 5100 Å rest wavelength and L$_{IR}$ is the 1 – 1000 μm infrared luminosity (the details can be found in the notes of Table 1 in Paper I).

The optical spectral classifications are quoted from Veilleux et al. [1999]: S1 means Seyfert

1, S2 means Seyfert 2, L means LINER, HII means star-forming galaxies. The interaction classes (or merger classes) are from Veilleux et al. [2002]: I–First approach, II–First contact, III(a/b)–Pre-merger (Wide binary/Close binary), IV(a/b)–Merger (Diffuse/Compact), V–Old Merger, Iso–Isolated, Tpl–triplet. The fraction of the bolometric luminosity produced by the AGN, or simply AGN fractions, are the average values derived in Veilleux et al. [2009b]. The AGN luminosities are defined as the bolometric luminosities multiplied by the AGN fractions.

2.2.3.2 X-ray Data

Published X-ray data and measurements exist for 14 out of the 21 objects: Those for the 3 quasars (QSO-B0157+001, 3C 273, Mrk 231) also studied in Paper I are from Teng and Veilleux [2010], Teng et al. [2014], Veilleux et al. [2014], Ricci et al. [2017] Those for the remaining 11 sources are from a series of X-ray studies of ULIRGs and quasars [Teng et al., 2005, Teng and Veilleux, 2010].

Following Paper I, the X-ray weakness of AGN/quasars can be described with the X-ray to optical spectral index, $\alpha_{OX} \equiv 0.372 log[(F(2\ \mathrm{keV})/F(3000\text{Å})]$ [e.g., Brandt et al., 2000]. While α_{OX} is measured for most nearby quasars, there are virtually no published measurements for the ULIRGs in our sample. Instead, we have defined an alternative X-ray to FUV spectral index, $\alpha_{UV,X}$, based on the ratio of the soft X-ray (0.5–2 keV) flux to the FUV flux from GALEX [Martin et al., 2005], where $\alpha_{UV,X} \equiv log[F(0.5-2\ \mathrm{keV})/F(FUV)]$. These results are listed in Table 5.1.

For the QUEST quasars studied in Paper I, there is a clear positive correlation between $\alpha_{UV,X}$ and α_{OX} (see Fig. 2.1), with a p-value $\simeq 2\times10^{-5}$ from the Kendall tau test (the null hypothesis is no correlation), which demonstrates that $\alpha_{UV,X}$ is indeed a good surrogate for α_{OX}. For the quasars without published 0.5–2 keV flux from *Chandra* or *XMM-Newton* and/or FUV flux from *GALEX*, we convert their α_{OX} listed in Paper I to $\alpha_{UV,X}$ by adopting the relation $\alpha_{UV,X}= 2.17\alpha_{OX}+2.26$, which is obtained from a linear fit to the quasars with both $\alpha_{UV,X}$ and α_{OX} measurements.

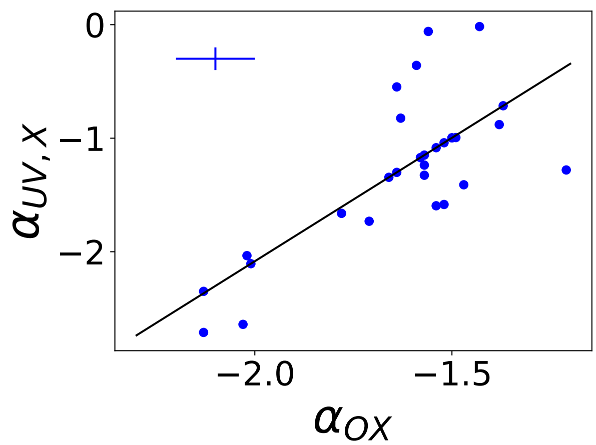

Figure 2.1: The X-ray to optical spectral index α_{OX} versus the X-ray to FUV spectral index $\alpha_{UV,X}$ for the quasars in Paper I. The two indices are defined as $\alpha_{OX} \equiv 0.372 log[(F(2\,\mathrm{keV})/F(3000\text{Å})]$ and $\alpha_{UV,X} \equiv log[F(0.5-2\,\mathrm{keV})/F(FUV)]$, respectively. The solid line is a linear fit to the data points. The errors on α_{OX} and $\alpha_{UV,X}$ are uncertain, and largely associated with the uncertainties in the analyses of the X-ray spectra, as described in, e.g., Teng and Veilleux [2010]. The cross in the upper left corner of the figure indicates $\pm$ 0.1 dex errors adopted in the Kendall tau test and the fit.

2.2.3.3 Optical Spectra

The Gemini/GMOS IFU spectra from Rupke and Veilleux [2013a], Rupke et al. [2017], or the SDSS spectra [Eisenstein et al., 2011] are adopted as the optical spectra for our objects by default unless explicitly stated otherwise (the GMOS data are adopted by default whenever both GMOS and SDSS data are available for the same object). The long-slit, optical spectra of all objects but 3C 273 are retrieved from Veilleux et al. [1999], and the optical spectrum of 3C 273 is retrieved from Buttiglione et al. [2009]. They are adopted as the default optical spectra whenever the Gemini/GMOS and SDSS spectra are not available.

For these spectra, the continua are modeled with either stellar population synthesis (SPS) models [González Delgado et al., 2005] adopting pPXF [Cappellari, 2017] or 4th-order polynomials and/or power-law function with customized Python software utilizing LMFIT [Newville et al., 2016], on a case-by-case basis. The properties of the [O III] λ5007 and Hα emission lines are then measured from these continuum-subtracted optical spectra.

2.2.3.4 AGN Fractions of Starburst-dominated ULIRGs

Most of the key AGN and host galaxy properties of the QUEST quasars from Paper I and the starburst-dominated ULIRGs from M15 are tabulated in these papers. One exception is the AGN fractions of the ULIRGs in M15, which are estimated based on the IRAS-based 25 μm to 60 μm flux ratios (F25/F60) listed in Table 1 of M15. Specifically, the AGN fraction is calculated adopting the best-fit to the trend presented in Fig. 36(c) in Veilleux et al. [2009b]:

2.3 Results from the HST Data Analysis

In this section, we present the major results from our analysis of the *HST/COS* spectra. First, the properties regarding Lyα emission are examined in Sec. 2.3.1; Second, the measurement of FUV continuum luminosity is briefly described in Sec. 2.3.2; Finally, the properties of O VI $\lambda\lambda$1032, 1038 and N V $\lambda\lambda$1238, 1243 absorbers are discussed in Sec. 2.3.3.

2.3.1 Lyα Emission

2.3.1.1 Detection Rates

The Lyα transition falls within the wavelength range of the observations for 19 of the 21 objects. Among the 19 objects, the Lyα emission is detected (S/N $>$ 3) in 15 of them, including F07599 where the Lyα emission is heavily affected by deep, broad and narrow N V $\lambda\lambda$1238, 1243 absorption features (and perhaps also broad Lyα absorption). After Lyα, N V $\lambda\lambda$1238, 1243 and O VI $\lambda\lambda$1032, 1038 are the most frequently detected emission lines in our sample (notice that our G130M spectra do not cover Si IV and C IV). Descriptions about the presence of emission/absorption features other than Lyα in our objects may be found in Appendix A.1.

2.3.1.2 Line Profiles

The Lyα profiles of the 15 Lyα detections are presented in Fig. 2.2. For these objects, the Lyα emission is the most prominent feature in the observed spectral range, except for F07599, where the Lyα line is severely suppressed by a highly blueshifted broad absorption line (BAL) and several less blueshifted narrow N V 1238, 1243 absorption features. As a result, a relatively robust measurement of the Lyα profile of F07599 is impossible, and this source is left out from the analyses to characterize the Lyα profiles in the following sections.

The flux and EWs of the entire Lyα profiles are measured in wavelength windows customized for each object based on their line widths. The local continuum of each object is determined by fitting the line-free windows adjacent to the Lyα features with power-law or low-order polynomials (order $\leq$ 2). The contamination from nearby N V emission is subtracted for sources

Mrk 1014, F05189, 3C 273, and F21219, where the N V doublet are modeled as Gaussian profiles. The foreground absorption features and absorption lines from other species at the systemic velocity are interpolated over with cubic splines. For the non-detections, the 3-σ upper limits on the flux of Lyα are estimated in a velocity window of -1000 to $+1000$ km s^{-1}.

We adopt a non-parametric approach to characterize the Lyα profiles quantitatively: the velocities v_{50} and v_{80} (velocities at 50 and 80 percentiles of the total flux calculated from the red side of the line), the line width W_{80} (which encloses the central 80 percent of the total flux), and the line asymmetry A_{91} ($[v_{90}+v_{10}]/W_{80}$), where v_{90} and v_{10} are the velocities at 90 and 10 percentiles of the total flux calculated from the red side of the line) are the primary measurements adopted for our analyses in the following sections. All velocities are calculated with respect to the systemic redshifts listed in Table 5.1. Table 2.3 summarizes the results. A visualization of these non-parametric measurements is shown in Fig. 4.3.

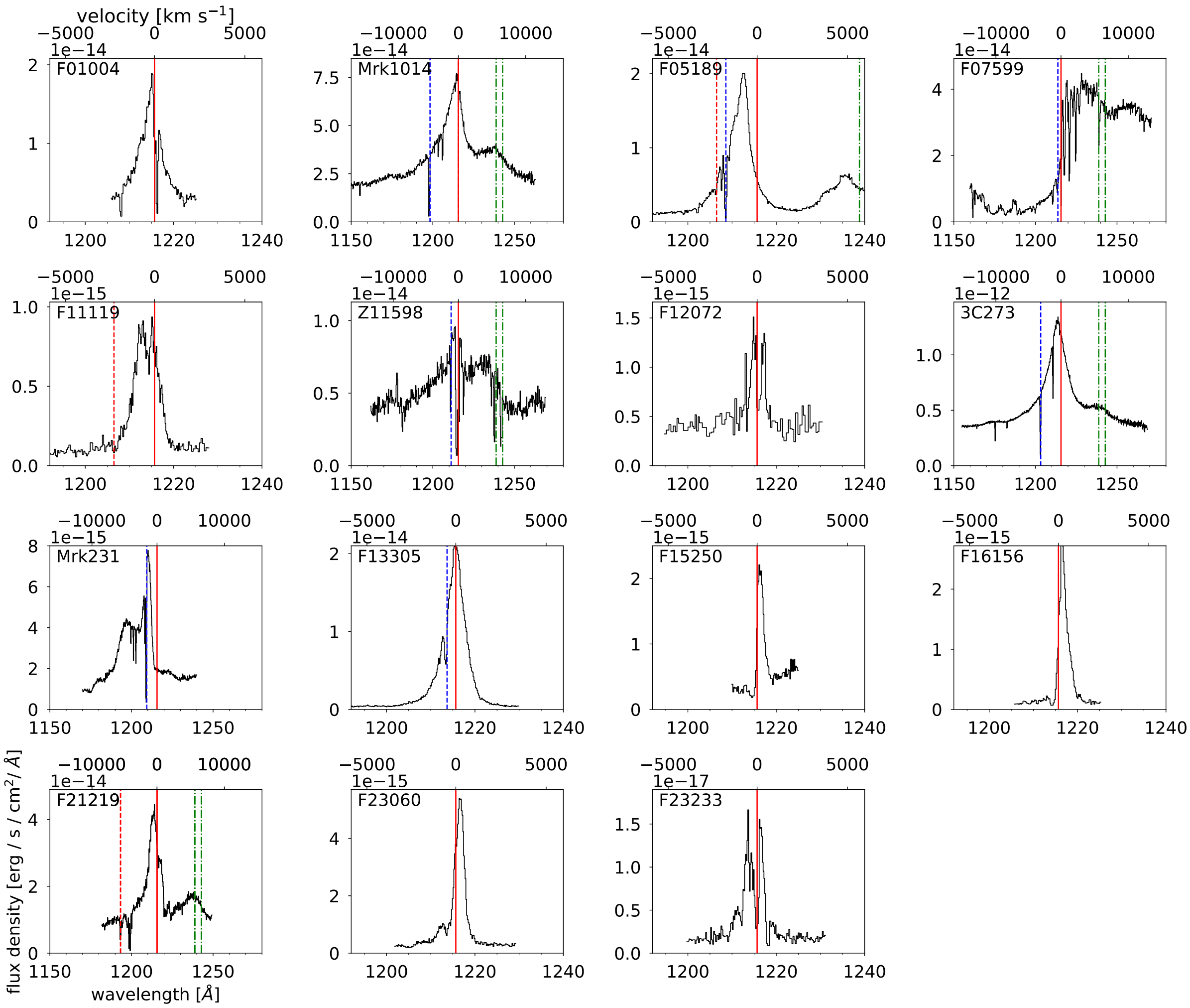

Figure 2.2: Lyα profiles of the 14 objects with clear Lyα emission and the one with a potential detection F07599. The spectra are shown in each object's rest-frame. The velocities relative to the Lyα transition are shown on the top of each panel, and the zero velocities are indicated by the vertical solid lines. The zero-velocities of the N V $\lambda\lambda$1238, 1243 doublet are indicated by the vertical, green dash-dotted lines when they are blended with the Lyα emission. Other strong absorption features at the systemic velocities are indicated by vertical dashed lines in red. Foreground absorption features at z$\simeq$0 due to the Milky Way are indicated by dashed lines in blue. The flux scale for the vertical axis in units of erg s^{-1} cm^{-2} Å^{-1} is listed in the upper left corner above each panel. To help with the visual comparison among different objects, the x-axes are set to two fixed wavelength ranges (1192–1240 Å or 1150–1280 Å) depending on the widths of the lines.

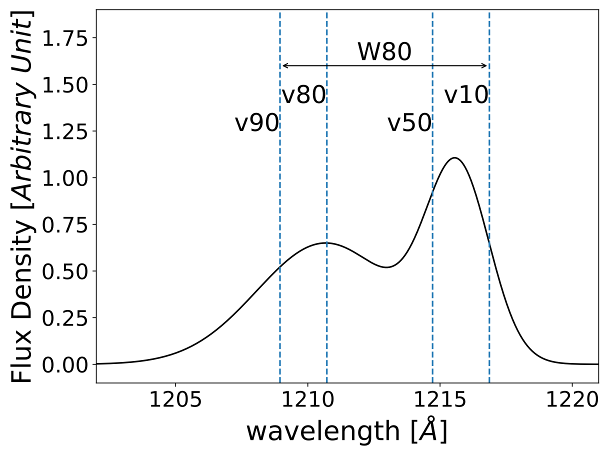

Figure 2.3: Example of a line profile illustrating the various non-parametric kinematic parameters used in this paper. The vertical dashed lines mark the locations of v_{90}, v_{80}, v_{50}, and v_{10} for the mock emission-line profile shown in the figure. W_{80} is defined as the line width between v_{90} and v_{10}, and the line asymmetry A_{91} is [v_{90}+v_{10}]/W_{80} (not shown in the figure).

Blueshifted wings of the Lyα emission are often seen across our sample (12 out of the 14 objects with robustly measured Lyα profiles show $v_{80} < 0$ and line asymmetry $A_{91} < 0$), while the P-Cygni-like profile (blueshifted absorption accompanied by redshifted emission) is only seen in F15250 (in F16156, a weak blueshifted wing is seen in the Lyα emission blueward of the strong blueshifted absorption feature, and the overall Lyα profile is thus not P-Cygni-like). This is in clear contrast with the prevalence of P-Cygni-like profiles seen in low-redshift star-forming galaxies [e.g., Wofford et al., 2013]. The blueshift of the velocity centroid of the Lyα line is also prevalent in our sample, where 11 out of the 14 objects with Lyα detections show $v_{50} < 0$. Moreover, in two Type 1 sources, 3C 273 and Mrk 1014, the broad Lyα emission (accompanied by broad N V $\lambda\lambda$1238, 1243 emission, when the spectrum covers this region) shows line width typical for the broad emission line region (BELR) of AGN, which is often the case for low-redshift Type 1 AGN and quasars [e.g., Shull et al., 2012]. Finally, Lyα absorption features near systemic velocities are clearly seen in 9 objects.

Table 2.3. Lyα Measurements

Name (1)	log(Flux) [erg cm^{-2} s^{-1}] (2)	log(Lum.) [erg s^{-1}] (3)	EW [Å] (4)	v_{50} [km s^{-1}] (5)	v_{80} [km s^{-1}] (6)	W_{80} [km s^{-1}] (7)	A_{91} (8)	log[f_{esc}(Lyα)] (9)
F01004	-13.09±0.02	42.48±0.02	27.8±4.7	-228±42	-788±78	1792±51	-0.25±0.14	0.12±0.49
Mrk 1014	-11.74±0.006	44.13±0.006	102.7±0.3	-1274±153	-5453±654	10876±1305	-0.62±0.12	-0.22±0.32
F04103	$<$-14.07	$<$41.49	...	...	...	...	...	$<$-2.36
F05189	-12.79±0.02	41.86±0.02	164.0±56.8	-913±71	-1782±159	2748±50	-0.87±0.22	-1.29±0.30
F07599	...	...	...	...	...	...	...	...
F08572	$<$-12.86	$<$42.05	...	...	...	...	...	$<$-0.28
F11119	-14.17±0.05	41.85±0.05	80.8±39.8	-467±211	-1104±245	2170±548	-0.53±0.97	-3.89±0.32
Z11598	-12.65±0.003	43.15±0.003	70.5±2.3	-1739±591	-6517±2216	12766±4340	-0.51±0.31	0.34±0.44
F12072	-14.23±0.07	41.41±0.07	17.2±10.2	-75±100	-743±150	1601±122	-0.25±0.65	-0.62±0.07
3C 273	-10.67±0.04	45.18±0.04	53.0±8.3	-624±340	-2988±792	7875±10	-0.32±0.53	-0.08±0.36
Mrk 231	-13.08±0.03	41.54±0.03	53.2±10.2	-2771±371	-4731±309	4698±20	-1.34±0.31	-2.64±0.80
F13218	...	...	...	...	...	...	...	...
F13305	-12.72±0.02	43.06±0.02	307.1±257.9	-20±58	-599±97	1775±18	-0.15±0.15	-0.19±0.48
Mrk 273	$<$-12.85	$<$41.68	...	...	...	...	...	$<$-0.91
F14070	...	...	...	...	...	...	...	...
F15001	$<$-14.09	$<$41.78	...	...	...	...	...	$<$-0.80

2.3.1.3 Comparison of the Lyα and Optical Emission Line Profiles

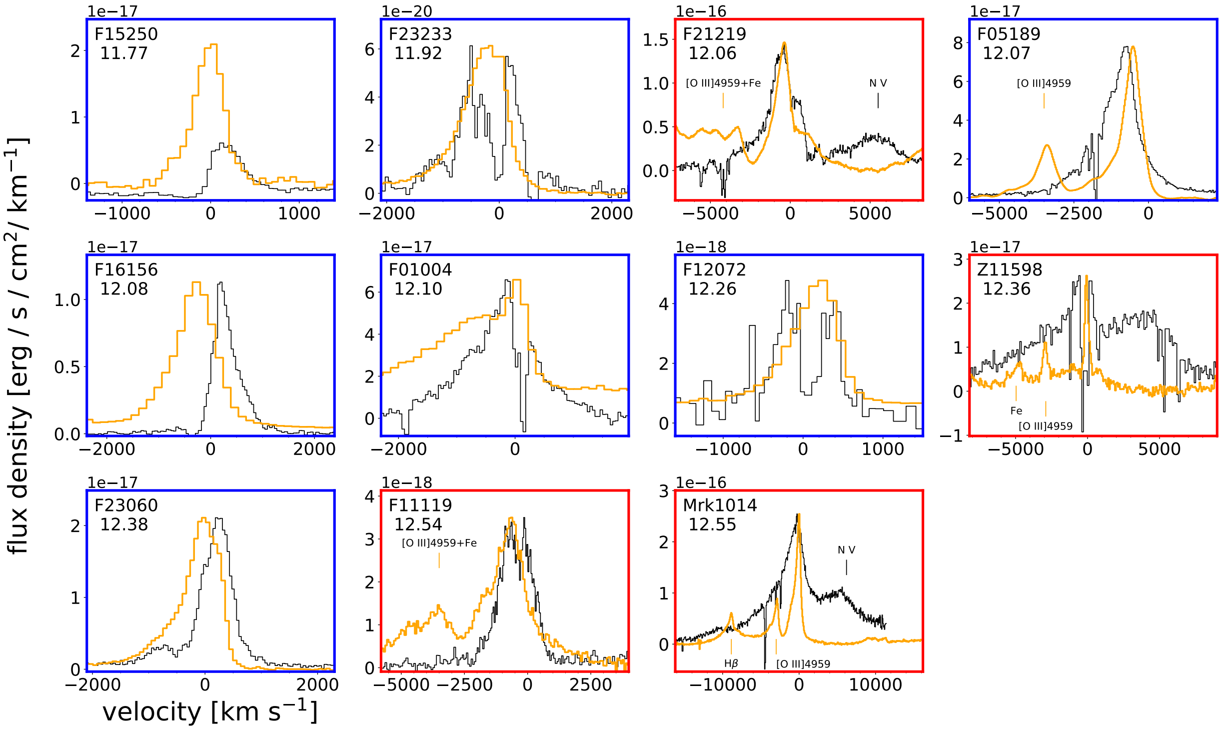

Figure 2.4: Comparison of Lyα profiles (black) with [O III] λ5007 emission lines (orange) for the 11 objects in our sample with both Lyα detections and [O III] λ5007 observations. The flux scale on the vertical axis refers to the Lyα line and the scale factor in units of erg s^{-1} cm^{-2} km^{-1} s is listed in the upper left corner above each panel. The [O III] emission line profiles are re-scaled for better visualization. Nearby emission features from N V in the FUV and those from Hβ, [O III] λ4959, and Fe in the optical are marked with black and orange vertical bars when those features are present, respectively. The panels are ordered in increasing AGN luminosities, which are indicated in the top left corner of each panel under the object name (in log units of solar luminosities). The panel frames of Type 1 AGN are marked in red and those of type 2 AGN are marked in blue.

The observed Lyα profiles in these dusty ULIRGs are likely affected by complex radiative transfer effects due to the resonant nature of the transition. While it is impossible to derive the intrinsic profile of the resonant Lyα line with our data, the non-resonant optical emission lines (e.g. [O III] λ5007 forbidden line, Hα recombination line) provide a point of reference since they are less affected by absorption and scattering. Qualitatively, we may therefore infer the extent to

Table 2.3 (cont'd)

Name	log(Flux) [erg cm^{-2} s^{-1}]	log(Lum.) [erg s^{-1}]	EW [Å]	v_{50} [km s^{-1}]	v_{80} [km s^{-1}]	W_{80} [km s^{-1}]	A_{91}	log[f_{esc}(Lyα)]
(1)	(2)	(3)	(4)	(5)	(6)	(7)	(8)	(9)
F15250	-15.32±0.11	39.55±0.11	0.7±18.0	394±7	359±7	112±78	7.28±5.09	-1.41±0.37
F16156	-13.94±0.06	41.73±0.06	62.8±66.8	331±78	142±85	749±62	1.12±2.33	-1.33±0.34
F21219	-12.21±0.02	43.31±0.02	46.3±4.0	-384±86	-1488±180	4036±48	-0.20±0.12	-0.81±0.44
F23060	-13.57±0.05	42.36±0.05	90.4±80.2	219±69	-228±201	1535±89	-0.10±1.06	-2.47±0.36
F23233	-15.88±0.06	39.65±0.06	36.8±18.2	-278±188	-709±166	1600±582	-0.45±1.20	-2.10±1.10

Note. — Columnn (2): Observed Lyα flux (cgs units) in logarithm. Column (3): Lyα luminosity (cgs units) in logarithm. Column (4): Lyα EW in units of Å. Column (5): v_{50} of Lyα profile in units of km s^{-1}. Column (6): v_{80} of Lyα profile in units of km s^{-1}. Column (7): W_{80} of Lyα profile in units of km s^{-1}. Column (8): A_{91} of Lyα. Column (9): Logarithm of Lyα escape fraction as defined in Sec. 2.3.1.4. Note that for F13218 and F14070, the Lyα transition is not covered by the observations, while for F07599, the Lyα feature cannot be measured robustly mainly due to contamination from the N V BAL.

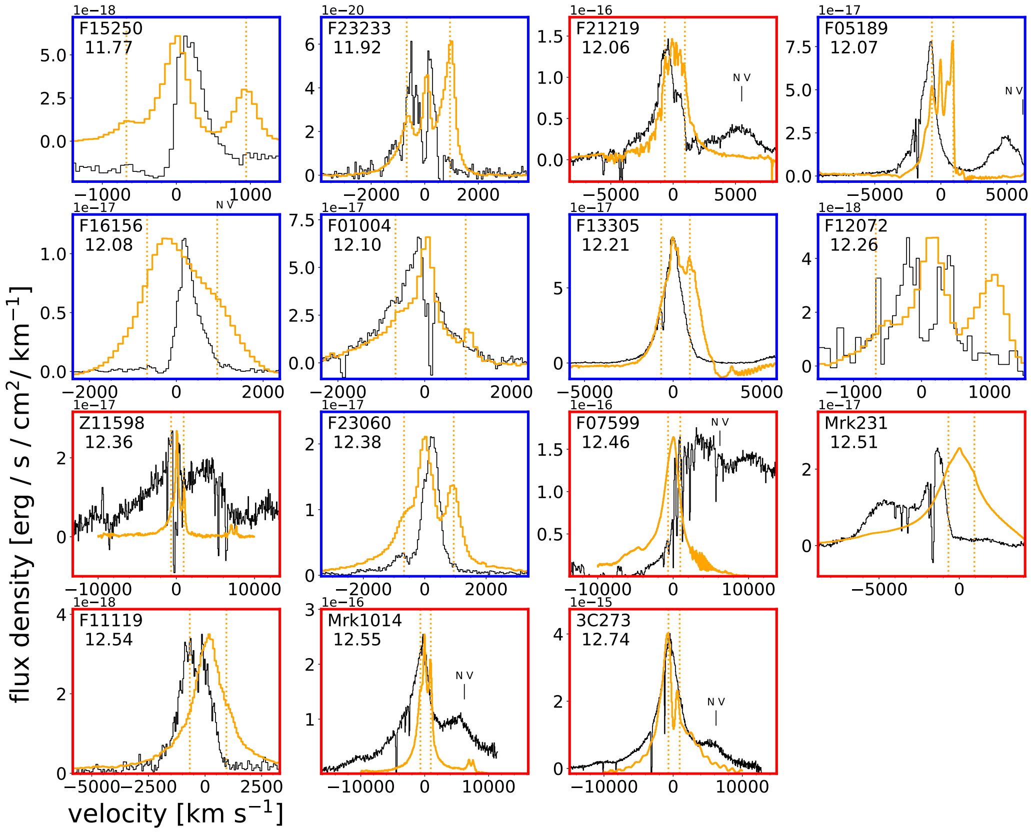

Figure 2.5: Same as Fig. 2.4 but for the comparison of the Lyα (black) and Hα (orange) emission lines for the 15 objects with Lyα detections. The nearby N V emission are marked with black bars when those features are present. Note that, in some cases, the strong [N II] $\lambda\lambda$6548, 6583 emission lines in the optical near -674 km s^{-1} and $+944$ km s^{-1} (marked by orange dotted lines) make this comparison difficult.

which Lyα photons are absorbed and/or scattered, by comparing the Lyα and optical line profiles.

In Fig. 2.4 and 2.5, we plot the Lyα profiles in comparison with the [O III] λ5007 profiles and the Hα profiles. All of these line profiles are continuum-subtracted and rescaled for better visualization. In total, 11 objects with [O III] λ5007 observations and 15 objects with Hα observations show Lyα detections. The measurements of the [O III] λ5007 and Hα profiles are summarized in Table 2.4. At first glance, one similarity between the Lyα profiles and the non-resonant line profiles is the occurrence of blueshifted emission line wings in many objects. Blueshifted [O III] λ5007 (and, to a lesser extent, Hα) emission is a tell-tale signature of ionized gas outflows, so the blueshifted Lyα emission may also arise from the outflowing gas. In addition, Lyα emission is generally broader than or comparable in width to the [O III] λ5007 and Hα emission. Otherwise, the Lyα profiles are diverse among the objects in our sample and no apparent trend is seen between the profiles of Lyα and the non-resonant optical lines. We will discuss these results further in Sec. 2.4.2.

2.3.1.4 Lyα Escape Fraction

At first, it may be surprising that significant Lyα emission is observed from these dusty ULIRGs given the implied huge optical depth to Lyα photons. In this section, we quantify the escape of Lyα photons by calculating the Lyα escape fraction.

Under Case B recombination, the ionized region is optically thick to the Lyman series, and the intrinsic F(Lyα)/F(Hα) flux ratio depends only on the electron density and temperature. Adopting the low density limit where $n_e << n_{e,crit} = 1.55 \times 10^4$ cm^{-3}, the collisions can be safely neglected. The intrinsic Lyα flux is then predicted to be 8.1 times the intrinsic Hα flux [Hummer and Storey, 1987, Draine, 2011].

Galaxies usually show Lyα-to-Hα flux ratios much less than the predicted Case B ratio. We can therefore describe the suppression of Lyα photons by comparing the observed Lyα flux to the intrinsic values indicated by the Hα emission. The escape fraction of Lyα photons can thus be defined as

$$f_{esc}(\text{Ly}\alpha) \ = \frac{F(\text{Ly}\alpha)}{8.1 \times F(\text{H}\alpha)_{cor}}. \tag{2.1}$$

The intrinsic Hα flux is calculated from the observed Hα flux, corrected for the nebular reddening using the Cardelli et al. [1989a] reddening curve, namely

$$F_{cor}(\text{H}\alpha) = F_{obs}(\text{H}\alpha) \times 10^{1.012E(B-V)}. \tag{2.2}$$

and the $E(B-V)$ is calculated from the Balmer decrement:

$$E(B-V) = \frac{1}{0.9692} \log \left[\frac{(F(\text{H}\alpha)/F(\text{H}\beta))_{\text{obs}}}{(F(\text{H}\alpha)/F(\text{H}\beta))_{\text{int}}} \right] \tag{2.3}$$

We set the intrinsic Hα/Hβ ratio to 3.1 for all but one objects as they show optical spectral features consistent with AGN activity. The only exception is F01004: it is located in the star-forming region in the BPT and VO87 diagnostic line ratio diagrams [Baldwin et al., 1981, Veilleux and Osterbrock, 1987, Osterbrock and Ferland, 2006], and we set the intrinsic Hα/Hβ ratio of this object to 2.87.

Table 2.4. Optical Spectroscopic Measurements

Name	$E(B-V)$	log[Flux(Hα)] [erg cm^{-2} s^{-1}]	cor,Hα	$v_{50,H\alpha}$ [km s^{-1}]	$v_{80,H\alpha}$ [km s^{-1}]	$W_{80,H\alpha}$ [km s^{-1}]	$A_{91,H\alpha}$	$v_{50,[O\ III]}$ [km s^{-1}]	$v_{80,[O\ III]}$ [km s^{-1}]	$W_{80,[O\ III]}$ [km s^{-1}]	$A_{91,[O\ III]}$
(1)	(2)	(3)	(4)	(5)	(6)	(7)	(8)	(9)	(10)	(11)	(12)
F01004	0.05±0.004	-14.05±0.03	0.86	111±100	-688±100	1398±141	-0.54±0.11	-563±199	-1560±200	2591±282	-0.58±0.13
Mrk 1014	0.24±0.02	-12.42±0.04	0.98	113±69	-1061±69	4901±98	0.19±0.02	-147±69	-768±69	1519±98	-0.42±0.07
F04103	1.29±0.13	-12.54±0.03	0.82	...	...	...	...	...	...	...	...
F05189	1.02±0.10	-12.34±0.04	0.86	-354±20	-904±20	1588±29	-0.90±0.02	-661±27	-1195±27	1415±38	-1.38±0.05
F07599	...	-10.03±0.03	0.68	642±3760	323±4079	957±5393	1.48±10.06	...	...	...	...
F08572	...	-13.36±0.03	0.75	...	...	...	...	...	...	...	...
F11119	...	-11.19±0.03	1.00	144±69	-1029±69	4970±98	0.00±0.02	-667±69	-1427±69	2278±98	-0.62±0.05
Z11598	...	-13.69±0.03	0.62	172±69	-1071±69	4901±98	-0.38±0.02	-64±60	-1734±60	4057±84	-0.31±0.02
F12072	0.10±0.001	-14.80±0.001	1.33	49±87	-213±88	1051±124	-0.03±0.12	-121±37	-831±37	1642±53	-0.38±0.03
3C 273	...	-11.50±0.05	1.00	637±89	-2031±89	7277±125	0.00±0.02	...	...	...	...
Mrk 231	...	-11.14±0.04	0.62	-321±20	-2421±20	6396±29	-0.29±0.00	...	...	...	...
F13218	0.73±0.07	-10.09±0.04	0.80	-400±18	-1730±18	2924±25	-0.76±0.01	-1064±69	-1755±69	2140±98	-0.98±0.06
F13305	1.18±0.12	-13.45±0.04	1.01	17±97	-371±97	1066±137	0.15±0.13	55±127	-453±127	1398±180	0.14±0.13
Mrk 273	1.94±0.19	-12.70±0.03	0.72	...	...	...	...	...	...	...	...
F14070	2.11±0.21	-12.82±0.04	1.22	...	...	...	...	...	...	...	...
F15001	1.04±0.10	-14.00±0.05	0.62	-54±69	-330±69	897±98	-0.37±0.12	-107±69	-590±69	1036±98	-0.69±0.11

The Hα fluxes are measured from spectra gathered from literature, as described in Sec. 2.2.3.3, and can be divided into three groups: (1) Gemini/GMOS IFU observations; (2) SDSS spectra; (3) long-slit spectra from Veilleux et al. [1999]. Some of our objects are point sources or show very compact morphology in the narrow-band Hα images (based on the GMOS data) or R-band images [from SDSS or Veilleux et al., 1999], so no aperture corrections are needed for their Hα flux in the calculation of Lyα escape fraction. However, for the more extended objects, the aperture difference between the COS FUV spectroscopy and the optical observations need to be taken into account, as the throughput of the 2.5$''$ COS aperture drops sharply beyond the central 0.4$''$.

In practice, the aperture correction is negligible if at least one of the following three criteria is met: (1) it is a Type 1 AGN; (2) the PSF contribution to its overall flux in the R-band image is more than 50% based on the measurements in Veilleux et al. [2002]; (3) the R-band effective radius is less than 1$''$ based on the measurements in Veilleux et al. [2002]. For the other objects, aperture corrections are needed to account for the rapid decrease of COS throughput at large radius as mentioned above. Specifically, we calculate the aperture correction factors for each group of optical observations separately: (i) for the GMOS IFU observations, we generate the Hα flux maps based on the data cube, and use the COS throughput function to vignette the Hα flux maps within the region with radius r $<$ 1.25$''$. The aperture correction factor is then the vignetted Hα flux within r $<$ 1.25$''$(corresponding to the COS aperture) divided by the original Hα flux within the same aperture; (ii) for the SDSS spectra, we adopt the r-band images as surrogates for the Hα flux maps. We then vignette the r-band images within the same COS throughput function, and the aperture correction factor is the vignetted r-band flux within r $<$ 1.25$''$ divided by the original r-band flux within SDSS aperture (D=3$''$ or D=2$''$); (iii) for the long-slit spectra from

Table 2.4 (cont'd)

Name	$E(B-V)$	log[Flux(Hα)] [erg cm^{-2} s^{-1}]	cor,Hα	$v_{50,H\alpha}$ [km s^{-1}]	$v_{80,H\alpha}$ [km s^{-1}]	$W_{80,H\alpha}$ [km s^{-1}]	$A_{91,H\alpha}$	$v_{50,[O\ III]}$ [km s^{-1}]	$v_{80,[O\ III]}$ [km s^{-1}]	$W_{80,[O\ III]}$ [km s^{-1}]	$A_{91,[O\ III]}$
(1)	(2)	(3)	(4)	(5)	(6)	(7)	(8)	(9)	(10)	(11)	(12)
F15250	0.62±0.06	-14.60±0.04	0.60	51±69	-87±69	552±98	0.35±0.19	67±69	-71±69	483±98	0.32±0.21
F16156	0.71±0.07	-13.39±0.03	0.75	123±112	-439±113	1909±159	0.19±0.08	-54±147	-644±148	1474±208	-0.27±0.15
F21219	...	-12.17±0.04	0.73	11±4285	-788±5083	2627±6278	0.20±2.44	-490±131	-1147±132	3015±185	0.20±0.06
F23060	1.15±0.11	-12.03±0.03	1.04	133±69	-419±69	2071±98	0.13±0.05	12±69	-403±69	1104±98	-0.35±0.09
F23233	0.59±0.06	-14.70±0.05	1.02	70±69	-344±69	828±98	-0.32±0.12	-189±69	-673±69	1381±98	-0.57±0.08

Note. — Columnn (2): Color excess based on the Balmer decrement measured from the optical spectra described in Sec. 2.2.3.3. Columnn (3): Extinction-corrected Hα flux in logarithm and cgs units. Columnn (4): Appeture correction factor applied to the Hα flux in the calculation of $f_{esc}(\mathrm{Ly}\alpha)$. Column (5)–(8): Kinematic properties v_{50}, v_{80}, W_{80}, and A_{91} of Hα emission. Column (9)–(12): Kinematic properties v_{50}, v_{80}, W_{80}, and A_{91} of [O III] λ5007 emission.

Veilleux et al. [1999], we follow the same logic as adopted for the SDSS spectra but use the R-band images in Kim et al. [2002]. The aperture correction factor is thus the vignetted R-band flux within r $< 1.25''$ divided by the original R-band flux within the extraction region of the long-slit spectra ($2''\times 5$ kpc).

The aperture correction factors adopted in the calculations and resulting Lyα escape fractions are listed in Tables 2.4 and 2.3, respectively.

2.3.2 Continuum Luminosity at 1125 Å

As a surrogate for the FUV continuum luminosity adopted in Paper I, the monochromatic luminosities at rest-frame 1125 Å, log(λL_{1125}), are measured whenever the continuum is detected, with a bandpass of 20 Å. These results are recorded in Table 5.1.

2.3.3 FUV Absorption Features

The focus of this section is the strongest metal absorption features detected in our objects, O VI $\lambda\lambda$1032, 1038 and N V $\lambda\lambda$1238, 1243, tracers of the highly ionized gas in these systems. Only 12 out of the 21 objects have continuum S/N in the vicinity of O VI $\lambda\lambda$1032, 1038 and/or N V $\lambda\lambda$1238, 1243 that are high enough (S/N $\gtrsim$ 10 in a 500 km s^{-1} window) to allow for the detection of corresponding absorption lines. Out of these 12 objects, 6 objects show O VI and/or N V absorption features associated with the galaxy (velocity centroid $<$ 13000 km s^{-1} and not from intervening systems), and the velocity centroids of these absorption features are all blueshifted. One more object, F15250, may display a N V absorption feature, but the doublet is so close to a group of geo-coronal emission lines that the N V 1239 transition is heavily contaminated and no robust measurements of the N V feature can be made. Our estimates for the EW and centroid velocity of the N V 1242 absorber alone are $\sim$0.3 Å and -500 km s^{-1}, respectively, which has not taken into account the infilling from the N V $\lambda\lambda$1238, 1243 emission. This source is excluded from the discussions related to the absorption features in the following sections.

The properties of these detected O VI and/or N V absorption features vary wildly: F07599 shows a $>$25000 km s^{-1} wide N V $\lambda\lambda$1238, 1243 BAL accompanied by narrower absorbers at smaller velocities, whereas F23060 shows relatively narrow and shallow N V $\lambda\lambda$1238, 1243 absorption features on top of the N V $\lambda\lambda$1238, 1243 emission. Overall, the absorption features in F07599 and F01004 fall in the BAL category (velocity width $>$ 2000 km s^{-1}), while all other absorption features are classified as narrow absorption lines (NAL; velocity width $<$ 500 km s^{-1}). The object-by-object description of these absorption features is given in Appendix A.1.

To quantify the strength of these absorbers, we follow the same procedure as in Paper I. First, we fit the continuum and/or broad emission lines (Lyα, O VI, N V) with low-order polynomials or Gaussian profiles. After the spectra are normalized by the best-fits from the continuum and/or broad emission line fits, these absorbers are quantified using a non-parametric approach, where we measure the total velocity-integrated EWs of the outflowing absorbers in the object's rest frame,

$$W_{eq} = \int [1 - f(\lambda)] d\lambda, \tag{2.4}$$

the weighted average outflow velocity

$$v_{wtavg} = \frac{\int v[1 - f(v)] dv}{W_{eq}}, \tag{2.5}$$

and the weighted outflow velocity dispersion,

$$\sigma_{wtavg} = \{\frac{\int (v - v_{wtavg})^2 [1 - f(v)] dv}{W_{eq}}\}^{\frac{1}{2}}. \tag{2.6}$$

The results are summarized in Table 2.5.

Table 2.5. Properties of the O VI and N V Absorption Features

Name	W_{eq} [Å]	v_{wtavg} [km s^{-1}]	σ_{rms} [km s^{-1}]	log($N_{ion,d}$) [cm^{-2}]	$C_{f,d}$	# comp.	log(N_{ion}) [cm^{-2}]	C_f
(1)	(2)	(3)	(4)	(5)	(6)	(7)	(8)	
F01004, O VI	10.59 ±0.26	-2720 ±110	1470 ±120	...	...	1	>17.1	...
F01004, N V	<0.14	...	...	...	...	...	...	...
Mrk 1014, O VI	<0.09	...	...	...	...	...	...	...
Mrk 1014, N V	<0.13	...	...	...	...	...	...	...
F05189, N V	<0.07	...	...	...	...	...	...	...
F07599, N V	55.39 ±0.07	-12690 ±20	4620 ±10	...	...	1	>17.2	...
Z11598, O VI	2.03 ±0.12	-190 ±30	90 ±40	>16.4	0.80±0.05	2	>16.3, 14.5±0.3,	0.90±0.03, 1(f)
Z11598, N V	2.07 ±0.12	-170 ±30	100 ±30	>16.1	0.57±0.22	1	>15.9	0.82±0.03
3C 273, O VI	<0.04	...	...	...	...	...	...	...
3C 273, N V	<0.04	...	...	...	...	...	...	...
Mrk 231 N V	<0.18	...	...	...	...	...	...	...
F13218, O VI	2.23 ±0.18	-250 ±40	150 ±50	>15.6	0.66±0.12	3	>15.7, >15.2, >15.9	0.79±0.05, 0.79±0.09, 0.55±0.04
F13305, N V	<0.07	...	...	...	...	...	...	...
F21219, O VI	1.17 ±0.05	-4400 ±190	180 ±20	...	...	4	14.1±0.2, 14.5±0.2, 14.2±0.1, 14.2±0.1	1(f), 1(f), 1(f), 1(f)
F21219, N V	1.28 ±0.05	-4430 ±300	190 ±30	14.8±0.2	0.78±0.20	4	14.4±0.1, 13.6±0.1,	1(f), 1(f), 1(f), 1(f)

2.3.3.1 Evidence of Partial Covering for the O VI and N V Doublets

The profiles of the resolved O VI and N V doublets may be used to derive the basic characteristics of the absorbing cloud – background source system. For the absorption features in Z11598 and F13218, there is evidence of partial covering: the optical depth ratio of the spectrally resolved doublet deviates from the theoretical expectation from a simple model where the foreground cloud is illuminated by the background point source with a 100% covering fraction.

For the cases where the optical depths of the doublets (proportional to λf_{osc}, the product of wavelength and oscillator strength) differ by a factor of $\sim$2 (like O VI $\lambda\lambda$1032, 1038 and N V $\lambda\lambda$1238, 1243), and the continuum intensity is normalized to unity, the coverage fraction (or covering factor, C_f) as a function of velocity may be obtained. Following Hamann et al. [1997a], in the simple situation where the two transitions of the doublet do not overlap with each other, we have

$$C_f(v) = \frac{I_1(v)^2 - 2I_1(v) + 1}{I_2(v) - 2I_1(v) + 1}; \quad I_1 > I_2 \geq I_1^2 \tag{2.7}$$

$$C_f(v) = 1; \quad I_2 < I_1^2 \tag{2.8}$$

$$C_f(v) = 1 - I_1(v); \quad I_2 \geq I_1 \tag{2.9}$$

I_1 and I_2 are the normalized intensities of the weaker and stronger absorption lines, respectively, and C_f is the covering factor.

Then the optical depth as a function of the velocity can be written as

$$\tau_1(v) = ln(\frac{C_f(v)}{I_1(v) + C_f(v) - 1}) \tag{2.10}$$

Table 2.5 (cont'd)

Name (1)	W_{eq} [Å] (2)	v_{wtavg} [km s^{-1}] (3)	σ_{rms} [km s^{-1}] (4)	log(N$_{ion,d}$) [cm^{-2}] (5)	C$_{f,d}$ (6)	# comp. (7)	log(N$_{ion}$) [cm^{-2}] (8)	C$_f$
F23060, N V	1.34 ±0.24	-610 ±150	160 ±130	...	...	2	14.2±0.1, 13.5±0.1 14.2±1.6, 14.1±1.6	1(f), 1(f)

Note. — Column (1): Object and absorption feature name; Column (2)–(4): Velocity-integrated EW, W_{eq} (eq. 2.4), average depth-weighted velocity v_{wtavg} (eq. 2.5), and average depth-weighted velocity dispersion σ_{rms} (eq. 2.6) of the absorption lines; Column (5): Ion column densities obtained from the analysis of the absorption doublet with partial covering model as described in Sec. 2.3.3.1; Column (6): Velocity-weighted covering fractions calculated from the same analysis for ion column densities in Column (5); Column (7): Number of components in the best-fits from the Voigt profile fits as described in Sec. 2.3.3.2. Notice that the O VI absorption in F01004 and the N V absorption of F07599 are BAL, and the 1-component fit is only tentative/experimental, with the aim to capture the overall absorption profile. Column (8): Ion column densities from the Voigt profile fits. The values for individual components from the best-fit model are separated by comma. This is also True for Column (9); Column (9): Covering fractions from the Voigt profile fits. The flag "f" in parenthesis indicates that the covering fraction is fixed to the corresponding value in the fits.

$$\tau_2(v) = 2\tau_1(v) \tag{2.11}$$

The column density of the ion can then be obtained by integrating the optical depth over the velocity adopting

$$N_{ion} = \frac{m_e c}{\pi e^2 f \lambda} \int \tau(v) dv \tag{2.12}$$

The resulting values of N_{ion} are listed in Table 2.5.

2.3.3.2 Voigt Profile Fitting of O VI and N V Absorbers

A popular approach to quantify the absorption features is to fit them with the product of individual components assuming Voigt profiles for the optical depth distribution in frequency (or velocity, wavelength) space. As discussed in Sec. 2.3.3.1, there is evidence for partial covering in a few objects. To account for this, we also include a constant covering fraction parameter to each component of the model. The final model of the normalized intensity can then be written as

$$I(\nu) = \prod \{1 - C_f[1 - e^{-\tau(\nu)}]\} \tag{2.13}$$

$$\tau(\nu|N, b, z) = N\sigma_0 f_{\text{osc}} \Phi(\nu|b, z) \tag{2.14}$$

C_f, τ, ν, N, b, f_{osc}, and σ_0 are the covering fraction parameter, optical depth, frequency, ion column density, Doppler parameter, oscillator strength, and cross section, respectively. $\Phi(\nu|b, z)$ is the normalized Voigt profile. The adopted atomic parameters are taken from Morton [2003].

In the fitting procedures, the model described above is further convolved with the line-spread function of HST/COS tabulated on the HST/COS website[3]. We adopt a customized software built on the non-linear least-squares fit implemented in LMFIT to search for the best-fit model. In our software, a velocity component is added to the model if the Bayesian Information Criterion (BIC) [Ivezić et al., 2019] decreases, and this process stops when the minimum BIC value is found. The model with the lowest BIC value is then chosen as the best-fit to the data, which is also confirmed by a visual inspection. In addition, we have tested this by manually fitting the absorption line profile with n+1 components when n components are required by the best fit. The change in total column density is in general $\lesssim$0.1 (in logarithm), within the uncertainty of total column density derived from the best-fit model. The uncertainties of the best-fit parameters are calculated from the 1-σ (68.3%) confidence interval adopting the conf_interval function of LMFIT, which takes into account the covariances between blended absorption components.

The best fits for all absorbers clearly detected in our sample are shown in Fig. 2.6. The covering factor, C_f, is fixed to unity in two objects: for F21219, the fit is unable to break the degeneracy between the covering factor and ion column density; for F23060 no evidence of partial covering is suggested by the data. For Z11598 and F13218, the ion column densities are reported as lower limits due to the saturation of the absorption features. Additionally, the fits for the N V BAL in F07599 and O VI BAL in F01004 are highly uncertain given the model parameter degeneracy caused by the saturation and smoothness of the absorption feature, and the large uncertainties in the continuum determination.

Following Paper I, our fitting scheme assumes that the velocity dependence of the optical depth can be parameterized as the sum of discrete independent components with Voigt profiles

[3]https://www.stsci.edu/hst/instrumentation/cos/performance/spectral-resolution

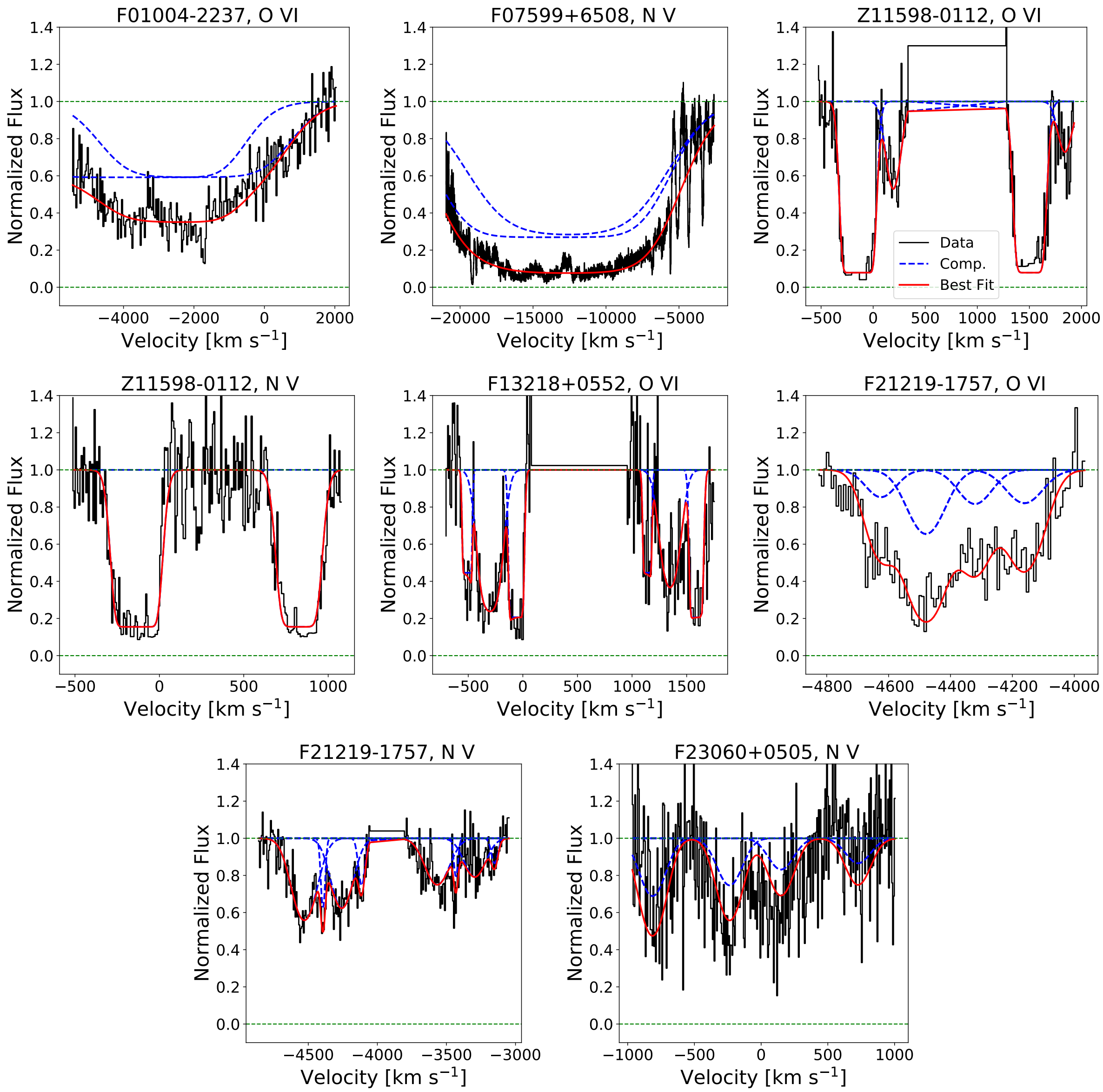

Figure 2.6: Best fits to the O VI λλ1032, 1038 and N V λλ1238, 1243 absorption features detected in our sample of ULIRGs using multi-component Voigt profile fitting. Notice that for the BAL in F01004 and F07599, the single-component fits are tentative/experimental, only aiming to capture the overall shape of the BAL. In each panel, the normalized flux density is shown by the black solid curve. The overall best-fit model and individual components of this model are shown by the red solid curve and blue dashed curves, respectively. All spectra are normalized to the local continuum and shown in the rest-frame of the bluer transitions of corresponding objects.

and constant covering fractions, and that the individual absorbers simply overlap with each other along the line-of-sight. In reality, the C_f is probably a more complex function of velocities [Arav et al., 2005, 2008, 2013], and the absorbing material may completely overlap, partially overlap or not overlap each other. While our approach cannot account for these details, it is sufficient to meet our primary goal, which is to characterize the overall strength and kinematics of these absorbers, and put constraints on the ion column density.

The column densities and covering fractions from these fits are summarized in Table 2.5. For sources Z11598, F13218 and F21219, the results are consistent with those obtained from the analysis of the absorption doublets with partial covering model as described in Sec. 2.3.3.1. Further discussion based on these fits is postponed until Sec. 2.5.

2.4 Origin of the Lyα Emission

Intuitively, strong Lyα emission is not expected in dusty ULIRGs due to the huge optical depth. The origin of Lyα emission in our objects is therefore worth investigating. In this section, we focus on three factors that may help with the production and/or escape of Lyα photons in our ULIRG sample:

(i) AGN: The AGN activity may intrinsically produce more Lyα photons than what we have assumed. For example, the gas density may be so high in the broad line region (and perhaps also narrow line region) of AGN that collisional excitation becomes important in promoting Lyα emission [e.g., Dijkstra, 2017]. Radiation from the AGN may also ionize the gas and destroy the dust in the Lyα-emitting regions and material along the line-of-sight, and therefore reduce the overall opacity to the Lyα emission. (ii) Outflow: The blueshifted Lyα emission may come from the outflowing gas. The velocity offset between the outflow and the interstellar medium decreases the optical depth to the Lyα emission radiated from the fast-moving gas. The outflow can also create low opacity pathways for Lyα photons by clearing out the gas and dust. In addition, the outflow may have broken out of the dusty ISM so that Lyα photons can escape freely. (iii) Dust: The Lyα photons are heavily affected by complicated, dust-related radiative transfer effects, which directly affect the observed properties of the Lyα emission in ULIRGs.

In our analyses, we adopt Kendall tau correlation tests to examine potential correlations between the properties of Lyα emission and those of the AGN, outflows, and dust reddening. Specifically, we adopt the method from Isobe et al. [1986] to compute the Kendall tau correlation coefficient. The p-value of null hypothesis (no correlation) is calculated to show the statistical significance of the correlation. This method can handle censored data, which is the case for EW$_{Ly\alpha}$ and $f_{esc}(\mathrm{Ly}\alpha)$. We use the implementation of pymccorrelation [Privon et al., 2020], which perturbs the data with Monte Carlo method to compute the error in the correlation coefficient [Curran, 2014]. To expand the dynamic ranges of the variables in the analyses, by default, we also include the results of the starburst-dominated ULIRGs from M15, whenever possible. The results from these correlation tests are summarized in Table 2.6.

Table 2.6. Correlation Tests with the Lyα Properties

x (1)	y (2)	sample (3)	N (4)	p-value (5)	r (6)
L_{AGN}	$EW_{Ly\alpha}$	A	20	0.002	$0.49^{+0.13}_{-0.14}$
L_{AGN}	f_{esc}(Lyα)	A	26	0.062	$0.26^{+0.16}_{-0.16}$
L_{AGN}	v_{80}	A	14	0.058	$-0.38^{+0.17}_{-0.15}$
L_{AGN}	v_{50}	A	14	0.095	$-0.34^{+0.18}_{-0.15}$
L_{AGN}	W_{80}	A	14	0.066	$0.37^{+0.18}_{-0.18}$
f_{AGN}	$EW_{Ly\alpha}$	A	20	0.023	$0.37^{+0.13}_{-0.14}$
f_{AGN}	f_{esc}(Lyα)	A	26	0.068	$0.25^{+0.14}_{-0.14}$
f_{AGN}	v_{80}	A	14	0.470	$-0.08^{+0.19}_{-0.20}$
f_{AGN}	v_{50}	A	14	0.429	$-0.08^{+0.22}_{-0.21}$
f_{AGN}	W_{80}	A	14	0.439	$-0.08^{+0.20}_{-0.22}$
$v_{80,[O\ III]}$	$EW_{Ly\alpha}$	A	18	0.064	$-0.32^{+0.19}_{-0.16}$
$v_{80,[O\ III]}$	f_{esc}(Lyα)	A	20	0.049	$-0.32^{+0.20}_{-0.16}$
$v_{80,[O\ III]}$	v_{80}	A	18	<0.001	$0.72^{+0.08}_{-0.11}$
$v_{80,[O\ III]}$	v_{80}	B	12	0.003	$0.65^{+0.14}_{-0.20}$
$v_{80,[O\ III]}$	v_{80}	C	8	0.008	$0.77^{+0.13}_{-0.23}$
$v_{50,[O\ III]}$	$EW_{Ly\alpha}$	B	12	0.398	$-0.06^{+0.30}_{-0.24}$
$v_{50,[O\ III]}$	f_{esc}(Lyα)	B	13	0.381	$0.04^{+0.26}_{-0.26}$
$v_{50,[O\ III]}$	v_{50}	B	12	0.041	$0.45^{+0.18}_{-0.21}$
$v_{50,[O\ III]}$	v_{50}	C	8	0.013	$0.72^{+0.15}_{-0.26}$
$W_{80,[O\ III]}$	$EW_{Ly\alpha}$	B	12	0.439	$-0.05^{+0.25}_{-0.25}$
$W_{80,[O\ III]}$	f_{esc}(Lyα)	B	14	0.228	$0.23^{+0.19}_{-0.22}$
$W_{80,[O\ III]}$	W_{80}	B	12	0.007	$0.60^{+0.14}_{-0.18}$
$W_{80,[O\ III]}$	W_{80}	C	8	0.083	$0.49^{+0.27}_{-0.27}$
$A_{91,[O\ III]}$	$EW_{Ly\alpha}$	B	12	0.285	$-0.20^{+0.28}_{-0.24}$
$A_{91,[O\ III]}$	f_{esc}(Lyα)	B	14	0.468	$0.10^{+0.16}_{-0.18}$
$A_{91,[O\ III]}$	A_{91}	B	12	0.012	$0.56^{+0.13}_{-0.17}$

Table 2.6 (cont'd)

x (1)	y (2)	sample (3)	N (4)	p-value (5)	r (6)
$A_{91,[O\ III]}$	A_{91}	C	8	0.017	$0.69^{+0.17}_{-0.20}$
$v_{80,H\alpha}$	EW$_{Ly\alpha}$	B	14	0.174	$-0.26^{+0.29}_{-0.23}$
$v_{80,H\alpha}$	f_{esc}(Lyα)	B	17	0.428	$-0.06^{+0.20}_{-0.20}$
$v_{80,H\alpha}$	v_{80}	B	14	0.001	$0.64^{+0.10}_{-0.13}$
$v_{50,H\alpha}$	EW$_{Ly\alpha}$	B	14	0.534	$-0.03^{+0.19}_{-0.18}$
$v_{50,H\alpha}$	f_{esc}(Lyα)	B	15	0.316	$0.13^{+0.20}_{-0.26}$
$v_{50,H\alpha}$	v_{50}	B	14	0.437	$0.01^{+0.22}_{-0.24}$
$W_{80,H\alpha}$	EW$_{Ly\alpha}$	B	14	0.203	$0.23^{+0.21}_{-0.28}$
$W_{80,H\alpha}$	f_{esc}(Lyα)	B	16	0.411	$-0.03^{+0.23}_{-0.21}$
$W_{80,H\alpha}$	W_{80}	B	14	0.005	$0.56^{+0.13}_{-0.14}$
$A_{91,H\alpha}$	EW$_{Ly\alpha}$	B	14	0.373	$0.00^{+0.27}_{-0.26}$
$A_{91,H\alpha}$	f_{esc}(Lyα)	B	16	0.466	$-0.10^{+0.18}_{-0.16}$
$A_{91,H\alpha}$	A_{91}	B	14	0.039	$0.41^{+0.16}_{-0.20}$
$E(B-V)$	f_{esc}(Lyα)	A	20	0.371	$0.00^{+0.20}_{-0.22}$

Note. — Column (1): Independent variable (AGN and host galaxy property). Column (2): Dependent variable (Lyα property). Column (3): Flag for the sample adopted in the analysis. A: Our ULIRG sample + the ULIRG sample from M15; B: Our ULIRG sample alone; C: Sources with Type 2 AGN in our ULIRG sample. Column (4): Number of data points; Column (4) p-value of null hypothesis (no correlation) from the Kendall tau correlation test; Column (5) Kendall tau correlation coefficient r with the associated 1-σ error.

2.4.1 Effect of the AGN

First, we examine the possible link between the strength of the AGN (more specifically, the AGN luminosities, L$_{AGN}$, and AGN fractions, f$_{AGN}$; see Table 5.1) and the properties of Lyα emission. As shown in Fig. 2.7, the EWs of Lyα (EW$_{Ly\alpha}$) increase with both L$_{AGN}$ and f$_{AGN}$. The p-values are ∼0.002 and ∼0.023 based on the Kendall tau tests, respectively. In addition, L$_{AGN}$ may also correlate with the kinematic properties of Lyα (v_{80}, v_{50} A_{91} and W_{80} of Lyα; p-values $\simeq$ 0.06–0.10). As an example, v_{80} of Lyα are plotted against L$_{AGN}$ and f$_{AGN}$ in Fig. 2.8. These weak trends are mainly driven by the Type 1 sources with small v_{80} and large W_{80}: indeed, the correlations are not statistically significant (p-values $>$ 0.1) when the Type 1 sources are excluded.

Next, we explore the behavior of the Lyα escape fraction, f_{esc}(Lyα), with the strength of the AGN, as shown in Fig. 2.9. There are possible positive correlations between L$_{AGN}$ and f_{esc}(Lyα) (p-value $\simeq$ 0.062), and between f$_{AGN}$ and f_{esc}(Lyα) (p-value $\simeq$ 0.068). However, we note that these correlations are no longer significant (p-values $\simeq$ 0.2 and 0.4, respectively) if we exclude the data points of the starburst-dominated ULIRGs from M15.

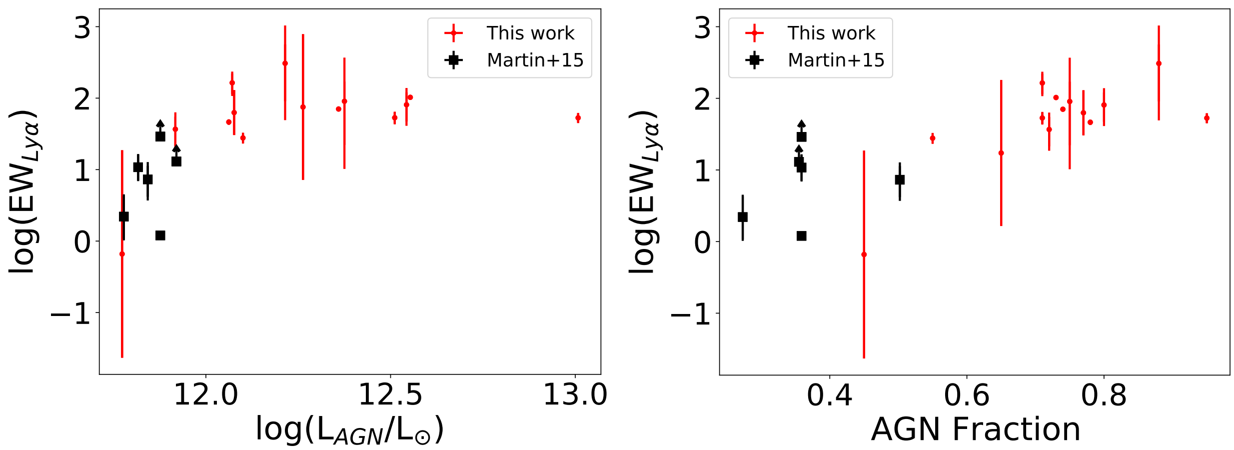

Figure 2.7: The Lyα EWs for the ULIRGs in our sample (red) and those from M15 (black) versus AGN luminosities (left) and AGN fractions (right). There are statistically significant positive correlations between L$_{AGN}$ and EW$_{Ly\alpha}$, and between f$_{AGN}$ and EW$_{Ly\alpha}$.

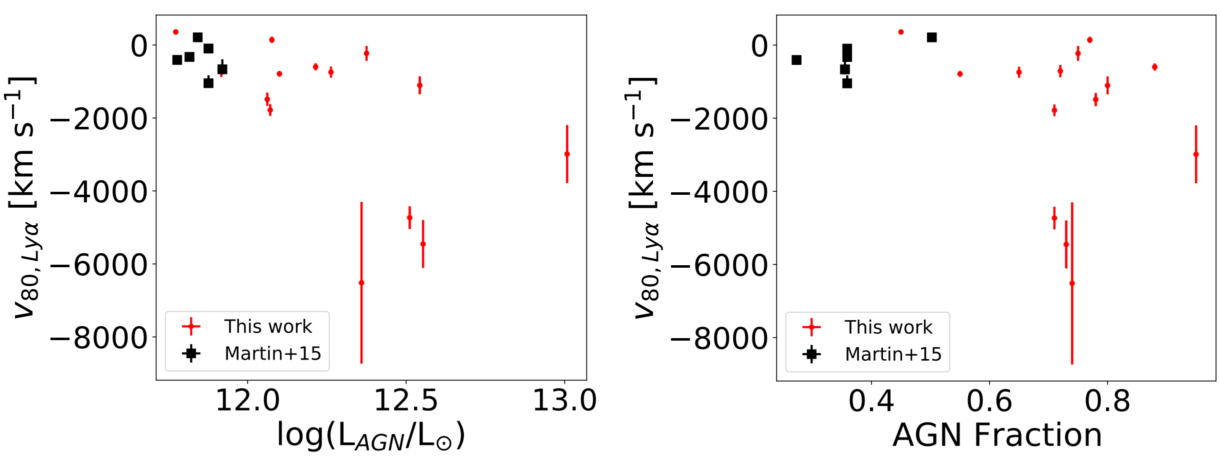

Figure 2.8: The 80-percentile velocities v_{80} of Lyα for the ULIRGs in our sample (red) and those from M15 (black) versus AGN luminosities (left) and AGN fractions (right). There are weak correlations between L$_{AGN}$ and v_{80}, and between f$_{AGN}$ and v_{80}, which are, however, mainly driven by the Type 1 sources with small v_{80}.

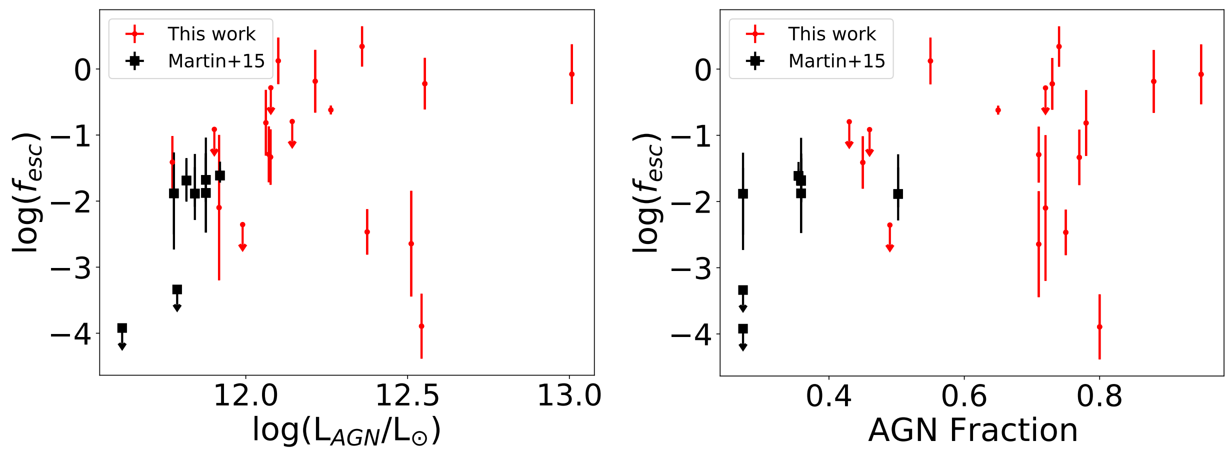

Figure 2.9: The Lyα escape fractions for the ULIRGs in our sample (red) and those from M15 (black) versus AGN luminosities (left) and AGN fractions (right). There may be weak correlations between L_{AGN} and f_{esc}(Lyα), and between f_{AGN} and f_{esc}(Lyα), when both the data from our sample and sources in Martin+15 are considered.

2.4.2 Effect of the Outflow

The prevalence of blueshifted Lyα emission line profiles in our sample, as stated in Sec. 2.3.1, hints at a potential link between outflows and the Lyα emission in our objects. Therefore, we start by simply checking whether there is a correlation between the $EW_{Ly\alpha}$ and v_{80} of Lyα, and confirm a positive result (p-value $\simeq$ 0.02). However, we note that this trend disappears (p-values $>$ 0.1) if we do not include the starburst-dominated objects from M15. Similarly, we have also checked the potential correlation between f_{esc}(Lyα) and v_{80} of Lyα, but no statistically significant trend is present (p-value $\simeq$ 0.13).

2.4.2.1 Connection with the Ionized Outflow in Emission

The blueshift of the non-resonant, forbidden emission [O III] λ5007 line in galaxies is strong evidence for ionized gas outflows [Veilleux et al., 2005a]. To investigate the connection between the blueshift of the Lyα emission and [O III] outflowing gas, it is thus natural to deter-

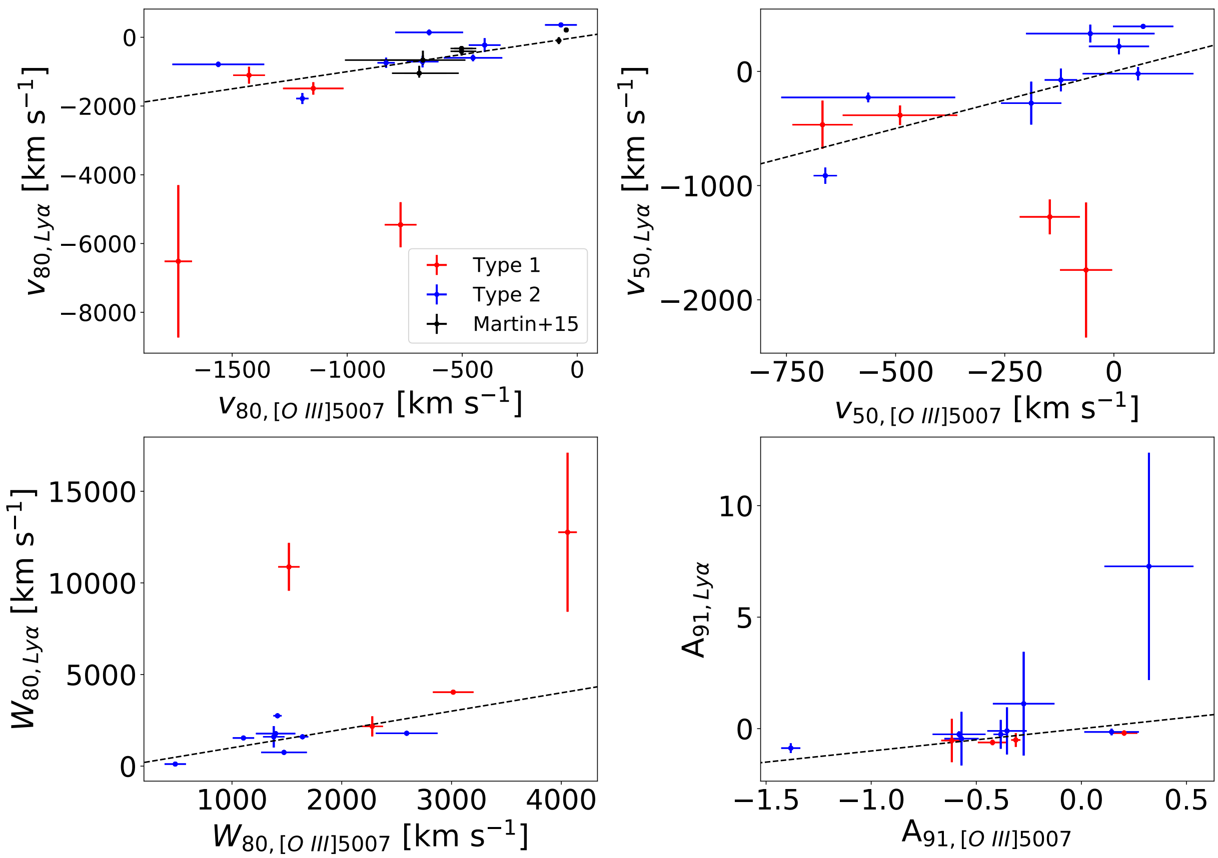

Figure 2.10: Comparisons of the kinematic properties derived from Lyα and [O III] λ5007. From top left to bottom right, v_{80}, v_{50}, W_{80}, and A_{91} are shown. The ULIRGs with Type 1 and Type 2 AGN in our sample are shown in red and blue, respectively. In the upper-left panel, the ULIRGs from M15 are shown in black. The black dashed lines indicate the 1:1 equality lines. The v_{80} of Lyα and [O III] λ5007 emission lines correlate with each other. Other kinematic properties of the Lyα and [O III] λ5007 emission lines are also correlated but less significantly.

mine whether the kinematic properties derived from the Lyα emission line are correlated with those based on the [O III] λ5007 emission. This comparison is shown in Fig. 2.10.

The most significant trend observed in our sample is the positive correlation between v_{80} of Lyα and [O III] λ5007, with p-value < 0.001. This trend still holds if the data from M15 are excluded (p-values $\simeq$ 0.003), or if only the type 2 sources are considered in the analysis (p-value $\simeq$ 0.008). The values of v_{50}, W_{80}, and A_{91} of Lyα also show positive correlations with those of [O III] λ5007, although they are statistically less significant (p-values of $\sim$0.007 – 0.041 from the Kendall tau tests[4]; see Table 2.6).

Additionally, as shown in Fig. 2.11, there may be weak correlations between $v_{80,[O\ III]}$ (notice that this quantity is negative in the case of outflows) and $\mathrm{EW}_{Ly\alpha}$ (p-value $\simeq$ 0.064), and between $v_{80,[O\ III]}$ and $f_{esc}(\mathrm{Ly}\alpha)$ (p-value $\simeq$ 0.049). This suggests that, to some extent, outflows may help clear the path for Lyα photons to escape. However, these weak trends are no longer significant when the objects from M15 are excluded. Moreover, no statistically significant trends are visible when considering the other kinematic properties of [O III] λ5007 ($v_{50,[O\ III]}$, $W_{80,[O\ III]}$, and $A_{91,[O\ III]}$).

For the sake of completeness, we also briefly discuss the strong Hα line emission in these objects. We note that v_{80}, W_{80}, and A_{91} of Hα are positively correlated with those of Lyα (p-value $\simeq$ 0.001–0.039; see Table 2.6), whereas no correlation is seen between v_{50} of Hα and Lyα (p-value $\simeq$ 0.437). While blueshifted Hα emission may indicate outflowing gas, Hα is likely dominated by the emission from the broad emission line region (BELR) in Type 1 sources (e.g. 3C 273, Mrk 1014; see Fig. 2.5). In addition, the nearby [N II] $\lambda\lambda$6548, 6583 emission lines add uncertainty to the kinematic measurements based on Hα. Therefore, we do not use the Hα-based kinematics to examine the link between the blueshifts of Lyα and the ionized outflows in the remainder of the paper.

2.4.2.2 Connection with the O VI and/or N V Outflows

As discussed in Sec. 2.3.3, highly ionized O VI and/or N V outflows are detected in the HST/COS spectra of our ULIRGs. Among the 9 objects with both Lyα measurements and con-

[4] As a reminder, in the analyses including $v_{50,[O\ III]}$, $W_{80,[O\ III]}$, and $A_{91,[O\ III]}$, we do not consider the sources from M15 as the corresponding measurements are not publicly available.

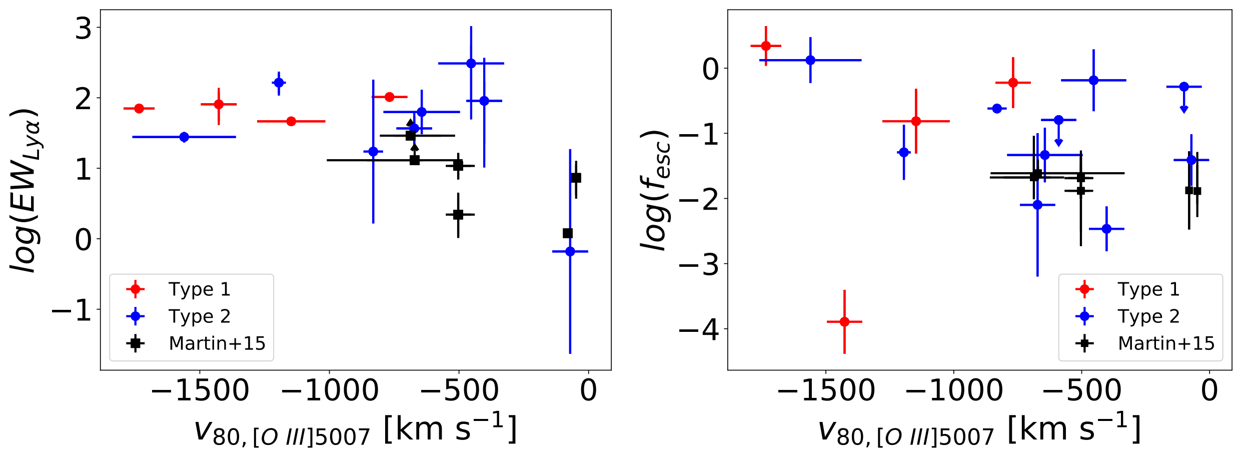

Figure 2.11: The Lyα EWs (left) and Lyα escape fractions (right) for the Type 1 (red) and Type 2 (blue) ULIRGs in our sample and the starburst-dominated ULIRGs from M15 (black) as function of the 80-percentile velocities v_{80} of [O III] λ5007 emission lines. There are weak correlations between $v_{80,[O\ III]}$ and EW$_{Ly\alpha}$, and between $v_{80,[O\ III]}$ and $f_{esc}(\text{Ly}\alpha)$, when both the data from our sample and sources in Martin+15 are considered.

tinuum S/N high enough to allow for relatively solid detection of O VI and/or N V absorption features, 4 of them show O VI and/or N V outflows. There is no clear difference in the mean values and overall ranges of the Lyα escape fractions between the objects with and without O VI and/or N V outflows. The mean value of the Lyα EWs in the objects without outflow detection in O VI and/or NV is higher than those with outflows by $\sim$60%. However, these results are based on a very small sample, so no statistically robust conclusion may be drawn.

2.4.2.3 Connection with the Neutral Phase Outflows

Neutral gas outflows, traced by the blueshifted Na I D $\lambda\lambda$5890, 5896 absorption features, are often detected in ULIRGs [e.g., Rupke et al., 2005c, Rupke and Veilleux, 2011, 2013a, Rupke et al., 2017]. As shown in Fig. 2.12, three of our objects have both blueshifted Lyα emission and blueshifted interstellar Na I D absorption features with similar kinematics. Specifically, for F05189, v_{50} of Lyα emission is similar to that of the blueshifted component of the Na I D absorption (~-400 km s^{-1}). For F11119, the blueshifted peak of the Lyα emission and v_{50} of Na I D absorption have a similar velocity of ~-800 km s^{-1}. For Mrk 231, v_{50} of Na I D absorption (~-5000 km s^{-1}) is close to the velocity of the peak of the blueshifted wing of Lyα emission. Overall, if the blueshifted Lyα emission is indeed tracing the outflowing gas, as argued in Section 2.4.2.1, the results above hint at a possible connection between the outflowing gas traced by blueshifted Lyα and the outflowing neutral gas in these three objects. For instance, Lyα could be scattered off of the outflowing neutral gas traced by Na I D. However, given the very small number of objects where the Lyα $-$ Na I D comparison was possible, these results may not apply to all objects in the sample.

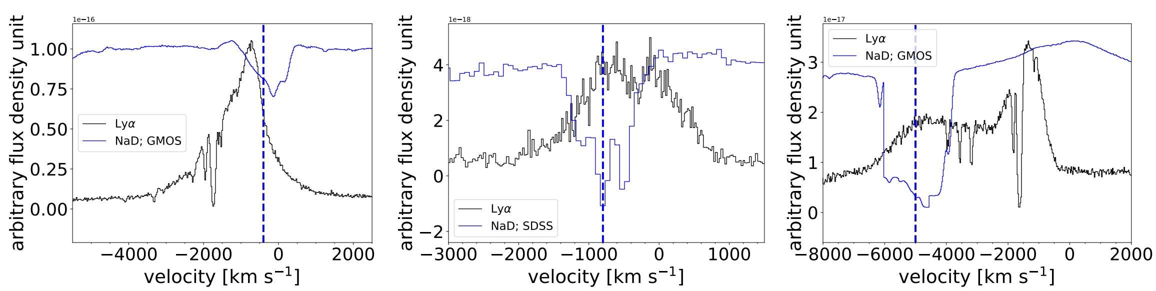

Figure 2.12: Comparison between the Lyα (black) and Na I D $\lambda\lambda$5890, 5896 (blue) profiles for sources F05189 (left), F11119 (middle) and Mrk 231 (right). The blue dashed lines indicate the v_{50} of the outflowing Na I D $\lambda\lambda$5890, 5896 component from Rupke et al. [2005c, excluding the systemic component in F05189]. The spectra are scaled for display purposes and the y axes are in arbitrary flux density units.

2.4.3 Effect of Dust

Complex dust-related radiative transfer processes may shape the observed Lyα emission. In the following, we explore how dust and its distribution within the galaxy may affect the escape of Lyα photons qualitatively, by examining the relation between the nebular line color excess, $E(B-V)$ (reflecting dust reddening of the line-emitting gas) and f_{esc}(Lyα). A more quantitative analysis on this issue requires a careful modelling of the radiative transfer processes, which is beyond the scope of this paper.

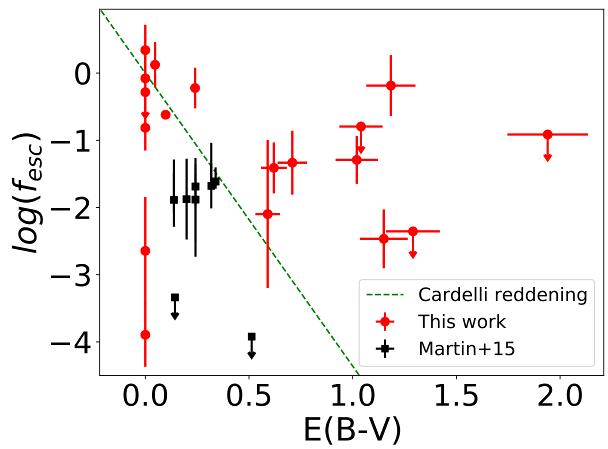

Figure 2.13: Lyα escape fractions, f_{esc}(Lyα), for the AGN-dominated ULIRGs in our sample (red: Type 1 AGN; blue: Type 2 AGN) and the starburst-dominated ULIRGs from M15 (black) as a function of the color excess $E(B-V)$. The green dashed line indicates the continuum attenuation at the wavelength of Lyα transition as given by a Cardelli et al. [1989a] reddening curve and the color excess (measured from the Balmer decrement).

In Fig. 2.13, we plot f_{esc}(Lyα) as a function of $E(B-V)$ for both our objects and the starburst-dominated ULIRGs from M15. Also shown in the figure is the expected f_{esc}(Lyα) given the continuum attenuation at the Lyα transition derived from the values of $E(B-V)$ based on the Cardelli et al. [1989a] reddening curve. In the figure, there is a lack of correlation between the $E(B-V)$ and f_{esc}(Lyα) (p-value $\simeq$ 0.371 from the Kendall tau test, see Table 2.6), which is inconsistent with the naive expectation that f_{esc}(Lyα) should decrease with increasing $E(B-V)$. In addition, the Lyα emission in 6 out of the 14 ULIRGs with clear Lyα detections show f_{esc}(Lyα) much higher than the values expected from the reddening curve. Similar phenomena have been seen in nearby Lyα-emitting galaxies with $E(B-V) \gtrsim 0.3$, where Lyα emission is on average several times stronger than expected [Scarlata et al., 2009, Atek et al., 2014, Hayes et al., 2014].

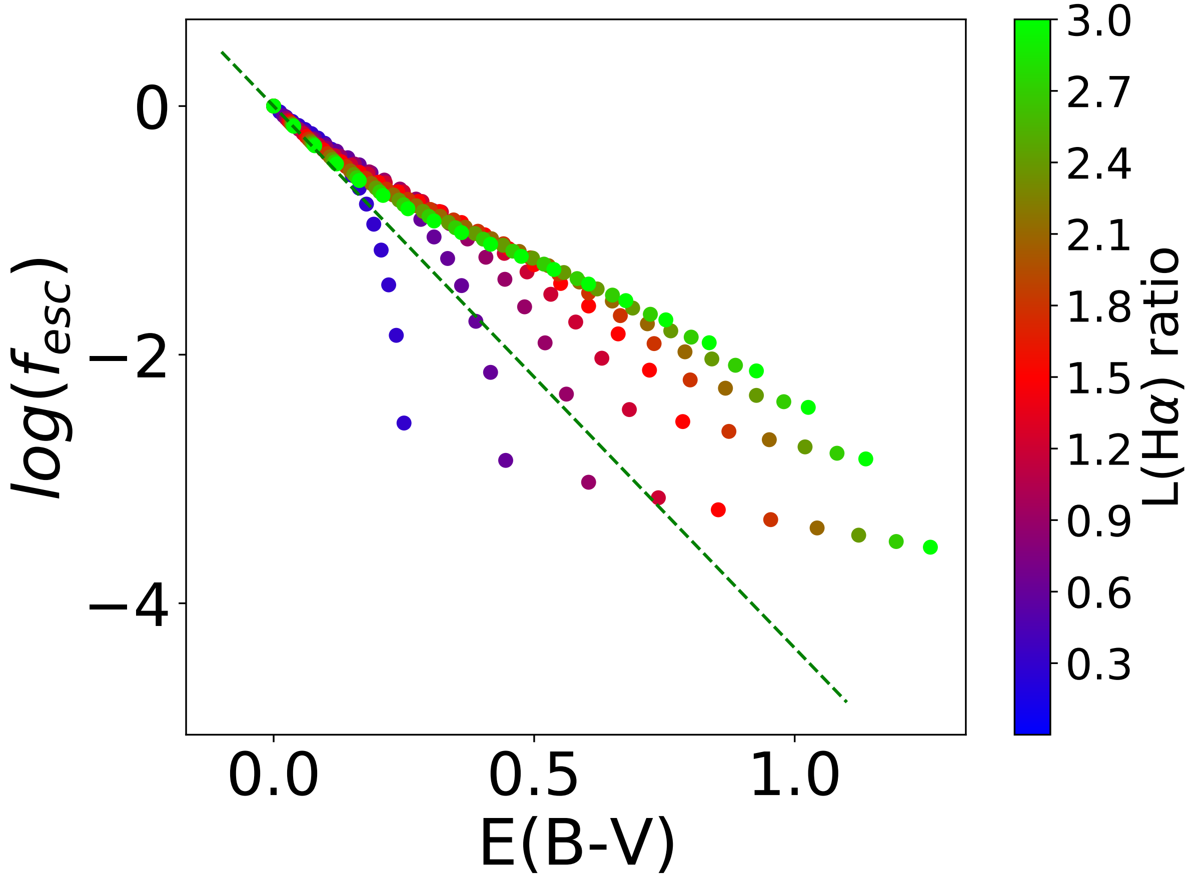

Figure 2.14: $f_{esc}(\mathrm{Ly}\alpha)$ as a function of $E(B-V)$ from a simple model reflecting the effect of mixing two ionized gas clouds: one cloud with no dust content and unity Hα luminosity, and the other one with increasing dust reddening and Hα luminosity. The Hα luminosity ratio of the dusty cloud to the dust-free cloud is indicated by the color of the data point. Along each track of data points with the same color, the $E(B-V)$ of the dusty cloud increases from left to right. The green dashed line indicates the same continuum attenuation as shown in Fig. 2.13.

The two phenomena described above may be caused by the fact that our observations reflect the integrated properties of regions with various dust extinction within one galaxy. The observed emission lines come from both the dusty regions (more likely located in the central parts of the systems) and dust-free/less dusty regions such as broad line region of the AGN, off-nuclear H II region, diffused ionized gas, tidally stripped gas during the merging process or even outflowing gas at large distance from the nucleus. The observed Lyα flux and $E(B-V)$ are the integrated values of all these regions with different weights, which may therefore lead to large scatters in the relation between $E(B-V)$ and $f_{esc}(\mathrm{Ly}\alpha)$. The higher $f_{esc}(\mathrm{Ly}\alpha)$ at a given $E(B-V)$ may be explained if dusty regions bias the overall $E(B-V)$ to a value higher than those of less dusty regions where most of the observed Lyα emission comes from [this scenario has been pointed out in previous work; e.g., Atek et al., 2014]. To illustrate this point, we build a simple model that considers the total Lyα and Balmer emission lines from two ionized gas clouds: one with zero dust reddening, and one with increasing dust reddening. The Hα luminosity ratios of the two regions are also varied. The overall $E(B-V)$ and $f_{esc}(\mathrm{Ly}\alpha)$ integrated over the two gas clouds are shown in Fig. 2.14. At large $E(B-V)$, the $f_{esc}(\mathrm{Ly}\alpha)$ can be easily larger than the expected values based on the dust extinction curve, adopting case B. In addition, the overall distribution of the data points can also mimic the scatter/non-correlation seen in Fig. 2.13.

Similarly, the enhancement of $f_{esc}(\mathrm{Ly}\alpha)$ may also be caused by the internal geometry of the ISM and the dust distribution within it that, together, change the behavior of Lyα photons with respect to dust attenuation. At least two possible solutions have been proposed by previous works: (i) Atek et al. [2009] and Finkelstein et al. [2009] have invoked the Neufeld [1991] geometry where dust is embedded within the H I clumps of a multiphase ISM, and the scattering of Lyα photons prevents them from encountering dust. However, radiative transport simulations show that this effective "boost" of Lyα is very difficult unless parameters are carefully fine-tuned [Laursen et al., 2013, Duval et al., 2014]. The predicted increase of Lyα EW with measured attenuation is not observed in our sample. (ii) Instead, Scarlata et al. [2009] argue for a scenario that is also built upon a clumpy dust distribution. It neither requires preservational scattering as in scenario (i) nor predicts that Lyα EW increase with $E(B-V)$.

Alternatively, the higher-than-expected $f_{esc}(\mathrm{Ly}\alpha)$ in the 6 sources may be caused by higher intrinsic Lyα emission. Such deviation from case B may be caused by the high density gas within the BELR of the AGN, where the collisional excitation enhances the intrinsic Lyα emission. Nevertheless, following this logic, it may be odd that the higher-than-expected $f_{esc}(\mathrm{Ly}\alpha)$ are mostly seen in Type 2 sources rather than Type 1 sources where the Lyα enhancement due to the dense BELR should be more prominent. For example, in the Type 1 source 3C 273, while the broad Lyα emission line resembles the broad Hα emission line (see Fig. 2.5) and is thus likely originated from the BELR, the $f_{esc}(\mathrm{Ly}\alpha)$ in 3C 273 is close to the expected value under case B condition.

2.4.4 Overall Trends

In short, the analyses above indicate that the EWs of Lyα are more closely related to the strength of AGN activity (e.g., L_{AGN}, f_{AGN}), while the blueshifts of Lyα emission are more closely linked to those of non-resonant optical emission lines tracing ionized gas outflows. It is likely that the AGN activity governs the overall production of Lyα emission and the outflowing gas generates the blueshifted Lyα emission.

Additionally, the Lyα escape fractions, $f_{esc}(\mathrm{Ly}\alpha)$, tend to be slightly higher in sources with stronger AGN and faster outflows. Nevertheless, the $f_{esc}(\mathrm{Ly}\alpha)$ does not correlate with the dust reddening, $E(B-V)$, and 6 out of the 14 objects show $f_{esc}(\mathrm{Ly}\alpha)$ higher than the expectation from attenuation adopting case B conditions and the extinction curve from Cardelli et al. [1989a].

2.5 O VI and N V Absorbers in the ULIRGs

2.5.1 Origin of the O VI and N V Absorbers

We now turn our attention to the O VI and N V absorption features. Given the general blueshifts of these features, they are most likely tracing gas driven out of these galaxies by the starburst and/or AGN. Other possible origins include tidal debris from the galaxy merger, intervening circumgalactic medium (CGM), and stellar absorption.

Following Paper I, the characteristics of O VI and N V absorption features that indicate a quasar-driven wind origin include (1) line profiles that are broad and smooth compared to the thermal line widths (10–20 km s^{-1} for N^{4+} and O^{5+}) ions at temperature T $\simeq 10^{4.5}$ – $10^{5.5}$ K, (2) line ratios of the doublets O VI λ1032/λ1038 and N V λ1238/λ1243 that imply partial covering of the quasar emission source, and perhaps (3) large column densities in these high-ionization ions and/or high O VI/H I column density ratio [Hamann et al., 1997b,a, Tripp et al., 2008, Hamann et al., 2019].

All blueshifted O VI and N V absorbers detected in the 6 ULIRGs meet criterion (1) except for the 2 narrow ($\sigma \sim 30\ km\ s^{-1}$) components out of the 3 components in the best-fit O VI profile of F13218 and the 2 narrow ($\sigma \sim 20 - 30\ km\ s^{-1}$) components out of the 4 components in the best-fit N V profile of F21219[5]. In addition, the O VI and N V absorption features in Z11598 and F13218 meet criterion (2), and the deep BAL features in F01004 and F07599 suggest potentially high column densities in agreement with criterion (3). So, in the end, all 6 ULIRGs show certain O VI and N V absorption features consistent with quasar-driven winds. This translates into an

[5]The narrow line widths of these components do not rule out their outflow origin. AGN outflows can also show combinations of smooth broad components with narrow comps superimposed [e.g., Yuan et al., 2002]

Table 2.7. Estimated Outflow Energetics for O VI and N V Absorptions

Name	log(dM/dt) [$M_\odot$ yr^{-1}]	log(dp/dt) [g cm s^{-2}]	log(dE/dt) [erg s^{-1}]
(1)	(2)	(3)	(4)
F01004, O VI	>-2.6	>32.3	>40.6
F07599, N V	>-1.0	>34.4	>43.3
Z11598, O VI	>-3.9	>29.7	>36.7
Z11598, N V	>-4.0	>29.7	>36.9
F13218, O VI	>-4.7	>29.3	>36.7
F21219, O VI	>-4.7	>30.3	>38.6
F21219, N V	>-4.0	>31.0	>39.3
F23060, N V	>-5.1	>29.1	>36.6

Note. — Column (1): Object and absorption feature names; Column (2)–(4): Estimated lower limits of mass, momentum, and kinetic energy outflow rates as described in Sec. 2.5.2. A radial distance of 0.1 pc, an ionization correction factor of 0.2 [e.g., Tripp and Savage, 2000], and a solar metallicity are adopted in the calculation. The absorption features in F01004 and F07599 are broad absorption lines (BAL), and the lower limits listed are just a rough estimation from a tentative/experimental single component fit to the BAL.

apparent outflow incidence rate of $\sim$50%, close to that of the quasar sample in Paper I. We will expand on this topic in Sec. 2.6.

In contrast, the redshifted component of the O VI $\lambda\lambda$1032, 1038 absorption feature in Z11598 may arise from tidal debris or infalling gas. It is not likely associated with the CGM since such relatively strong N V absorption line is rarely found in CGM studies at the low redshift [Werk et al., 2016], but with several notable exceptions [Ding et al., 2003, Lehner et al., 2009, Savage et al., 2010, Tripp et al., 2011, Muzahid et al., 2015, Rosenwasser et al., 2018, Gatkine et al., 2019, Zahedy et al., 2020]. In addition, we cannot rule out the possibility that the two narrow components ($|v| \lesssim 500$ km s^{-1}, $\sigma \sim 30\ km\ s^{-1}$) in the O VI profile of F13218 come from the turbulent ISM and/or CGM of the system.

2.5.2 Location and Energetics of the Outflows

Here we start with the constraints on the location of the O VI and N V absorbers detected in our ULIRG sample. In Z11598 and F13218 (and perhaps also all other 4 ULIRG with detected absorbers), the O VI and/or N V absorption features are deeper than the FUV continuum level, implying that part of the O VI and N V emission produced in the BELR is also absorbed. These absorbers are thus located outside the BELR which has a scale of

$$r_{BELR} \simeq 0.1(\frac{\lambda L_\lambda(1350\mathring{A})}{2\times 10^{46}\ \mathrm{erg\ s^{-1}}})^{0.55}\ \mathrm{pc} \tag{2.15}$$

[e.g., Kaspi et al., 2005, 2007, Bentz et al., 2013]. The equation (16) above is based on the C IV-traced BELR size luminosity relation from equation (2) in Kaspi et al. [2007], and the denominator, 2×10^{46} erg s^{-1}, corresponds to the $\lambda L_\lambda(1350\ \mathring{A})$ of 3C 273. This typical scale is also consistent with the VLTI/GRAVITY result on the size of the BELR of 3C 273 [$r \simeq 0.12\pm$ 0.03 pc; Gravity Collaboration et al., 2018].

As for the upper limit on the radial distance of the outflows, qualitative constraints exist for the two objects with evidence of partial covering, Z11598 and F21219. The distance of the outflows in these two sources cannot be significantly larger than the size of the region where the continuum radiation comes from. The evidence of partial covering in these two objects also sets interesting limits on the size of the absorbing cloud: If the absorbing material is a single uniform cloud with a 100% filling factor, the cloud size should thus be $\lesssim$0.1 pc. However, if the absorbing material is made of multiple clouds, the partial covering may instead reflect the small filling factor of the clouds, and the sizes of individual clouds may be much smaller than 0.1 pc.

The mass, momentum, and kinetic energy outflow rates of the highly ionized outflow detected in our sample are estimated using the following equations:

$$\frac{dE}{dt} = 3.3 \times 10^{39}(\frac{Q}{0.15})(\frac{N_H}{10^{22}cm^{-2}})(\frac{R}{0.1pc})v_{1000}^3 \tag{2.16}$$

$$\frac{dp}{dt} = 6.7 \times 10^{32}(\frac{Q}{0.15})(\frac{N_H}{10^{22}cm^{-2}})(\frac{R}{0.1pc})v_{1000}^2 \tag{2.17}$$

$$\frac{dm}{dt} = 0.003(\frac{Q}{0.15})(\frac{N_H}{10^{22}cm^{-2}})(\frac{R}{0.1pc})v_{1000} \tag{2.18}$$

In the equations above, Q is an approximate global outflow covering factor quoted from Paper I, based on the incidence of mini-BALs in the SDSS quasars [Trump et al., 2006, Knigge et al., 2008, Gibson et al., 2009, Allen et al., 2011]; R is the radial distance of the outflow and the value of 0.1 pc is a place-holder adopted for illustrative purposes; N_H is the column density of hydrogen, and v_{1000} is the outflow velocity in units of 1000 km s^{-1} obtained from the Voigt profile fits described in Sec. 2.3.3.2.

Note that the Voigt profile fits are highly uncertain for the O VI BAL in F01004, and the N V BAL in F07599, as stated in Sec. 2.3.3.2. Therefore, only rough estimations of the ion column densities may be obtained from the fits. For Z11598 and F13218, the O VI and N V absorption features are also saturated despite their much narrower line widths, so the corresponding ion column densities from the fits are also uncertain. Nevertheless, the results derived from the Voigt profile fits are consistent with those derived from analyzing the absorption doublet with partial covering model, as described in Sec. 2.3.3.1 (see Table 2.5). For the N V absorption in F21219, the ion column density acquired from the analysis with partial covering model is a bit higher than that from the Voigt profile fits, which is expected as the partial covering factor, while fixed to unity in the Voigt profile fit, should be less than unity.

Next, the ion column densities are converted into hydrogen column densities. The metal abundance and ionization correction factor needed for the conversion can, in principle, be determined from elaborate photoionization modeling when multiple absorbers from both high- and low-ionization species are present [e.g., Arav et al., 2013, Haislmaier et al., 2021], but this information is not available for our objects. For simplicity, we adopt a solar abundance [while super-solar metallicities are also reported in the literature; e.g., Moe et al., 2009] and a ionization correction factor of 0.2 [which is a conservative upper limit reported in the literature; e.g., Tripp and Savage, 2000] in the calculations. As discussed at the beginning of this section, the radial distances of these absorbers are largely unconstrained, other than the fact that the absorbers in Z11598 and F13218 are located outside of the BELR ($r \gtrsim 0.1$ pc). Adopting these aforementioned values, the obtained mass, momentum, and energy outflow rates are likely lower limits as reported in Table 4.4. In general, they are modest ($\lesssim$1%) compared with the star formation rates, AGN radiation momenta, and AGN luminosities of the systems. However, for the highly saturated O VI BAL in F01004 and N V BAL in F07599, the column density of the outflowing gas and thus the outflow energetics are probably severely underestimated.

2.6 O VI and N V Absorbers in the Combined ULIRG + Quasar Sample

In this section, we explore the properties of the highly ionized O VI and N V absorbers along the ULIRG-QSO merger sequence [e.g., see Sanders et al., 1988, Hopkins et al., 2009, Veilleux et al., 2009b, and references therein] by combining the 11 ULIRGs with high enough continuum S/N to allow for O VI and N V absorption detections (ULIRG F15250 is excluded from the analysis given that the N V absorption feature is highly uncertain due to contamination from geo-coronal emission) and the 30 quasars presented in Paper I (3 of the 33 quasars in Paper I overlap with the ULIRG sample and are thus already included). In total, 6 ULIRGs (see Sec. 2.3.3) and 17 quasars (see Section 7.1 in Paper I) show O VI and N V absorbers indicative of quasar-driven outflows. In addition, to be consistent with the analyses in Paper I and to maximize the sample size for better statistics, we also include the narrow O VI and/or N V absorption features in the 3 quasars from Paper I that do not meet our criteria for quasar-driven outflows. The absorption features in these three objects are relatively narrow ($\sigma_{rms}\simeq$ 10–30 km s^{-1}) and are redshifted in two of these objects.

2.6.1 Overall Incidence Rates and Regressions

Based on the measurements listed in Table 2.5, while quite uncertain due to the small sample size, we can estimate the incidence rate of absorption features in the ULIRG-only sample. Adopting the β distribution [Cameron, 2011] used in Paper I, we obtain an incidence rate of $\sim$55% (1-σ range: $\sim$40%–68%) for the detection of O VI or N V or both absorption features. This is similar to the rate of $\sim$61% (1-σ range: $\sim$52%–68%) obtained in Paper I, which is based on the quasar sample alone. In the combined ULIRG + quasar sample, the overall incidence rate of O VI or N V or both absorption features is $\sim$63% (1-σ range: $\sim$55%–70%).

Next, we explore how the incidence rates and properties (velocity-integrated EWs, W_{eq}, depth-weighted velocities, v_{wtavg}, and velocity dispersions, σ_{rms}) of the O VI and N V absorption features depend on the AGN and host galaxy properties of our objects, adopting the β distribution above and regressions described below. Following Paper I, we apply linear regressions adopting the Bayesian model in LINMIX_ERR [Kelly, 2007]. We use the Metropolis-Hastings sampler and a single Gaussian to represent the distribution of the parameters. LINMIX_ERR allows censored values for dependent variables (y), which is the case for W_{eq}. The only exceptions involve N_H(X-ray), where both x and y values are censored, in which case we adopt the Kendall tau correlation test described at the beginning of Sec. 2.4. For both methods, we calculated the correlation coefficients r and their 1-σ errors. A perfect correlation gives $r = 1$ and a perfect anti-correlation gives an $r = -1$. A sample with no correlation at all gives $r = 0$. In addition, we have computed the significance of a correlation, P(r), as the fraction of correlation coefficients $r \leq 0$ ($r \geq 0$) for a positive (negative) correlation[6]. For LINMIX_ERR, the distribution of r are acquired from the posterior distribution, while for pymccorrelation, they are obtained from the Monte Carlo perturbations.

For the regressions, we do not take O VI and N V data as independent measurements. Therefore, when measurements are available for both doublets in a given source, we take the average of the measurements (either detection or limit) from the two lines. If only one line is detected, we use the measurement for the detection. In addition, when multiple X-ray measurements exist for a source, we take the average of them. Errors in L_{bol}, L_{IR}, $L_{\rm IR}/L_{\rm BOL}$, $L_{\rm FIR}/L_{\rm BOL}$, and $\alpha_{UV,X}$ are unknown or largely uncertain, so for the regressions we fix their errors to ± 0.1 dex [7]. For λL_{1125}, we ignore the negligible statistical measurement errors. As examples, the final data points adopted for the regressions are shown in the inset panels of Fig. 2.15 and 2.16.

[6]From LINMIX_ERR, it is technically difficult to calculate the classic p-value in null hypothesis significance testing. Nevertheless, our definition of P(r) can describe the significance of the correlation similarly. Like p-value < 0.05, P(r) < 0.05 also indicates a statistically significant correlation: it suggests that the possibility is 95% for the correlation coefficient r to be larger (smaller) than 0, in the case of a positive (negative) correlation. Note that this P(r) was called p-value in Paper I, which is abandoned in this Paper II to avoid ambiguity.

[7]Note that the results of the regression analysis do not change even if we adopt larger errors of up to ± 0.5 dex.

Table 2.8. Incidence Rates of O VI and N V Absorbers in the Combined ULIRG + Quasar Sample

Line (1)	Detection (2)	Total (3)	Fraction (1-σ range) (4)
All Quasars and ULIRGs			
O VI	17	25	0.68(0.58–0.76)
N V	17	34	0.50(0.42–0.58)
Both	8	18	0.44(0.34–0.56)
Any	26	41	0.63(0.55–0.70)
$L_{AGN} < 12.1$			
O VI	9	15	0.60(0.47–0.71)
N V	15	27	0.56(0.46–0.64)
Both	6	10	0.60(0.44–0.73)
Any	13	21	0.62(0.51–0.71)
$L_{AGN} \geq 12.1$			
O VI	7	9	0.78(0.59–0.86)
N V	1	5	0.20(0.12–0.45)
Both	2	8	0.25(0.16–0.44)
Any	12	19	0.63(0.51–0.72)
N_H(X-ray)$< 10^{22}$ cm^{-2}			
O VI	6	14	0.43(0.31–0.56)
N V	5	16	0.31(0.22–0.44)
Both	1	8	0.12(0.08–0.32)
Any	3	12	0.25(0.17–0.41)
N_H(X-ray)$\geq 10^{22}$ cm^{-2}			
O VI	9	9	1.00(0.83–0.98)
N V	10	15	0.67(0.53–0.76)
Both	4	6	0.67(0.45–0.79)
Any	16	21	0.76(0.65–0.83)
X-ray to FUV Spectral Index $\alpha_{UV,X} <$ -1.3			

Table 2.8 (cont'd)

Line (1)	Detection (2)	Total (3)	Fraction (1-σ range) (4)
O VI	10	13	0.77(0.62–0.85)
N V	9	17	0.53(0.41–0.64)
Both	4	8	0.50(0.34–0.66)
Any	15	17	0.88(0.76–0.92)
X-ray to FUV Spectral Index $\alpha_{UV,X} \geq$ -1.3			
O VI	1	2	0.50(0.25–0.75)
N V	4	9	0.44(0.30–0.60)
Both	3	8	0.38(0.25–0.55)
Any	9	20	0.45(0.35–0.56)

Note. — Column (1): Feature(s) used in the statistical analysis. "Both" means both O VI and N V doublets and "Any" means either O VI or N V doublet or both; Column (2): Number of objects with detected absorption features; Column (3): Total number of objects with enough continuum S/N ratios to allow for detections of corresponding absorption features; Column (4): Fraction of objects with detected absorption features. The two numbers in parentheses indicate the 1-σ range (68% probability) of the fraction of objects with detected absorption features, computed from the β distribution [Cameron, 2011].

2.6.2 Dependence on the X-ray Properties

The dependence of the incidence rates on several primary AGN/host galaxy properties are listed in Table 2.8. The regression results between the AGN/host galaxy properties and the properties of the absorption features (W_{eq}, v_{wtavg}, and σ_{rms}) are listed in Table 2.9. In brief, we find that the incidence rates of the absorption features do not depend on the AGN/host galaxy properties, such as the bolometric luminosities, AGN luminosities, AGN fractions, IR luminosities, FIR luminosities, FIR-to-bolometric luminosity ratios, and FUV luminosities (note that only a few key quantities are listed in Table 2.8). Similarly, no statistically significant (P(r) $<$ 0.05, $|r| >> 0$) trends are seen between these AGN/galaxy properties and the properties of the absorption features. These negative results are largely consistent with those in Paper I based on the quasar-only sample.

Nevertheless, as discussed in Paper I, the incidence rate and properties of the absorption features do correlate with several X-ray properties of the sources. We examine these trends with the ULIRG + quasar sample below. In general, we find that the incidence rate of the absorption features is higher in the X-ray weak (relative to their UV luminosities, as quantified by $\alpha_{UV,X}$ described in Sec. 2.2.3.2) or absorbed sources (Table 2.8). We also find that the W_{eq}, v_{wtavg} and σ_{rms} of the absorption features correlate with $\alpha_{UV,X}$ (see Table 2.9).

The incidence rates of the absorption features (either O VI or N V or both) are 88% (1-σ range: 76%–92%) for the objects with $\alpha_{UV,X} < -1.3$[8] and 45% (1-σ range: 35%–56%) for those with $\alpha_{UV,X} \geq -1.3$. Such difference is statistically significant with a p-value of ∼0.014, adopting the scipy.stats implementation of the Fisher exact test with a null hypothesis that galaxies with $\alpha_{UV,X} < -1.3$ and $\alpha_{UV,X} \geq -1.3$ are equally likely to show O VI or N V absorption features. Additionally, as shown in Fig. 2.15, the objects with lower $\alpha_{UV,X}$ tend to have larger W_{eq}, smaller v_{wtavg}, and larger σ_{rms}, where the regressions give correlation coefficients r of $-0.59^{+0.15}_{-0.11}$, $0.48^{+0.15}_{-0.19}$ and $-0.50^{+0.18}_{-0.16}$, respectively. These results in general confirm or strengthen those from Paper I based on the quasar-only sample and α_{OX}: the incidence rates in Paper I were found to be 75% (1-σ range: 59%–83%) versus 55% (1-σ range: 44%–65%) for sources with $\alpha_{OX} < -1.6$ and $\alpha_{OX} \geq -1.6$ (This difference was not considered significant since the p-value was ∼0.45, adopting the same Fisher test on the difference between the incidence rates), and the correlation coefficients r for the trends between the α_{OX} and the W_{eq}, v_{wtavg}, and σ_{rms}, were $-0.62^{+0.17}_{-0.13}$, $0.31^{+0.21}_{-0.24}$ and $-0.55^{+0.20}_{-0.15}$, respectively.

Similarly, the incidence rate of absorption features for sources with N_H(X-ray) $> 10^{22}$

[8] The value -1.3 is chosen since (1) it divides the sample into two groups with approximately equal numbers of objects; (2) it corresponds to an α_{OX} of ~ -1.7 as adopted in Paper I.

cm^{-2} is 76% (1-σ range: 65%–83%), whereas the rate for those with lower N$_H$(X-ray) is 25% (1-σ range: 17%–41%). This result is almost identical to that obtained in Paper I. Moreover, as shown in Fig. 2.16, the W_{eq} of the absorption features may be higher in objects with higher N$_H$(X-ray), which is consistent with the result from Paper I: The correlation coefficients r are $0.24^{+0.03}_{-0.03}$ for the ULIRG + quasar sample and $0.19^{+0.03}_{-0.03}$ for the quasar-only sample, respectively. As for the v_{wtavg} and σ_{rms} of the absorption features, their lack of dependence on the N$_H$(X-ray) found in Paper I remains.

Furthermore, other trends seen among the quasars in Paper I that involve the X-ray luminosities are not statistically significantly anymore when the ULIRGs are included. These include the trend between W_{eq} of the absorption features and the hard X-ray (2–10 keV) luminosities (r changes from $-0.51^{+0.20}_{-0.15}$ to $-0.09^{+0.24}_{-0.23}$), those between v_{wtavg} and σ_{rms} of the absorption features and the soft X-ray (0.5–2 keV) to "total" X-ray (0.5–10 keV) luminosity ratios (r change from $-0.69^{+0.13}_{-0.20}$ and $-0.54^{+0.24}_{-0.18}$ to $-0.18^{+0.26}_{-0.24}$ and $-0.06^{+0.27}_{-0.27}$, respectively), and those between v_{wtavg} and σ_{rms} and the X-ray to bolometric luminosity ratios (r change from $0.64^{+0.14}_{-0.20}$ and $-0.61^{+0.21}_{-0.15}$ to $-0.26^{+0.23}_{-0.21}$ and $0.32^{+0.20}_{-0.23}$, respectively).

Table 2.9. Regression Analysis on the O VI and N V Absorbers in the Combined ULIRG+Quasar Sample

y (1)	x (2)	N (3)	P(r) (4)	r (5)
$W_{\rm eq}$	$\log(L_{\rm BOL}/L_{\odot})$	39	0.157	$-0.18^{+0.18}_{-0.17}$
$W_{\rm eq}$	$\log[\lambda L_{1125}/{\rm erg~s^{-1}}]$	36	0.210	$-0.16^{+0.20}_{-0.18}$
$W_{\rm eq}$	AGN fraction	38	0.126	$-0.40^{+0.35}_{-0.33}$
$W_{\rm eq}$	$\log(L_{\rm AGN}/L_{\odot})$	38	0.088	$-0.25^{+0.18}_{-0.17}$
$W_{\rm eq}$	$\underline{\alpha_{UV,X}}$	35	<0.001	$-0.59^{+0.15}_{-0.11}$
$W_{\rm eq}$	$\log(L_{\rm IR}/L_{\rm BOL})$	39	0.058	$0.33^{+0.18}_{-0.20}$
$W_{\rm eq}$	$\log(L_{\rm FIR}/L_{\rm BOL})$	38	0.225	$-0.13^{+0.18}_{-0.18}$
$W_{\rm eq}$	$\log[N({\rm H})/{\rm cm^{-2}}]$	32	<0.001	$0.24^{+0.03}_{-0.03}$
$W_{\rm eq}$	Γ	34	0.202	$0.17^{+0.19}_{-0.20}$
$W_{\rm eq}$	$\log[L(0.5-2~{\rm keV})/{\rm erg~s^{-1}}]$	30	0.256	$-0.14^{+0.21}_{-0.20}$
$W_{\rm eq}$	$\log[L(2-10~{\rm keV})/{\rm erg~s^{-1}}]$	34	0.327	$-0.09^{+0.19}_{-0.19}$
$W_{\rm eq}$	$\log[L(0.5-10~{\rm keV})/{\rm erg~s^{-1}}]$	30	0.220	$-0.15^{+0.20}_{-0.19}$
$W_{\rm eq}$	$\log[L(0.5-2~{\rm keV})/L(0.5-10~{\rm keV})]$	30	0.357	$-0.09^{+0.24}_{-0.23}$
$W_{\rm eq}$	$\log[L(0.5-10~{\rm keV})/L_{\rm BOL}]$	30	0.243	$-0.15^{+0.21}_{-0.20}$
v_{wtavg}	$\log(L_{\rm BOL}/L_{\odot})$	26	0.168	$-0.21^{+0.22}_{-0.21}$
v_{wtavg}	$\log[\lambda L_{1125}/{\rm erg~s^{-1}}]$	24	0.225	$-0.17^{+0.22}_{-0.20}$
v_{wtavg}	AGN fraction	25	0.186	$0.43^{+0.37}_{-0.49}$
v_{wtavg}	$\log(L_{\rm AGN}/L_{\odot})$	25	0.142	$-0.25^{+0.23}_{-0.20}$
v_{wtavg}	$\underline{\alpha_{UV,X}}$	24	0.011	$0.48^{+0.15}_{-0.19}$
v_{wtavg}	$\log(L_{\rm IR}/L_{\rm BOL})$	26	0.407	$0.07^{+0.29}_{-0.28}$
v_{wtavg}	$\log(L_{\rm FIR}/L_{\rm BOL})$	26	0.280	$-0.13^{+0.21}_{-0.21}$
v_{wtavg}	$\log[N({\rm H})/{\rm cm^{-2}}]$	19	0.012	$-0.19^{+0.08}_{-0.07}$
v_{wtavg}	Γ	22	0.402	$-0.06^{+0.24}_{-0.24}$
v_{wtavg}	$\log[L(0.5-2~{\rm keV})/{\rm erg~s^{-1}}]$	21	0.126	$-0.27^{+0.23}_{-0.20}$
v_{wtavg}	$\log[L(2-10~{\rm keV})/{\rm erg~s^{-1}}]$	22	0.127	$-0.26^{+0.23}_{-0.20}$
v_{wtavg}	$\log[L(0.5-10~{\rm keV})/{\rm erg~s^{-1}}]$	21	0.119	$-0.27^{+0.23}_{-0.21}$

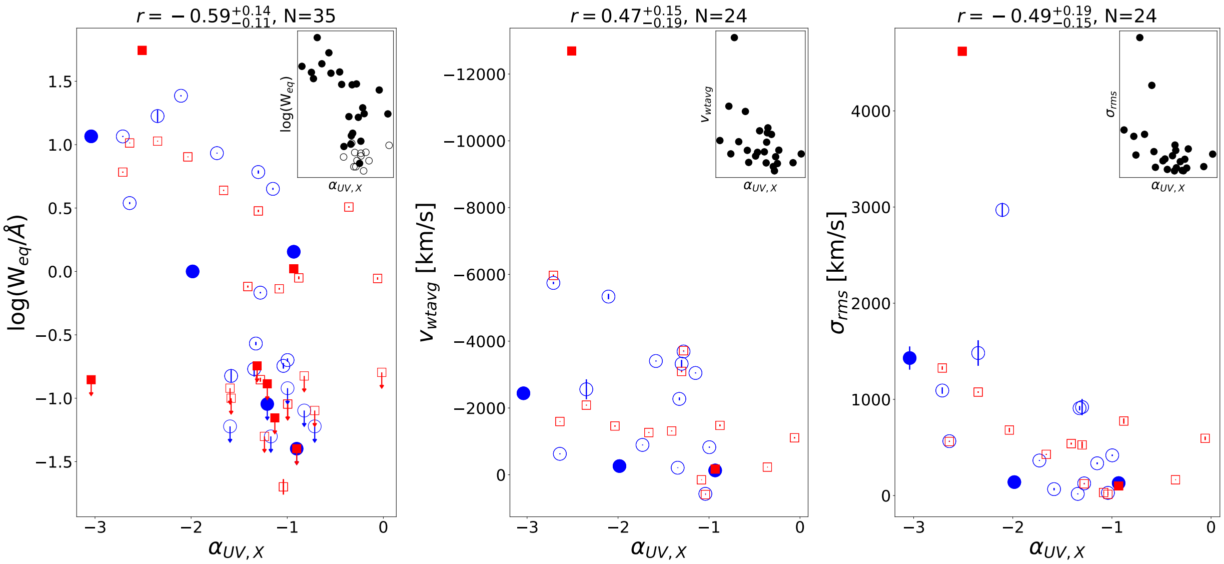

Figure 2.15: The velocity-integrated EWs, W_{eq} (left), depth-weighted velocities, v_{wtavg} (middle) and depth-weighted velocity dispersions, σ_{rms} (right) for the O VI (blue circle) or N V (red square) absorption features in ULIRGs (filled symbols) and quasars (hollow symbols) as function of $\alpha_{UV,X}$. The actual data points used in the regressions, in which O VI and N V quantities and/or X-ray measurements are averaged for a given source, are shown in each inset panel. The solid symbols are detections, while the open symbols are censored values in one or both quantities plotted. The regression results (correlation coefficients r with 1-σ errors, and number of data points in the inset panel, N; see the 3rd paragraph in Sec. 2.6.1 for more information) are shown above each panel.

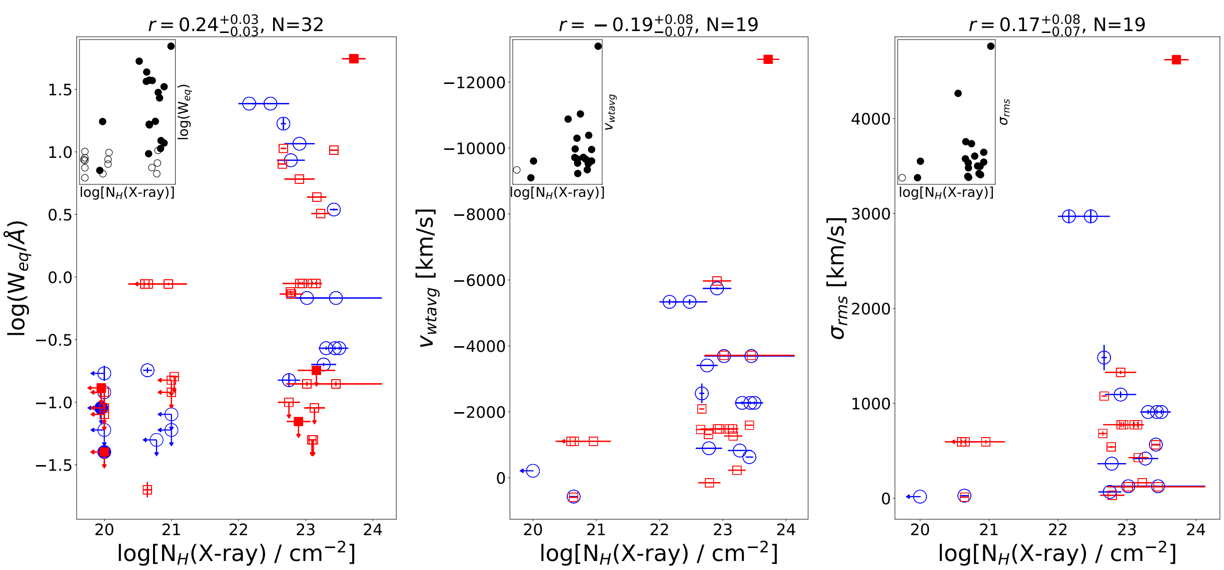

Figure 2.16: Same as Fig. 2.15 but as function of the logarithm of the X-ray absorbing column densities N_H(X-ray).

Table 2.9 (cont'd)

y (1)	x (2)	N (3)	P(r) (4)	r (5)
v_{wtavg}	$\log[L(0.5-2\ \mathrm{keV})/L(0.5-10\ \mathrm{keV})]$	21	0.244	$-0.18^{+0.26}_{-0.24}$
v_{wtavg}	$\log[L(0.5-10\ \mathrm{keV})/L_{\mathrm{BOL}}]$	21	0.139	$-0.26^{+0.23}_{-0.21}$
σ_{rms}	$\log(L_{\mathrm{BOL}}/L_{\odot})$	26	0.162	$0.21^{+0.19}_{-0.21}$
σ_{rms}	$\log[\lambda L_{1125}/\mathrm{erg\ s^{-1}}]$	24	0.449	$-0.03^{+0.24}_{-0.22}$
σ_{rms}	AGN fraction	25	0.208	$-0.33^{+0.40}_{-0.34}$
σ_{rms}	$\log(L_{\mathrm{AGN}}/L_{\odot})$	25	0.134	$0.25^{+0.20}_{-0.22}$
σ_{rms}	$\underline{\alpha_{UV,X}}$	24	0.005	$-0.50^{+0.18}_{-0.16}$
σ_{rms}	$\log(L_{\mathrm{IR}}/L_{\mathrm{BOL}})$	26	0.449	$0.04^{+0.28}_{-0.28}$
σ_{rms}	$\log(L_{\mathrm{FIR}}/L_{\mathrm{BOL}})$	26	0.241	$0.14^{+0.20}_{-0.21}$
σ_{rms}	$\log[N(\mathrm{H})/\mathrm{cm^{-2}}]$	19	<0.001	$0.17^{+0.08}_{-0.07}$
σ_{rms}	Γ	22	0.437	$0.04^{+0.22}_{-0.23}$
σ_{rms}	$\log[L(0.5-2\ \mathrm{keV})/\mathrm{erg\ s^{-1}}]$	21	0.082	$0.32^{+0.20}_{-0.23}$
σ_{rms}	$\log[L(2-10\ \mathrm{keV})/\mathrm{erg\ s^{-1}}]$	22	0.082	$0.33^{+0.19}_{-0.23}$
σ_{rms}	$\log[L(0.5-10\ \mathrm{keV})/\mathrm{erg\ s^{-1}}]$	21	0.097	$0.32^{+0.20}_{-0.24}$
σ_{rms}	$\log[L(0.5-2\ \mathrm{keV})/L(0.5-10\ \mathrm{keV})]$	21	0.426	$0.06^{+0.27}_{-0.27}$
σ_{rms}	$\log[L(0.5-10\ \mathrm{keV})/L_{\mathrm{BOL}}]$	21	0.085	$0.32^{+0.20}_{-0.23}$

Note. — Column (1): Dependent variable (O VI/N V absorption line property). Column (2): Independent variable (quasar/host property). Underlined entries under col. (2) indicate relatively strong correlations with P(r) $<$ 0.05 and $|r| \gtrsim 0.5$. Column (3): Number of data points. Column (4): Probabilities for the correlation coefficients r to be $\leq$0 (for positive correlation) and $\geq$0 (for negative correlation), as defined in the 3rd paragraph in Sec. 2.6.1. Column (5): Correlation coefficients r and their 1-σ errors.

2.6.3 Radiation Pressure as the Most Plausible Wind-Driving Mechanism

Overall, the results from the analyses of the combined ULIRG + quasar sample reinforce the main conclusions of Paper I: (i) The incidence rate and properties of the O VI and N V absorption features (i.e., EWs, outflow velocities and outflow velocity dispersions) are positively correlated with the X-ray weakness of the sources. (ii) The incidence rate of these absorption features is higher in sources with larger X-ray absorbing column densities. The EWs of absorption features may also be higher in such sources.

This dependence of the incidence rate, EWs and kinematic properties of these outflows on the X-ray weakness and/or absorbing columns of the sources can best be explained if these outflows are radiatively driven. As discussed in detail in Section 7.3 of Paper I, the combined radiative force ["force multiplier"; Arav and Li, 1994] is greatly suppressed when the gas is over-ionized by the extreme-ultraviolet (EUV)/X-ray photons, becoming too transparent to be radiatively accelerated effectively. The successful launching of a radiatively-driven wind thus depends on whether this ionizing EUV/X-ray radiation is shielded and/or intrinsically weak.

In the first case, the over-ionized material may serve as a radiative shield to soften the ionizing spectrum enough so that the outflow material downstream can be effectively accelerated [Murray et al., 1995, Proga and Kallman, 2004, Proga, 2007, Sim et al., 2010]. However, as mentioned in Paper I, the predicted strong near-UV absorption features near systemic velocity produced by the shielding material [e.g., Hamann et al., 2013] are in general not observed in our sample. In the second case, it is proposed that the X-ray emission in weak-lined "wind-dominated" quasars are intrinsically faint and unabsorbed [Richards et al., 2011, Wu et al., 2011, Luo et al., 2015, Veilleux et al., 2016]. In our sample, several sources with fast O VI/N V outflows show evidence of intrinsically weak X-ray emission, including F07599, PG1001 and PG1004 [Luo et al., 2013, 2014]. More sensitive hard X-ray ($>$10 keV) observations of our sample would shed light on the exact origin of this X-ray weakness.

Apart from the aforementioned trends with X-ray weakness, the new data on the ULIRGs do not add significantly more support to the radiatively driven wind scenario. The lack of positive trends between the maximum velocities of the outflows and the optical, UV, bolometric luminosities or the Eddington ratios is likely due to the limited dynamic range of properties of the combined ULIRG+quasar sample, and noise in the predicted correlations associated with projection effects and variance in the launching radius and efficiency of the radiative acceleration associated with the complex microphysics of the photon interaction with the clouds (Paper I). Furthermore, we find no other case of line-locking among the outflows of ULIRGs (line-locking was observed in the outflows of two quasars in Paper I). Lastly, as in Paper I, no evidence is present that radiation pressure on dust grains is an important contributor to the radiative acceleration in our sample (the outflow properties do not correlate with the mid-, far-, and total (1 – 1000 μm) infrared excesses). While the alternative thermal wind and "blast wave" models cannot be formally ruled out by our data, these models cannot readily explain the observed connection between the outflow properties and X-ray weakness and absorbing column densities (interested readers are referred to Section 7.3 of Paper I for a more detailed discussion of these models).

2.6.4 The Effects of Stochasticity of AGN-Outflow Activity

Intuitively, the lack of correlations between the properties of the O VI and/or N V outflows and those of the AGN is unexpected given that these winds are driven by the AGN. Together with the result that the outflow incidence rate in the ULIRG sample is virtually identical to that in the quasar sample, it may imply that the launching of these quasar-driven outflows is a stochastic phenomenon throughout the late merger stages. This is consistent with the picture that the triggering of AGN activity has a significant chaotic/random component in local gas-rich mergers and AGN [e.g., Davies et al., 2007, Veilleux et al., 2009b]. Given this stochasticity of AGN activity, Veilleux et al. [2009b] warns that a sample size of $\gtrsim$50-100 may be needed to detect any trends with merger phase. Time delays between bursts in AGN activity, the ejection of the material driven this AGN activity, and the detection of the ejected material on pc and kpc scales also likely complicate this picture [Veilleux et al., 2017].

2.7 Summary

As part II of an HST/COS FUV spectroscopic study of the QUEST (Quasar/ULIRG Evolutionary Study) sample of local quasars and ULIRGs, we have systematically analyzed a sample of 21 low-redshift (z<0.3) ULIRGs, examining both the Lyα emission line and O VI $\lambda\lambda$1032, 1038 and N V $\lambda\lambda$1238, 1243 absorption features. For the Lyα analysis, the results of the starburst-dominated ULIRGs from Martin et al. [2015] (M15) are combined with ours, when possible. For the analysis of the O VI and N V absorption features, the results of the quasar sample from Veilleux et al. [2022] (Paper I) are also combined with ours, when appropriate. The main conclusions of our analyses can be summarized as follows:

- Lyα line emission is detected in 15 out of the 19 objects where Lyα lies within the wavelength range of the observations. Blueshifted line centroids and/or wings of Lyα emission are often seen in our sample, where 12 out of the 14 objects with robustly measured Lyα profiles show 80-percentile velocities $v_{80} \lesssim 0$. See Fig. 2.2, Table 2.3, and Section 2.3.1.

- The equivalent widths of Lyα increase with increasing AGN fractions and AGN luminosities. The strength of the Lyα emission is therefore correlated with that of the AGN. See Fig. 2.7, Fig. 2.9, and Section 2.4.1.

- The blueshifted line centroids and/or wings of the Lyα emission correlate with those of the non-resonant optical emission lines. The 80-percentile velocities v_{80} of Lyα are positively correlated with those of [O III] λ5007 (or Hα), with the highest statistical significance among all kinematic properties measured from the data. This suggests that the blueshifted wings of Lyα emission are physically linked to the ionized outflowing gas. There is also a possible connection between the blueshifted Lyα emission lines and the blueshifted Na I D $\lambda\lambda$5890, 5896 absorption lines tracing the cool neutral-atomic gas outflows, although the sample size (3) in this case is very limited. See Fig. 2.10, Fig. 2.12, and Section 2.4.2.

- For 6 of the 14 objects with clear Lyα detections, the Lyα escape fractions, calculated as the observed Lyα flux divided by the intrinsic Lyα flux expected from the extinction-corrected Hα flux, are higher than the values expected under Case B recombination adopting Cardelli et al. [1989a] reddening law. Weak, positive correlations exist between the Lyα escape fractions and the AGN strength (e.g. L_{AGN}, f_{AGN}) or outflow velocities (e.g. $-v_{80,[O\ III]}$). See Fig. 2.9, Fig. 2.11, Section 2.4.1, and Section 2.4.2.

- Among the 12 objects with good continuum S/N, at least 6 objects show clear O VI and/or N V absorbers. The velocity centroids of these absorbers are all blueshifted and show large ranges of depth-weighted velocities (from ~ -12690 to -170 km s^{-1}) and depth-weighted velocity dispersions (from $\sim$100 to 4600 km s^{-1}). They are likely tracing quasar-driven outflows based on their broad and smooth profiles, as well as the evidence for partial covering in several objects. The implied incidence rate of highly ionized gas outflows in our ULIRG sample ($\sim$50%) is similar to that of the QUEST quasars in Paper I ($\sim$60%). See Table 2.5, Table 2.8, Section 2.3.3, and Section 2.5.1.

- The locations of these O VI and N V outflows are not well constrained, although they are probably located outside of the broad emission line regions since the absorption features are deeper than the underlying continuum level in at least two (and perhaps all six) ULIRGs. The lower limits on the power and momenta of these outflows, based on conservative values of the metal abundances, ionization corrections, and radial distances of the outflowing material, are generally modest compared with the radiative luminosities and momenta of the central energy source (AGN+starburst). See Table 4.4 and Section 2.5.2.

- When combining the results on the ULIRGs presented in this paper with those on the QUEST quasar sample from Paper I, we find that the incidence rates of O VI and/or N V absorption features are higher in the X-ray weak sources with smaller X-ray-to-UV indices, $\alpha_{UV,X}$. Specifically, the incidence rate of either O VI or N V or both absorption features is 88% (1-σ range: 76%–92%) in objects with $\alpha_{UV,X} < -1.3$, and 45% (1-σ range: 35%–56%) in objects with $\alpha_{UV,X} \geq -1.3$. Similarly, the equivalent widths, weighted outflow velocities, and weighted velocity dispersions of these features are higher in the X-ray weak sources. These results reinforce the main conclusions of Paper I and favor radiative acceleration as the dominant driving mechanism. See Fig. 2.15, Table 2.8, Table 2.9, and Section 2.6.2.

- As found in Paper I, the incidence rate of O VI or N V or both absorption features for sources with X-ray absorbing column densities N_H(X-ray) $> 10^{22}$ cm^{-2} is larger (76%; 1-σ range: 65%–83%) than the rate among those with lower N_H(X-ray) (25%; 1-σ range: 17%–41%). The equivalent widths of the O VI and N V absorption features may also be higher in sources with larger X-ray absorbing column densities. See Fig. 2.16, Table 2.8, Table 2.9, and Section 2.6.2.

- Apart from the aforementioned correlations with the X-ray properties of the sources, the properties of the outflows do not correlate with those of the AGN/host galaxies along the late-stage merger sequence (i.e. from AGN-dominated ULIRGs to quasars). Since the incidence rate of outflows found in our AGN-dominated ULIRGs is also virtually the same as that in the quasars, these results suggest that the launching of these quasar-driven outflows is stochastic throughout the late merger stages. A rigorous exploration of the outflow properties along the merger sequence would require a larger ($\gtrsim$50-100) sample that covers equally well the pre-merger and late-merger stages of ULIRGs. See Section 2.6.4.

Chapter 3: Elliptical Galaxy in the Making: The Dual Active Galactic Nuclei and Metal-enriched Halo of Mrk 273

3.1 Introduction

Major mergers of gas-rich galaxies may lead to the formation of elliptical galaxies and the growth of supermassive black holes. (Ultra)luminous infrared galaxies [(U)LIRGs, log(L_{IR}) $\geq$ (12)11 L$\odot$, e.g. Sanders and Mirabel, 1996] are generally considered good examples of such merging process [e.g. Sanders et al., 1988, Veilleux et al., 2002, Hopkins et al., 2009]. Powerful outflows, driven by the central quasar and/or cicumnuclear starburst, have been invoked to quench or regulate star formation in the merger remnants, creating a population of "red and dead" ellipticals and setting up the observed tight black hole - galaxy relations [e.g. Veilleux et al., 2005b, Fabian, 2012, Kormendy and Ho, 2013a]. There is growing observational support for these influential outflows, at both local and high-redshift universe [e.g. Cicone et al., 2015, Zakamska et al., 2016a, Harrison, 2017, Rupke et al., 2017, Veilleux et al., 2017, and references therein].

Recent deep *Chandra* observations have revealed giant ($\simeq$ 50 kpc), X-ray-emitting gaseous halos in two of the nearest (U)LIRGs: NGC 6240 [113 Mpc; 150 ksec; Nardini et al., 2013] and Mrk 231 [200 Mpc; 500 ksec; Veilleux et al., 2014]. In both sources, super-solar α/Fe abundance ratios are measured throughout the halo. In order to produce the amount of α elements detected in these halos, star formation activity over an extended period of time ($\lesssim$0.1 Gyr) is required if a star formation rate (SFR) at the current level is assumed. Repeated outflow events, like the ones currently seen in both objects, have been suggested as one plausible mechanism to help carry the α elements produced in the circumnuclear region all the way to the halo, on scales of several tens of kpc [e.g. Nardini et al., 2013, Veilleux et al., 2014]. Such outflow-driven metal transport is directly seen in the nearby starburst M82, though on a significantly smaller spatial scale [on the order of $\sim$ 10 kpc, e.g. Konami et al., 2011].

Another contentious issue in these galaxy mergers is the duty cycle of black-hole accretion activity. The inward-flowing gas induced by the merging activity has long be thought as one important fueling mechanism for Active Galactic Nucleus (AGN) [e.g. Di Matteo et al., 2005], although the observational evidence in support of this scenario is still incomplete. Hard X-ray observations can penetrate the high column densities usually found in the central regions of those galaxies, and thus serve as a good probe for the AGN activity that might be otherwise hidden by dense clouds. Over the last decade, dozens of nearby kpc-scale dual AGN have been found serendipitously in interacting galaxies through X-ray observations [e.g. Komossa et al., 2003, Koss et al., 2011, De Rosa et al., 2018]

Being the second nearest ULIRG (176 Mpc[1]; $\sim$0.74 kpc arcsec^{-1}), Mrk 273 is an excellent laboratory to explore the effect of feedback and dual AGN activity. Mrk 273 is brighter in the X-ray (2-10 keV) than Arp 220, the nearest ULIRG, and is well known to harbor a large X-ray halo, based on an old 44-ksec *Chandra* exposure analyzed in Xia et al. [2002] and reanalyzed in a series of papers [Ptak et al., 2003, Grimes et al., 2005, Teng and Veilleux, 2010, Iwasawa

[1] Based on a redshift z = 0.0377 and a cosmology with H_0 = 69.6 km s^{-1} Mpc^{-1}, Ω_{matter} = 0.286, and Ω_{vacuum} = 0.714. [Bennett et al., 2014]

et al., 2011b,a]. The halo of Mrk 273 appears to be unrelated to the brightest tidal features, as the southern tidal tail casts a shadow on the nebula emission; Super-solar α element abundance has been tentatively reported in this halo, but this is based on a spectrum with only 300 counts [Iwasawa et al., 2011a]. More recently, a remarkable AGN-driven, bipolar ionized outflow has been detected in this object, on a scale of $\sim$ 4 kpc [Rupke and Veilleux, 2013b], accompanied by warm and cold molecular outflows [U et al., 2013, Veilleux et al., 2013b, Cicone et al., 2014]. Outflowing ionized gas has also been detected on a larger scale of $\sim$ 10 kpc [Rodríguez Zaurín et al., 2014].

Mrk 273 is a late merger with dual nuclei in the mid-infrared[2], located 0.75 kpc apart in projection, similar to that of NGC 6240 ($\sim$ 0.74 kpc), but larger than that in Arp 220 (0.33 kpc) and Mrk 231 [coalesced into a single nucleus; Surace et al., 1998, Veilleux et al., 2002]. While the existence of an AGN in the southwest nucleus (hereafter SW nucleus) has been demonstrated at multiple wavelengths [e.g. Sanders et al., 1988, Veilleux et al., 1999, 2009b, Teng et al., 2009, Iwasawa et al., 2011a], the nature of the northeast nucleus (hereafter NE nucleus) is still controversial. The NE nucleus is seen in the near-infrared [Armus et al., 1990, Surace et al., 2000, Scoville et al., 2000]. Downes and Solomon [1998] suggests that the NE nucleus is an extreme compact starburst with a high luminosity density, similar to the western nucleus of Arp 220. High-resolution radio continuum imaging supports this hypothesis [Carilli and Taylor, 2000, Bondi et al., 2005]. Meanwhile, integral field spectroscopy of the nuclear region by Colina et al. [1999] shows characteristic of LINER for the NE nucleus. A point-like hard X-ray source has

[2]High-resolution radio observations have revealed a third component in the southeast of the central region of Mrk 273 [Condon et al., 1991, Smith et al., 1998], which is only weakly detected in the near-infrared [Scoville et al., 2000]. The steep radio spectrum of this component perhaps points to a starburst origin [Bondi et al., 2005]. Also, it is not detected in the X-ray (>2 keV) based on the *Chandra* data, and is thought to be a candidate star cluster [Iwasawa et al., 2011a].

been identified with the NE nucleus [Xia et al., 2002, González-Martín et al., 2006], suggesting the existence of a heavily absorbed AGN. In Iwasawa et al. [2011a], the tentative detection of Fe Kα line emission associated with the NE nucleus supports this scenario. Nevertheless, the S/N of the data is insufficient to determine whether the Fe Kα emission originates only from the NE nucleus or there is contamination from the SW nucleus. A fast-rotating molecular gas disk and coronal line [Si VI] 1.964μm emission flowing from the NE nucleus is revealed in U et al. [2013], which also favors the existence of a heavily absorbed AGN, although it is not a unique interpretation. Additionally, Mrk 273 was also detected, though the nuclei were unresolved, above 10 keV in the X-ray by *Suzaku* [Teng et al., 2009] and *NuSTAR* [Teng et al., 2015]. Spectral fitting and variability analysis of these data suggest the presence of a single, partially covered, and heavily obscured AGN. A recent re-analysis of the *NuSTAR* data by Iwasawa et al. [2018] assumed a double nucleus model, suggesting that the spectrum above 10 keV can be modeled by two heavily absorbed AGN. They also discussed the X-ray variability of Mrk 273 over more than a decade. The uncorrelated variability above and below 10 keV may suggest that two distinct sources are present in the respective bands.

In this paper, we analyze newly obtained 200 ksec *Chandra* data of Mrk 273, in combination with the old 44 ksec data, to explore the dual AGN activity, the outflow, and the extended X-ray halo. The paper is organized as follows. In Section 3.2, the datasets and reduction procedures are described. In Section 3.3, the main results are presented. A discussion of the implications is presented in Section 3.4, and the conclusions are summarized in Section 3.5.

3.2 Observation and Data Reduction

3.2.1 Chandra Observations

Mrk 273 was aimed at the back-illuminated S3 detector of ACIS. The rationale behind the setup used for the new 200-ksec observation (PID 17700440; PI Veilleux) was to match the observational parameters of the ~ 44 ksec exposures obtained in 2000 and analyzed in Xia et al. [2002], and thus to facilitate the task of combining both data sets into a single ~ 244 ks exposure when appropriate.

Due to scheduling constraints, the planned 200-ksec observation was divided into five segments of 61, 32, 35, 34 and 38 ksec, with the first one taken on 2016 Sep. 6, and the other four obtained on 2017 Feb. 14, 16, 18, and 26, respectively. All the observations were performed in 1/2 subarray mode in order to avoid pileup and take advantage of *Chandra*'s excellent angular resolution ($\sim 0\farcs5$).

In this paper, effort has been taken to combine both the old ~ 44 ks observation and new 200 ks observations together when appropriate. For convenience, the archival data analyzed by Xia et al. [2002] are denoted as the 2000 data, and all other data observed recently in year 2016-2017 are denoted as the 2016 data.

Data reduction was carried out through standard *Chandra* data analysis package CIAO 4.8 and CALDB 4.7. All the data were reprocessed using the CIAO script *chandra_repro*. The *deflare* routine was used to detect and discard any possible flare in the data, where data with background count rate exceeds 3 standard deviations from the mean of the distribution are removed. No attempt was taken to deconvolve the data using, e.g., Lucy or EMC2 algorithms [Lucy, 1974, Esch et al., 2004, Karovska et al., 2005]. This strategy better preserves diffuse features and possible slight asymmetries in the point-spread function (PSF).

The images were merged for analysis using the CIAO script *merge_obs*. In the hard X-ray band (2-8 keV), the response of ACIS-S has not changed to a noticeable extent, so a direct stack of the hard X-ray images in counts of all data was adopted to generate the images. In the soft X-ray band (0.4-2 keV), however, the response of ACIS-S has dropped significantly (factor of $\sim$ 2). Therefore, images of both datasets in flux units were produced after accounting for the energy dependence of the exposure maps at different epochs.

All the spectral extractions were done by the CIAO script *specextract*, and the combined spectrum was generated by the script *combine_spectrum*. The spectra were binned to 15 counts bin^{-1} when the total number of counts was high enough, while the rest of them were binned mildly to 1 counts bin^{-1} in order to conserve a good energy resolution. The spectral fittings were done by XSPEC version 12.9.0 [Arnaud, 1996]. The χ^2 statistic was used by default when the spectra were binned to 15 counts bin^{-1}. The CSTAT statistic [Cash, 1979] was used when the spectra were binned to 1 counts bin^{-1}, and the default MCMC method in XSPEC was used to calculate the errors of the measurements.[3]

3.2.2 Ancillary Datasets

In order to better understand the *Chandra* observation, multi-wavelength ancillary data were gathered from the literature and archives.

[3]When applying CSTAT statistic, unbinned spectra with bins of zero counts will bias the results of the fit. The spectra are thus mildly binned to 1 counts bin^{-1} to avoid this problem. See section *cstat* on "http://cxc.harvard.edu/sherpa4.4/statistics/index.html", as well as sections *Poisson data (cstat)* and *Poisson data with Poisson background (cstat)* in "https://heasarc.gsfc.nasa.gov/xanadu/xsp ec/manual/XSappendixStatistics.html" for more information.

The reduced Hubble Space Telescope (HST) I-band image taken with the F814W filter of ACS [Armus et al., 2009, Kim et al., 2013] and H-band image taken with the NIC2 F160W filter of NICMOS [Scoville et al., 2000, Cresci et al., 2007] were downloaded from the Hubble Legacy Archive. The I-band image was used to trace the stellar component of the galaxy, and the H-band image was used to locate the two nuclei within Mrk 273. The continuum-subtracted, narrow-band [O III] λ5007 image from Rodríguez Zaurín et al. [2014] was used to trace the spatial distribution of the ionization cones and outflowing gas. The continuum-subtracted, narrow-band Hαimage from Spence et al. [2016] was used to trace the large-scale Hα emission.

3.3 Results

3.3.1 Overview of the Chandra Data

The stacked images of the 2000+2016 data are shown in Figure 3.1. In general, the hard X-ray emission (2-7 keV) is confined to the nuclear region. Similarities between the soft X-ray emission (0.4-2 keV) and the HST I-band image are present for the brighter regions, but much less so for the fainter X-ray emission.

Firstly, there is significant extended X-ray emission south of the galaxy, tracing the hot halo gas on a scale of $\sim$ 40 kpc $\times$ 40 kpc. Apparently the gas is not associated with the tidal tail, since it is much more extended than the tidal tail in the east-west direction. This nebula (hereafter called the Southern Nebula) has been reported in previous studies [e.g. Iwasawa et al., 2011a], but the structure of the nebula in these older data is not as clear due to fewer counts. In addition, northeast of the galaxy main body (i.e. the stellar component as seen in HST I-band, excluding the tidal tail in the south), there is also faint, extended X-ray emission (hereafter called

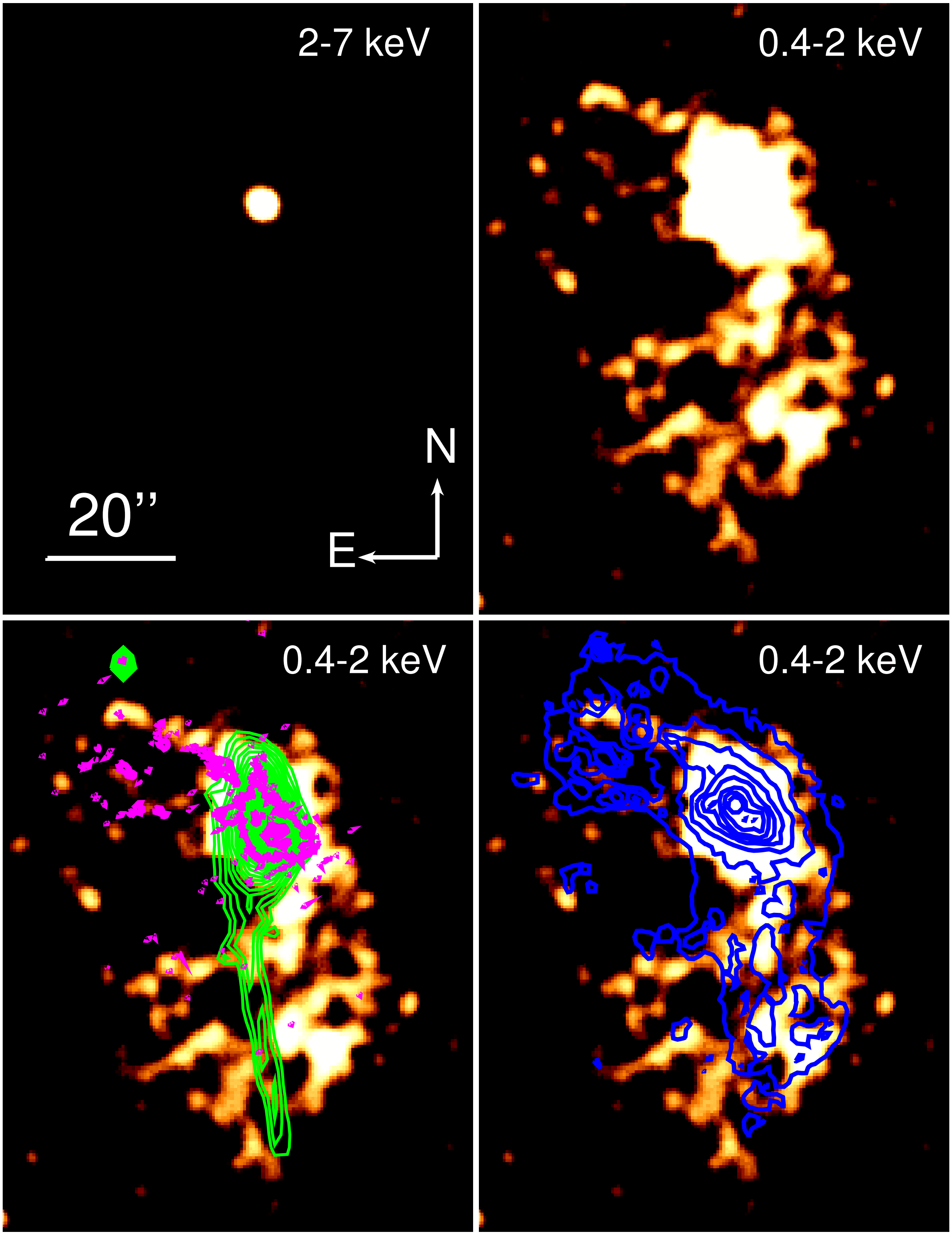

Figure 3.1: Merged and smoothed X-ray images from all observations (244 ksec in total) in energy bands 2.0-7.0 keV (*Top Left*) and 0.4-2.0 keV (*Top Right & Bottom*). In the bottom left panel, the HST I-band image is over-plotted in magenta contours and the continuum-subtracted [O III] λ5007 image from Rodríguez Zaurín et al. [2014] is over-plotted in green contours. In the bottom right panel, the continuum-subtracted Hα image from Spence et al. [2016] is over-plotted in blue contours. The images are on different logarithmic scales. North is up and East is to the left. The linear spatial scale is 0.74 kpc arcsec^{-1}.

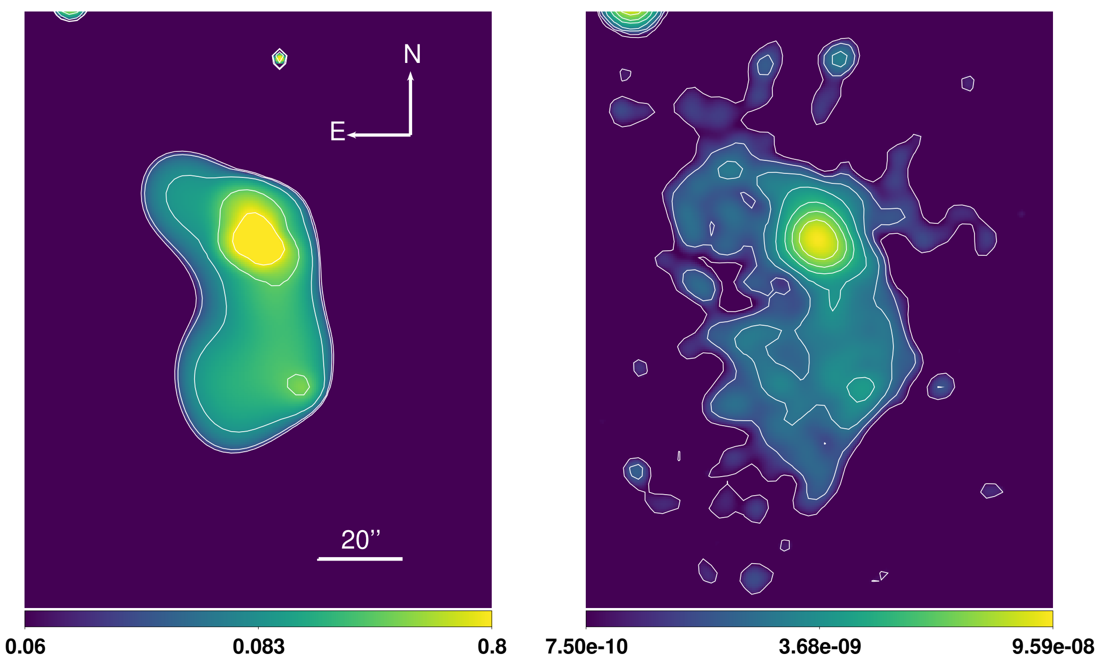

Figure 3.2: Adaptively smoothed images from all combined observations (244 ksec in total), on logarithmic scales. North is up and East is to the left. *Left:* Image in the 0.4-7.0 keV band in counts. The CIAO script *csmooth* was used for the smoothing, in order to emphasize the faint, extended emission in the image. The contours are at 2, 3, 5, 10 and 25σ. *Right:* Image in the 0.4-1.0 keV band, in units of photons cm^{-2} s^{-1} . The CIAO script *dmimgadapt* was used for the smoothing. It provided a superior resolution of the bright small-scale structures when compared to the script *csmooth*, while keeping the extended structures. The contours are at 2, 3, 5, 10, 25, 50, 100σ.

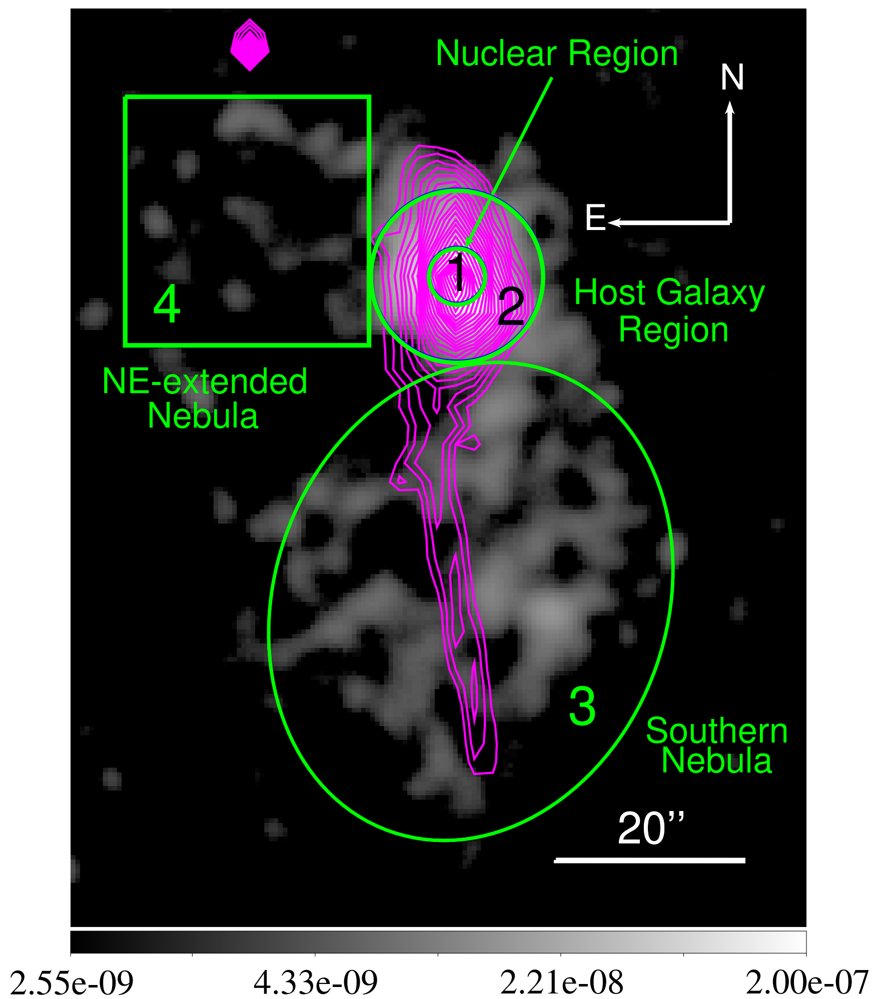

Figure 3.3: The different spatial regions used for the analyses presented in Section 3.3. Region 1: Nuclear Region, denoted by the green aperture with $3''$ in radius. Region 2: Host Galaxy Region, denoted by the green circular annulus with an inner radius of $3''$ and an outer radius of $9''$. Region 3: Southern Nebula region, denoted by the green ellipse in the south. Region 4: Extended emission in the northeast (i.e. NE-extended Nebula), denoted by the green box to the northeast. The grayscale image is in the 0.4-2.0 keV band, in units of photons cm^{-2} s^{-1} and on a logarithm scale. The overlaid magenta contours are generated from the HST I-band image.

NE-extended Nebula), which overlaps with the large-scale extended [O III] λ5007 emission seen in Rodríguez Zaurín et al. [2014].

The narrow-band Hα image presented in Spence et al. [2016] shows extended nebulae south and northeast of the galaxy main body, as shown in blue contours in the bottom right panel of Figure 3.1. These Hα nebulae resemble the Southern Nebula and the NE-extended Nebula in the X-ray, suggesting a possible connection between these nebulae.

Adaptively smoothed images are presented in Figure 3.2. In the left panel, the stacked 0.4-7 keV image from the combined 2000+2016 data was adaptively smoothed with CIAO script *csmooth*, which emphasized the faint extended structures in the image. In the right panel, the stacked, exposure-corrected 0.4-1.0 keV image from the same data was adaptively smoothed with another CIAO script *dmimgadapt*. It provided a superior resolution of the bright small-scale structures when compared to the script *csmooth*, while preserving the extended structures. The energy band of 0.4-1.0 keV was chosen for a best demonstration of the soft X-ray nebulae.

In order to further examine the X-ray emission in detail, the galaxy is divided into four different spatial regions for analysis, as shown and described in Figure 3.3. The observed counts of those regions are summarized in Table 3.1, respectively. The results of these analyses are discussed next.

3.3.2 Nuclear Region (Region 1)

3.3.2.1 Radial Profile of the Hard X-ray Emission

The 4-6 keV image and the corresponding radial profiles in the Nuclear Region are shown in Figure 3.4. The peak of the X-ray image overlaps with the SW nucleus seen in the HST

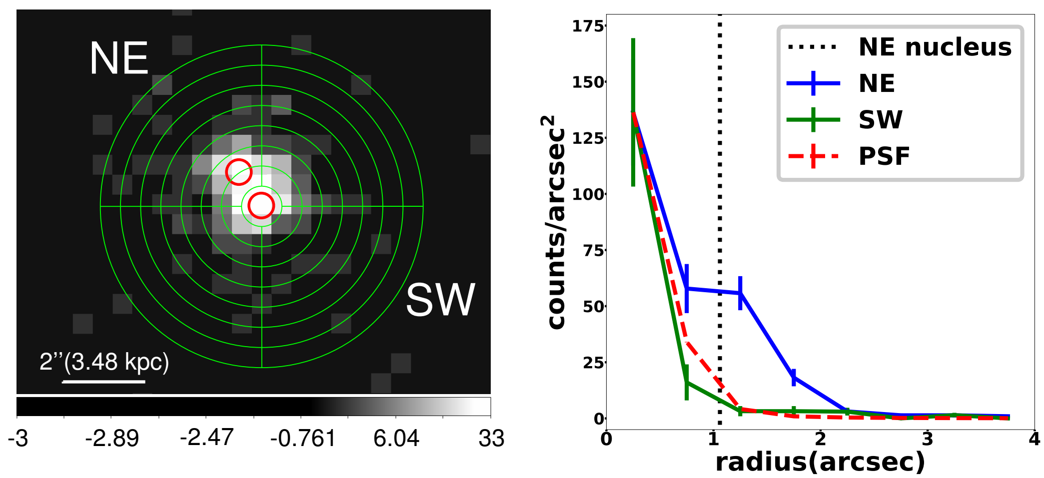

Figure 3.4: *Left*: Image of the Nuclear Region in the 4-6 keV band, with sector annuli used to extract the radial profiles from the image. The spatial scale of the image is larger than the size of the Nuclear Region defined in Figure 3.3 for better visualization. The annuli are centered on the peak of the emission (i.e. the SW nucleus) and are divided into four sectors with same area. The sectors in the northeast and southwest are denoted as NE and SW sectors separately. The image is shown in gray scale and in units of counts. It is scaled in logarithm and adjusted to show the full extent of the faint, hard X-ray emission. The two red circles denote the NE and SW nuclei seen in the HST H-band (F160W) image. The HST H-band (F160W) image and X-ray image are aligned following the same procedure described in Section 3.3.1 in Iwasawa et al. [2011a]. *Right*: radial profiles of different sector annuli shown in the left panel, as well as the one from the PSF. The x-axis is the median radius for each sector annulus. A secondary maximum is obvious in the radial profile of NE sector (Blue). As a comparison, neither the radial profile of the SW sector (green) nor that of the PSF (red-dashed) shows a secondary maximum. The PSF profile is simulated with the ray-tracing code ChaRT and MARX [Davis et al., 2012]. The black dotted line denotes the center of the NE nucleus. The pixel scale is $0\farcs49$ (0.38 kpc).

Table 3.1. Summary of Counts in the Data Sets

Region	Counts[a]	
	2000 data	2016 data
Nuclear Region (1)	1348	2681
SW nucleus	449	719
NE nucleus	204	647
Host Galaxy Region (2)	553	850
Southern Nebula (3)	376	680
NE-extended Nebula (4)	98	202

[a]For the Nuclear Region, SW nucleus and NE nucleus, the counts in 0.4-8 keV are shown; for the others, the counts in 0.4-2 keV are shown.

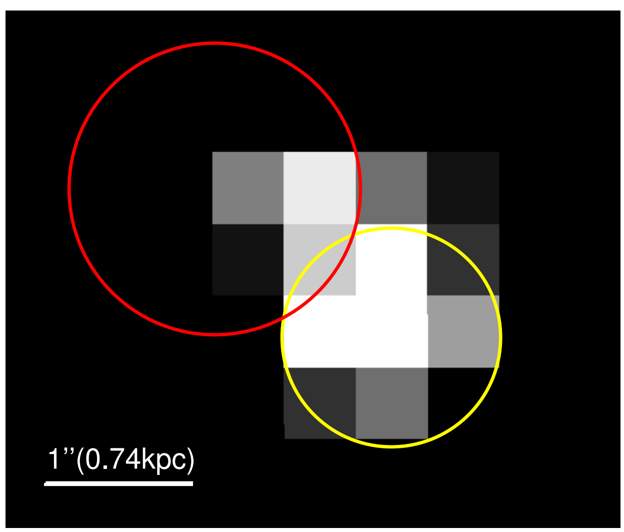

Figure 3.5: The spectral extraction regions for the SW and NE nuclei. The yellow aperture denotes the extraction region for the SW nucleus, which is $0\farcs75$ in radius. The red aperture denotes the extraction region for the NE nucleus, which is $1''$ in radius. The grayscale image is the stacked 4-6 keV image of the 2016 data. The pixel scale is $0\farcs49$ (0.38 kpc).

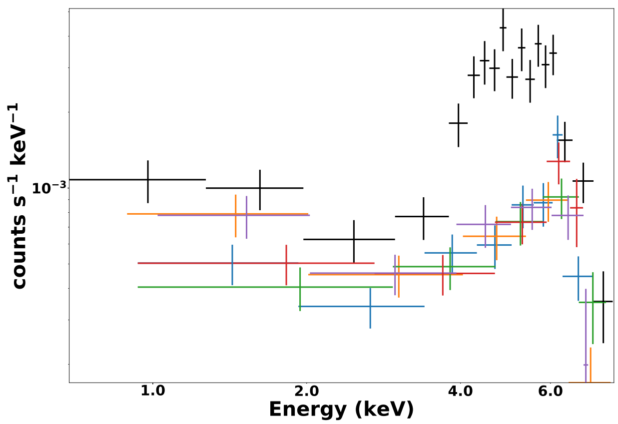

Figure 3.6: The original spectra of the SW nucleus, extracted from the yellow aperture defined in Figure 3.5. *Black spectrum*: the spectrum from the 2000 data. *Colored spectra*: spectra of individual observations from the 2016 data. All the spectra were binned to a minimum S/N of 3 bin^{-1}.

NICMOS H-band (F160W) image. A possible secondary peak can also be seen by eye in the X-ray image, which is associated with the NE nucleus seen in the H-band image. In addition, the radial profiles of the surface brightness along the northeast (NE) and southwest (SW) directions are compared. The profiles are centered on the peak of the X-ray image. The radial profile along the northeast direction confirms the secondary peak identified by eye.

3.3.2.2 SW Nucleus

Previous studies have revealed AGN activity in the central region of Mrk 273 [e.g. Colina et al., 1999, Scoville et al., 2000, Iwasawa et al., 2011a], and a possible dual AGN was suggested by Iwasawa et al. [2011a], U et al. [2013], and Iwasawa et al. [2018]. The analysis of hard X-ray image in Section 3.3.2.1 also suggests the possibility of dual AGN activity. In order to further explore the nature of the two nuclei, spectra of both SW nucleus and NE nucleus were extracted from apertures defined in Figure 3.5.

For the SW nucleus, the aperture was centered on the peak of the hard X-ray flux. It

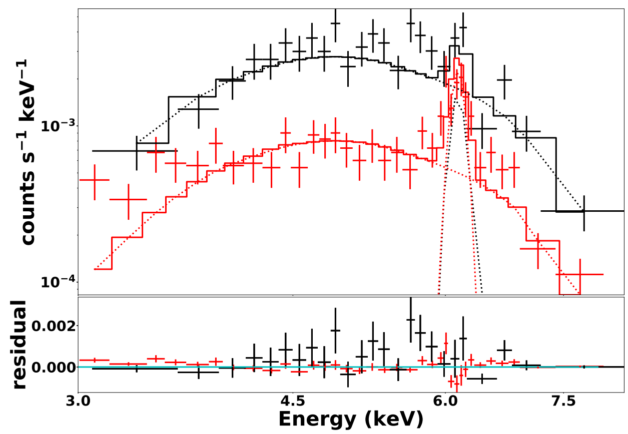

Figure 3.7: Top: simultaneous fitting to the spectra of the SW nucleus from the 2000 data (black) and the 2016 data (red). Only data in the energy range of 3-8 keV is considered. The model is made up of one absorbed power-law component and an Fe Kα line. All parameters for the two epochs are tied together except the normalizations for the power-law component and the Fe Kα line. The best-fit parameters are summarized in Table 3.2. The model is shown in solid lines and the components of it are shown in dotted lines. Bottom: residuals (data minus model).

was chosen to include the majority of the emission from the SW nucleus revealed by the NICMOS/NIC2 F160W image, and the radius of the aperture was $0\farcs75$. The original spectra of the SW nucleus extracted from the 2000 and 2016 data are shown in Figure 3.6. In general, the spectra from each individual observation of the 2016 data remains similar to each other. The spectrum from the 2000 data, however, shows clearly stronger emission in the hard X-ray band.

In order to improve the signal-to-noise ratio, all the spectra from the 2016 data were combined into one, while the spectrum from the 2000 data was left alone. A comparison of the two spectra in the energy range of 3-8 keV is shown in Figure 3.7. Again, it is clear that the hard X-ray emission has decreased significantly from the year 2000 to 2016-2017. By fitting the spectra in the 3-8 keV band from the 2000 and 2016 data separately, we find that both the absorption column density and the intrinsic luminosity of the AGN varies over the years (N$_H$ = $3.62^{+1.83}_{-0.72}$ $\times$ 10^{23} cm^{-2} and 4-8 keV flux = $9.98^{+2.73}_{-1.36}\times$ 10^{-13} erg s^{-1} cm^{-2} for the 2000 data, and N$_H$ = $1.22^{+0.43}_{-0.29}$ $\times$ 10^{23} cm^{-2} and 4-8 keV flux = $1.31^{+0.12}_{-0.10}$ $\times$ 10^{-13} erg s^{-1} cm^{-2} for the 2016 data, respectively[4]). In the following, we search for the origin of this drop of flux in the hard X-ray.

We first assume that only the intrinsic luminosity of the AGN has decreased over the years. Following this scenario, both spectra from the 2000 data and the 2016 data were fitted in 3-8 keV energy range simultaneously, with a model made up of one absorbed power-law component and an Fe Kα line. All parameters for the two epochs were tied together except the normalizations for the power-law component and the Fe Kα line. As a first trial, the photon index of the power-law component was set as a free parameter. The fit is acceptable (reduced χ^2 = 1.50), except that it gives a power-law photon index of ~ 0.6, which is unreasonably small for an AGN. For example, this value is well below the measured lower limit [Γ=1.4, see Figure 8 in Ueda et al., 2014] for the *Swift/BAT* hard X-ray selected AGN. The photon indices derived in the same paper are Γ=1.94 with a standard deviation of 0.09 for Type 1 AGN and Γ=1.84 with a standard deviation of 0.15 for Type 2 AGN. Therefore, we fixed the power-law index to the standard value of Γ=1.9 [e.g. see Piconcelli et al., 2005, Ishibashi and Courvoisier, 2010, Ueda et al., 2014, and references therein]. The best-fit model gave a reduced χ^2 of 1.51 (i.e. it is virtually the same as when Γ was left as a free parameter). The results are shown in Figure 3.7 and the best-fit parameters are summarized in Table 3.2. Although not statistically significant, there are possible residuals corresponding to other iron lines with energy higher than 6.4 keV in the rest frame. From year 2000 to year 2016-2017, the total flux in 3-8 keV without absorption correction has decreased from 3.10×10^{-13} erg s^{-1} cm^{-2} to 1.21×10^{-13} erg s^{-1} cm^{-2}. This is consistent with the variability on a scale of several years seen from observations at different epochs as discussed in Xia et al. [2002], Teng et al. [2009, 2015] and Iwasawa et al. [2018].

[4]In this statement and those below, the errors from the spectral fits correspond to a confidence range of 90%, or $\sim\pm1.6\sigma$

Alternatively, an increase in the column density of the absorbing material in front of the central engine alone can also lead to the observed decrease of the hard X-ray flux. A model with tied power-law photon indices and normalizations but independent absorption column densities was fitted to the data. However, the reduced χ^2 (2.7) from this fit is poor. Therefore, these results seem to favor the first scenario where the decrease of the hard X-ray luminosity is caused by the fading of the central engine. However, we cannot formally rule out the possibility that both scenarios could be at work simultaneously, since we have to fix the photon indices of the power-laws in our fits due to the degeneracies among the parameters, which might bias our results.

The measured hard X-ray (4-8 keV) continuum fluxes from the SW nucleus are $\sim 3.2\times10^{-13}$ erg s^{-1} cm^{-2} in the 2013 *XMM-Newton* data [with the contribution of the NE nucleus subtracted; Iwasawa et al., 2018] and $\sim 7.2\times10^{-14}$ erg s^{-1} cm^{-2} measured in the 2016 *Chandra* data, respectively (here we assumed that the continuum flux of the NE nucleus in the 2013 *XMM-Newton* data was the same as that measured in the 2016 *Chandra* data, given that the flux of the NE nucleus remained the same in 2000 and 2016-2017). The corresponding Fe Kα line fluxes of the SW nucleus are $\sim 3.6\times10^{-6}$ photons cm^{-2} s^{-1} for the 2013 *XMM-Newton* data [Iwasawa et al., 2018] and $\sim 5.2\times10^{-6}$ photons cm^{-2} s^{-1} for the 2016 *Chandra* data, respectively. Over these $\sim$ 3 years, the continuum flux has therefore dropped by a factor of ~ 4.4, while the Fe Kα line flux has increased by a factor of ~ 1.4. Therefore the line emission has not followed the continuum precisely. This sets a lower limit on the physical scale of the inner edge of the torus ($\sim$ 1 pc) if the Fe Kα line arises from that region. Note that this argument only relies on the fact that the fluxes of the Fe line and the continuum have changed differently over the years; the exact change in flux does not matter here.

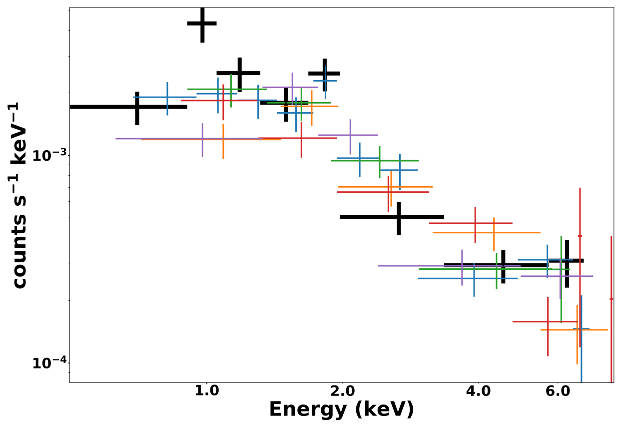

Figure 3.8: The original spectra of the NE nucleus, extracted from the red aperture defined in Figure 3.5. *Black spectrum*: the spectrum from the 2000 data. *Colored spectra*: spectra of each individual observation from the 2016 data. All the spectra were binned to a minimum S/N of 3 bin^{-1}.

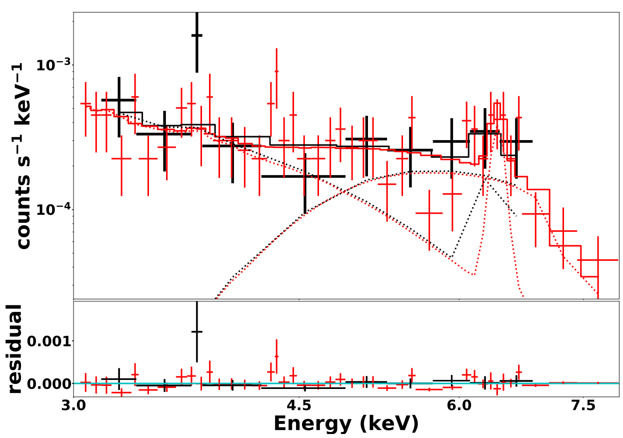

Figure 3.9: Top: simultaneous fitting to the spectra of the NE nucleus from the 2000 data (black) and the 2016 data (red) in the 3-8 keV range. The model consists of a thermal gas component (MEKAL) with variable Fe abundance, and a power-law component with absorption. The best-fit parameters are summarized in Table 3.2. The spectra shown in this figure are binned to 5 counts bin^{-1} only for the purpose of better visualization, while the spectra were binned to 1 counts bin^{-1} in the fit. The model is shown in solid lines and the components of it are shown in dotted lines. Bottom: residuals (data minus model).

3.3.2.3 NE Nucleus

For the NE nucleus, the aperture was chosen to include all the hard X-ray emission in the vicinity of the secondary peak seen in the 4-6 keV image. The radius of the aperture was chosen to be $1''$, in order to contain as much hard X-ray emission associated with the NE nucleus as possible, but minimize the overlap with the aperture used for the SW nucleus.

As shown in Figure 3.6, the hard X-ray flux of the SW nucleus has dropped by $\sim 60\%$ from 2000 to 2016, making the hard X-ray emission from the NE nucleus less contaminated by emission from the SW nucleus. As a result, the spectra of the NE nucleus from the 2016 data are less affected by the hard X-ray emission from the SW nucleus. All the spectra of the NE nucleus from the 2016 data were combined for this analysis.

The raw spectra are shown in Figure 3.8, and the combined spectrum from the 2016 data is shown in Figure 3.9. Due to the limited counts obtained, the spectral features critical for the spectral fitting are washed out if the spectra are binned to 15 counts bin^{-1}. Unbinned spectra, in this case, have bins with zero counts and will therefore bias the results (see footnote 3 on page 3). Therefore, the spectra were binned mildly to 1 counts bin^{-1}, and the CSTAT statistic was used for the fits. The spectra were fitted in the energy range of 3-8 keV, with a model consisting of a thermal gas component with variable Fe abundance [Mewe-Kaastra-Liedahl or MEKAL, see Liedahl et al., 1995, and references therein] and Galactic absorption [with column density of 9×10^{19} cm^{-2}, see Kalberla et al., 2005], as well as a power-law component with absorption. The photon index of the power-law component was fixed at 1.9, as adopted for the SW nucleus. The best-fit models are shown in Figure 3.9. The best-fit results are listed in Table 3.2.

We have also fitted the spectra of the NE nucleus in the full energy range (0.4-8 keV) with the same model, and the results of the best fit are consistent with those obtained from the fit in the energy range of 3-8 keV. Specifically, a temperature of kT=$6.24^{+3.86}_{-2.37}$ keV for the thermal component and an absorption column density of N_H=$9.00^{+4.98}_{-3.22}\times10^{23}$ cm^{-2} for the power-law component were obtained. They are omitted in Table 3.2 to avoid redundancy. These results suggest the co-existence of a very hot, Fe XXV-line-emitting gas and a heavily absorbed AGN.

In order to gain a better knowledge of the Fe emission line from the NE nucleus, we also fitted the spectra with a model consisting of an absorbed power-law, a zero-metallicity thermal gas component, and an Fe line with Gaussian profile. The fit failed to converge when the absorption column density for the power-law and the temperature of the thermal gas component were set as free parameters. We have thus fixed those parameters to their best-fit values obtained from the fits with the power-law plus MEKAL model described in the last paragraph. The results of the new fit are summarized in Table 3.2. While the Fe line seen in the SW nucleus is Fe Kα with a rest frame energy of 6.4 keV, the dominant Fe line seen in the NE nucleus is instead Fe XXV with a rest-frame energy of $\sim$6.7 keV. The broad width of the Fe XXV line suggests that the line is blended with other highly-ionized Fe lines.

Another evidence of AGN activity in the NE nucleus comes from the shape of the hard X-ray continuum. As shown in Figure 3.10, 8 parallel pseudo slits were used to extract spectra across the Nuclear Region. All the slits are perpendicular to the vector connecting the SW and NE nucleus. The spectra are shown in Figure 3.11.

The flux (in units of counts s^{-1} keV^{-1}) in the two energy bins, 4-5 keV and 6.5-8 keV in the observer's frame, were used to monitor the variation of the continuum across the pseudo slits. The Fe Kα 6.4 keV line and highly ionized Fe XXV 6.7 keV line (possibly blended with other highly ionized Fe lines) are located in 6-6.3 keV and 6.3-6.5 keV energy bins in the observer's

Table 3.2. Results from Fits of the Individual SW and NE Nuclei

Model Component[a]	Parameters	SW nucleus 2000 data[b]	SW nucleus 2016 data[b]	NE nucleus 2000+2016 data[c]	
PL	N_H[d]	$2.79^{+0.30}_{-0.22}$ (t)	$2.79^{+0.30}_{-0.22}$ (t)	$6.78^{+4.99}_{-3.31}$	6.78(fixed)
	Γ	1.9(fixed)	1.9(fixed)	1.9(fixed)	1.9(fixed)
Fe Line	E_{line}[e]	$6.36^{+0.04}_{-0.04}$ (t)	$6.36^{+0.04}_{-0.04}$ (t)	N/A	$6.64^{+0.11}_{-0.11}$
	width[e]	$0.11^{+0.02}_{-0.02}$ (t)	$0.11^{+0.02}_{-0.02}$ (t)	N/A	$0.20^{+0.07}_{-0.07}$
	EW[e]	$0.23^{+0.06}_{-0.05}$	$0.95^{+0.05}_{-0.12}$	N/A	$0.70^{+0.99}_{-0.29}$
	flux[f]	$3.67^{+2.35}_{-2.35}$	$5.18^{+0.07}_{-0.07}$	N/A	$0.98^{+0.62}_{-0.58}$
MEKAL	N_H[d]	N/A	N/A	0.0009(fixed)	0.0009(fixed)
	kT[g]	N/A	N/A	$7.21^{+4.47}_{-2.29}$	7.21(fixed)
	$Z/Z_\odot$	N/A	N/A	$2.31^{+1.16}_{-1.46}$[h]	0(fixed)
Flux (4-8 keV)[i]		$2.94^{+0.50}_{-0.50}$	$1.16^{+0.24}_{-0.24}$	$0.39^{+0.01}_{-0.22}$[k]	
Flux (4-8 keV, absorption corrected)[i]		$5.74^{+0.95}_{-0.95}$	$2.29^{+0.51}_{-0.51}$	$1.60^{+0.04}_{-0.85}$[k]	
Luminosity (4-8 keV, absorption corrected)[j]		$1.22^{+0.20}_{-0.20}$	$0.49^{+0.11}_{-0.11}$	$0.35^{+0.01}_{-0.18}$[k]	
χ^2_ν (DOF)[l]		1.5(52)	1.5(52)	-	-
cstat(DOF)[m]		-	-	158.2(201)	156.7(201)

[a]Different model components used in the fitting. They are the absorbed power-law component (PL), the Fe line with Gaussian profile, as well as the thermal, hot diffuse gas component (MEKAL). "N/A" means that the component is not included in the corresponding model. All the errors listed correspond to a confidence range of 90%, or $\sim\pm1.6\sigma$. For the data fitted with the CSTAT statistic (i.e., the results of the NE nucleus), the errors are derived from the default MCMC method implemented in XSPEC.

[b]The results of the simultaneous fitting to the spectra of the SW nucleus from the 2000 data and 2016 data, assuming that the change of hard X-ray flux is caused by the intrinsic variability of the central engine. Label (t) means the corresponding parameters are tied together in the fitting.

[c]The spectra from the 2000 data and 2016 data are fitted simultaneously.

[d]Absorption column density. In units of 10^{23} cm^{-2}.

[e]In the rest frame and in units of keV.

[f]In units of 10^{-6} photons s^{-1} cm^{-2}.

[g]In units of keV.

[h]Abundance of Fe in units of solar abundance. All other elements are fixed at solar abundance.

[i]In units of 10^{-13} ergs cm^{-2} s^{-1}.

[j]In units of 10^{43} ergs s^{-1}.

[k]The results of the four fits are combined together for simplicity, where the errors represent the full range of the fluxes and luminosities obtained for the four fits.

[l]The reduced χ^2 (χ^2_ν) from the fits and the corresponding degrees of freedom (DOF).

[m]The CSTAT statistics from the fits and the corresponding degrees of freedom (DOF).

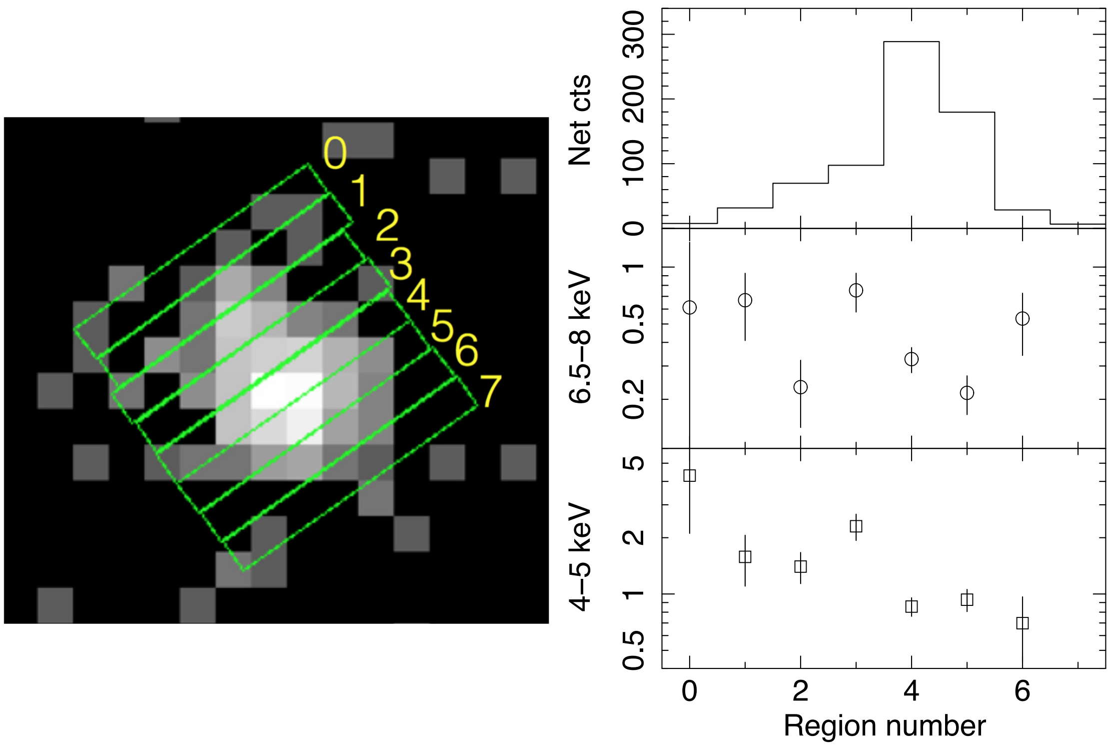

Figure 3.10: *Left:* 8 pseudo slits used to extract spectra across the Nuclear Region. The grayscale image is at 6.5-8 keV in the observer's frame. *Right:* the histogram showing the total counts of different slits in 4-8 keV band (top), as well as the relative flux in the 6.5-8 keV band (middle) and 4-5 keV band (bottom) normalized to the flux in the 5-6 keV band. For slit 7, the 5-6 keV flux is formally negative and the corresponding data points are thus not shown in the middle and bottom panels.

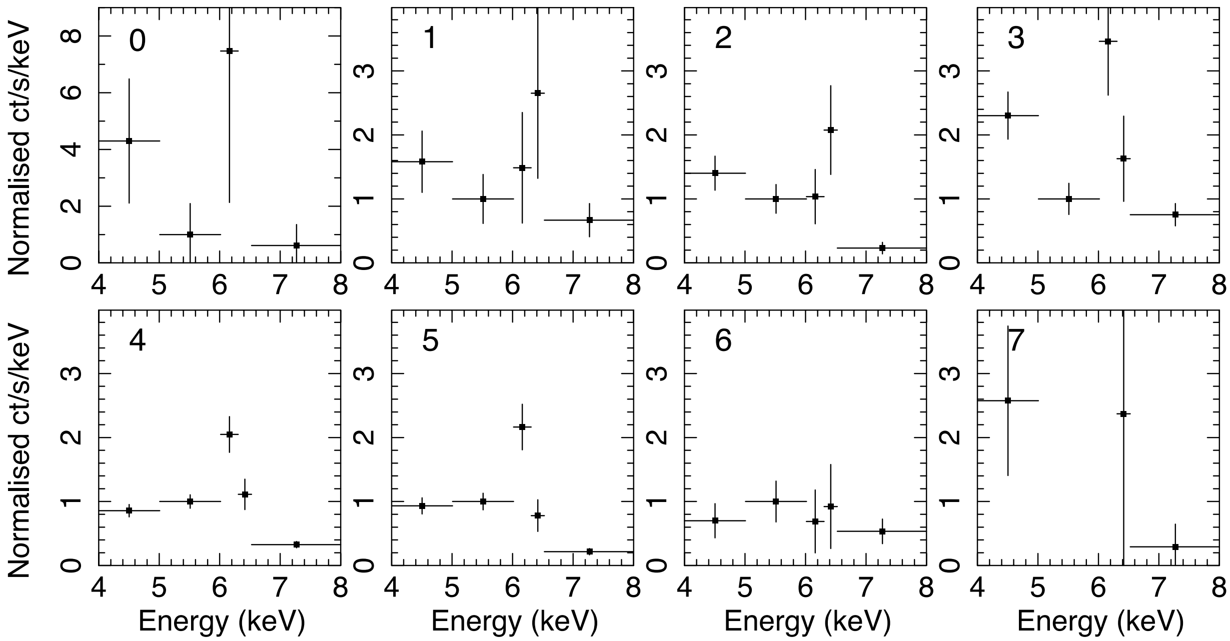

Figure 3.11: Spectra extracted from the 8 pseudo slits, which are normalized at the 5-6 keV bin. The only exception is slit 7 where the 5-6 keV data point is formally negative, and the normalization of the spectrum is thus chosen arbitrarily. The slit names are shown in the top left corner of each panel. The 4-5 keV and 6.5-8 keV bins in the observer's frame were used to monitor the variation of the continuum across the pseudo slits. The Fe Kα 6.4 keV line and highly ionized Fe XXV 6.7 keV line (possibly blended with other highly ionized Fe lines) are located in 6-6.3 keV and 6.3-6.5 keV energy bins in the observer's frame respectively.

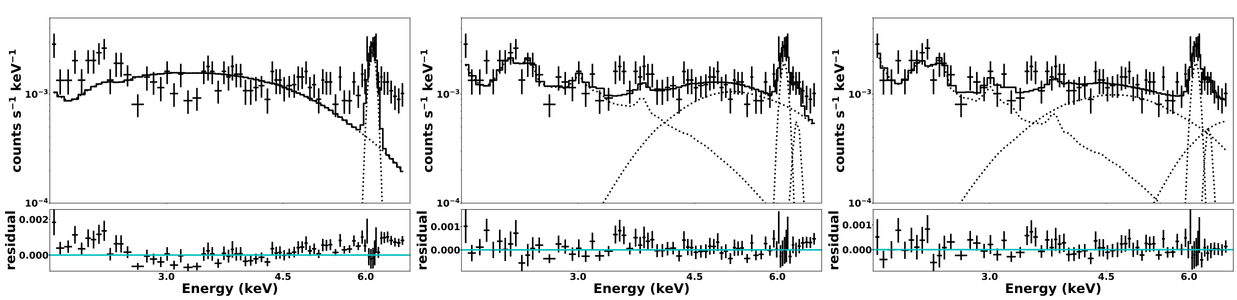

Figure 3.12: Top: the fits of the spectrum of the Nuclear Region from the 2016 data at 2-7 keV. The model is made up of: *Left:* one absorbed power-law component with photon index fixed at 1.9 and an Fe line. *Middle:* one absorbed power-law component with photon index fixed at 1.9, an absorbed thermal gas component (MEKAL) and an Fe line. *Right:* two absorbed power-law components with photon index fixed at 1.9, an absorbed thermal gas component (MEKAL) and an Fe line. It is clear that only one power-law component cannot explain the spectrum (left panel). The models are shown in solid lines and the components of them are shown in dotted lines. Bottom: residuals (data minus model).

frame separately. Therefore, the line emission do not contribute to the 4-5 keV and 6.5-8 keV bins.

At the position of the SW nucleus (slits 4 and 5), the 4-8 keV flux peaks, but the flux in both the 6.5-8 keV and 4-5 keV bins are relatively low. At the position of the NE nucleus (slits 1 and 2), the fluxes in both the 6.5-8 keV and 4-5 keV bins are larger than those in the SW nucleus. Firstly, the higher flux in the 6.5-8 keV bin of the NE nucleus suggests a harder continuum than that of the SW nucleus. This perhaps implies the existence of a more heavily-obscured AGN in the NE nucleus, compared to the one in the SW nucleus. Next, the higher flux in the 4-5 keV bin of the NE nucleus, together with the strong Fe XXV 6.7 keV line seen at the same location, suggests a significant contribution from a hot gas component.

The absorption-corrected flux of the NE nucleus in the 4-8 keV band is $\sim 1.6 \times 10^{-13}$ erg s^{-1} cm^{-2}, and it is lower than the 5.6×10^{-13} erg s^{-1} cm^{-2} estimated in Iwasawa et al. [2018]. This difference might be due partly by the fact that the former is calculated from an aperture of $1''$ in radius while the latter is estimated from the decomposition of the *NuSTAR* spectrum (extracted from an aperture with a radius of $0'.8$). The value estimated from the *NuSTAR* data thus sets an upper limit to the flux of the NE nucleus.

The heavily-absorbed nature of the AGN in the NE nucleus is also consistent with observations at other wavelengths. The high absorption column density is supported by the previous infrared and radio observations. The NE nucleus contains most of the molecular gas in the system within an extremely compact core [radius $\sim$ 120 pc, see Downes and Solomon, 1998], and the NE nucleus is the source of most of the mid-infrared luminosity [Soifer et al., 2000]. Near-infrared integral field spectroscopy of the inner kiloparsec of Mrk 273 associates high-ionization coronal line emission ([Si VI] 1.964 μm) with the SE radio source (radio component to the south of the NE nucleus, see footnote 2 on page 2 for more information), which is likely caused by photoionization from the AGN in the NE nucleus [U et al., 2013].

In addition, current radio data suggest that the radio emission of the NE nucleus arises primarily from multiple radio supernovae and/or supernovae remnants, and it is thus dominated by the starburst [e.g. Carilli and Taylor, 2000, Bondi et al., 2005]. The X-ray data agree with these radio observations that the starburst dominates here, as the X-ray emission in the soft band (< 2 keV) is consistent with emission from hot, diffuse gas most likely heated by the starburst activity. However, possible radio emission from an obscured nucleus (if present) cannot be ruled out. Indeed, there is also tentative evidence that one of the compact radio components associated with the NE nucleus may be the radio counterpart of an AGN [Bondi et al., 2005]. This is consistent with our result that a heavily obscured AGN exists in the NE nucleus based on the X-ray data.

Overall, the multi-wavelength data suggest the coexistence of a heavily absorbed AGN and a hot gas component heated primarily by the starburst in the NE nucleus.

3.3.2.4 The Spectra of the Nuclear Region

To get a global view of the Nuclear Region, we extracted spectra from Region 1 in Figure 3.3 for analysis. All the spectra from the 2016 data were combined as a single spectrum for fitting, while the spectrum from the 2000 data was left alone. The AGN emission and thermal emission from the hot gas within the Nuclear Region should be treated separately due to their different physical origin. Therefore, spectra with energy range of 0.4 - 2 keV and those with energy range of 2-7 keV were fitted separately.

There is no sign of contribution from the scattering/reflection emission of the AGN in the 0.4 - 2 keV band. This is supported by the fact that no point-like peak is seen in the image in the soft X-ray band. We therefore conclude that a model with thermal gas component(s) is enough to describe the data. In order to constrain the temperature and metal abundance of the thermal gas component in the Nuclear Region, simultaneous fitting of both the 2000 data and the 2016 data was carried over the 0.4 - 2.0 keV energy range. A single temperature, hot diffuse gas (MEKAL) model could not describe the data (χ^2_ν = 3.1).

A model made up of two thermal gas components with variable metal abundance for individual elements (hereafter called VMEKAL) was then used in the simultaneous fitting. As stated above, there is intense starburst activity happening in the Nuclear Region. It is therefore natural to expect that the metallicity pattern of the hot, X-ray emitting gas in this region is similar to that of the yield of SNe II (hereafter called SNe II metallicity pattern). On the other hand, a deviation from the SNe II metallicity pattern is also possible if there is significant amount of gas not enriched by the SNe II. Therefore, three metallicity patterns were tested in the fits for completeness. For Pattern A, both gas components had the SNe II metallicity pattern used in Iwasawa et al. [2011b]. For Pattern B, Z(Si), Z(O), and Z(Fe) of both gas components were set as free parameters, and Z(Ne)=Z(Si)=Z(Mg). Besides, all other elements were fixed at solar values. For Pattern C, the SNe II metallicity pattern used in Pattern A was adopted for the hotter gas component, and the metallicity pattern used in Pattern B was adopted for the cooler gas component.

The best-fit temperature of the two gas components are $0.75^{+0.07}_{-0.08}$ keV and $2.21^{+3.83}_{-0.73}$ keV, respectively. For the abundance ratios, all three fitting approaches adopted above agree that super-solar α/Fe ratios are measured in both gas components, while the absolute values for individual element abundances are not exactly the same. The median values of the best-fit model parameters and their associated errors for the cooler gas component obtained from the fits above are adopted for further analysis (see Table 3.3). The α/Fe ratio of the hotter gas component is SNe II-like, and is omitted in Table 3.3 for simplicity.

For the spectrum with energy range of 2-7 keV, the fit was carried out on 2016 data. As a first trial, a model made up of a single absorbed power-law component and an Fe line was used. As shown in the left panel of Figure 3.12, it can hardly describe the data (χ^2_ν = 3.0). Secondly, a hot thermal gas component (MEKAL) was added to the model. As shown in the middle panel of Figure 3.12, the model matches the data better (χ^2_ν = 0.95). The best-fit temperature of the thermal gas component is $2.18^{+1.80}_{-0.52}$ keV, which is consistent with that of the hotter gas component used in the fit of 0.4-2 keV spectra ($2.21^{+3.83}_{-0.73}$ keV). However, the flux of the best-fit model tends to be systematically lower than that of the data beyond 6.5 keV in the observer's frame, suggesting the possible existence of another hard X-ray component.

Another heavily absorbed power-law component was thus added to the model, as shown in the right panel of Figure 3.12. The best-fit model gives a reduced χ^2 of 0.8, and the absorption column densities of the two power-law component are $\sim 2.1{\times}10^{23}$ cm^{-2} and $\sim 1{\times}10^{24}$ cm^{-2} respectively. The error for the latter is relatively large, which is on the order of $5{\times}10^{23}$ cm^{-2}. This is probably caused by the degeneracies among the fit parameters, most likely the degeneracy between the absorption column density and the temperature of the hot gas. These results agree with those obtained in the fits of the SW and NE nuclei separately (Table 3.2). They are also broadly consistent with the values listed in Iwasawa et al. [2018] ($2.6^{+0.9}_{-1.1}{\times}10^{23}$ cm^{-2} and $1.4^{+0.7}_{-0.4}{\times}10^{24}$ cm^{-2}, respectively), which are obtained from the fit of *NuSTAR* data.

For the absorption-corrected flux of the two power-law components, the value of the less absorbed power-law component ($1.97^{+0.34}_{-0.09}{\times}10^{-13}$ ergs cm^{-2} s^{-1}) agrees with that obtained from the 0.″75-aperture spectrum of the SW nucleus listed in Table 3.2, while the value for the more absorbed one (corresponding to the NE nucleus) is not well constrained ($<2\times10^{-12}$ergs cm^{-2} s^{-1}). Together with the results presented in Section 3.3.2.2 and 3.3.2.3, our results of the two heavily absorbed AGN are in general consistent with those obtained in Iwasawa et al. [2018].

3.3.3 Host Galaxy Region (Region 2)

The spectra of the host galaxy were extracted from Region 2 in Figure 3.3 (i.e. excluding Region 1). To constrain the temperature and metallicity of the thermal gas in this region, simultaneous fitting to the spectra from both the 2000 data and the 2016 data was carried out. As the flux above 2 keV is negligible in the spectra, the model was only a thermal gas (VMEKAL) with Galactic absorption, and the fit was confined to 0.4-2 keV range. Again, the abundance of O, Si, and Fe were set as independent variables, and the abundances of Mg and Ne were tied to that of Si. The abundances of all other elements were fixed at solar values. The spectra and the best-fit model are shown in Figure 3.13, and the results from the fits are summarized in Table 3.3. In general, the temperature of the thermal gas is similar to that of the cooler gas component in the Nuclear Region (kT $\sim$ 0.73 keV and kT $\sim$ 0.75 keV, respectively). However, the Host Galaxy Region has a lower α/Fe ratio ($1.7^{+1.6}_{-1.6}$) than that seen in the Nuclear Region (α/Fe ratio=$6.6^{+3.5}_{-3.7}$) at the $\sim$2–σ level. There is a non-negligible, intrinsic absorption in this region (see Table 3.3), which is not surprising given the dusty nature of Mrk 273 [$A_V \geqslant 15$, derived from the ISO SWS with an aperture of 20″, which covers the whole galaxy except the tidal tail; Genzel et al., 1998].

One thing to notice is that the absolute values of the abundances are quite low and they should be quoted with caution. When thermal spectra of different temperatures are summed

Table 3.3. Comparison among the Physical Properties of the Thermal Gas Component in Different Regions

Model Parameter[a]	Nuclear Region[b]	Host Galaxy Region	Ionization Cone	Southern Nebula		NE-extended Nebula
				2016 data	2000 + 2016 data	
N_H[c]	$0.23^{+0.07}_{-0.05}$	$0.03^{+0.005}_{-0.006}$	0.009(fix)	0.009(fix)	0.009(fix)	0.009(fix)
kT (keV)	$0.75^{+0.07}_{-0.08}$	$0.73^{+0.08}_{-0.10}$	$0.82^{+0.09}_{-0.08}$	$0.60^{+0.10}_{-0.10}$	$0.57^{+0.06}_{-0.07}$	$0.31^{+0.07}_{-0.01}$
n_e[d]	24	21	16	3	3	2
$O/O_\odot$	$0.59^{+0.48}_{-0.34}$	$0.48^{+0.40}_{-0.21}$	$0.44^{+0.45}_{-0.24}$	$0.79^{+1.14}_{-0.40}$	$0.83^{+1.05}_{-0.22}$	$0.16^{+0.63}_{-0.05}$
$Si/Si_\odot$	$0.53^{+0.20}_{-0.22}$	$0.17^{+0.14}_{-0.15}$	$0.37^{+0.14}_{-0.22}$	$1.00^{+2.13}_{-0.04}$	$1.32^{+1.74}_{-0.16}$	$0.64^{+1.25}_{-0.30}$
$Fe/Fe_\odot$	$0.08^{+0.03}_{-0.03}$	$0.10^{+0.03}_{-0.05}$	$0.11^{+0.04}_{-0.04}$	$0.22^{+0.56}_{-0.06}$	$0.30^{+0.30}_{-0.05}$	$0.31^{+0.14}_{-0.11}$
α/Fe[e]	$6.6^{+3.5}_{-3.7}$	$1.7^{+1.6}_{-1.6}$	$3.3^{+4.2}_{-2.6}$	$4.6^{+7.1}_{-2.3}$	$4.5^{+3.1}_{-1.9}$	$2.1^{+5.9}_{-1.8}$
flux (0.4-2 keV)[f]	$7.96^{+0.49}_{-0.22}$	$3.75^{+0.17}_{-0.18}$	$1.00^{+0.06}_{-0.08}$	$1.88^{+0.20}_{-0.16}$	$1.78^{+0.13}_{-0.12}$	$0.54^{+0.08}_{-0.08}$
luminosity (0.4-2 keV)[g]	$2.63^{+0.16}_{-0.07}$	$1.24^{+0.06}_{-0.06}$	$0.33^{+0.02}_{-0.03}$	$0.62^{+0.07}_{-0.05}$	$0.59^{+0.04}_{-0.04}$	$0.18^{+0.03}_{-0.03}$
χ^2_ν(DOF)[h]	1.4(93)	0.9(67)	-	-	-	-
cstat(DOF)[i]	-	-	142.8(178)	103.8(72)	124.9(121)	45.6(41)

[a]Fitting Model: For the Nuclear Region, the model is two hot gas components with absorption (i.e. phabs(VMEKAL)+phabs(VMEKAL) in XSPEC). For all other regions, the model is just one hot gas component with absorption (i.e. phabs(VMEKAL) in XSPEC). The absorption column densities are fixed to the Galactic value of 9×10^{19} cm^{-2} when necessary. All other elemental abundance not included in the table are fixed at solar values. All the results are from the simultaneous fitting to both the 2000 data and 2016 data. All the errors listed correspond to a confidence range of 90%, or $\sim\pm1.6\sigma$. For the data fitted with the CSTAT statistic, the errors are derived from the default MCMC method implemented in XSPEC.

[b]The median values obtained for the cooler gas component are listed. See Section 3.3.2.4 for more details.

[c]The absorption column density, in units of 10^{22} cm^{-2}.

[d]Electron number density, in units of 10^{-3} cm^{-3}. Spherical volumes with a filling factor of 1 are assumed in the calculation except for the Ionization Cone Region, where a bi-cone with an opening angle of 75° and a filling factor of 1 is assumed.

[e]Abundance ratios of α elements to Fe, determined by the ratio of Si (row 4) and Fe (row 5) abundance. The values are rounded to one decimal. For the data fitted with the χ^2 statistic, the errors were obtained assuming standard error propagation: $\sigma_{a/b} = \sqrt{(\sigma_a/b)^2 + (\sigma_b a/b^2)^2}$. For the data fitted with the CSTAT statistic, the errors were derived from the default MCMC method in XSPEC.

[f]In units of 10^{-14} erg s^{-1} cm^{-2}, absorption corrected.

[g]In units of 10^{41} erg s^{-1}, absorption corrected.

[h]The reduced χ^2 (χ^2_ν) from the fits and the corresponding degrees of freedom (DOF).

[i]The CSTAT statistics and the corresponding degrees of freedom (DOF). The spectra were binned to 1 counts bin^{-1}.

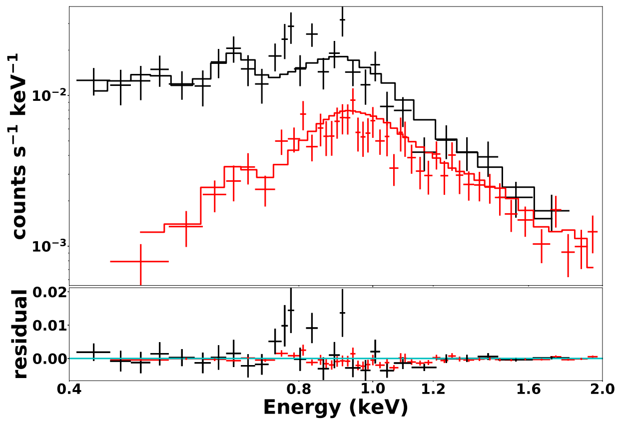

Figure 3.13: Top: the results from the fits of spectra from the Host Galaxy Region (Region 2 as shown in Figure 3.3). Spectra from both the 2000 data (black) and the 2016 data (red) in the energy range of 0.4-2.0 keV were used. The model (solid lines) is only an absorbed thermal gas component with variable abundance of different elements(VMEKAL). The abundances of O, Si (Ne, Mg), and Fe are set as independent variables, while all other elements are fixed at solar values. The best-fit parameters are summarized in Table 3.3. Bottom: residuals (data minus model).

together, emission-line features could be diluted and the best-fit abundance values might yield a falsely low value [e.g. Buote et al., 1999]. Therefore, there might actually be multi-temperature gas with higher metallicity in this region, although a two-temperature gas model does not improve the fit (i.e. the reduced χ^2 has only changed by $\sim 3\%$). Nevertheless, the relative abundance ratios of different metals are much less affected by the effect described above, since all the measured metal abundances are affected in a similar way.

3.3.4 Ionization Cones and Outflow

Galactic outflows are usually multi-phase [e.g. Veilleux et al., 2005b]. The multi-phase nature of galactic outflows is not well understood. Since the outflow in Mrk 273 has been detected in the ionized and neutral gas phases [$\sim$ 4 kpc; Rupke and Veilleux, 2013b, Rodríguez Zaurín et al., 2014], as well as the molecular gas phase [$\sim$ 550 pc; U et al., 2013, Veilleux et al., 2013b,

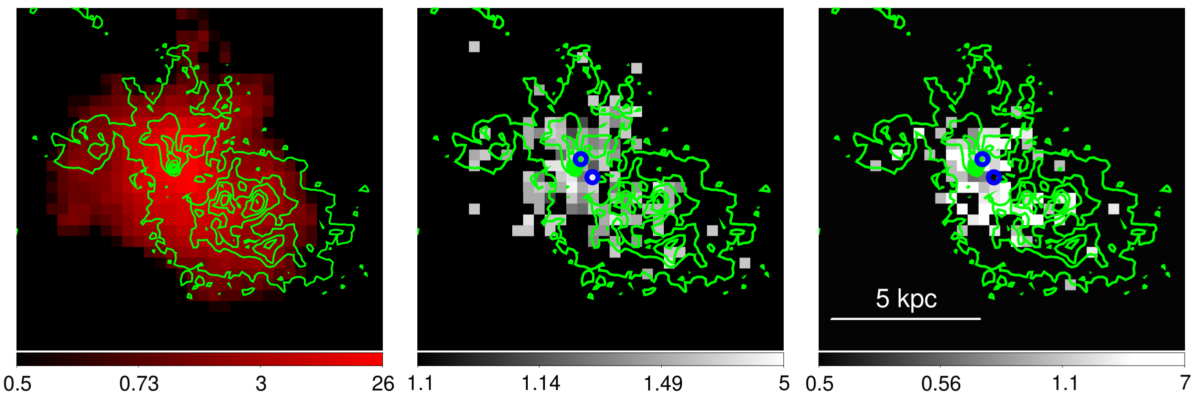

Figure 3.14: *Left*: the image at 1-3 keV within Region 2. The image is on a logarithm scale and in units of counts. *Middle*: the map of 1-3 keV to 0.4-1 keV counts ratios. Pixels with counts fewer than 1 are excluded. *Right*: Si to Fe L line ratio maps, showing the significant Si XIII 1.85 keV emission (without continuum subtraction) southwest and northeast the two nuclei. Pixels with counts fewer than 1 are excluded. In all the three panels, the overlaid green contours are the [O III] λ5007 emission, tracing the ionization cones and outflowing gas in optical and the two blue circles denote the location of the two nuclei.

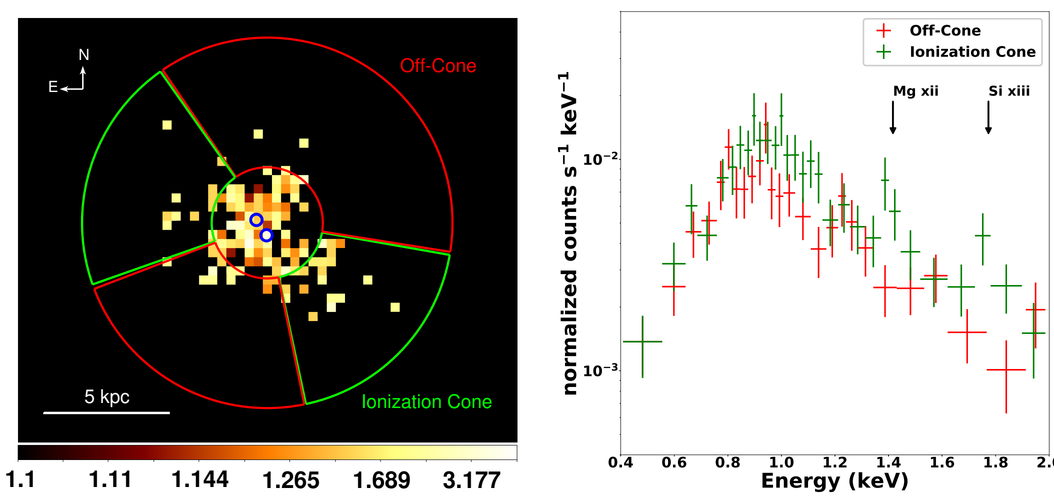

Figure 3.15: *Left*: the same 1-3 keV to 0.4-1 keV flux ratio map as shown in the middle panel of Figure 3.14 but on a different color scale, over-plotted with the extraction regions (annulus sectors) for Ionization Cone Region (green) and Off-Cone Region (red). The grayscale image is on a logarithm scale and in units of counts. *Right*: spectra of the 2016 data extracted from the Ionization Cone Region and Off-Cone Region shown in the left panel. The spectra are both binned to a minimum S/N of 3.5 bin^{-1} and normalized at the first energy bin.

Cicone et al., 2014, Aladro et al., 2018], it is important to also explore the hot, X-ray-emitting phase of the outflow. For this, we examined ≤ 3 keV X-ray emission where this hot phase may be seen.

The 1-3 keV image in counts, 1-3 keV to 0.4-1 keV ratio map and the Si to Fe-L line ratio map within the Host Galaxy Region and Nuclear Region (Region 1 & 2) are shown in Figure 3.14. The Si to Fe-L line ratio map was generated from the division of the narrow-band images of the Si XIII 1.85 keV line emission (1.78-1.95 keV) and Fe-L line emission (0.85-1.0 keV). The ratio map of Mg XII 1.47 keV to Fe-L line was also obtained, which is similar to the Si to Fe-L line ratio map and is left out to avoid redundancy. Spatially extended 1-3 keV emission and Si (also Mg) line emission are clearly seen on a scale of ~ 7 kpc $\times$ 7 kpc, suggesting the existence of highly ionized, hot gas. Within the Nuclear Region ($\lesssim$2 kpc), starburst, AGN and/or shocks caused by the outflowing gas impacting the ambient material can all be responsible for the ionization/heating of the gas, and it is hard to distinguish them based on the current *Chandra* data. However, excesses of 1-3 keV emission and Si XIII 1.85 keV (also Mg XII 1.47 keV) line emission are seen both southwest and northeast of the two nuclei, at a mean distance of ~ 5 kpc in projection. Both of the excesses are coincident with the [O III] λ5007 ionization cones seen in Rodríguez Zaurín et al. [2014], which also traces the outflowing gas along the same direction. This tentatively suggests that the excesses of 1-3 keV and Si XIII 1.85 keV (also Mg XII 1.47 keV) line emission are related to the outflowing, hot gas.

The Host Galaxy Region was divided into Ionization Cone Region (green sector annuli) and Off-Cone Region (red sector annuli), based on the location of the [O III] λ5007 emission as well as the excesses in the 1-3 keV and Si XIII 1.85 keV (also Mg XII 1.47 keV) line emission, which is shown in the left panel of Figure 3.15. Spectra were then extracted from the Ionization Cone

Region and Off-Cone Region separately. The combined spectra from the 2016 data are shown in the right panel of Figure 3.15. In the spectrum of the Ionization Cone Region, emission feature of Mg XII 1.47 keV and Si XIII 1.85 keV lines are seen, which are absent in the spectrum of the Off-Cone Region. Fitting the two emission lines with Gaussian profile gives equivalent widths of $\sim$ 0.04 keV and $\lesssim$0.01 keV respectively. These emission lines suggest the existence of highly ionized gas and/or high α-element abundance in the Ionization Cone Region, and corresponding outflowing gas too.

One thing to notice is that the outflow on this spatial scale is probably not confined only to the Ionization Cone Region. According to the integral field spectroscopy in Colina et al. [1999] and Rupke and Veilleux [2013b], the outflows on smaller scales have different orientations (i.e. North-South for $\lesssim$1 kpc and Northwest-Southeast for $\lesssim$4 kpc). The outflow likely continues to move outwards in a similar direction but perhaps a wider opening angle, and the outflowing gas in the Ionization Cone Region may be part of this outflow.

For the spectra from the Ionization Cone Region, a single-temperature gas model with variable abundance for elements O, Si (tied with Mg, Ne), Fe (VMEKAL) and Galactic absorption was used for the fitting. The α/Fe ratio in this region is $3.3^{+4.2}_{-2.6}$. These results are summarized in Table 3.3.

Additionally, the possible temperature difference of the gas in the Ionization Cone Region and Off-Cone Region was explored by fitting a single-temperature gas model with SNe II metallicity pattern adopted in Iwasawa et al. [2011b] to the spectra. The temperatures derived from the fits are kT=$0.82^{+0.09}_{-0.08}$ keV for the Ionization Cone Region and kT=$0.51^{+0.10}_{-0.12}$ keV for the Off-Cone Region. The higher temperature in the Ionization Cone Region suggests possible heating from photoionization and/or shocks induced by the outflow. This result is consistent with the idea mentioned in Section 3.3.3 that the Host Galaxy Region is made up of multiple gas components of different temperatures.

3.3.5 Southern Nebula (Region 3)

3.3.5.1 Soft X-ray Image

In order to study the spatially extended halo emission, an image in flux unit is needed. To obtain such an image, the dependence of the collecting area on the energy and position as well as the effective exposure in different regions of the detector needs to be taken into account properly. The image of the Southern Nebula in flux unit was produced with the CIAO script *flux_image* for each observation. In order to obtain the spectral weights needed to produce the exposure map, preliminary spectra were extracted from an elliptical region (Region 3 in Figure 3.3) for each observation. All the spectra from the 2016 data were combined into one single spectrum. The combined 2016 spectrum and 2000 spectrum were then fitted with a single-temperature gas model (MEKAL) simultaneously, and the best-fit model spectra were used to generate the spectrum weights for exposure maps of each observation separately. Finally, all the images were combined.

The final product, the image of the Southern Nebula in flux unit, is shown in both the right panel of Figure 3.2 and Figure 3.3. Soft X-ray emission is seen extending up to $\sim$ 40 kpc in the directions both perpendicular to and along the tidal tail. Apparently, the X-ray emission is suppressed in the tidal tail region seen in the optical image, where a decrease of $\sim$ 23% in the surface brightness is measured, compared to that of the whole Southern Nebula. This suggests further that the X-ray emission is not exclusively caused by the tidal effects, which is discussed further in Section 3.4 [see also Iwasawa et al., 2011a].

3.3.5.2 Spectra

The spectra of both the 2000 and the 2016 data were extracted from Region 3 in Figure 3.3. As the 2000 data were taken 16 years before the 2016 data, the instrument response of ACIS-S in the soft X-ray has changed significantly. As shown in Table 3.1, only $\sim$ 680 counts were obtained in 2016-2017 for the Southern Nebula. Although the spectrum from the 2016 data seems more noisy, it does not mean that the data are of lower quality compared to the 2000 data. In Figure 3.16, the 2000 and 2016 data were binned with the same method, i.e., at least 5 counts bin^{-1} for visualization. As more counts were obtained in the 2016 spectrum, the bin size of the 2016 spectrum (in units of keV) is much smaller than that of the 2000 spectrum (e.g., this can be seen most clearly in the 1.6-2.0 keV data in Fig 16). This is why the 2016 spectrum appear more "noisy" than they actually are. In order to get robust measurements from the spectra of the Southern Nebula region, the spectral fitting was carried out as follows.

We firstly checked whether a model with fixed, solar abundance can fit the data. For this exercise, the spectra were binned to 15 counts bin^{-1} so the χ^2 statistics and F-test could be applied. The fits gave a χ^2 of 87.5 with a DOF of 55 in the case of the fixed solar abundance, and a χ^2 of 49.2 with a DOF of 52 for the variable abundance model. The p-value of the F-test is very low ($\sim$1.2$\times$10^{-6}), implying that the fixed abundance model is not sufficient to properly describe the data.

We then turned to the model with variable abundances. Firstly, only spectra from the 2016 data were combined and fitted. In agreement with Iwasawa et al. [2011a], emission features of Mg XI 1.34 keV and Si XIII 1.85 keV are seen by eye in the spectrum. Such line emission suggests the existence of abundant α elements in the nebula. The spectrum was binned to 1

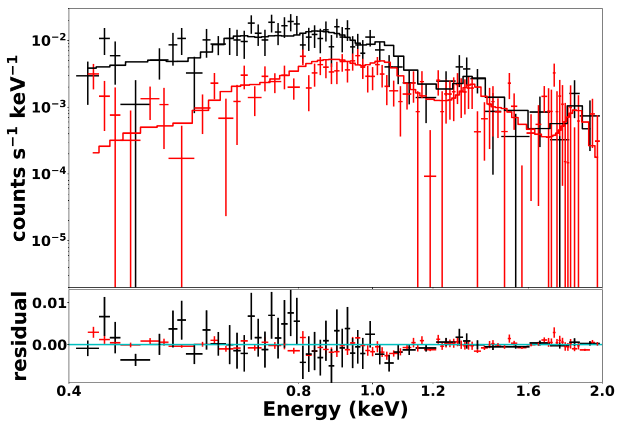

Figure 3.16: Top: simultaneous fitting to the spectra of the Southern Nebula from 2000 data (black) and 2016 data (red). A thermal gas model (VMEKAL) is fitted to the spectra and shown in solid lines. The abundances of O, Si (Ne, Mg), and Fe are all set as independent variables. The spectra shown are binned to 5 counts bin^{-1} only for the purpose of better visualization only, while the spectra were binned to 1 counts bin^{-1} in the fit. The best-fit parameters are summarized in Table 3.3. Bottom: residuals (data minus model).

counts bin^{-1} and the CSTAT statistic was used for the fit. The spectrum was fitted with a single-temperature gas model (VMEKAL) with Galactic absorption. Specifically, the abundances of Si, Mg, and Ne were tied together, while those of O and Fe were left as independent variables respectively. The abundance for all other elements not mentioned above were fixed at solar values. The corresponding results from the fits are summarized in Table 3.3.

The robustness of the results to the change of the abundance assumption was investigated. This was explored by setting the abundance of all other elements free in the fitting, but they had not changed the results from the fits to a noticeable extent. This is expected, since no line features of those elements are strong enough to affect the results of the fit in the spectral range of 0.4-2 keV. As a result, all those elements were fixed at solar values in the fits below.

Secondly, simultaneous fitting to both the 2000 and the 2016 data was carried out. Again, the spectra were binned to 1 counts bin^{-1} and the CSTAT statistic was used for the fit. The model and the parameter settings were the same as the one used when the 2016 data alone was fitted.

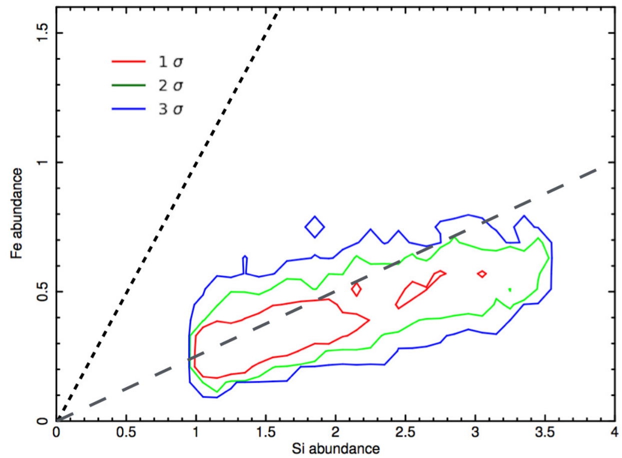

Figure 3.17: The probability contours of the Si (Ne,Mg) and Fe abundances (in solar units) for the Southern Nebula, using MCMC method and based on the results of the simultaneous fit to the spectra shown in Figure 3.16. The contours shown are for one, two and three sigma confidence levels. The black dotted line and gray dashed line denote the α/Fe ratios of 1 and 4, respectively.

The results are summarized in Table 3.3. In general, the two fits give results that are consistent with each other. Taking into account the errors, both fits give the same temperature for the nebula. The largest difference of the two fits lies in the absolute metallicity, but both results still broadly agree with each other.

As stated at the end of the Section 3.2.1, the uncertainty of the α/Fe ratio was obtained through the default Markov Chain Monte Carlo (MCMC) method implemented in XSPEC when the CSTAT statistic was used. The probability contours of Si (Ne, Mg) and Fe abundances are shown in Figure 3.17, based on the simultaneous fit of the 2000 and 2016 data. It can be seen that, although the absolute values of Si (Ne, Mg) and Fe abundance are uncertain, the ratio of α/Fe is constrained relatively well by the data (α/Fe = $4.5^{+3.1}_{-1.9}$ for $\sim \pm 1.6\sigma$, or α/Fe = $4.5^{+5.5}_{-2.4}$ for $\sim \pm 3\sigma$). The detection of a super-solar α/Fe ratio in the Southern Nebula is therefore robust (>3σ).

3.3.5.3 Search for Spatial Variations within the Nebula

The spatial variations of physical properties within the Southern Nebula may help reveal the origin of the hot gas. The possible spatial variations of the temperature and metallicity of the hot gas were explored.

Spectra were extracted from regions on both the east and west sides of the tidal tail for inspection. The temperatures of the western and eastern parts of the Southern Nebula agree with each other and are similar to the value of the whole nebula (kT $\sim$ 0.57 keV), taking the errors into consideration. The relative metal abundance ratios of the two parts also show similar values to those of the whole nebula (α/Fe $= 4.5^{+3.1}_{-1.9}$). There is a hint that the absolute metal abundance in the western part of the nebula is systematically larger than that in the eastern part and that in the whole nebula. However, the uncertainties in the abundance are quite large (a factor of $\gtrsim$2) and this result is thus not conclusive. Moreover, the difference between the north and south parts of the Southern Nebula was also explored. Again, no clear difference was seen in either the temperature or the metallicity pattern.

However, a detailed analysis of the narrow-band images centered on the Mg XI 1.34 keV line and Si XIII 1.85 keV line have revealed tentative spatial variations within the Southern Nebula. As shown in Figure 3.18, there are separate Mg XI 1.34 keV bright region (Mg-bright region) and Si XIII 1.85 keV bright region (Si-bright region) within the Southern Nebula. The spectra of both regions as well as the spectrum for the whole Southern Nebula are shown in Figure 3.19, and similar temperatures (kT $\sim$ 0.57 keV) were obtained for all spectra by fitting a thermal gas model to them. The spectra demonstrates the stronger Mg XI 1.34 keV line and Si XIII 1.85 keV line emission in corresponding regions respectively. As Si and Mg are both α elements, the

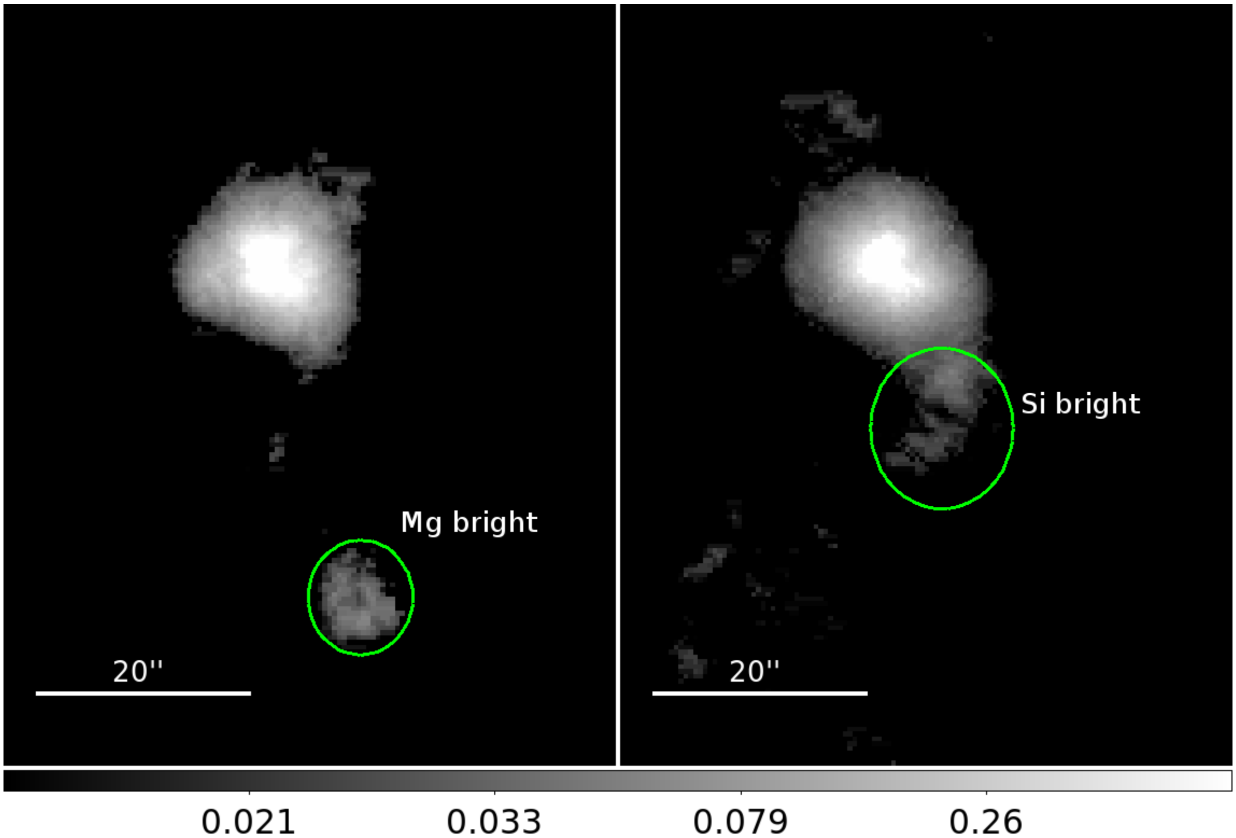

Figure 3.18: *Left*: image of Mg XI 1.34 keV emission (1.25-1.45 keV) from stacked 2000 and 2016 data. *Right*: image of Si XIII 1.85 keV emission (1.78-1.95 keV) from the same data. On the left panel, an emission region dominated by Mg XI 1.34 keV emission is shown, while on the right panel, another region dominated by Si XIII 1.85 keV emission is shown. Neither images are continuum subtracted. They are adaptively smoothed by FTOOL *fadapt* [http://heasarc.gsfc.nasa.gov/ftools/; see Blackburn, 1995] with the same parameter settings, and are on a logarithm scale and in units of counts.

relative abundance of these two elements should not vary much in different regions. One possible explanation for this variation is that the ionization states in the two regions are different, where the Si-bright region is more highly ionized than the Mg-bright region. The low S/N ($\lesssim$3) of these emission features prevent us from carrying out a more quantitative modeling of this apparent variation.

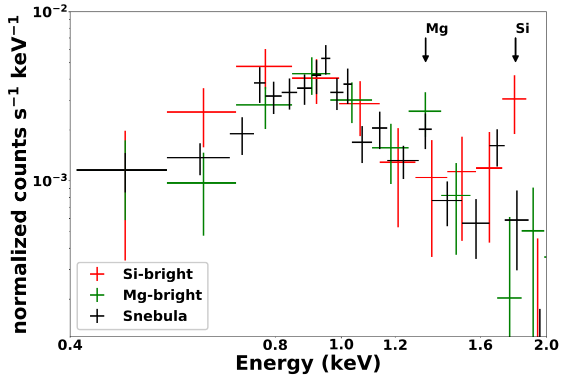

Figure 3.19: The spectra from Si-bright region (red) and Mg-bright (green) region as shown in Figure 3.18, as well as the whole Southern Nebula (black). All spectra are normalized at the first energy bin. Locations of Mg and Si emission features are denoted with arrows.

3.3.6 NE-extended Nebula (Region 4)

Denoted as Region 4 in Figure 3.3, there is extended emission to the northeast of the galaxy (i.e. NE-extended Nebula), which is spatially associated with the extended, [O III] λ5007 emission studied in Rodríguez Zaurín et al. [2014], most likely photoionized by the central AGN. The spectra were fitted in the same way that has been used for the Southern Nebula. The spectra for this region were fitted with a single-temperature gas model with Galactic absorption. The spectra were mildly binned to 1 counts bin^{-1} and the CSTAT statistic was used. The results from the fits are summarized in Table 3.3, and the spectra are shown in Figure 3.20. Compared to the Southern Nebula, the temperature of this extended emission is significantly lower, perhaps $\sim$ 1/2 of that in the Southern Nebula. The α/Fe ratio in this region ($2.1^{+5.9}_{-1.8}$) seems slightly lower than that in the Southern Nebula ($4.5^{+3.1}_{-1.9}$), but only at the $\sim$1–σ level so it is not significant. The differences in temperature and perhaps in α/Fe ratio between the NE-extended Nebula and the Southern Nebula probably point to their different origins. See Sections 4.1.1-4.1.3 for a discussion of these results.

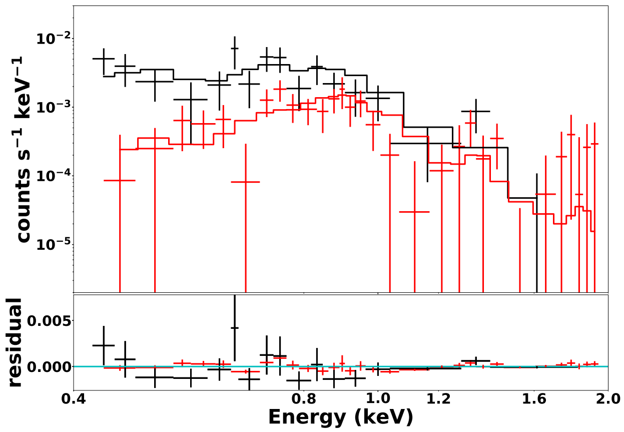

Figure 3.20: Top: simultaneous fitting to the spectra of the NE-extended Nebula (Region 4 in Figure 3.3) from the 2000 data (black) and 2016 data (red). A thermal gas model (VMEKAL) is fitted to the spectra and shown in solid lines. The abundances of O, Si (Ne, Mg), and Fe are all set as independent variables. The best-fit parameters are summarized in Table 3.3. The spectra shown are binned to 5 counts bin^{-1} only for the purpose of better visualization, while the spectra were binned to 1 counts bin^{-1} in the fit. Bottom: residuals (data minus model).

3.4 Discussion

3.4.1 Origin of the Southern Nebula

An order-of-magnitude estimation of the total thermal energy and gas mass of the Southern Nebula was carried out. Despite the apparent irregular shape of the soft X-ray emission, it is assumed that the emission is generated in a sphere with a radius of 20 kpc and a filling factor of 1. Based on this simplification and the mean number density of 3×10^{-3} cm^{-3} derived from the fits (see Table 3.3), a total energy of $\sim 1.2\times10^{58}$ ergs and a total mass of $\sim 1.5\times10^{9}$ $\mathrm{M}_{\odot}$ are obtained. The amount of kinetic energy deposited during a merger of two identical progenitors is of the order $M_g v_c^2/8$, where M_g is the mass of the X-ray-emitting gas and v_c is the relative speed during the collision [see Nardini et al., 2013]. In the case of Mrk 273, $v_c \sim 1250$ km s^{-1} is needed, which is significantly faster than the characteristic speed of head-on collisions in non-cluster environments [e.g., $\sim$ 800 km s^{-1} in Taffy Galaxies; Braine et al., 2003]. This implies the existence of additional energy source for the nebula.

3.4.1.1 Extra Heating in the Southern Nebula

As shown in Table 3.3, the measured temperature of the nebula is $0.57^{+0.06}_{-0.07}$ keV. Assuming the virialization of the hot gas and an NFW density profile for the dark matter halo [Navarro et al., 1997], the gas virial temperature can be written as follows:

$$kT_{\rm vir} = \frac{1}{2}\mu m_p \frac{GM_{\rm vir}}{r_{\rm vir}} \simeq 0.135 \left(\frac{M_{\rm vir}}{10^{12} M_{\odot}}\right) \left(\frac{r_{\rm vir}}{100 \text{ kpc}}\right)^{-1} \text{ keV},$$

By further assuming the relations between the virial radius and both the halo mass and redshift presented in Mo and White [2002], the dark matter halo mass can be obtained through the equation $kT_{vir} \sim 0.042\ M_{12}^{2/3}(1+z)$ keV, where M_{12} is the virial mass expressed in units of 10^{12} $\mathrm{M}_{\odot}$. Similar to what is suggested for NGC 6240 in Nardini et al. [2013], a possible evolutionary scenario consistent with the temperature ($\sim$ 0.57 keV) of the nebula is that of a cold dark matter halo with a total virial mass of $\sim 10^{13}$ $\mathrm{M}_{\odot}$ formed at z $\sim$ 2.

This is almost an order of magnitude more massive than that of the Milky Way ($\sim 1.3 \times 10^{12}$ $\mathrm{M}_{\odot}$, see McMillan [2011] for details.) In addition, this value distinguishes group-scale halos from galaxy-scale halos [see Humphrey et al., 2006]. The mass of the dark matter halo estimated here is unreasonably high, given the stellar mass of Mrk 273 [$\sim 10^{11}$ $\mathrm{M}_{\odot}$; see Veilleux et al., 2002, Rodríguez Zaurín et al., 2009, U et al., 2012] and its dynamical mass [$\sim 10^{12}$ $\mathrm{M}_{\odot}$, based on the velocity dispersion of the CO absorption features in the near-infrared, and assuming a King model with tidal radius to core radius of $\sim$ 50; Tacconi et al., 2002] of Mrk 273. Therefore, extra heating mechanism for the hot gas is at work.

On the contrary, the NE-extended Nebula shows a lower temperature of $0.31^{+0.07}_{-0.01}$ keV. Following the same procedure used for the Southern Nebula, a dark matter halo mass of $\sim 3.5\times10^{12}$ $\mathrm{M}_{\odot}$ is obtained, which is a more reasonable value for the halo mass of Mrk 273. Compared to the Southern Nebula, the NE-extended Nebula is thus more likely to be the pre-existing, virialized gaseous halo.

3.4.1.2 Heating Source of the Gas

Both galactic outflows generated from the nuclear/circumnuclear region and the merging activity can heat the gas in the nebula. It is thus necessary to discuss their relative importance.

One way to estimate it is to look at the required shock velocity. Assuming that the gas is heated up after being swept by an adiabatic shock, the temperature of the gas can be derived as $kT_{\rm s} = 3\mu m_p v_{\rm s}^2/16$, where $v_{\rm s}$ is the speed of the shock front. Adopting kT=0.57 keV (see Table 3.3), the $v_{\rm s}$ will be 710 km s^{-1}, which is too high for the relative orbit speeds within a merging system like Mrk 273 (e.g. the inferred orbital velocity of the two nuclei of NGC 6240 is just 155 km s^{-1}; see Tecza et al. [2000] for details). In addition, the maximum speed of the non-outflowing ionized gas only reaches a maximum of 350 km s^{-1}, as is measured through the narrow component of Hαemission in Rupke and Veilleux [2013b]. Therefore, the merging activity alone seems not capable of causing shocks with required $v_{\rm s}$.

As is presented in Section 3.3.4, hot gas (kT $\sim$ 0.8 keV, see Table 3.3) associated with the ionization cones and outflowing gas extends to a scale of $\gtrsim$5 kpc $\times$ 5 kpc. This outflowing hot gas might be the heating source for the Southern Nebula after it moves outward to a larger scale. Similar cases of hot gas heated by the AGN and/or starburst triggered outflow have been observed in several other galaxies [e.g. Wang et al., 2014, Tombesi et al., 2016, 2017]. In addition, high velocity outflow in Mrk 273 has been detected in the ionized and neutral gas phases [$\sim$ 4 kpc; Rupke and Veilleux, 2013b, Rodríguez Zaurín et al., 2014], as well as the molecular gas phase [$\sim$ 550 pc; U et al., 2013, Veilleux et al., 2013b, Cicone et al., 2014, Aladro et al., 2018]. The ionized outflow has been observed to reach a speed as high as $\sim$ 1500 km s^{-1} in projection, while the molecular outflow reaches a maximum speed of $\sim$ 900 km s^{-1} in projection. These high-speed outflows may be capable of causing adiabatic shocks with $v_{\rm s} \sim$ 710 km s^{-1} in the nebula, if there is no significant decrease in the outflow speed before they reach the nebula.

3.4.1.3 The α-elements Enrichment through Outflow

Another independent piece of evidence regarding the origin of the nebulae comes from the α/Fe abundance ratio of the hot gas. Iron is nearly entirely produced from Type Ia supernovae (SNe; i.e., exploded white dwarfs in close binary systems), while the majority of α elements originate from Type II SNe (i.e., core-collapsed massive stars). Based on the prediction of nucleosynthesis models for Type II SNe [e.g, Heger and Woosley, 2010, Nomoto et al., 2006, 2013], Si/Fe ratios can reach as high as $\sim$ 3-5 $\times$ solar value, while ratios of $\sim$ 0.5 solar value are expected from Type Ia SNe [e.g, Nagataki and Sato, 1998, Seitenzahl et al., 2013]. Therefore, the α/Fe ratios can provide information about how the gas was enriched.

The high α/Fe ratios in both the Nuclear Region (Region 1; $6.6^{+3.5}_{-3.7}$) and the Southern Nebula (Region 3; $4.5^{+3.1}_{-1.9}$) might indicate a physical connection between the two, perhaps through the outflow generated in the Nuclear Region. Similar evidence for the transport of α-enhanced material out to a scale $\lesssim$10 kpc by galactic winds has been seen in other nearby galaxies [e.g., M82; Tsuru et al., 2007, Ranalli et al., 2008, Konami et al., 2011, and references therein].

3.4.1.4 The Need for Multiple Outflow Events

If indeed the Southern Nebula is heated and enriched through the outflow, there are several reasons to believe that multiple outflow events are involved.

First of all, the maximum silicon yield of a Type II SNe is $\sim$ 0.1 – 0.3 $\mathrm{M}_{\odot}$ for a massive-star progenitor with $Z \leq 0.02$ [e.g, Nomoto et al., 2013]. The total amount of silicon within the Southern Nebula is estimated to be $\sim 2{\times}10^{6}$ $\mathrm{M}_{\odot}$, adopting a derived gas mass of $\sim 1.5{\times}10^{9}$ $\mathrm{M}_{\odot}$ and assuming a 1.5 $\times$ solar abundance for silicon estimated from the spectra. This can be translated into $1{\times}10^{7}$ Type II SNe. Given the current star formation rate[5] of $\sim$160 $\mathrm{M}_{\odot}$ yr^{-1}, a continuous star formation activity of $\gtrsim 10^{7}$ yr is required. It is thus very unlikely that the current star formation contributes solely to the enrichment. Past starforming and/or starburst activities over a much longer time scale are required. Detailed spectral analyses of the circum-nuclear region have indeed revealed stellar populations both young (3-60 Myr) and old (0.7-12.5 Gyr) [see Raimann et al., 2003, Rodríguez Zaurín et al., 2009, for details].

Secondly, the characteristic time scale needed for the outflow to affect the Southern Nebula on a spatial scale of $\sim$ 40 kpc can be estimated. The average outflow speed of warm ionized gas in projection is $\sim$ 1000 km s^{-1} [measured from the average $\mathrm{V}_{98\%}$ of the Hα emission, see column (7) of Table 3 in Rupke and Veilleux, 2013b]. Assuming that the outflow travels with a constant speed of 1000 km s^{-1}, a time scale of 40 Myr is needed for it to reach the full extent of

[5] The SFR is quoted from Veilleux et al. 2009, and the contamination from the AGN is subtracted in the calculation. They have used six different methods to calculate the AGN fraction, which are based on the mid-infrared line ratios, PAH equivalent width, mid-infrared colors, and mid-to-far infrared continuum ratios. The mean AGN fraction of the six methods is used in the calculation, and the uncertainty in the AGN fraction is $\sim$15%. See Veilleux et al. [2009b] for more details.

the Southern Nebula.

Moreover, as no significant spatial variations of the α/Fe ratio are seen within the Nebula, the whole duration of the enrichment might be as long as the dynamical time scale of ~ 0.1 Gyr, which is measured from the sound-crossing time, $D/c_s = D(5kT/3\mu m_p)^{-1/2}$. The age of the current outflow in warm ionized phase is $\lesssim$10 Myr, based on its velocity and spatial extent [Rupke and Veilleux, 2013b, Rodríguez Zaurín et al., 2014]. As a result, the current outflow alone cannot be responsible for the α-elements enrichment already observed in the Southern Nebula.

In all, multiple outflow events in the past, on a time scale of $\lesssim$0.1 Gyr, are required to explain the super-solar α/Fe ratio in the Southern Nebula. The merger event might have helped further erase spatial fluctuations in the α/Fe ratio within the nebula [similar to the case of Mrk 231, Veilleux et al., 2014].

3.4.1.5 Comparison with the Hα Nebula

As shown in the bottom right panel of Figure 3.1, the brighter portion of the extended Hα emission south of the galaxy (T $\sim 10^4$ K) resembles the Southern Nebula in the X-ray (T $\sim$ 7×10^6 K). The eastern part of the Southern Nebula in the X-ray seems to be more luminous and extended than the Hα nebula, although this may be caused by the different sensitivity of the X-ray and Hα observations. Spence et al. [2016] argue that the southern Hα nebula is not related to the large scale outflow, based on the moderate velocity shifts ($|\Delta V| \lesssim 250$ km s^{-1}) and line width (FWHM $\lesssim 350$ km s^{-1}) measured in the emission lines. However, these results do not formally rule out the possibility that the Hα nebula represents the accumulated reservoir of the outflowing gas if the turbulence caused by the outflows dissipated away as the material cooled down from $\sim$

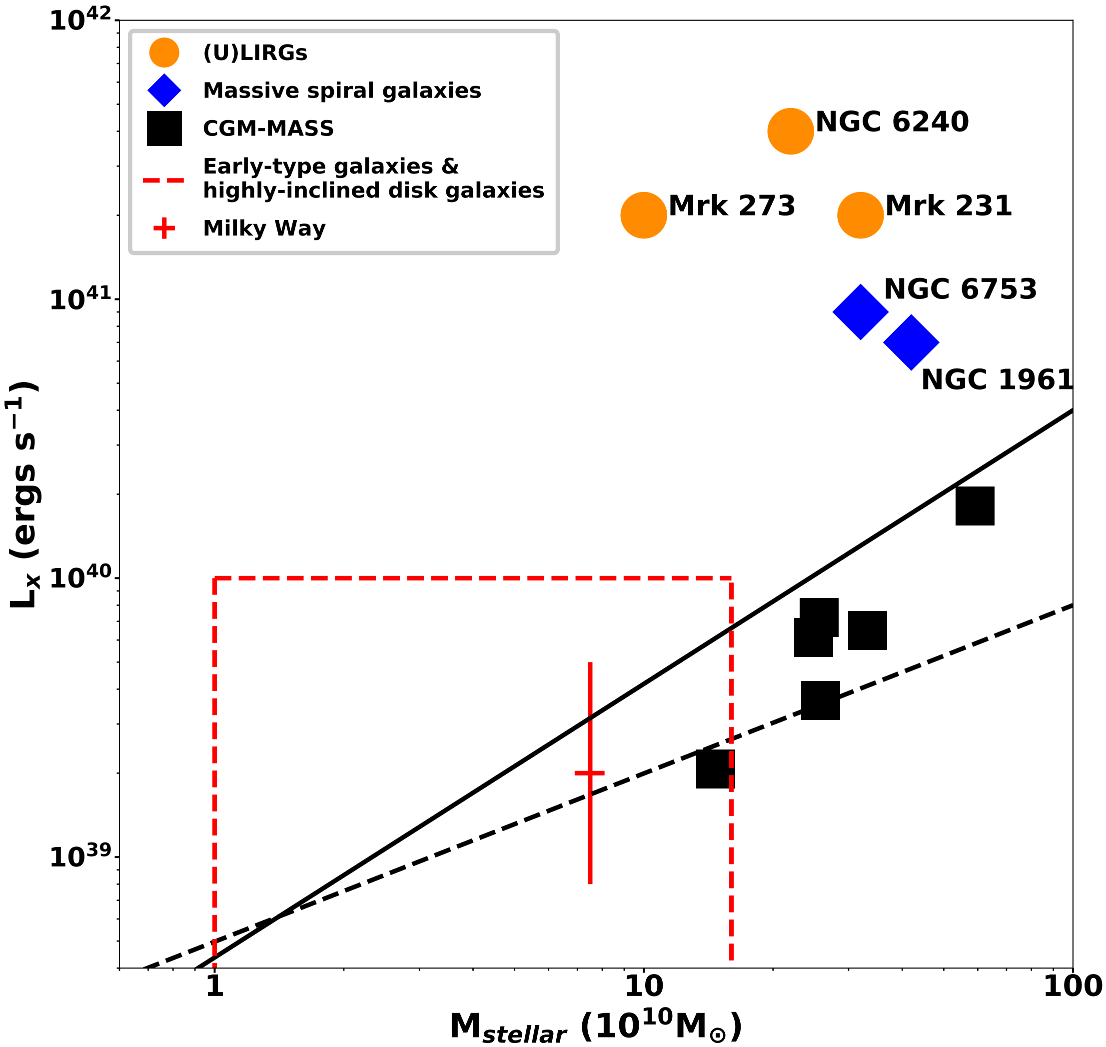

Figure 3.21: Comparison of the nebula emission from (U)LIRGs and those from other galaxies with similar stellar mass. The x, y axis are the stellar mass and soft X-ray (∼0.5-2 keV) luminosity. The filled circles, diamonds, squares and red cross denote (U)LIRGs (this work), massive spiral galaxies [Anderson et al., 2016, Bogdán et al., 2017] as well as CGM-MASS galaxies and the Milky Way [Li et al., 2017]. The sizes of the labels represent the typical errors of the measurements, except that the error bars are drawn for the Milky Way. The region enclosed by the red dashed line represents the rough location of early-type galaxies from the ATLAS^{3D} [Kim and Fabbiano, 2015] and MASSIVE [Goulding et al., 2016] surveys in the corresponding mass range, as well as nearby highly-inclined disk galaxies [Li and Wang, 2013a,b, Li et al., 2014]. The black solid line and black dashed line are linear and non-linear fits to the non-starburst field galaxies respectively [see Li et al., 2017, for more details].

7×10^6 K to $\sim 10^4$ K. The high temperature and high α/Fe ratio of the Southern Nebula favor an outflow-related origin.

3.4.2 X-ray Nebulae at Different Merger Stages

The α-enriched, luminous X-ray nebulae have been discovered in mergers at different stages: Mrk 273 (close-pair), NGC 6240 (close-pair), and Mrk 231 (coalesced). The total luminosity of the nebula within Mrk 273 in 0.4-2 keV band is 2×10^{41} erg s^{-1} (adding up nebula emission in Region 2, 3 and 4), which is comparable to those of the nebulae within Mrk 231 [2×10^{41} erg s^{-1} in 0.5-2.0 keV band, Veilleux et al., 2014] and NGC 6240 [4×10^{41} erg s^{-1} in 0.4-2.5 keV band, Nardini et al., 2013]. As shown in Figure 3.21, the soft X-ray emission of these nebulae is more luminous than that of galaxies with similar stellar mass, including massive spiral galaxies [Anderson et al., 2016, Bogdán et al., 2017], CGM-MASS galaxies [Li et al., 2017], highly-inclined disk galaxies [Li and Wang, 2013a,b, Li et al., 2014] as well as early-type galaxies from the ATLAS^{3D} [Kim and Fabbiano, 2015] and MASSIVE [Goulding et al., 2016] surveys in the corresponding mass range.

Assuming that the X-ray nebulae in (U)LIRGs are in a quasi-equilibrium state, the heating of the gas should be balanced by the radiative cooling. If this assumption is valid, the brighter nebula emission suggests significant excess energy input from the outflow events and merging process.

The basic properties of the X-ray nebulae in the three (U)LIRGs are summarized in Table 3.4. In general, the three nebulae are quite similar to each other, in terms of luminosity, temperature and α/Fe ratio. The existence of these similar X-ray nebulae in mergers at different stages

Table 3.4. Properties of the X-ray Nebulae within the three (U)LIRGs

Physical Property	Mrk 273	NGC 6240 [a]	Mrk 231 [b]
merger stage	close pair	close pair	coalesced
nuclear separation	0.75 kpc	0.74 kpc	–
L_{nebula} [c]	$\sim 2 \times 10^{41}$	$\sim 4 \times 10^{41}$	$\sim 2 \times 10^{41}$
T (keV)	~0.57	~0.65	~0.67, 0.27
n_e [d]	~3	~2.5	~0.97, 0.92
M_{gas} [e]	~6	~10	~7
α/Fe	$4.5^{+3.1}_{-1.9}$	$4.0^{+2.1f}_{-1.8}$	$3.3^{+2.2}_{-1.7}$, - [f]

[a]Nardini et al. [2013].

[b]Veilleux et al. [2014]. The best-fit model is made up of two gas components.

[c]Soft X-ray luminosity of the nebulae, in units of erg s^{-1}. The luminosities are in 0.4-2.0 keV band for Mrk 273, in 0.4-2.5 keV band for NGC 6240 and in 0.5-2.0 keV band for Mrk 231.

[d]Electron number densities, in units of 10^{-3} cm^{-3}.

[e]Total mass of the hot gas, in units of 10^9 $M_\odot$. For Mrk 273, the sum of the gas mass in Region 2, 3 and 4 is listed. For Mrk 231, the sum of the mass for the two gas components is listed.

[f]The values are not directly listed in the corresponding papers. They are estimated based on the information listed in the Table 3 of Nardini et al. [2013] and the Table 2 of Veilleux et al. [2014].

reinforces the picture that multiple outflow events over a time scale of $\lesssim$0.1 Gyr must be at work during the whole merging process.

3.4.3 The α/Fe ratios in (U)LIRGs and Early-type Galaxies

Super-solar α/Fe ratios are typically measured in the old stellar populations of early-type galaxies [e.g. Worthey, 1998, Graves et al., 2010, Conroy et al., 2014, Kriek et al., 2016] and the hot interstellar medium of some post-merger early-type galaxies with relatively young stellar populations [e.g. Kim et al., 2012]. These results are most likely due to either a short timescale of star formation (efficient quenching before the onset of Type Ia SNe) or variations in the initial mass function (IMF). Given the mass outflow rate and gas content of Mrk 273, the implied gas depletion timescale is only $\sim$ 10 Myr [Cicone et al., 2014]. The outflow in Mrk 273 might thus be able to quench star formation on this short timescale, if the ejected gas does not return to the center to form stars. Therefore, the super-solar α/Fe ratio measured in the Nuclear Region (Region 1) of Mrk 273 may be the result of the on-going rapid starburst/quenching process.

3.5 Conclusions

We have combined a deep, 200 ksec *Chandra* ACIS-S observation of Mrk 273 with 44 ksec archival data acquired with the same instrument and setup. The main results are summarized as follows.

- The AGN associated with the SW nucleus is confirmed by the new data. A secondary peak exists in the hard X-ray images (especially 4-6 keV), which is associated with the NE nucleus at a projected distance of 0.75 kpc from the SW nucleus.

- The hard X-ray (3-8 keV) spectrum of the SW nucleus is well explained by a heavily absorbed AGN (N_H = $2.79^{+0.30}_{-0.22}\times10^{23}$ cm^{-2}. In this statement and those below, the errors from the spectral fits correspond to a confidence range of 90%, or $\sim\pm1.6\sigma$). The hard X-ray flux of the SW nucleus has dropped by $\sim$ 60% from the year 2000 to the year 2016. The decrease seems to be caused by the fading of the intrinsic luminosity of the central engine, although an increase in the column density of the absorbing material cannot be formally ruled out.

- The hard X-ray (3-8 keV) spectrum of the NE nucleus is best explained by a combination of a heavily obscured AGN (N_H = $6.78^{+4.99}_{-3.31} \times 10^{23}$ cm^{-2}) and a hot gas component (kT $\sim$ 3 keV). A harder X-ray continuum compared to that of the SW nucleus is detected in the NE nucleus at 6.5-8 keV. An Fe XXV line (6.7 keV rest frame) is found in the spectrum of the NE nucleus, while the strength of Fe Kα line is not well constrained by the current data.

- A single power-law component cannot describe the hard X-ray spectrum of the Nuclear Region (r<3$''$, $\sim$ 2 kpc). Significant residuals above 6.5 keV in the observer's frame still exists after a hot (kT $\sim$ 3 keV) gas component is added to the model. Adding a second power-law component improves the fit (although reduced $\chi^2 \sim$ 0.8). These results favor the existence of a dual AGN.

- Spatially extended excesses of 1-3 keV emission and Si XIII 1.85 keV (also Mg XII 1.47 keV) line emission are found to be coincident with the optical [O III] λ5007 emission tracing the ionization cones and outflowing gas out to $\sim$ 5 kpc. An α/Fe ratio of $3.3^{+4.2}_{-2.6}$ is measured in this hot, X-ray emitting gas.

- The temperature of the cooler gas component in the Nuclear Region (kT=$0.75^{+0.07}_{-0.08}$ keV) is similar to that of the gas in the Host Galaxy Region (kT=$0.73^{+0.08}_{-0.10}$ keV). They are both higher than that of the Southern Nebula (kT=$0.57^{+0.06}_{-0.07}$ keV) and that of the NE-extended Nebula (kT=$0.31^{+0.07}_{-0.01}$ keV). No clear spatial variation is seen within the Southern Nebula itself.

- Super-solar α/Fe ratios are measured in the Nuclear Region ($6.6^{+3.5}_{-3.7}$) and the Southern Nebula ($4.5^{+3.1}_{-1.9}$). However, lower α/Fe ratios are derived in the Host Galaxy Region ($1.7^{+1.6}_{-1.6}$, different at the $\sim$2–σ level) and perhaps also in the NE-extended Nebula ($2.1^{+5.9}_{-1.8}$, although the uncertainties are large).

- These data suggest that the hot gas in the Southern Nebula has been heated and enriched by multiple outflows originated from the Nuclear Region, on a time scale of $\lesssim$0.1 Gyr. A similar origin has been suggested for the large-scale nebulae around Mrk 231 and NGC 6240. In contrast, the NE-extended Nebula is likely the pre-existing gas in the halo, which has not been affected by the outflows yet.

Chapter 4: Integral Field Spectroscopy of Fast Outflows in Dwarf Galaxies with AGN

4.1 Introduction

While it is believed that supermassive black holes (SMBH, with masses $M_{BH} \simeq 10^6 - 10^9$ $\mathrm{M}_\odot$) are ubiquitous in the centers of massive galaxies at the present epoch, the rate of incidence of (S)MBH in dwarf galaxies with stellar masses $\mathrm{M}_\star \lesssim 10^{9.5}$ $\mathrm{M}_\odot$ (roughly that of the Large Magellanic Cloud) is not well determined. The direct detection of SMBH in dwarf galaxies based on the stellar and gas dynamics within the gravitational sphere of influence of the SMBH is extremely challenging, although there have been recent efforts producing promising results [Nguyen et al., 2018, 2019]. Nevertheless, recent studies have revealed active galactic nuclei (AGN) in dwarf galaxies through diagnostics in the optical [e.g. Greene and Ho, 2007, Dong et al., 2012, Reines et al., 2013, Moran et al., 2014, Dickey et al., 2019, Mezcua and Domínguez Sánchez, 2020], near and mid-infrared [e.g. Sartori et al., 2015, Hood et al., 2017, Riffel, 2020], X-rays [e.g. Pardo et al., 2016, Mezcua et al., 2018], as well as from optical variability [e.g. Baldassare et al., 2018], opening a new window for systematic studies of (S)MBH in dwarfs [see Greene et al., 2019, for a recent review].

There is a general consensus that feedback processes likely play a vital role in the evolution of dwarf galaxies, given their shallow potential well [e.g. Veilleux et al., 2005a, 2020]. Stellar processes have long been considered the main source of feedback in dwarf galaxies [e.g. Larson, 1974, Veilleux et al., 2005a, Heckman and Thompson, 2017, Martín-Navarro and Mezcua, 2018]. However, it is still debated whether such stellar feedback is effective enough to reproduce the properties of the dwarf galaxies we see today [e.g. Garrison-Kimmel et al., 2013]. Given the growing number of AGN detected in dwarf galaxies, it is also important to consider the possible impact of AGN feedback. Few studies have explored this issue systematically. Plausible evidence of star formation quenching induced by AGN feedback in dwarf galaxies has been reported by Penny et al. [2018]. Bradford et al. [2018] have also found that the global HI content may be lower in dwarf galaxies with AGN, perhaps due to AGN feedback. In addition, radio observations have revealed radio jets in dwarf galaxies that are as powerful as those observed in more massive systems [Mezcua et al., 2019]. From the theoretical perspective, analytic analyses from Silk [2017] and Dashyan et al. [2018] have pointed out the possibly significant effects of AGN feedback in dwarfs. New simulations by Koudmani et al. [2019, 2020] suggest that AGN boost the energetics of outflows in dwarf galaxies.

Powerful, kpc-scale outflows triggered by luminous AGN has been regarded as strong observational evidence of on-going AGN feedback [e.g. Rupke and Veilleux, 2011, 2013a,b, 2015, Rupke et al., 2017, Liu et al., 2013a,b, Harrison et al., 2014, Westmoquette et al., 2013, Ramos Almeida et al., 2019], which may impact even the circumgalactic medium [e.g. Veilleux et al., 2014, Lau, Liu et al., 2019]. It is thus interesting to explore if similar outflows can be found in dwarf galaxies with AGN. Recently, Manzano-King et al. [2019] have observed a sample of 29 dwarf galaxies with AGN using Keck LRIS long-slit spectroscopy. Spatially extended (up to $\sim$2 kpc in radius), rapid outflows (median velocity offsets $\lesssim$180 km s^{-1}, 80-percentile widths W_{80}

$\lesssim$ 1600 km s^{-1}) have been discovered in a third of the sources from the sample, suggesting that AGN feedback may be significant in these dwarf galaxies. More recently, a parsec-scale radio jet was reported in one of the targets with a reported outflow, adding evidence for AGN feedback in these dwarf galaxies [Yang et al., 2020]. However, while the results from the long-slit spectra are tantalizing, they do not capture the two-dimensional morphology of the outflows. Integral field spectroscopy (IFS) that provides full two-dimensional coverage with high spatial resolution is needed to map the outflows and fully quantify the true impact of these outflows on the dwarf hosts.

In this paper, we analyze newly obtained IFS data of eight dwarf galaxies with AGN showing the fastest and brightest outflowing gas in the sample studied by Manzano-King et al. [2019] and Manzano-King and Canalizo [2020]. The eight targets were observed with Keck/KCWI, and two of the targets were also observed with Gemini/GMOS. This paper is organized as follows. In Section 4.2, the data sets, physical properties of the targets measured from the IFS and ancillary data, and reduction procedures are described. The analysis techniques adopted in this paper are described in Section 4.3. The main results are presented in Section 4.4 and detailed in Appendix C.1. The implications of these results are discussed in Section 4.5, and the conclusions are summarized in Section 4.6. Throughout the paper, we assume a ΛCDM cosmology with H_0 = 69.3 km s^{-1} Mpc^{-1}, $\Omega_{\rm m}$ = 0.287, and $\Omega_\Lambda = 0.713$ [Hinshaw et al., 2013].

4.2 Sample, Observations, & Data Reduction

4.2.1 Sample

We observed 8 out of the 29 dwarf galaxies with AGN studied in Manzano-King et al. [2019]. The 29 sources were originally selected from samples of dwarf galaxies with AGN in recent literatures based on Baldwin, Phillips & Telervich and Veilleux & Osterbrock 1987 [hereafter BPT and VO87, respectively; Baldwin et al., 1981, Veilleux and Osterbrock, 1987] line ratio diagrams [Reines et al., 2013, Moran et al., 2014] and mid-infrared diagnosis [Sartori et al., 2015]. The readers are referred to Manzano-King et al. [2019] for more details.

All targets are confirmed to host AGN based on the AGN-like line ratiosAll targets show AGN-like line ratios as measured from the Keck/LRIS long-slit spectra extracted from the central 1″ region. Many of the targets show further evidence of hosting AGN, including i) the detection of strong He II λ4686 and [Ne V] λ3426 emission in the Keck LRIS long-slit spectra and KCWI spectra; ii) the detection of coronal emission lines in the near-infrared spectra of these objects (Bohn et al. 2020, in prep.). In addition, the highly ionized [Fe X] λ6375 line (I.P.=233.6 eV) is detected within the central 0.6″ of target J0906+56 based on the GMOS Integral Field Unit (IFU) spectra reported here; Targets J0906+56 and J0954+47 also show hard X-ray emission originating from AGN activity [Baldassare et al., 2017a]. The basic physical properties of the 8 targets in our sample, including those from the NASA-Sloan Altas[1] (NSA), are summarized in Table 5.1.

[1] http://www.nsatlas.org/data

Table 4.1. Properties of the Targets

Name (1)	Short Name (2)	Redshift (3)	$\log(M_{\rm stellar}/M_\odot)$ (4)	R_{50} (5)	$\log(L_{[OIII]})$ (6)	C_{bol} (7)	$\log(L_{AGN})$ (8)	SFR (9)
SDSS J010005.94−011059.0	J0100−01	0.0517	9.47	1.2	$40.96^{+0.03}_{-0.04}$	142	43.5	<0.6
SDSS J081145.29+232825.7	J0811+23	0.0159	9.02	0.6	$39.63^{+0.05}_{-0.06}$	87	42.0	<0.01
SDSS J084025.54+181858.9	J0840+18	0.0151	9.28	1.0	$39.96^{+0.02}_{-0.02}$	87	42.0	<0.01
SDSS J084234.51+031930.7	J0842+03	0.0291	9.34	1.0	$40.51^{+0.03}_{-0.03}$	142	43.1	<0.3
SDSS J090613.75+561015.5	J0906+56	0.0467	9.36	1.5	$41.15^{+0.01}_{-0.01}$	142	43.7	<0.3
SDSS J095418.16+471725.1	J0954+47	0.0327	9.12	2.0	$41.36^{+0.02}_{-0.02}$	142	43.9	<0.3
SDSS J100551.19+125740.6	J1005+12	0.00938	9.97	1.0	$40.20^{+0.05}_{-0.06}$	142	43.2	<0.1
SDSS J100935.66+265648.9	J1009+26	0.0145	8.77	0.7	$40.48^{+0.01}_{-0.01}$	142	43.0	<0.1

Note. — Column (1): SDSS name of the target; Column (2): Short name of the target used in this paper; Column (3): Redshift of the target measured from the stellar fit to the spectrum integrated over the KCWI data cube; Column (4): Stellar mass from the NSA; Column (5): Half-light radius from the NSA, in unit of kpc; Column (6): Total [O III] λ5007 luminosity based on the observed total [O III] λ5007 fluxes within the field of view of the KCWI data without extinction correction, in units of erg s^{-1}; Column (7): [O III]-to-bolometric luminosity correction factor adopted from Lamastra et al. [2009]; Column (8): Bolometric AGN luminosity, based on the extinction-corrected [O III] luminosity, in units of erg s^{-1}; Column (9): Upper limit on the star formation rate based on the extinction-corrected [O II] $\lambda\lambda$3726, 3729 flux from the KCWI data, in units of $M_\odot$ yr^{-1}. Here we assume that $1/3$ of the [O II] $\lambda\lambda$3726, 3729 emission is from the star formation activity, following Ho [2005].

4.2.2 Observations

4.2.2.1 GMOS Observations

J0906+56 and J0842+03 were observed through Gemini fast-turnaround (FT) programs GN-2019A-FT-109 and GS-2019A-FT-105 (PI S. Veilleux). The GMOS IFU [Allington-Smith et al., 2002, Gimeno et al., 2016] data were taken on 2019-04-04 and 2019-04-05 at Gemini-N for J0906+56, and on 2019-04-28 and 2019-04-29 at Gemini-S for J0842+03. The GMOS IFU 1-slit, B600 mode was used for both targets, and the spectral resolution was ∼100 km s^{-1} FWHM at 4610 Å. The field of view of this GMOS setup is 3.5″×5″. The details of the observations are summarized in Table 4.2.

We measured the point spread function (PSF) of the IFS data by fitting single 2-D Gaussian profiles to bright stars in the acquisition images of each target. The mean values of the measured FWHM (0.60″ for J0906+56 and 0.55″ for J0842+03) were used as the empirical Gaussian

Table 4.2. Summary of Observations

Name	Telescope/Instrument	Dates	Grating(Slicer)	t_{exp}	PSF	Range	PA	FOV	5-σ detection limit ($\times10^{-17}$)
(1)	(2)	(3)	(4)	(5)	(6)	(7)	(8)	(9)	(10)
J0100−01	Keck/KCWI	2020-01-30	BL(Small)	1200+600	1.2″	3500–5500 Å	51.0	8″×20″	9
J0811+23	Keck/KCWI	2020-01-30	BL(Medium)	4×1200	1.2″	3500–5500 Å	0.0	16″×20″	1
J0840+18	Keck/KCWI	2020-01-30	BL(Medium)	3×1200	1.2″	3500–5500 Å	101.0	16″×20″	1
J0842+03	Gemini/GMOS	2019-04-28,29	B600	8×1125	0.55″	3750–7070 Å	122.0	3.5″×5″	1
J0842+03	Keck/KCWI	2020-01-31	BL(Small)	2×1200	0.9″	3500–5500 Å	290.0	8″×20″	1
J0906+56	Gemini/GMOS	2019-04-04,05	B600	8×1155	0.6″	3880–7200 Å[a]	273.0	3.5″×5″	3
J0906+56	Keck/KCWI	2020-01-31	BL(Small)	2×1200+280	0.9″	3500–5500 Å	0.0	8″×20″	2
J0954+47	Keck/KCWI	2020-01-30	BL(Small)	5×1200	1.2″	3500–5500 Å	0.0	8″×20″	2
J1005+12	Keck/KCWI	2020-01-30	BL(Small)	6×600	1.2″	3500–5500 Å	60.0	8″×20″	3
J1009+26	Keck/KCWI	2020-01-30	BL(Small)	7×600	1.2″	3500–5500 Å	45.5	8″×20″	5

Note. — Column (1): Short name of the target; Column (2): Telescope and instrument used for the observations; Column (3): Date of the observation; Column (4): Grating adopted in the observation, slicer configuration adopted for the corresponding KCWI observation is also shown in the bracket; Column (5): Exposure time of the observation in seconds; Column (6): FWHM of the PSF measured from the acquisition image (GMOS data) or IFU observation of the spectrophotometric standard star (KCWI data); Column (7): Spectral coverage of the data set; Column (8): Position angle of the IFU in degrees measured East of North; Column (9): Full field of view of the IFU. (10): 5-σ detection limit for a [O III] λ5007 emission line with FWHM of 1000 km s^{-1}, in units of erg cm^{-2} s^{-1} $arcsec^{-2}$. The typical uncertainty of the listed values is ∼30%

[a] The data with wavelength shorter than 5000 Å were discarded in the analysis due to the low S/N.

PSF for the IFS data. Whether these PSF are a good approximation for our analysis can be checked by comparing the PSF of the acquisition images of the standard stars with those of the IFS frames on the stars themselves. We find that the former is more extended than the latter, i.e., the average FWHM of the PSF for the acquisition images is $\sim$90% larger than that of the IFS frames in arcseconds, although the former is only $\sim$15% larger than the latter in unit of image pixel size. This suggests that the FWHM of the PSF determined from the acquisition images overestimate those of the science observations. Thus, the use of PSF measurements derived from the acquisition images in our analysis conservatively overestimates the true size of the PSF in the IFS observations on our targets.

4.2.2.2 KCWI Data

All targets were observed with KCWI [Morrissey et al., 2018] through Keck program 2019-U217 (PI G. Canalizo) on 2020-01-31 and 2020-02-01. All targets were observed with BL grating. J0811+23 and J0840+18 were observed with the medium-slicer setup (spectral resolution $\sim$160 km s^{-1} FWHM at 4550 Å), while the others were observed with the small-slicer setup (spectral resolution $\sim$80 km s^{-1} FWHM at 4550 Å). The details of the observations are summarized in Table 4.2.

We measured the PSF of these IFU observations from the observations of spectrophotometric standard stars taken before, in between, and after the on-target observations, where single 2-D Gaussian profiles were fit to the narrow-band images (5000–5100 Å) of those standard stars reconstructed from the data cubes. For one of the targets, J0842+03, a nearby bright star fell in the field-of-view and was thus observed simultaneously with the target in one science exposure. The same 2-D Gaussian fit was applied to it and the results were compared with other PSF measurements. For each night, all individual measurements of the PSF described above broadly agree with each other, and the median FWHM of these best-fit Gaussian profiles were adopted as the FWHM of the PSF for further analysis. Notice that we do not have measurements for the PSF taken at the same time of the on-target science observations, therefore, the variations in the size of the actual PSF may be larger. This speculation is based on the variation of the DIMM seeing measured by the Mauna Kea Weather Center[2], which ranges from $0.4''$ to $0.8''$ throughout the two observation nights.

4.2.3 Data Reduction

4.2.3.1 GMOS Data

Both GMOS data sets were reduced with the standard Gemini Pyraf package (v1.14), supplemented by scripts from IFSRED library [Rupke, 2014b]. We followed the standard processes listed in the GMOS data reduction manual, except that we did not apply scattered light removal for the science frames. This was based on the fact that i) there was no clear features indicative of scattered light in the raw data and ii) the attempt to apply scattered light removal led to significant and unphysical wiggles in the extracted spectra.

The final data cubes were generated by combining individual exposures of each target using script IFSR_MOSAIC from the IFSRED library. The wavelength solutions were further verified by checking the sky emission lines (mainly [O I] $\lambda5577$, and also weaker [O I] $\lambda6300$ and [O I] $\lambda6364$). For J0906+56, the differences between the measured line centers of the sky emission

[2] `http://mkwc.ifa.hawaii.edu/current/seeing/index.cgi`

and the reference values are between -10 km s^{-1} and 10 km s^{-1}. The differences are randomly distributed across the data cube and no pattern is seen. Therefore, no further correction was applied to the wavelength calibration.

However, for target J0842+03, shifts of up to $\sim$5 Å between the measured and reference line centers of the sky line [O I] λ5577 were seen. The arc exposure for this target was taken eleven days after the science observations, perhaps explaining these large shifts. Additional corrections were applied to modify the wavelength solutions: i) For each exposure, the zero-point shifts of the spectra were corrected using the sky emission [O I] λ5577; ii) for the final combined data cube, small ($\lesssim$ 0.8 Å), wavelength dependent shifts in the wavelength solution were further corrected by adding shifts $\Delta(\lambda)$, where $\Delta(\lambda/\text{Å}) = 0.0016(\lambda/\text{Å}) - 9.06$ is the best-fit linear fit to the shifts between the measured line centers and the expected ones calculated from the emission-line redshift determined from the Keck/LRIS spectrum (Manzano-King, private communication). The strong optical emission lines [O III] λ5007, Hα, [N II] $\lambda\lambda$6548, 6583, and [S II] $\lambda\lambda$6716, 6731 were included in the fit. We further required that $\Delta(\lambda_{[O\ I]\lambda5577}/\text{Å})$ = 0, i.e., zero shifts at the wavelength of sky emission line [O I] λ5577. The residuals of the best-fit are $\lesssim$ 0.15 Å in general.

4.2.3.2 KCWI Data

The KCWI data sets were reduced with the KCWI data reduction pipeline and the IFSRED library. We followed the standard processes listed in the KCWI data reduction manual[3] for all targets. The data cubes generated from individual exposures were resampled to

[3] https://github.com/Keck-DataReductionPipelines/KcwiDRP/blob/master/AAAREADME

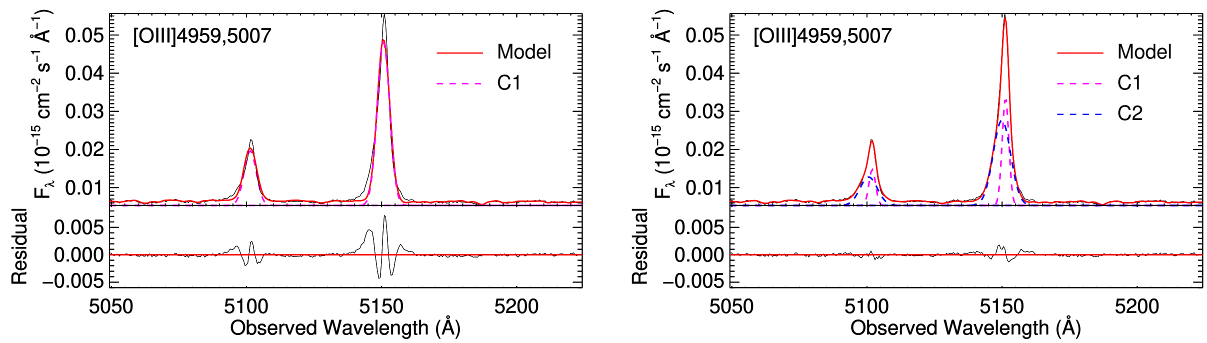

Figure 4.1: Examples of fits to the [O III] $\lambda\lambda$4959, 5007 line profiles for J0842+03 using (left panel) one Gaussian component and (right panel) two Gaussian components. In each panel, the top spectrum in black is the observed data, while the solid red curve is the best fit model and the dashed curves represent the individual Gaussian components (C1, C2). The residuals after subtraction of the best-fit models from the data are shown in solid black curve at the bottom, and the y=0 line is shown in red.

$0.15'' \times 0.15''$ (small-slicer setup) or $0.29'' \times 0.29''$ square spaxels (medium-slicer setup) using IFSR_KCWIRESAMPLE. The resampled data cubes of the same target were then combined into a single data cube using IFSR_MOSAIC.

4.3 Analysis

4.3.1 Voronoi Binning

The data cubes were mildly, spatially binned using the Voronoi binning method [Cappellari and Copin, 2003]. As our aim is to characterize the broad, blueshifted components in the emission lines (especially [O III] λ5007) which trace the outflows, we binned the data cube according to the signal-to-noise ratio (S/N) of the blue wing of the [O III] λ5007 emission line (calculated in the target-specific, 200 km s^{-1}-wide velocity window). The spaxels with S/N of the blue wing less than 1 were excluded from the binning, and each final spatial bin was required to reach a minimum S/N of 3.

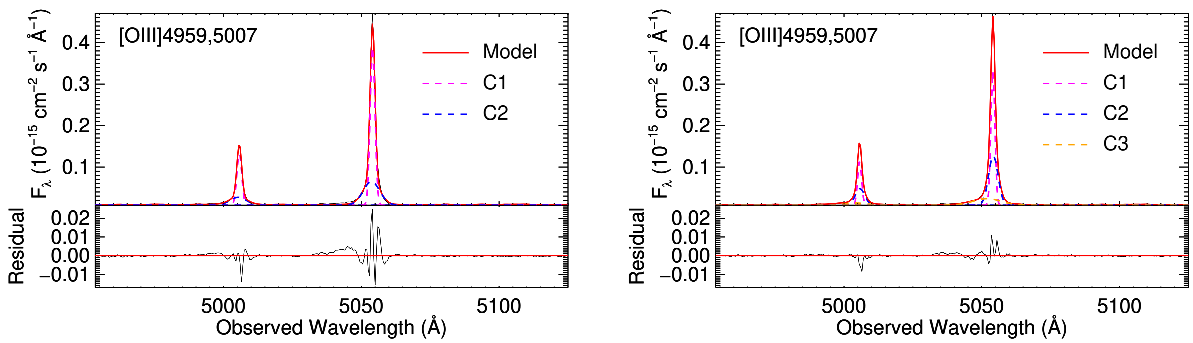

Figure 4.2: Examples of fits to the [O III] $\lambda\lambda$4959, 5007 line profiles for J1005+12 using (left panel) two Gaussian components and (right panel) three Gaussian components. The presentation of the data, fits, and residuals is the same as in Fig. 4.1.

4.3.2 Spectral Fits

The spectral fits utilized IDL library IFSFIT [Rupke, 2014a], supplemented by customized python scripts.

4.3.2.1 Fits to the [O III] $\lambda\lambda$4959, 5007 Emission

The [O III] $\lambda\lambda$4959, 5007 line emission from our targets shows the strongest blueshifted wings among all of the emission line tracers of the ionized outflow. In addition, the absence of other strong emission and absorption features in the vicinity of [O III] $\lambda\lambda$4959, 5007 makes the faint [O III] wing components easier to analyze. In order to capture the faintest signal from the outflows traced by those faint emission line wing, we started by solely fitting the [O III] $\lambda\lambda$4959, 5007 line emission. With the emission lines masked out, the stellar continuum was fit using the public software pPXF [Cappellari, 2017] with 0.5$\times$ solar metallicity stellar population synthesis (SPS) models from González Delgado et al. [2005]. Polynomials of order up to 4 were added to account for any non-stellar continua.

The continuum-subtracted [O III] $\lambda\lambda$4959, 5007 emission lines were then fitted with multiple Gaussian components using the IDL library MPFIT [Markwardt, 2012]. The line centers and line widths of the corresponding Gaussian components of both lines were tied together, and only the amplitudes were allowed to change freely. We did not fix the relative amplitude ratios of the doublet so that a fit was allowed when a Gaussian component was only detected in [O III] λ5007 but not in [O III] λ4959. We checked the flux ratios of the doublet from the best-fit results afterwards when applicable and found that they were very close to the theoretical expectation (within 2%). We allowed a maximum of three Gaussian components in the fits, and the required number of components in each spaxel was determined by a combination of software automation and visual inspection: An additional component was added to the best-fit model when 1) it was broader than the spectral resolution; 2) it had a S/N > 2; 3) it was not too broad to be robustly distinguished from the continuum (i.e., the peak S/N of individual spectral channel was required to be greater than 1.5 when the line width W_{80} was greater than 800 km s^{-1}). The best-fit parameters from the continuum and emission line fits were adopted as initial parameters for a second fit to check for convergence of the fit.

In order to check how the uncertainties on the fit to the stellar continuum might affect the results on the [O III] $\lambda\lambda$4959, 5007 emission lines, we also tried fitting the continuum with a straight line through the continuum-only windows adjacent to the [O III] $\lambda\lambda$4959, 5007 emission lines. The differences of the best-fit parameters of the [O III] $\lambda\lambda$4959, 5007 emission lines between the two continuum fitting schemes were on average less than 2%, indicating that the best-fit results were not sensitive to the choice of continuum fitting function in most cases.

Examples of the multi-Gaussian fits, using the KCWI spectra of targets J0842+03 and J1005+12, are shown in Figs. 4.1 and 4.2, respectively.

For J0842+03, a model with one Gaussian component cannot fit the spectra well ($\chi_\nu >> 1$). Two Gaussian components, the narrower C1 component, and the broader C2 component, are enough to describe the [O III] $\lambda\lambda$4959, 5007 emission profiles. For J1005+12, neither a model with one Gaussian component nor one with two Gaussian components can fit the [O III] $\lambda\lambda$4959, 5007 profiles well ($\chi_\nu >> 1$ and $\chi_\nu = 3.36$, respectively). Three Gaussian components are needed to properly fit the [O III] $\lambda\lambda$4959, 5007 line emission: the narrowest component (C1), the intermediate-width component (C2) and the broadest component (C3). For the rest of the paper, we name the individual velocity components with the same rule adopted here, i.e., the C1, C2, and C3 components are defined by their increasing line widths.

The results from these fits are discussed in detail in Appendix C.1 and summarized in Section 4.4.

4.3.2.2 Emission Line Fits to the Full Spectral Range

Emission line fits to the full spectral range were also carried out where all of the strong emission lines (Hα, Hβ, [O III] $\lambda\lambda$4959, 5007, [N II] $\lambda\lambda$6548, 6583, [S II] $\lambda\lambda$6716, 6731, and [O I] λ6300 in the GMOS data, Hβ, Hγ, [O II] $\lambda\lambda$3726, 3729, [Ne III] λ3869, and [O III] $\lambda\lambda$4959, 5007 in the KCWI data) were fit simultaneously. The continuum-subtracted spectra obtained from Section 4.3.2.1 were adopted for these fits. Following the routine adopted for the fit of the [O III] $\lambda\lambda$4959, 5007 emission lines alone, all of the emission lines were fitted with multiple Gaussian components, where the line centers and widths of the corresponding Gaussian components for each line were tied together. For each target, the maximum number of Gaussian components used in the fit was determined from the best fits of [O III] $\lambda\lambda$4959, 5007

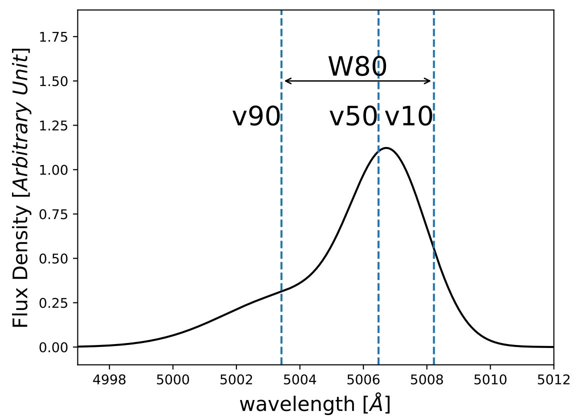

Figure 4.3: Example of a line profile illustrating the various non-parametric kinematic parameters used in this paper. The vertical dashed lines mark the locations of v_{10}, v_{50}, and v_{90} for the mock emission line profile shown in the figure. W_{80} is the line width between v_{90} and v_{10}.

emission described in Section 4.3.2.1. Based on the best-fit results obtained above, we did not detect additional, distinct broad hydrogen Balmer line emission that can be attributed to a genuine broad-line-region (BLR) in any of the eight targets.

4.3.3 Non-Parametric Measurements of the Emission Line Profiles

Non-parametric line profile measurements were utilized to describe the gas kinematics for both the individual Gaussian components and the overall line profiles. The details are described below, and an example is shown in Fig. 4.3.

i. v_{10} and v_{90} are the velocities at the 10th and 90th percentiles of the total flux, respectively, calculated starting from the red side of the line.

ii. W_{80} is the line width defined to encompass 80 percent of the total flux such that W_{80}=$v_{10}-$ v_{90}.

iii. v_{50} is the median velocity, the velocity at the 50th percentile of the total flux.

4.3.4 AGN Luminosities

The bolometric AGN luminosities (L_{AGN}) of our targets were calculated from the extinction-corrected [O III] λ5007 luminosities integrated over the entire IFS data cubes ($L_{[O\ III]}$) [4]. The extinction correction was determined from the Balmer decrement based on the spatially-integrated spectrum, assuming an intrinsic Hα/Hβ ratio of 2.87[5] for the GMOS data, or an intrinsic Hβ/Hγ ratio of 2.13 for the KCWI data [Case B, T=10^4 K; Osterbrock and Ferland, 2006] and the Cardelli et al. [1989b] extinction curve with $R_V = 3.1$. For J0100−01 and J0811+23, where Hγ is too weak to be measured robustly, the Balmer decrement was determined from the Hα/Hβ ratio measured from the SDSS spectra. We adopted the empirical bolometric correction factors in Lamastra et al. [2009]: L_{AGN}= 142 $L_{[O\ III]}$ and L_{AGN}= 87 $L_{[O\ III]}$ for $40 < \log(L_{[O\ III]}) < 42$ and $38 < \log(L_{[O\ III]}) < 40$ in cgs units, respectively. Note that the AGN luminosities calculated here may be affected by relatively large systematic errors since the intrinsic Balmer line ratio, the shape of the extinction curve, and the $L_{[O\ III]}$ to L_{AGN} correction factor in systems like our targets are uncertain. The observed $L_{[O\ III]}$ and derived L_{AGN} are summarized in Table 5.1.

[4] Based on the [O II]/[O III] vs [O III]/Hβ diagrams drawn from the KCWI data, at least ∼90% of the spaxels show AGN-like line ratios in each target. Consistently, all of our targets show AGN-like line ratios in the BPT and VO87 diagrams based on the Keck/LRIS spectra extracted from the central 1″ box regions. Moreover, for targets J0842+03 and J0906+56 where the BPT and VO87 diagrams can be derived from the GMOS IFU data, we find that the spaxels with AGN-like line ratios contribute at least ∼95% of the [O III] flux. Overall, the [O III] luminosities integrated over the entire data cubes are thus at most slight overestimates of the [O III] luminosities originating from the AGN.

[5] While studies have shown that the intrinsic Hα/Hβ ratio of AGN is 3.1 [Osterbrock and Ferland, 2006], we adopt the value 2.87 since (1) the intrinsic Balmer line ratios of AGN in these dwarf galaxies are poorly constrained due to a lack of dedicated studies; (2) in Section 4.5.3, we will compare our results of outflow energetics with those from some previous studies [e.g. Harrison et al., 2014, Rupke et al., 2017] where they adopted the value 2.87. Nevertheless, if we adopt instead an intrinsic Hα/Hβ value of 3.1 in our calculations, the derived AGN luminoisity will only decrease by ∼0.1 dex for our targets.

4.3.5 Upper Limits on the Star Formation Rates

Robust star formation rate (SFR) measurements of our targets cannot be obtained due to the lack of sensitive far-infrared data. None of the targets is detected in IRAS and AKARI all sky survey. An order-of-magnitude estimate of SFR for our targets can be derived by dividing the stellar mass with the Hubble time, assuming a constant star formation rate. For a stellar mass of log($M_{\rm stellar}$/M$_\odot$) $= 9.5$, this gives a SFR on the order of 0.2 M$_\odot$ yr^{-1}, an order of magnitude lower than the upper limits derived from the far-infrared data.

Star formation rates may also be estimated from [O II] $\lambda\lambda$3726, 3729 luminosities (L$_{[O\ II]}$) in AGN [e.g. Ho, 2005]. The derived SFR are in principle upper limits on the intrinsic SFR since the AGN contributes to the [O II] $\lambda\lambda$3726, 3729 fluxes. Adopting equation (10) in Kewley et al. [2004], we follow the same recipe in Ho [2005], where 1/3 of the [O II] emission comes from the star formation activity. The L$_{[O\ II]}$ was measured from the spatially-integrated KCWI spectra, and was corrected for extinction in the same way as that for L$_{[O\ III]}$. The gas-phase metallicity of the targets adopted in the calculations above were assumed to be solar (This is based on our ionization diagnosis in Section 4.4.3. Given that the [O II] $\lambda\lambda$3726, 3729 flux is dominated by the nuclear region and contaminated by AGN emission, a metallicity higher than the prediction from the stellar mass–metallicity relation is not surprising). These results are summarized in Table 5.1. Instead, if we use 0.5 $\times$ solar (LMC-like) metallicity [e.g. Garnett, 1999] in the calculations, the upper limits on SFR will be $\sim$20% lower. Therefore, the upper limits recorded in Table 5.1 are conservatively high.

To assess the upper limits on SFR derived above, we have also compared them to the median SFR listed in the MPA-JHU DR7 catalog based on SDSS data [Brinchmann et al., 2004].

One possible caveat of the SFR from MPA-JHU DR7 catalog is that they misclassify 6 out of the 8 targets studied here as starburst/star-forming galaxies. Therefore, for these 6 targets, there could be significant systematic errors in the SFR listed in the catalog. Moreover, even for the two targets classified as AGN (J0811+23 and J1005+12), the treatment of AGN contamination to the SFR measurements might still introduce certain systematic errors to the SFR. Nevertheless, from the comparison we find that (a) the median SFR measured within the SDSS fibers in the MPA-JHU catalog are all below our [O II]-based upper limits except for J0811+23 (SFR $\simeq$ 0.02 $M_\odot$ yr^{-1} from fiber SFR in catalog vs SFR $<$ 0.01 $M_\odot$ yr^{-1} from our [O II] data); (b) Even if we consider the total SFR (corrected for fiber loss) listed in the MPA-JHU catalog, only three targets show clearly higher SFR in the catalog than our [O II]-based upper limits (the largest difference is seen for J0906+56: total SFR $\simeq$ 0.74 $M_\odot$ yr^{-1} in the catalog vs SFR $<$ 0.3 $M_\odot$ yr^{-1} from our data), while the SFR of J0842+03 in the catalog is only 1/10 of the upper limit measured from our [O II] data. These differences are likely caused by the fact that the AGN emission in these targets are not modelled properly in the MPA-JHU catalog. In general, our [O II]-based upper limits are not systematically lower than the values from MPA-JHU catalog.

4.4 Outflows Detected in the Sample

The main results from our analysis of the IFS data are summarized in this section. The target-specific maps of the [O III] λ5007 flux and kinematics, globally and for each velocity component, the stellar kinematics, and the radial profiles of the fluxes from individual velocity components are discussed in Appendix C.1 (Fig. C.1–C.28). In addition, line ratio maps and the spatially resolved BPT and VO87 diagrams are shown for J0842+03 (Fig. C.13 and C.14) and J0906+56 (Fig. C.18 and C.19). In all cases, the systematic velocities of our targets are determined from the stellar velocities measured from the spectra integrated over the whole KCWI data cubes.

Table 4.3. Kinematic Properties of the Targets

Name (1)	N_{comp} (2)	Component (3)	Data Set (4)	Median v_{50} [km s^{-1}] (5)	Min v_{50} [km s^{-1}] (6)	Max v_{50} [km s^{-1}] (7)	Median W_{80} [km s^{-1}] (8)	Max W_{80} [km s^{-1}] (9)	v_{50}, int. [km s^{-1}] (10)	W_{80}, int. [km s^{-1}] (11)
J0100−01	2	C1	KCWI	−20	−60	0	120	210	...	...
		C2	KCWI	−40	−240	50	310	650	...	...
		Total	KCWI	−20	−130	0	220	440	−20	150
J0811+23	1	C1	KCWI	−40	−60	−20	140	220	−40	150
J0840+18	1	C1	KCWI	−10	−30	20	50	130	−10	50
J0842+03	2	C1	GMOS	−80	−110	−20	130	250	...	...
		C2	GMOS	−160	−220	−110	500	650	...	...
		Total	GMOS	−110	−150	−80	400	520	−120	420
		C1	KCWI	−30	−60	10	150	220	...	...
		C2	KCWI	−110	−160	−40	500	750	...	...
		Total	KCWI	−70	−110	−20	400	700	−60	320
J0906+56	3	C1	GMOS	−10	−30	30	30[a]	30[a]	...	...

Table 4.3 (cont'd)

Name	N$_{comp}$	Component	Data Set	Median v_{50} [km s^{-1}]	Min v_{50} [km s^{-1}]	Max v_{50} [km s^{-1}]	Median W_{80} [km s^{-1}]	Max W_{80} [km s^{-1}]	v_{50}, int. [km s^{-1}]	W_{80}, int. [km s^{-1}]
(1)	(2)	(3)	(4)	(5)	(6)	(7)	(8)	(9)	(10)	(11)
		C2	GMOS	30	−10	60	350	410	...	...
		C3	GMOS	−50	−100	40	920	1200	...	...
		Total	GMOS	0	−20	20	550	650	10	570
		C1	KCWI	−10	−50	50	110	140	...	...
		C2	KCWI	60	30	90	430	680	...	...
		C3	KCWI	−70	−150	10	980	1250	...	...
		Total	KCWI	10	−50	50	520	670	20	420
J0954+47	3	C1	KCWI	10	0	20	70	100	...	...
		C2	KCWI	0	−70	20	260	430	...	...
		C3	KCWI	−60	−80	0	730	1100	...	...
		Total	KCWI	0	−10	10	240	530	0	220
J1005+12	3	C1	KCWI	−20	−40	10	80	120	...	...
		C2	KCWI	−30	−100	50	440	710	...	...
		C3	KCWI	−140	−200	−60	730	1200	...	...

4.4.1 Gas Kinematics across Our Sample

The gas kinematic properties of the galaxies in our sample are summarized in Table 4.3. This includes basic statistics (min, max, median) on v_{50} and W_{80} for individual velocity components and the entire [O III] λ5007 line emission across the data cubes, as well as measurements of v_{50} and W_{80} from the spatially-integrated spectra.

Overall, we find that the number of velocity components needed to adequately fit the emission line profiles in our targets ranges from three for J0906+56, J0954+47, and J1005+12, two for J0100−01, J0842+03, and J1009+26, and one for targets J0811+23 and J0840+18.

The kinematic properties of the C3 components in J0906+56, J0954+47, and J1005+12, and the C2 components in J0100−01 and J0842+03, show strong evidence for outflows since they are very broad and/or significantly blueshifted with respect to the stellar velocity field derived from the same data (Their names are shown in black and marked with asterisks in Fig. 4.4 and 4.5. The kinematic properties of the C2 components in J0906+56, J0954+47, and J1005+12, as well as the C1 component in J0842+03 also suggest that they are at least part of, or affected by, the outflows in these systems. In addition, given the peculiar kinematics of the C2 component in J1009+26 and C1 component in J0811+23 relative to that of the stellar component, we argue in Appendix11 C.1 that they also likely represent outflowing gas in these objects (These last two groups of velocity components have relatively more ambiguous origins than the first group, so their names are shown in red in Fig. 4.4 and 4.5 to distinguish them from the first group. In the following discussion, we associate all of these velocity components with the outflows in these seven objects, and will refer to them as outflow components by default. In the end, only J0840+18 does not show any sign of outflowing gas in our IFS data, so it is omitted from the

Table 4.3 (cont'd)

Name	N_{comp}	Component	Data Set	Median v_{50} [km s^{-1}]	Min v_{50} [km s^{-1}]	Max v_{50} [km s^{-1}]	Median W_{80} [km s^{-1}]	Max W_{80} [km s^{-1}]	v_{50}, int. [km s^{-1}]	W_{80}, int. [km s^{-1}]
(1)	(2)	(3)	(4)	(5)	(6)	(7)	(8)	(9)	(10)	(11)
		Total	KCWI	−30	−60	10	300	680	−30	260
J1009+26	2	C1	KCWI	−10	−30	0	80	100	...	...
		C2	KCWI	−20	−60	40	210	480	...	...
		Total	KCWI	−10	−50	10	90	150	−20	90

Note. — Column (1): Short name of the target; Column (2): Number of velocity components required by the best-fit results from Section 4.3.2; (3): Individual velocity components (C1,C2,C3) and overall emission line profiles (Total) from the best fits; Column (4): Instrument used for the observations; Columns (5)-(7): Median, minimum and maximum values of v_{50} measured across the whole data cube. The spaxels with the highest and lowest 5% of v_{50} are excluded in the calculations. The values listed are rounded to the nearest 10 km s^{-1}; Columns (8)–(9): Median and maximum values of W_{80} measured across the whole data cube. The spaxels with the highest and lowest 5% of W_{80} are excluded in the calculations. The values listed are rounded to the nearest 10 km s^{-1}; Columns (10)–(11): v_{50} and W_{80} of the overall emission line profiles from the spatially-integrated spectra of the whole data cubes. The values listed are rounded to the nearest 10 km s^{-1}.

[a]Compared with the KCWI data, the GMOS data has a poorer spectral resolution (FWHM $\simeq$ 100 km s^{-1} vs 80 km s^{-1}) and a shallower depth (see Table 4.2). The significantly smaller line width of C1 component measured in the GMOS data is thus most likely due to that the decomposition of the emission line profile is less constrained in the GMOS data. Therefore, for this target, we adopt the KCWI-based line width measurements of the C1 components as the fiducial values in our analysis instead.

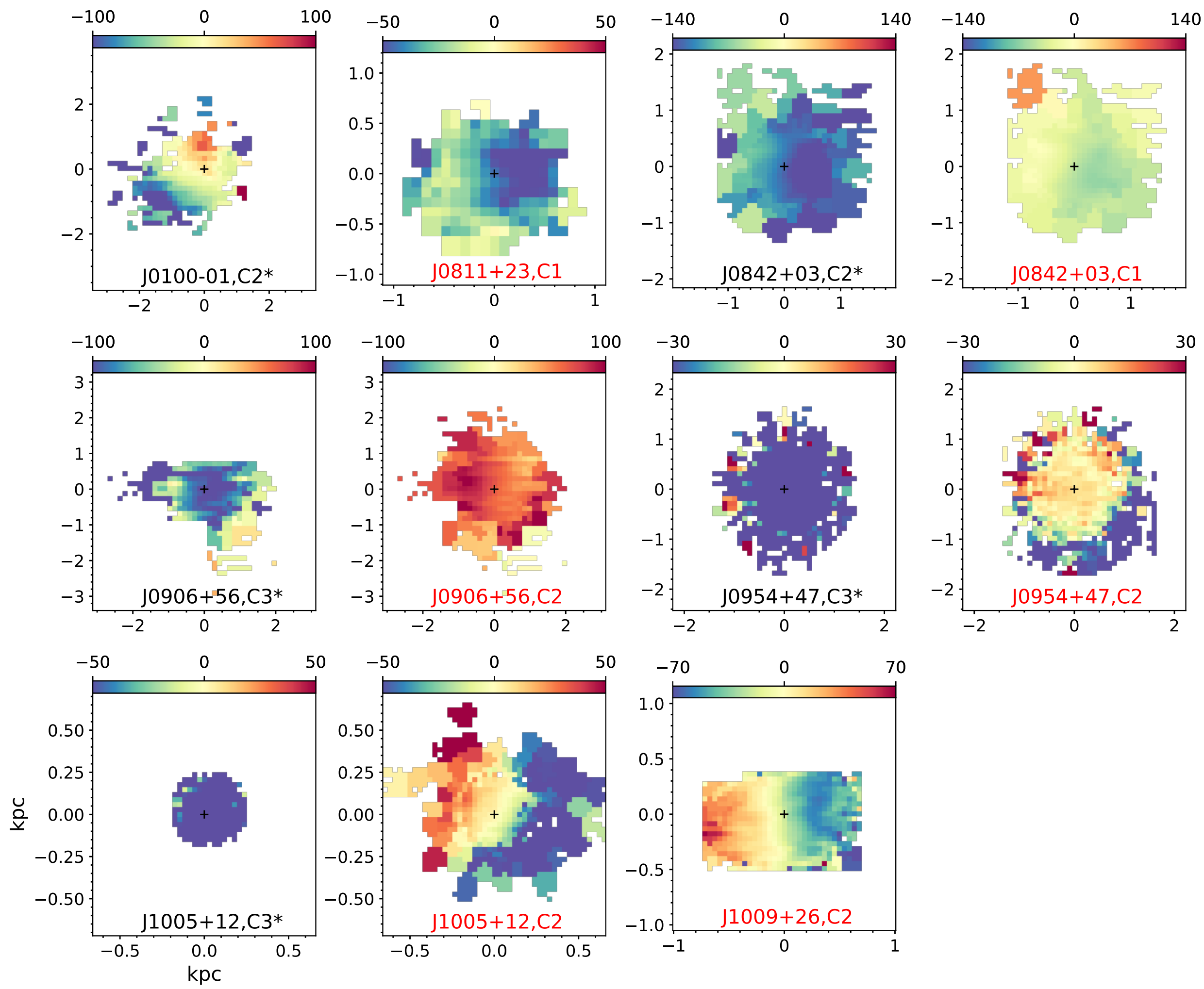

Figure 4.4: Median velocity (v_{50}) maps (in units of km s^{-1}) for the velocity components of [O III] λ5007 emission showing evidence of outflows in the seven targets with detected outflows. An overview of these outflow components is presented in Section 4.1 and the detailed analyses of these components in individual targets are presented in Appendix C.1. The name of the target and the corresponding velocity component is noted at the bottom of each panel: The components showing strong evidence for outflows are labelled in black and marked with asterisks, whereas those with relatively more uncertain origins are labelled in red, as stated in Section 4.4.1 and discussed in detail in the Appendix C.1. The color scale of each panel is set to be the same as that of the corresponding target-specific map in Appendix C.1, except for those of the C2 and C1 components of J0842+03, where the color scales are centered on 0 km s^{-1} instead. The black cross in each panel denotes the spaxel where the peak of the total [O III] λ5007 emission line flux falls.

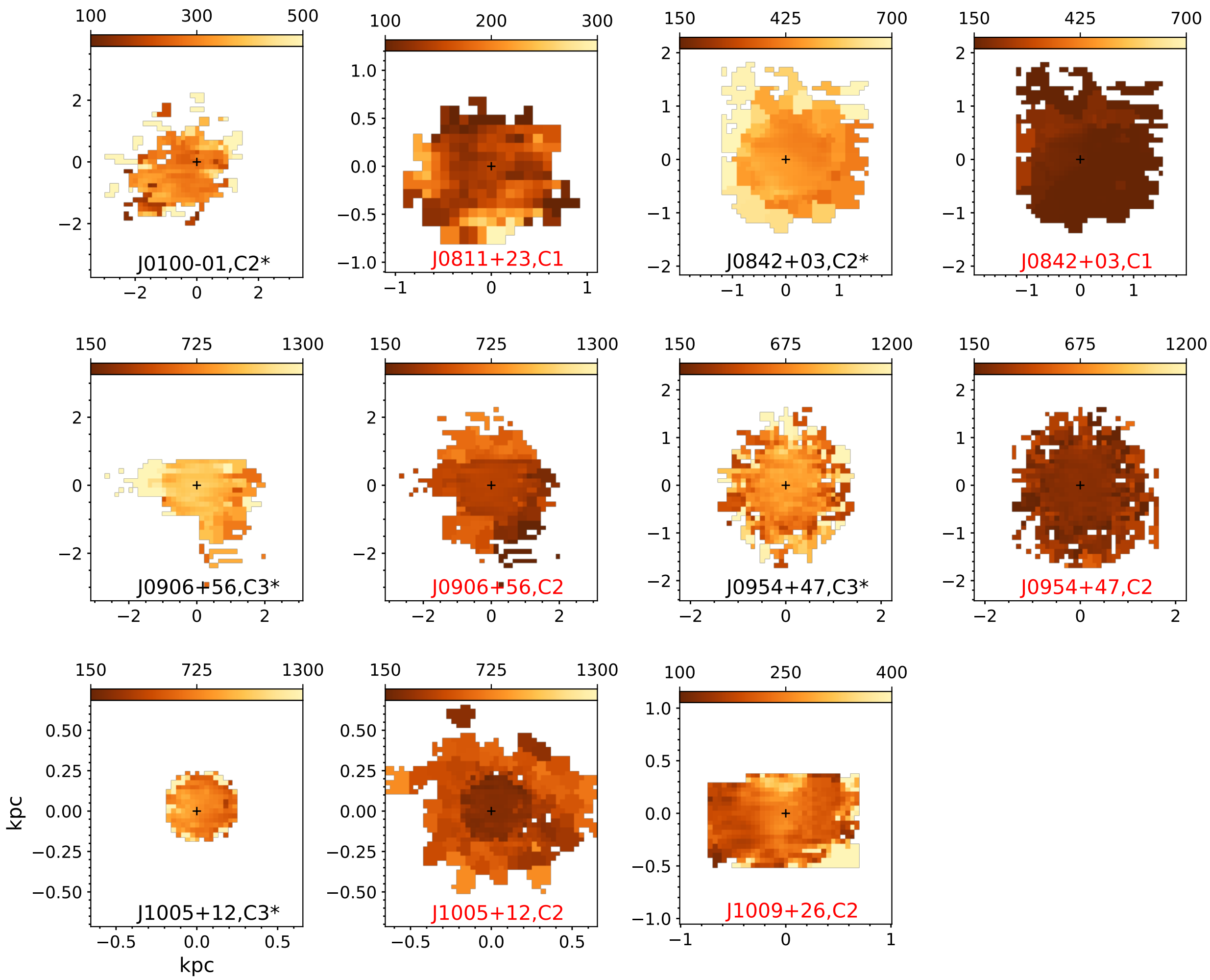

Figure 4.5: Same as Fig. 4.4 but for line width W_{80} (in units of km s^{-1}).

following discussion of the outflows, except when mentioned explicitly.

The kinematic properties of the outflows in these seven targets span a relatively large range in terms of line width and median velocities. Quantitatively, the maxima of W_{80} range from $\sim$220 km s^{-1} to $\sim$1200 km s^{-1}, and the minima of v_{50} range from $\sim$30 km s^{-1} to ~ -240 km s^{-1} based on our IFU data. The apparent morphology of these outflow-tracing components are in general symmetric with respect to the galaxy center, except for J0100$-$01 and J1009+26, which show biconical morphology in projection. In addition, significant non-radial velocity gradients/structures are also seen for the outflow components of targets J0811+23 and J0842+03, as well as the C2 components of targets J0954+47 and J1005+12. (see Fig. 4.4 and 4.5 for snapshots of the v_{50} and W_{80} maps of these components; see Appendix C.1 for additional target-specific flux and kinematic maps).

4.4.2 Spatial Extents of the Outflows

A key question is whether the outflows detected in our targets are extended on galactic scale. As shown in Fig. C.1–C.28 of Appendix C.1 and discussed in this Appendix, the analysis of the IFS data has revealed spatially resolved structures in the velocity fields of the outflow components, as well as excess flux relative to the PSF, in J0100$-$01, J0811+23, J0842+03, and J1009+26, strongly suggesting that the outflows in these galaxies are spatially resolved. Similarly, the C2 components in J0906+56, J0954+47, and J1005+12, and the C1 component in J0842+03 are also probably spatially resolved. However, the results of our analysis are inconclusive for the C3 components of J0906+56, J0954+47, and J1005+12.

An independent constraint on the spatial extent of the outflow components in J0906+56, J0954+47, and J1005+12 may be derived from a more formal deconvolution of the data cubes. For this, we follow a procedure explained in detail below, which is a simplified version of the deconvolution scheme introduced in Rupke et al. [2017]. First, we assume that the flux in the spaxel with the peak emission line flux (a $0.2'' \times 0.2''$ box for the GMOS data and a $0.15'' \times 0.15''$ one for the KCWI data) is dominated by AGN emission. The spectrum from this spaxel is treated as an AGN emission template from a point source. Next, we fit each spaxel n with this AGN template + smooth exponential continuum functions + host emission lines, according to:

$$I^n_{total} = C_{AGN} I^n_{AGN} + I^n_{exp,continuum} + I^n_{emission} \tag{4.1}$$

The scaling factor C_{AGN} for the AGN emission template and the exponential continuum functions in the equation are each the sum of four exponentials, so eq. (1) can be re-written as:

$$I^n_{total} = \sum_{i=1}^{4} I^n_i I^n_{AGN} + \sum_{j=1}^{4} I_j + I^n_{emission} \tag{4.2}$$

and the four exponentials are :

$$I^n_1 = a^n_1 e^{-b^n_1 <\lambda>} \tag{4.3}$$

$$I^n_2 = a^n_2 e^{-b^n_2 (1-<\lambda>)} \tag{4.4}$$

$$I_3^n = a_3^n(1 - e^{-b_3^n <\lambda>}) \tag{4.5}$$

$$I_4^n = a_4^n(1 - e^{-b_4^n(1-<\lambda>)}), \tag{4.6}$$

where $a_i^n \geq 0$; $b_i^n \geq 0$; $<\lambda>=\frac{\lambda-\lambda_{min}}{\lambda_{max}-\lambda_{min}}$; and $[\lambda_{min}, \lambda_{max}]$ is the fit range. These exponentials are adopted because they are monotonic and are positive-definite. The four exponentials allow for all combinations of concave/convex and monotonically increasing/decreasing. We have not used stellar templates in the fits above, since the stellar absorption features are not strong enough in individual spaxels to constrain the extra free parameters and the fits become divergent.

The host emission lines are modeled with a maximum of two Gaussian components. The fits are iterative. In step 1), the cores of the emission lines are masked and the continuum is fit with the AGN template + exponential continuum terms. In step 2), the best-fit model from step 1) is subtracted from the original spectrum, and the emission lines are fit. In 3), the best-fit emission line models are used to determine a better emission line mask window in the continuum fit, and then steps 1) through 3) are repeated until the best-fit results are stable.

The results of this analysis on J0906+56, J0954+47, and J1005+12 indicate 1) clear evidence for spatially extended narrow line emission originating on the scale of the host galaxy in all three targets; 2) blueshifted, broad line emission with a S/N of ~3–8 tracing the outflows in the host galaxy in the spatially-stacked spectra for all three targets. The line widths of these components fall in between those of the C3 and C2 components in these targets; 3) but inconclusive (S/N $\lesssim$ 2 in general) evidence for spatially resolved line emission from the outflow components. The same analysis conducted on the other four targets confirms the presence of spatially resolved, blueshifted and/or redshifted velocity components from the host galaxy, corresponding to the outflow components detected in our more detailed kinematic analysis (Appendix C.1).

Before concluding this section, it is important to repeat that the PSF deconvolution scheme described here relies on the assumption that the spectra used as AGN templates for these targets are indeed pure AGN emission (and thus from an unresolved point source). While the line ratios measured from these spectra fall in the AGN region in the BPT/VO87 diagrams (for the GMOS data of J0906+56) or the [O II]/[O III] vs [O III]/Hβ diagram (for the KCWI data), there are reasons to believe that emission from the host galaxies themselves still contributes significantly to the spectra. First and foremost, weak to moderate (S/N $\simeq$ 2–9) Mg I*b* absorption features of stellar origin are detected in these spectra. In addition, we carried out a separate, power-law continuum + stellar templates fit to the continuum emission of these spectra (in the ranges of $\sim$5000–7000 Å for the GMOS data, and $\sim$3600–5500 Å for the KCWI data). An AGN-like power-law continuum component is not formally needed in the best-fit results. Our PSF deconvolution procedure thus almost certainly overestimates (underestimates) the contribution from the unresolved AGN emission (resolved host emission), so the S/N of the spatially resolved outflow emission in J0906+56, J0954+47, and J1005+12 obtained above should therefore be considered conservative lower limits.

4.4.3 Outflow Ionization: AGN or Shocks?

The line ratio maps and spatially resolved BPT and VO87 diagrams for J0842+03 and J0906+56 (Figs. C.13 – C.14 and Figs. C.18 – C.19 in Appendix C.1, respectively) suggest that the outflows in our targets are largely photoionized by the AGN. Here we examine further the

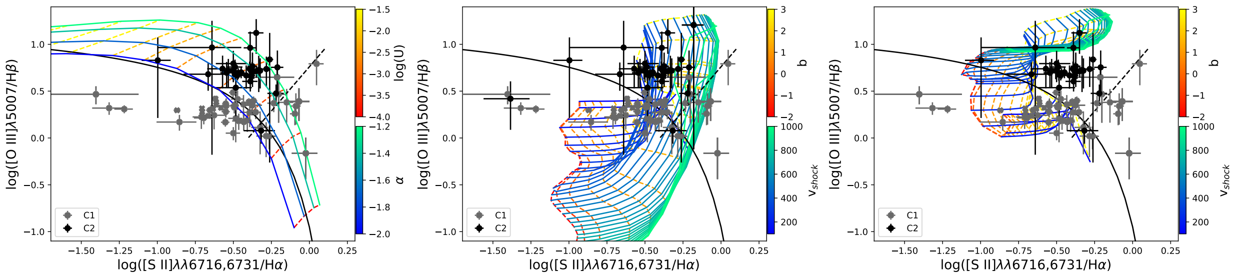

Figure 4.6: [O III]/Hβ vs [S II]/Hα for the C2 (black) and C1 (gray) components of J0842+03, compared with AGN (left), shock (middle) and shock+precursor (right) models. The grids of the AGN models are color-coded by the power-law indices and ionization parameters of the AGN, and those of the shock and shock+precursor models are color-coded by the values of magnetic parameter b and shock velocity v_{shock}. See Section 4.4.3 for more details on these model parameters. In all three panels, the black, solid lines are the theoretical line separating AGN (above right) and star-forming galaxies (below left) from Kewley et al. [2001]. The black, dashed lines are the theoretical line separating the Seyferts (above left) and LINERs (below right) defined in Kewley et al. [2006].

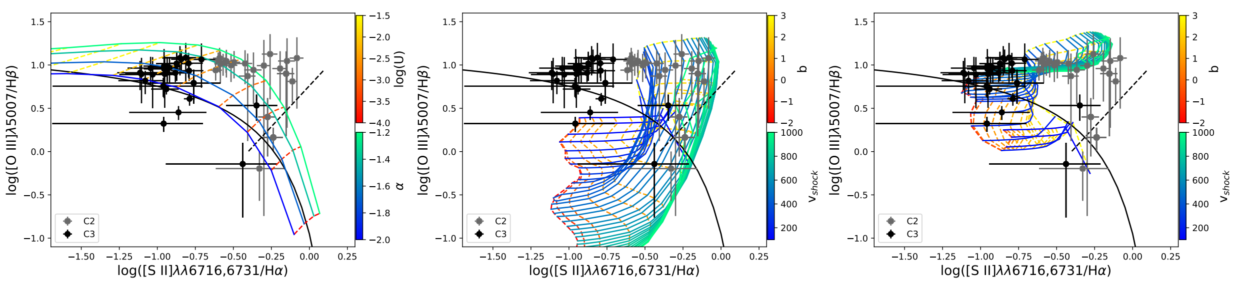

Figure 4.7: Same as Fig. 4.6 but for the C3 (black) and C2 (gray) components of J0906+56.

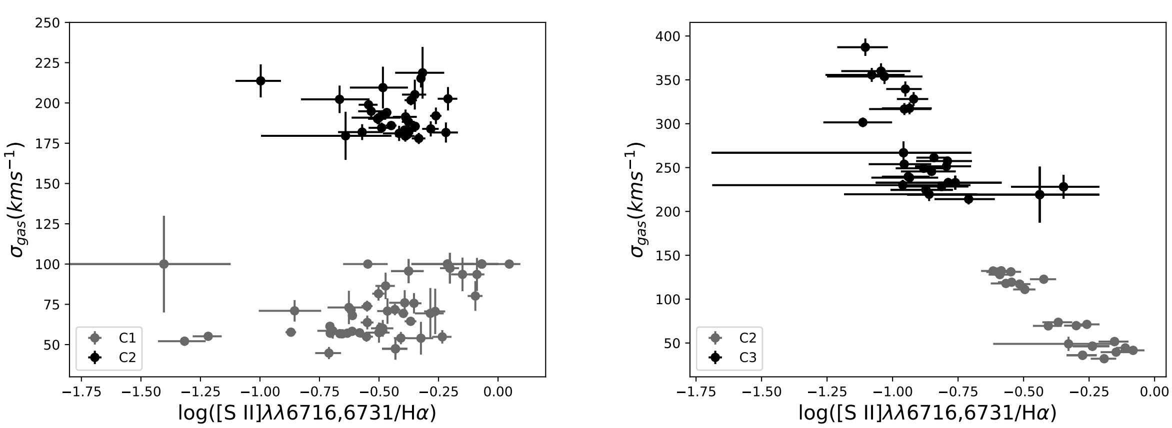

Figure 4.8: [S II]/Hα ratios versus gas velocity dispersions for the outflow components in J0842+03 (top) and J0906+56 (bottom) based on the GMOS data.

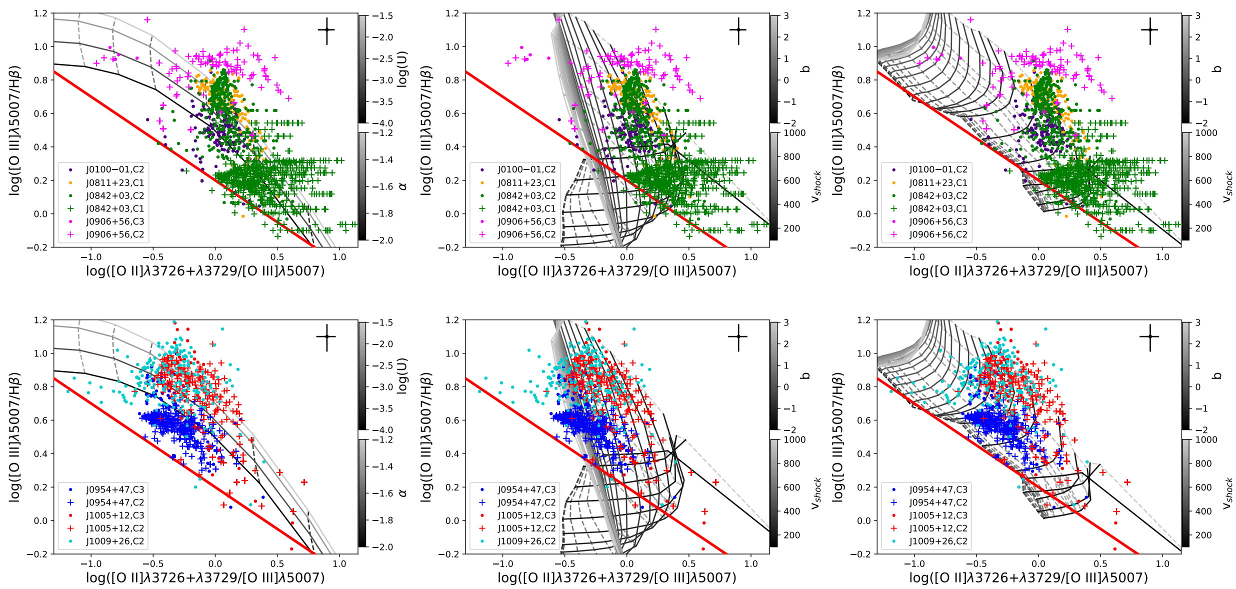

Figure 4.9: [O II]/[O III] vs [O III]/Hβ for the outflow components of all seven targets (1st row: C2 component in J0100−01, C1 component in J0811+23, C2 and C1 components in J0842+03, as well as C3 and C2 components in J0906+56; 2nd row: C3 and C2 components in J0954+47 and J1005+12, as well as C2 component in J1009+26) based on the KCWI data, compared with AGN (left column), shock (middle column) and shock+precursor (right column) models (gray-scale model grids). The median values of the errors of the data points are noted by the black crosses on the top right corners. For the AGN models, the constant power-law indices of the AGN are drawn in solid lines and the constant ionization parameters are drawn in dashed lines. For the shock and shock+precursor models, the constant magnetic parameters b are drawn in dashed lines, and the constant shock velocities v_{shock} are drawn in solid lines. The red, solid lines represent the approximate upper boundary of line ratios that can be generated by star-forming activity, based on the Starburst99 models with continuous star formation history from Levesque et al. [2010]. See Section 4.4.3 for more details on the model parameters.

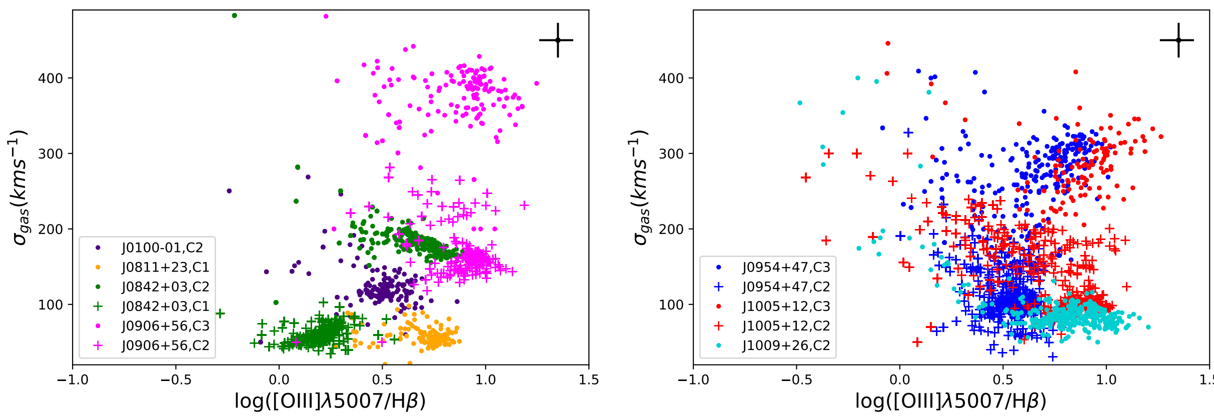

Figure 4.10: [O III]/Hβ ratios versus gas velocity dispersions for the outflowing gas in all seven targets (The results are split into two panels for a better view of the data points) with detected outflows based on the KCWI data. The median values of the errors of the data points are shown as the black crosses in the top-right corners.

evidence that supports this statement. In particular, we examine the possibility that fast shocks caused by the interaction of the outflows with the surrounding ISM may contribute, or even dominate, the heating and ionization of the outflowing gas. Shock excitation is a telltale sign of fast starburst-driven winds [Veilleux and Rupke, 2002, Sharp and Bland-Hawthorn, 2010], and has also been suspected in a few AGN-driven outflows [e.g. Hinkle et al., 2019].

First, we compare the BPT and VO87 line ratios measured in the clear outflow components, C2 and C1 components in J0842+03 and C3 and C2 components in J0906+56, to those of typical AGN models [Groves et al., 2004] and shock models [Allen et al., 2008] extracted from the ITERA library [Groves and Allen, 2010]. For the AGN models, the free parameters are the gas number density, the metallicity, the photon index of the AGN continuum, α, and the ionization parameter U, where $U \equiv n_{\rm ion}/n_e$, where $n_{\rm ion}$ is the density of ionizing photons and n_e is the electron density. We find that the line ratios probed by our data are not sensitive to the gas number density in the range (100–1000 cm^{-3}) relevant to our targets. We further compared the AGN models with metallicity of 0.5 $\times$ solar and solar to the data, and conclude that the one with solar metallicity is a better match to the data. Therefore, the gas number density and metallicity of the AGN model grids are fixed at 1000 cm^{-3} and solar values in our following model comparison, respectively. For the shock models, we consider two types of models, one where only the ionization from the shock itself is considered (called shock model hereafter), and one where the ionization is caused by both the shock and the precursor region ahead of the shock front (called shock+precursor model hereafter). The free parameters for both sets of models are the pre-shock particle number density n, the metallicity, the shock velocity v$_{shock}$, and the magnetic parameter $b \equiv log[B/n^{\frac{1}{2}}/(1\ \mu G\ cm^{\frac{2}{3}})]$ (where B is the transverse magnetic field). We have fixed the pre-shock particle number density n to 1000 cm^{-3} and the metallicity to solar value, which follows the same set-up as that for the AGN models. The full extent of the line ratio predictions from the shock and shock+precursor models with other density and metallicity settings is mostly covered by the model grids we adopt here, and they are thus omitted from the discussion below.

The results for the [O III]/Hβ vs [S II]/Hα diagram are shown in Fig. 4.6 for J0842+03 and Fig. 4.7 for J0906+56, where the comparison with the AGN, shocks, and shock+precursor models are displayed in the left, middle, and right panels, respectively. The results for the other two VO87 diagnostic diagrams, [O III]/Hβ vs [N II]/Hα and [O III]/Hβ vs [O I]/Hα, are in general similar to those from the [O III]/Hβ vs [S II]/Hα diagram in terms of how well the data and the models match with each other. They are thus omitted in the following discussion.

For the C2 component of J0842+03, the AGN models match the observed line ratios with $-3.5 \lesssim$ log(U) $\lesssim -2$ and $-2 \lesssim \alpha \lesssim -1.2$. The shock models can reproduce the majority of the observed line ratios with relatively large b parameters ($\gtrsim$1.5) and small shock velocities

($\lesssim$700 km s^{-1}). As for the shock+precursor models, either the observed [O III]/Hβ ratios or the [S II]/Hα ratios are systematically lower than the model predictions, by $\sim$0.3 dex on average. For the C1 component, most of the data points lie in, or close to the region for the star-forming galaxies in the diagram. This is consistent with their systematically lower [O III]/Hβ ratios compared to the AGN models. However, the shock and shock+precursor models are apparently better matches to the line ratios of the C1 component.

For J0906+56, the observed [O III]/Hβ and [S II]/Hα ratios can be mostly reproduced by AGN models with ionization parameters in the range of $-3 \lesssim \log(\mathrm{U}) \lesssim -1$ and photon indices in the full range provided by the model grids ($-2 < \alpha < -1.2$). However, either the observed [O III]/Hβ ratios or the [S II]/Hα ratios are systematically larger than the predictions of shock models by at least $\sim$0.3 dex, contrary to the case for J0842+03. This discrepancy becomes larger as the shock velocity increases. Once the ionization from the precursor region is considered, the model predictions match the observed line ratios almost as well as the AGN models, although the data have few constraints on the shock velocity and the b parameters. As for the C2 component, the AGN models still match the data relatively well, except that $\sim$1/3 of the data points show slightly higher [O III]/Hβ ratios. The shock models with relatively high b parameter ($\gtrsim$1) are also a good match to the data. Finally, the shock+precursor models have some trouble explaining $\sim$1/2 of the data points with lower [O III]/Hβ ratios.

Overall, the AGN models more easily reproduce the observed [O III]/Hβ and [S II]/Hα ratios of the C2 component in J0842+03 and C3 component in J0906+56. The shock models generate line ratios consistent with observations for J0842+03 but not for J0906+56, while the shock+precursor models match the observations for J0906+56 but not for J0842+03. As for the C1 component in J0842+03, the AGN models are a worse match to the data, which agrees with the expectation that it is contaminated by emission from the host galaxy, as discussed in Appendix C.1.4. Nevertheless, the AGN and shock models can both explain the line ratios of the C2 component in J0906+56 apparently.

Second, as shown in Fig. 4.8, there is no positive correlation between the emission line widths (σ_{gas}) and the [S II]/Hα line ratios for the individual outflow components of targets J0842+03 and J0906+56, contrary to theoretical predictions [e.g., Allen et al., 2008] and what is usually found in systems where shocks are the dominant source of ionization [e.g. Veilleux et al., 1995, Allen et al., 1999, Sharp and Bland-Hawthorn, 2010, Rich et al., 2011, 2012, 2014, Ho et al., 2014]. This conclusion still holds even when we consider the two outflow components together in each target. Overall, these results suggest that shock ionization is not important in J0842+03 and J0906+56. The outflowing gas in these two objects thus appears to be primarily photoionized by the AGN.

For the other targets, where only KCWI data are available, the [N II] $\lambda\lambda$6548, 6583, [S II] $\lambda\lambda$6716, 6731, [O I] λ6300, and Hα emission lines are not covered by the data, so we cannot directly compare the results with model predictions in the BPT and VO87 diagrams. Instead, we compare the KCWI data-based line ratios of the outflow components with model predictions in the [O II]/[O III] vs [O III]/Hβ diagrams as shown in Fig. 4.9. The emission line fluxes are extinction corrected in the same way as stated in Section 4.3.4. The same AGN, shock, and shock+precursor models as those shown in Fig. 4.6 and Fig. 4.7 are adopted in this analysis. Additionally, we plot the approximate upper boundary of line ratios predicted by a set of star-forming galaxy models from Levesque et al. [2010] as a red solid line in Fig. 4.9. Excluding the outflow components with possible contribution from non-outflowing gas (i.e., C2 components in J0906+56, J0954+47, and J1005+12, as well as C1 component in J0842+03), the results suggest that: (1) the star-forming models cannot reproduce the observed line ratios of the outflowing gas in the targets, therefore indicating that massive young stars are not the dominant ionization source in the outflowing gas; (2) the predictions from the shock models can match the observed line ratios of the outflowing gas relatively well, although the models may not be able to explain the observed data with the highest [O III]/Hβ ratios and lowest [O II]/[O III] ratios; (3) the AGN and shock+precursor models can explain the observed line ratios equally well and are both slightly better matches to the observations than the shock models. Moreover, the C2 component of J0906+56 and the C1 component of J0842+03 have lower [O II]/[O III] ratios than the predictions of all three model sets in general, and the C2 component of J0954+47 have lower [O III]/Hβ ratios than those of the AGN models. These results are consistent with our conclusions in Appendix C.1.4, C.1.5, and C.1.6 that these outflow components are partially contaminated by emission from non-outflowing gas.

Next, we have examined the [O III]/Hβ line ratios vs the emission line widths (σ_{gas}) based on the KCWI data for all seven targets with detected outflows in Fig. 4.10. To the first order, one would expect a positive correlation between the [O III]/Hβ line ratios and gas velocity dispersions [e.g., see Fig. 16 & 17 in Allen et al., 2008]. However, no such clear correlation is seen in our data, which is a similar conclusion to that derived from the [S II]/Hα ratios. In addition, for the C2 components in both J0100$-$01 and J1009+26, their observed line widths are significantly smaller (by $\sim$300–400 km s^{-1} on average) than the shock velocities predicted by the shock and shock+precursor models shown in the middle and right columns of Fig. 4.9. This is apparently contradictory to the expectation that the emission line velocity dispersion reflects the shock velocity when the shocks dominate the ionization of the gas. These results again suggest that shock ionization is not important in our targets.

Overall, our analysis indicates that AGN is most likely the dominant source of ionization for the outflows in our targets.

4.4.4 Electron Densities of the Outflows

The electron density, n_e, in the ionized gas may be derived from the [S II] λ6716/[S II] λ6731 ratios or [O II] λ3726/[O II] λ3729 ratios, following well-established calibrations [e.g., Sanders et al., 2016].

For the two targets in our sample with GMOS observations, the spatially-resolved electron density maps derived from the flux ratios of the total [S II] $\lambda\lambda$6716, 6731 line emission show possible radial trends of decreasing electron density outwards, but the errors on n_e are too large to draw robust ($>5\sigma$) conclusions. For the other targets, the electron density maps derived from the [O II] λ3726/[O II] λ3729 ratios from the KCWI data are even more noisy, which again prevent us from determining the radial trend of the electron densities. Consequently, the electron densities in individual velocity components cannot be measured reliably based on the spatially-resolved maps in these systems.

To check further the possible difference of [S II]-based electron densities among different velocity components, we then turn to use the spectra spatially integrated over the whole GMOS data cubes for targets J0842+03 and J0906+56, and the Keck/LRIS spectra for the other targets[6]. However, for most of our targets, the measured electron densities of the outflow components still show large uncertainties and thus no useful information of the electron density contrast among individual velocity components can be obtained from our data. The only exceptions are J0842+03

[6]Notice that for the Keck/LRIS data, the emission line profiles are fit with two Gaussian components as described in Manzano-King et al. [2019], and here the outflow components in J0100−01, J0811+23, J0954+47, J1005+12, and J1009+26 refer to the broad components from their best fits

and J1005+12, where no clear differences in electron densities are seen among individual velocity components. In the discussion below, we thus adopt the electron densities measured from the [S II] λ6716/[S II] λ6731 ratios based on the total line flux in each object as the electron densities for the outflowing gas (see Table 4.4).

4.4.5 Dust Extinction of the Outflows

From the GMOS data of J0842+03 and J0906+56, we find that the clearly outflowing line-emitting material (the C2 component in J0842+03 and the C3 component in J0906+56) has Hα/Hβ ratios that are higher than the intrinsic values of typical H II regions or AGN narrow line region [2.87 and 3.1, respectively; Osterbrock and Ferland, 2006], suggesting dust extinction affects the line emission of the outflows in these objects. Adopting the extinction curve from Cardelli et al. [1989b] with R_V = 3.1, the derived extinction values, A_V, measured from the spectra integrated over the whole data cube, are on the order of 1 mag. For comparison, the other velocity components in these two targets show slightly smaller A_V by ~0.2 magnitude on average. A more detailed look at the spatially-resolved A_V maps of the outflow components reveals possible radial trends of decreasing A_V at larger radii in both targets. As for the other targets observed with KCWI, the outflow components in Hγ are in general too faint to allow us to draw robust conclusions.

4.4.6 Comparison with the Keck/LRIS Data

The fast outflows in our targets were initially discovered by Manzano-King et al. [2019] based on Keck/LRIS long-slit data. The properties of the outflows measured from these long-slit data are in broad agreement with those reported here.

The column (10) in Table 4.2 lists the 5-σ detection limits of an [O III] λ5007 emission line with FWHM of 1000 km s^{-1} in the GMOS and KCWI data. Excluding the shallower observation of J0100−01, these detection limits are in general comparable to those of the Keck/LRIS data, which are in the range of $\sim$1–3$\times$10^{-17} erg cm^{-2} s^{-1} arcsec^{-2}.

In J0100−01, J0842+03, J0906+56, J0954+47, and J1005+12 (GMOS data and KCWI data with small slicer setup), the kinematic properties of the outflows (v_{50} and W_{80}) measured from these three data sets are similar, but the better spectral resolutions of the GMOS and KCWI IFS data compared with the LRIS data[7] reveal more details in the shapes of the emission line profiles in J0906+56, J0954+47, and J1005+12, where three Gaussian components are required to adequately describe the line profiles. The spatial extents of the outflows are broadly consistent with each other after taking into account the sensitivity of the various data sets.

In J0811+23 and J1009+26 (KCWI data with the medium and small slicer setup, respectively), blueshifted [O III] λ5007 velocity components are detected in both the Keck/LRIS and KCWI data sets, although they are narrower (by a factor of $\sim$3 on average) and show smaller blueshifts (by a factor of $\sim$4 on average) in the KCWI data when compared to those in the Keck/LRIS data. As for J0840+18 (KCWI data with medium slicer setup), a very faint ($\sim$2$\times$10^{-17} erg cm^{-2} s^{-1} arcsec^{-2}), broad ($W_{80} \simeq$ 1600 km s^{-1}), and redshifted ($v_{50} \simeq$ 150 km s^{-1}) velocity component is reported in the Keck/LRIS data, but it is not detected in the KCWI data. The origin of this apparent discrepancy is not clear although the slightly coarser spectral resolution of LRIS might make it more capable of detecting such a broad feature.

[7] Recall that FWHM $\simeq$ 100 km s^{-1} at 4610 Å for GMOS, $\simeq$ 80 km s^{-1} at 4550 Å for the small-slicer setup of KCWI, and $\simeq$ 190 km s^{-1} for Keck/LRIS [Manzano-King et al., 2019].

4.5 Discussion

4.5.1 Energetics of the Outflows

The ionized gas mass of the outflows can be calculated based on either the [O III] $\lambda\lambda$4959, 5007 line luminosity or the Balmer line (Hα or Hβ) luminosity of the outflowing, line-emitting gas. We have compared the ionized gas mass of the outflows based on these emission lines, and find that the [O III]-based values are systematically smaller than the Hα or Hβ-based values by $\sim$0.2 dex on average, assuming solar metallicity and following equation (29) in Veilleux et al. [2020] (If we assume instead a 0.5$\times$solar metallicity, the average difference increases to $\sim$0.5 dex). This difference may be caused by the uncertainties on the ionization fraction correction (which is assumed to be unity in the previous calculation) and gas-phase metallicity that is assumed in the [O III]-based ionized gas mass. In order to avoid introducing such uncertainties into our results, the best global fits (Section 4.3.2.2) to the Hα (GMOS data) and Hβ (KCWI data) line emission are thus used to calculate the energetics of the outflows in the following discussion. From Osterbrock and Ferland [2006] and assuming case B recombination with T = 10^4 K, we have

$$M_{\rm out} = 4.48\ {\rm M}_\odot \left(\frac{L_{H\alpha,corr}}{10^{35}\ {\rm erg\ s}^{-1}}\right)\left(\frac{< n_e >}{100\ {\rm cm}^{-3}}\right)^{-1} \tag{4.7}$$

where $L_{H\alpha,corr}$ is the extinction-corrected Hα luminosity using the measured Balmer decrement from the total emission line fluxes of the spatially-integrated spectra and adopting an intrinsic

Hα/Hβ ratio of 2.87, appropriate for Case B recombination [Osterbrock and Ferland, 2006], and the Cardelli et al. [1989b] extinction curve with R_V = 3.1. For the KCWI data sets, where Hα was not observed, we instead use the extinction-corrected Hβ luminosity $L_{H\beta,corr}$ and then convert it to $L_{H\alpha,corr}$ using $L_{H\alpha,corr}$ = 2.87 $L_{H\beta,corr}$ as above.

The calculations of the mass, momentum, and kinetic energy outflow rates depend on the spatial extent of the outflows. As discussed in Section 4.4.2, while the outflows in J0100−01, J0811+23, J0842+03, and J1009+26 are spatially resolved in the IFS data, our analysis of the IFS data on J0906+56, J0954+47, and J1005+12 does not provide a conclusive outflow size in these objects. For the later, we thus calculate the energetics of the outflows in both scenarios, one where the outflows are spatially resolved and one where they are not.

As presented in Section 4.4.1, while the outflows are mainly traced by the broadest/most blueshifted velocity components (C3 in J0906+56, J0954+47, J1005+12, C2 in J0100−01, J0842+03, J1009+26, and C1 in J0811+23) in the seven targets with detected outflows, the C2 components in J0906+56, J0954+47, and J1005+12, as well as the C1 component in J0842+03 may also trace significant portion of the outflowing gas in these systems. In the following calculations of the outflow energetics, we thus consider not only the primary outflow components of each target (C3 in J0906+56, J0954+47, J1005+12, C2 in J0100−01, J0842+03, J1009+26, and C1 in J0811+23), but also the C2 components in J0906+56, J0954+47, and J1005+12, as well as the C1 component in J0842+03, recording their results separately.

4.5.1.1 Spatially Resolved Outflows

We begin with the scenario where the detected outflows are spatially resolved. The mass, momentum, and kinetic energy outflow rates are calculated using a time-averaged, thin-shell, free wind model [e.g. Shih and Rupke, 2010, Rupke and Veilleux, 2013b], where the outflow is spherically-symmetric with a radius R_{out} in 3D space.

Specifically, the energetics are calculated by summing up quantities over individual spaxels:

$$dM/dt = \sum dm/dt = \sum \frac{m_{\rm out} v_{50,out} \sec\theta}{R_{out}} \tag{4.8}$$

$$dp/dt = \sum (v_{50,out} \sec\theta) dm/dt \tag{4.9}$$

$$dE/dt = \frac{1}{2} \sum [(v_{50,out} \sec\theta)^2 + 3\sigma_{out}^2]\, dm/dt \tag{4.10}$$

where $m_{\rm out}$, $v_{50,out}$, σ_{out} respectively are the ionized gas mass, absolute value of v_{50}, and velocity dispersion (= W_{80}/2.563) measured from the outflow components within individual spaxels. In these expressions, $\theta = \sin^{-1}(r_{spaxel}/R_{out})$, the angle between the velocity vector of the outflow in 3D space and the line-of-sight. R_{out}, again, is the radius of the spherically-symmetric outflow in 3D space, and is calculated as the maximum extent that the outflow components are detected (S/N of the outflow component of [O III] λ5007 emission > 2) in the sky plane plus half spaxel, converted to an equivalent physical distance. The half spaxel is added artificially since a spherical outflow is formally travelling perpendicular to the line-of-sight at the maximum radius R_{out} (i.e., the $v_{50,out}$ will be 0), and thus no outflow signal can be detected. r_{spaxel} is the projected distance on the sky of a given spaxel with respect to the spaxel with peak outflow flux. In the calculations above, we exclude the spaxels with emission line flux that fall in the lowest 5% of the full flux range. It should be emphasized that we adopt the [O III]-based R_{out} in the calculation instead of the Balmer-line-based values, which are in general smaller when measured through the fainter Hβ feature. The mass, momentum, and kinetic energy outflow rates scale as R_{out}^{-1} in the above equations and would thus be higher if the Hβ-based R_{out} were used in the calculations.

The electron densities used in the above equations are measured from the [S II] λ6716/[S II] λ6731 ratios, following the conversion presented in Sanders et al. [2016]. As discussed in details in Section 4.4.4, the [S II] λ6716/[S II] λ6731 ratios are calculated using the total line fluxes from the spatially-integrated GMOS spectra or the Keck/LRIS spectra for the other targets without GMOS observations (see Table 4.4). Neither the [S II] λ6716/[S II] λ6731 ratios of individual spaxels nor the [S II] λ6716/[S II] λ6731 ratios of the outflow components could be used due to their large uncertainties.

We multiply the energetics by a factor of two to account for the far side of the outflow that is blocked by the galaxy, except for the C2 component of J0906+56, which is purely redshifted and likely represents the back side of the outflow traced by the C3 component (see discussion in Appendix C.1.5.1). The results of the calculations are listed in Table 4.4.

It is important to point out that the geometries of the outflows in J0100−01 and J1009+26 may deviate significantly from the spherically-symmetric wind model adopted in the calculations, given the apparent biconical morphologies of the outflows on the sky plane. Nevertheless, if we assume a biconical geometry [e.g., bipolar super-bubble as adopted in Rupke and Veilleux, 2013b] for the outflows in these targets, the estimated change in the mass, momentum and kinetic energy outflow rates are comparable to the errors listed in Table 4.4. This may also be true for the C2 components in J0954+47 and J1005+12, if their apparent biconical/asymmetric morphologies on the sky plane arise from the geometry of the outflowing gas.

4.5.1.2 Spatially Unresolved Outflows

If instead the outflows are unresolved by the IFS data, the total mass of the outflowing gas remains unchanged, but the time-averaged mass, momentum, and kinetic energy outflow rates are affected since they depend inversely on the size of the outflows. As discussed above, the C3 components of J0906+56, J0954+47, and J1005+12 and the C2 component of J0906+56 may be spatially unresolved. In this scenario, we adopt $\frac{1}{2}$ × FWHM(PSF) as a conservative upper limit to the true outflow radius $R_{out,ur}$, and get:

$$dM/dt = \frac{M_{\rm out,tot} v_{out,tot}}{R_{out,ur}} \tag{4.11}$$

$$dp/dt = v_{out,tot} dM/dt \tag{4.12}$$

$$dE/dt = \frac{1}{2}(v_{50,out}^2 + 3\sigma_{out}^2) dM/dt \tag{4.13}$$

Table 4.4. Energetics of the Outflows

Name	Comp.	Data Set	n_e (cm^{-3})	log(M/M$_\odot$)	R$_{out}$(kpc)	R$_{out,ur}$(kpc)	log[(dM/dt)/(M$_\odot$ yr^{-1})] resolved	log[(dM/dt)/(M$_\odot$ yr^{-1})] unresolved	log[(dE/dt)/(erg s^{-1})] resolved	log[(dE/dt)/(erg s^{-1})] unresolved	log[(c dp/dt)]/(L$_\odot$)] resolved	log[(c dp/dt)]/(L$_\odot$)] unresolved
(1)	(2)	(3)	(4)	(5)	(6)	(7)	(8)	(9)	(10)	(11)	(12)	(13)
J0100−01	C2	KCWI	60±50	$7.3^{+0.3}_{-0.8}$	3.1	...	$-0.5^{+0.3}_{-0.8}$	...	$40.8^{+0.3}_{-0.8}$	...	$9.5^{+0.3}_{-0.8}$	...
J0811+23	C1	KCWI	590±160	$4.8^{+0.1}_{-0.1}$	0.9	...	$-2.5^{+0.1}_{-0.1}$	...	$37.1^{+0.1}_{-0.1}$	...	$6.8^{+0.1}_{-0.1}$	...
J0842+03	C2	GMOS	470±150	$5.4^{+0.1}_{-0.2}$	0.8	...	$-1.4^{+0.1}_{-0.2}$	...	$39.3^{+0.1}_{-0.2}$	...	$8.5^{+0.1}_{-0.2}$	...
	C1	GMOS		$5.4^{+0.2}_{-0.2}$	0.9	...	$-1.6^{+0.1}_{-0.2}$	...	$38.1^{+0.1}_{-0.1}$	...	$8.0^{+0.1}_{-0.2}$	...
	C2	KCWI		$5.9^{+0.1}_{-0.2}$	1.6	...	$-1.2^{+0.1}_{-0.2}$	...	$39.4^{+0.1}_{-0.2}$	...	$8.6^{+0.1}_{-0.2}$	...
	C1	KCWI		$6.0^{+0.1}_{-0.2}$	1.6	...	$-1.6^{+0.2}_{-0.3}$	...	$38.1^{+0.1}_{-0.1}$	...	$7.8^{+0.1}_{-0.1}$	...
J0906+56	C3	GMOS	570±360	$5.8^{+0.2}_{-0.4}$	1.1	0.3	$-1.8^{+0.2}_{-0.4}$	> -0.9	$39.2^{+0.2}_{-0.4}$	>40.2	$7.5^{+0.2}_{-0.4}$	>8.4
	C2	GMOS		$5.4^{+0.2}_{-0.4}$	1.2	0.3	$-2.1^{+0.2}_{-0.4}$	> -1.6	$37.8^{+0.2}_{-0.4}$	>38.7	$7.1^{+0.2}_{-0.4}$	>7.6
	C3	KCWI		$5.9^{+0.2}_{-0.4}$	2.1	0.4	$-1.5^{+0.2}_{-0.4}$	> -0.9	$39.9^{+0.2}_{-0.4}$	>40.3	$8.3^{+0.2}_{-0.4}$	>8.7
	C2	KCWI		$6.1^{+0.2}_{-0.4}$	2.2	0.4	$-1.4^{+0.2}_{-0.4}$	> -0.7	$39.1^{+0.2}_{-0.4}$	>39.7	$8.2^{+0.2}_{-0.4}$	>8.7
J0954+47	C3	KCWI	470±80	$5.8^{+0.1}_{-0.1}$	1.6	0.4	$-1.5^{+0.1}_{-0.1}$	> -1.0	$39.6^{+0.1}_{-0.1}$	>39.9	$8.2^{+0.1}_{-0.1}$	>8.4
	C2	KCWI		$6.3^{+0.1}_{-0.1}$	1.8	...	$-2.1^{+0.1}_{-0.1}$	...	$38.9^{+0.1}_{-0.1}$	...	$7.9^{+0.1}_{-0.1}$	...
J1005+12	C3	KCWI	450±100	$5.2^{+0.1}_{-0.1}$	0.3	0.1	$-1.2^{+0.1}_{-0.1}$	> -0.6	$40.1^{+0.1}_{-0.1}$	>40.4	$9.0^{+0.1}_{-0.1}$	>9.2
	C2	KCWI		$5.6^{+0.1}_{-0.1}$	0.7	...	$-1.7^{+0.1}_{-0.3}$	...	$38.8^{+0.1}_{-0.1}$	...	$7.8^{+0.1}_{-0.1}$	...
J1009+26	C2	KCWI	150±60	$5.5^{+0.2}_{-0.2}$	0.8	...	$-2.0^{+0.2}_{-0.2}$	...	$38.2^{+0.2}_{-0.2}$	...	$7.5^{+0.2}_{-0.2}$	...

Note. — Column (1): Short name of the target; Column (2): Individual outflow components from the best fits; Column (3): Instrument used for the observations; Column (4): Electron density measured from the [S II] $\lambda\lambda$6716, 6731 line ratio based on the total line flux from the spatially-integrated, GMOS spectra or keck/LRIS spectra (see Section 4.4.4); Column (5): Ionized gas mass of the corresponding outflow component; Column (6): Outflow radius adopted in the calculation of mass, momentum and kinetic energy outflow rates when the outflows are spatially resolved (Column (8), (10), and (12), respectively); Column (7): Outflow radius adopted in the calculation of mass, momentum and kinetic energy outflow rate when the outflow is spatially unresolved (Column (9), (11), and (13), respectively); (8): Ionized gas mass outflow rate of the corresponding outflow component when the outflow is spatially resolved; Column (9): Same as in Column (8) but with the assumption that the outflow is spatially unresolved; Column (10): Ionized gas kinetic energy outflow rate of the corresponding outflow component when the outflow is spatially resolved; Column (11): Same as in Column (10) but with the assumption that the outflow is spatially unresolved; Column (12): Ionized gas momentum outflow rate of the corresponding velocity component when the outflow is spatially resolved; Column (13): Same as in Column (12) but with the assumption that the outflow is spatially unresolved.

Here, $M_{\rm out,tot}$ is the total mass of the outflowing gas, and $R_{out,ur}$ is the upper limit on the radius of the outflow. The quantities $v_{50,out}$ and σ_{out} are the median values of v_{50} and σ (= W_{80}/2.563) of the outflow components measured across the data cube (see Table 4.3). The adopted electron densities are the same as those in the spatially resolved scenario. The lower limits on the outflow rates obtained under these assumptions are listed in Table 4.4.

4.5.2 Comparison with More Luminous AGN

The most direct measure of the magnitude of an outflow is its velocity. Various definitions have been used in literature to represent outflow velocities [e.g., see a brief summary in Sec. 3.1 in Veilleux et al., 2020]. W_{80} of the overall spatially integrated emission line profiles have been used as surrogates for characteristic outflow velocities in many studies [e.g. Liu et al., 2013a,b, Rodríguez Zaurín et al., 2013, Harrison et al., 2014, Zakamska and Greene, 2014]. In Fig. 4.11, the values of W_{80} derived from the [O III] λ5007 line emission integrated over our data cubes and the [O III] λ5007 luminosities ($L_{[O\ III]}$) of our targets are compared with published values in low-z AGN and/or Ultraluminous Infrared Galaxies (ULIRGs) with strong outflows. Remarkably, four of our targets (J0842+03, J0906+56, J0954+47, and J1005+12) have W_{80} that are comparable to those of AGN with $L_{[O\ III]}$ that are two orders of magnitude larger than those of our targets. However, in general, the data points suggest a positive correlation between [O III] λ5007 W_{80} and luminosities, spanning 4 orders of magnitude in $L_{[O\ III]}$ and 1.5 orders of magnitude in W_{80}. This correlation simply implies that more powerful AGN provide more energy to drive faster outflows.

A more physically meaningful, albeit also more model-dependent, estimate of the impor-

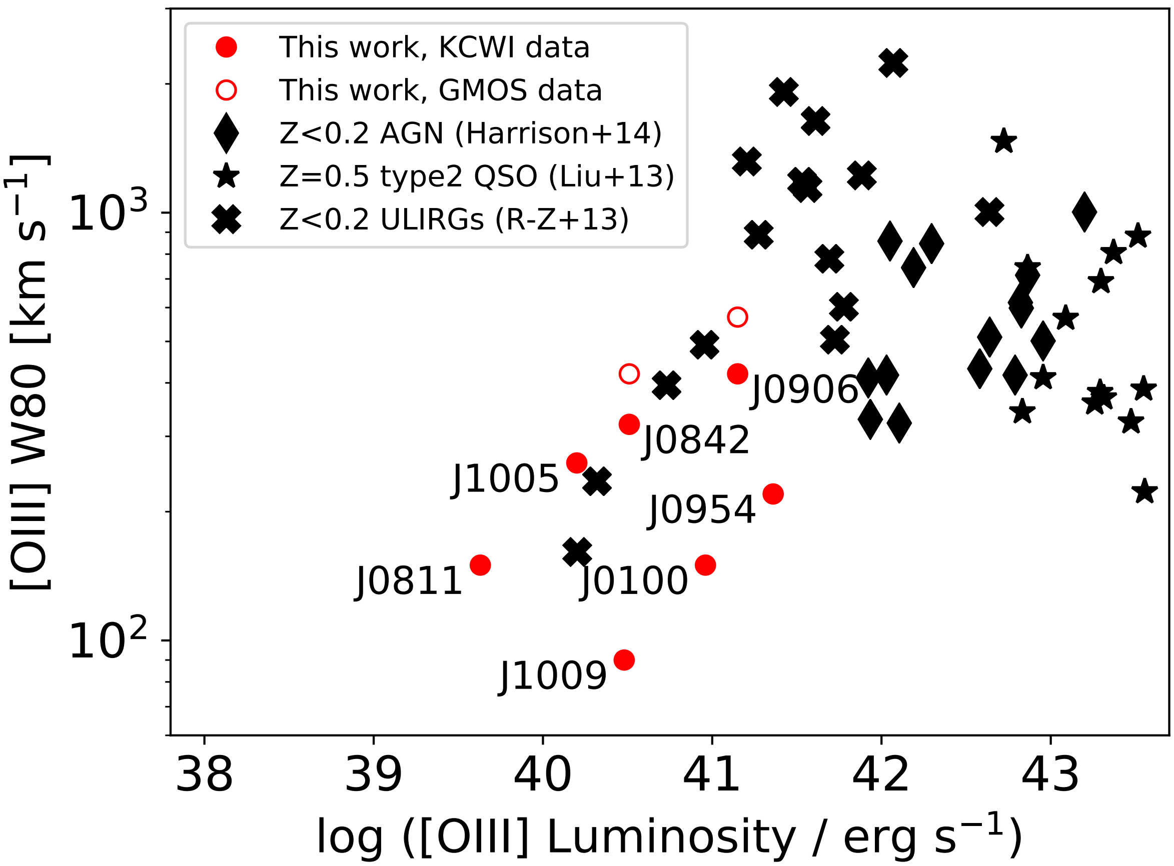

Figure 4.11: [O III] λ5007 line widths W_{80} vs [O III] λ5007 luminosities for the seven targets with detected outflows (red filled circles indicate the KCWI data and red open circles indicate the GMOS data of J0842+03 and J0906+56) as well as more luminous AGN and ULIRGs taken from the literature [black symbols; Liu et al., 2013a,b, Harrison et al., 2014, Rodríguez Zaurín et al., 2013], as indicated in the legend. All measurements refer to the total, spatially-integrated [O III] λ5007 line emission from each object. The typical errors of the measurements are similar to the size of the data points.

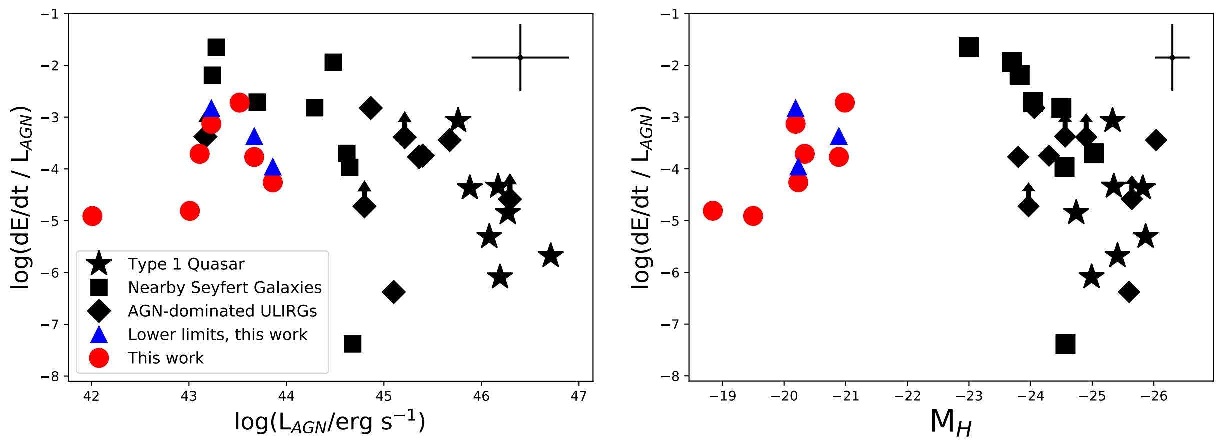

Figure 4.12: Ratios of the kinetic energy outflow rates, based on the KCWI data, to the AGN bolometric luminosities as a function of (left) the AGN bolometric luminosties and (right) H-band absolute magnitudes, for the seven targets with detected outflows in our sample (red circles) and lower limits (blue triangles) if the outflows in J0906+56, J0954+47, and J1005+12 are spatially unresolved (see Section 4.4.2 and 4.5.1.2). Here we have neglected the kinetic energy outflow rates calculated from the C2 components in J0906+56, J0954+47, J1005+12 and the C1 component in J0842+03 as their contributions are modest. Also plotted as a comparison are the values from a sample of $z < 0.3$ but more powerful type 1 quasars and nearby Seyfert galaxies from or collected by Rupke et al. [2017], as well as a sample of $z < 0.15$, AGN-dominated ULIRGs from Rose et al. [2018]. The absolute H-band magnitudes shown in the right panel are derived from the 2MASS [Skrutskie et al., 2006] H-band magnitudes taken from the IRSA/2MASS archive, except for those of the Type 1 quasars and three of the ULRIGs from Rose et al. [2018], which are the AGN-subtracted, host-only H-band magnitudes quoted from Veilleux et al. [2006, 2009a]. The estimated typical errors of the data points are noted as black crosses in the upper-right corners of both panels.

tance of an outflow is the kinetic energy outflow rate. In Fig. 4.12, the kinetic energy outflow rates of our targets (based on the KCWI data), normalized by their AGN luminosities (see Table 5.1), are compared with those of low-z Seyferts and type 1 quasars studied in Rupke et al. [2017], as well as those of the $z < 0.15$, AGN-dominated ULIRGs from Rose et al. [2018]. The results for the C2 components of J0906+56, J0954+47, and J1005+12, as well as the C1 component of J0842+03 are omitted in this analysis due to their relatively modest contribution, as they have on average $\sim$1 dex smaller dE/dt than those of either the C3 or C2 components of these targets. The values shown in this figure assume the spatially-resolved scenario by default (red filled circles; see Section 4.5.1.1) for all of our sources. For J0906+56, J0954+47, and J1005+12, we also show the lower limits obtained by assuming that the outflow components are spatially unresolved (blue filled triangles). The measurements of J0842+03 and J0906+56 based on the GMOS data are also omitted as they have dE/dt smaller than (but close to) those based on the KCWI data. Compared with our targets, those Seyferts and quasars have both more powerful AGN (with higher median AGN luminosity by $\sim$1 to 3 orders of magnitude) and more massive host galaxies (with brighter median H-band absolute magnitudes[8] by $\sim$4 to 5 mag.). Nevertheless, our targets have ratios of kinetic energy outflow rates to AGN luminosities that are comparable to those measured in the more luminous AGN. This result adds support to the idea that the outflows in the dwarf galaxies are scaled-down versions of the outflows in the more luminous AGN and are fun-

[8]The absolute H-band magnitudes of our targets and all other sources are derived from the 2MASS [Skrutskie et al., 2006] H-band magnitudes taken from the IRSA/2MASS archive `https://irsa.ipac.caltech.edu/cgi-bin/Gator/nph-scan?mission=irsa&submit=Select&projshort=2MASS`, except for those of the Type 1 quasars and three of the ULRIGs from Rose et al. [2018], which are the AGN-subtracted, host-only H-band magnitudes quoted from Veilleux et al. [2006, 2009a]. While the H-band magnitudes of the Seyfert galaxies are not AGN-subtracted, the contribution from the AGN is probably not substantial: the H-band magnitudes of the Seyfert galaxies are close to the QSO-subtracted ones of the Type 1 quasars, which is consistent with the fact that the stellar velocity dispersions of the two samples are comparable when they are measured or recorded in Rupke et al. [2017].

damentally driven by the same AGN processes. We examine this issue in more detail in Section 4.5.3.

4.5.3 What Drives these Outflows: AGN or Starbursts?

The results from the previous sections favor AGN-related processes as the main driver of the detected outflows. First, the velocities of the outflows detected in our dwarf galaxies are often large. The maximum W_{80} of outflow components in six targets exceed 600 km s^{-1}, including three that exceed 1000 km s^{-1}. If we adopt the definition of bulk outflow velocities V$_{out}$ $=W_{80}/1.3$ as in some studies [e.g. Liu et al., 2013b, Harrison et al., 2014, where they assume spherically-symmetric or wide-angle bi-cone outflows], six out of the seven targets with detected outflows have outflow velocities $\gtrsim$500 km s^{-1}. To put these numbers into perspective, a velocity of 500 km s^{-1} is equivalent to an energy of 1 keV per particle, and is difficult to achieve with stellar processes [Fabian, 2012]. The high velocities of the outflows seen in most of our targets thus suggest that AGN plays an important role in driving these outflows.

Second, as shown in Fig. 4.12 and discussed in Section 4.5.2, the AGN are also powerful enough to drive the outflows in our targets. The ratios of kinetic energy outflow rates to bolometric AGN luminosities of our targets are in the range of $\sim$1$\times$10^{-5} – 2$\times$10^{-3}. These ratios are far less than unity, and are within the range of values seen in other more luminous AGN, suggesting that the AGN are more than capable of driving these outflows.

The lower limits of the ionized gas mass entrainment efficiency η, defined as the ratio of ionized gas mass outflow rate over the star formation rate, are in the range of $\sim$0.1 – 0.8, with a median of $\sim$0.3 (the range and median are $\sim$0.1 – 0.6 and $\sim$0.2, respectively, if we exclude the contributions from the C2 components in J0906+56, J0954+47, and J1005+12, and from the C1 component in J0842+03). Note that these are lower limits since our adopted SFR are upper limits (see Section 4.3.5). This is comparable to the average value (∼0.19) measured for the neutral outflows in low-redshift, AGN/starburts-composite ULIRGs [Rupke et al., 2005c]. In the more luminous AGN, apparently higher η are reported in the literature. For example, $\eta \simeq 6-20$ are reported for a sample of $z < 0.2$ luminous type 2 AGN [Harrison et al., 2014]. Meanwhile, much lower η values, with a median of 0.8, are reported for a sample of type 1 quasars at z< 0.3 in Rupke et al. [2017] once the quasar emission is subtracted and both the neutral and ionized phases of the outflows are considered. In their sample, the median value of η drops further to 0.03 when the ionized phase alone is considered. In short, the η measured in our targets fall in the wide range seen in various studies of outflows in more luminous AGN. In addition, if the outflows in J0906+56, J0954+47, and J1005+12 are spatially unresolved, then the lower limits of η can be as high as ∼3, uncomfortably high for starburst-driven outflows in the low-z universe [e.g. Arribas et al., 2014, where $\eta < 1$ in general]. This is even more so if we also consider the possible contribution from the C2 components to the outflow energetics in these targets.

There is also circumstantial evidence against starburst driving of these outflows. Given the upper limits of SFR estimated from the [O II] $\lambda\lambda$3726, 3729 emission, all of the galaxies in our sample lie either slightly, or significantly, below the main sequence of star-forming galaxies in the low-z universe [e.g. Brinchmann et al., 2004], while the star formation-driven outflows are observed much more frequently in galaxies above the star formation main sequence [e.g. Heckman et al., 2015, Roberts-Borsani et al., 2020].

More quantitatively, we can examine if stellar processes are physically capable of driving the observed outflows. The typical kinetic energy output rate from core collapse supernovae is

$\sim 7\times10^{41}(\alpha_{SN}/0.02)(\dot{M}_\star/\mathrm{M}_\odot\ yr^{-1})$ [Veilleux et al., 2005a, 2020]. Adopting the SFR upper limits of our targets (Table 5.1), and assuming a constant supernovae rate of $\alpha_{SN} = 0.02$, the expected maximum kinetic energy output rates from core-collapse supernovae in our targets are in the range of $\sim 7\times10^{39}$ – 5×10^{41} erg s^{-1}, with a median of $\sim 2\times10^{41}$ erg s^{-1}. These are $\sim$6 – 720 times larger than the kinetic energy outflow rates based on the scenario that the outflows are spatially resolved. Stellar processes thus cannot be overlooked as a potential source of energy for these outflows.

However, it should be pointed out that we have only considered the warm ionized phase of the outflowing gas and adopted the energetics calculated in the spatially resolved scenario. If the outflows in J0906+56, J0954+47, and J1005+12 are spatially unresolved, the kinetic energy outflow rates may be comparable to, if not larger than, the kinetic energy output from the stellar process as estimated above. This argument is slightly stronger if we consider the contribution from the C2 components to the outflow energetics in these targets, too. Additionally, it is possible that a significant fraction of the energy is carried in a hot, thin gas phase instead, which has been predicted by recent simulations [e.g. Koudmani et al., 2019, 2020].

Overall, the outflows in our targets are likely driven by AGN, but we cannot formally rule out the possibility that star formation activity may also help in launching the outflows, as is often the case among low-z ULIRGs and luminous AGN [e.g. Rupke and Veilleux, 2013b, Harrison et al., 2014, Fluetsch et al., 2019]. More stringent constraints on the star formation rates of our targets need to be obtained before we can draw a more robust conclusion about the role of stellar processes in these outflows.

4.5.4 Does the Outflowing Gas Escape the Galaxies?

To help us evaluate the impact of these outflows on their host galaxies, it is interesting to examine the question of whether some of the outflowing gas is able to escape the host galaxy. This requires comparing the kinematics of the outflows with the local escape velocity, $v_{\rm esc}(r) = \sqrt{2[\Phi(\infty) - \Phi(r)]}$, where $\Phi(r)$ and $\Phi(\infty)$ are the values of the gravitational potential at r and $r = \infty$, respectively, in the case of a spherically-symmetric galaxy.

One may estimate the escape velocity in terms of observed quantities, like the circular velocity $v_{\rm circ}$ of the galaxy, by assuming a simple density profile such as that of a singular isothermal sphere. A conservative estimate of the escape velocity in that case gives $v_{\rm esc} \simeq 3v_{\rm circ}$ [Veilleux et al., 2020]. Our IFS data do not probe the flat portion of the rotation curve, so we adopt the maximum of the measured stellar velocities (v$_\star$) and velocity dispersions ($\sigma_\star$) to calculate the lower limits of the circular velocities in our targets, where $v_{\rm circ} = \sqrt{v_\star^2 + 2\sigma_\star^2}$ [e.g., See Section 2.4 of Veilleux et al., 2020]. We have not applied any deprojection corrections to the circular velocities and outflow velocities, given that the 3D morphologies of the outflows are poorly constrained.

Alternatively, the escape velocity may be derived by assuming a NFW dark matter density profile [Łokas and Mamon, 2001] and a total halo mass determined from abundance matching [Moster et al., 2013], which has been done in Manzano-King et al. [2019]. Since the escape velocity always peaks at the center, it can serve as a conservative upper limit to the escape velocity throughout the galaxy. For our targets, the escape velocities at r = 0 obtained through this approach are larger by $\sim$50% on average than those based on the empirical circular velocities above. We adopt the more conservative $r = 0$, NFW-based escape velocities in the remainder of our discussion.

Table 4.5. Outflow Escape Fractions

Target (1)	V_{esc} [km s^{-1}] (2)	f_{esc} (3)
J0100−01	320	1%
J0811+23	260	0.1%
J0842+03	300	6%
J0906+56	300	6%
J0954+47	320	1%
J1005+12	380	1%
J1009+26	240	0.3%

Note. — Column (1): Short name of the target; Column (2): Escape velocity at the center of each galaxy assuming a NFW density profile, rounded to the nearest 10 km s^{-1}; Column (3): Escape fraction of the [O III] λ5007 line emitting gas, based on flux rather than mass. This number does not take into account possible density contrasts between the outflowing and quiescent gas components in these systems and projection effects; see Section 4.5.4 for more details.

For all of the targets, we next define the escape fraction ($f_{\rm esc}$) as the ratio of [O III] λ5007 flux with absolute velocities larger than the escape velocity summed up across the data cube, to the total emission line flux in the whole data cube. Notice here that the escape fraction is defined as a flux ratio rather than a mass ratio, so it does not take into account possible density contrasts between the outflowing and quiescent (non-outflowing) gas components [e.g. Hinkle et al., 2019, Fluetsch et al., 2019, 2020], which may affect the luminosity-to-mass conversion factor. In addition, the values of $f_{\rm esc}$ obtained here are conservatively low since we have not applied deprojection corrections to the gas velocities in the outflows. Some fraction of the escaping gas may not be accounted for here if the velocities of this gas, projected along our line of sight, fall below $v_{\rm esc}$.

The results from our IFS data are summarized in Table 4.5. The escape fractions range from 0.1% to 6%. Taking into account that the escape velocities are likely overestimated for the reasons mentioned earlier and that the outflow velocities are potentially underestimated due to projection effects, this suggests that at least some small portion of the outflowing gas may travel a long way from the centers and help contribute to the metal enrichment of the circumgalactic medium in these dwarf galaxies [as reported in a number of studies; e.g. Bordoloi et al., 2014].

4.6 Conclusions

In this paper, we report the results from an integral field spectroscopic study with Gemini/GMOS and Keck/KCWI of the warm ionized gas in a sample of 8 low-redshift ($0.01 \lesssim z \lesssim 0.05$) dwarf galaxies with known AGN and suspected outflows. The main results are summarized as follows:

- Warm ionized outflows are detected in 7 out of the 8 targets. The IFS data in most targets reveal broad, blueshifted velocity components tracing rapid outflows (v_{50} down to ~ -240 km s^{-1} and W_{80} up to $\sim$1200 km s^{-1}) and narrow components tracing the rotation of the host galaxies. In J0906+56, J0954+47, and J1005+12, the multi-Gaussian fits require a third velocity component with intermediate line widths, which probably traces portion of the outflowing gas and/or turbulent gas. In J0811+23 and J0842+03, the narrow components are in general blueshifted and may trace the outflows or a mixture of outflowing and rotating gas in these systems.

- The two-dimensional velocity structures and radial profiles of the outflowing kinematic components indicate that the outflows are spatially resolved by the IFS data in at least four cases (J0842+03, J0100−01, J1009+26, J0811+23), with the emission extending up to $\sim$3 kpc from the galactic centers. In J0100−01 and J1009+26, the outflowing kinematic components show apparent biconical morphologies in projection. Additionally, clear non-radial velocity gradients/structures are also seen in those components of J0811+23 and J0842+03. In J0906+56, J0954+47, and J1005+12, the kinematic components that have intermediate line widths and probably trace part of the outflows are also spatially resolved. However, the fast outflows traced by the kinematic components with the broadest line widths in these targets are not clearly spatially resolved. An attempt at deconvolving the data cubes gives inconclusive results.

- The clearly outflowing gas in all of the targets have line ratios that are consistent with AGN photoionization. A general lack of positive correlation between the gas kinematics and the [S II]/Hα or [O III]/Hβ line ratios, and inconsistencies between the observed line ratios and the predictions from shock models, indicate that shocks likely do not play a major role in heating and ionizing the outflowing gas in these systems.

- Assuming a simple thin-shell, free wind model, the warm, ionized gas mass outflow rates of our targets range from $\sim 3\times10^{-3}$ to $\sim 3\times10^{-1}$ $M_\odot$ yr^{-1}, and the kinetic energy outflow rates range from $\sim 1\times10^{37}$ erg s^{-1} to $\sim 6\times10^{40}$ erg s^{-1} (excluding the contribution from the velocity components that likely trace portion of the outflows in targets J0842+03, J0906+56, J0954+47, and J1005+12). In J0906+56, J0954+47, and J1005+12, where the outflows may be spatially unresolved, the lower limits of the mass outflow rates and kinetic energy outflow rates are $\sim$2–10 times higher than those obtained in the scenario where they are spatially resolved.

- The overall emission line widths measured from the spatially-integrated spectra of our targets, together with the results from samples of more luminous AGN studied in the recent literature, show a positive trend with increasing [O III] λ5007 luminosities. When normalized by the bolometric AGN luminosities, the kinetic energy outflow rates of these outflows are comparable to those of more luminous AGN in massive systems. The outflows in these dwarf galaxies act as scaled-down versions of those in more luminous AGN, in shallower potential wells.

- The outflows are likely driven by the central AGN, since i) the outflows are faster than typical outflows driven by stellar processes; ii) the AGN is powerful enough to drive the outflows given the efficiency of other low-redshift AGN; (iii) the lower limits of the ionized gas mass entrainment efficiency (i.e. mass outflow rates to SFR $\simeq$ 0.1–0.8, based on the upper limits on SFR estimated from the [O II] $\lambda\lambda$3726, 3729 emission) fall in the wide range seen in various studies of outflows in more luminous AGN, and may be uncomfortably high (with lower limits up to $\sim$3) for starburst-driven outflows in the low-z universe if the outflows are spatially unresolved in targets J0906+56, J0954+47, and J1005+12; (iv) the dwarf galaxies of our sample all lie either slightly or significantly below the main sequence of star-forming galaxies, whereas starburst-driven outflows typically take place in star-forming galaxies above that main sequence. However, we cannot formally rule out, based on energetic arguments, the possibility that the star formation activity in these galaxies also partially contributes to driving these outflows.

- A small but non-negligible fraction (at least 0.1%–6%) of the outflowing ionized gas in our targets has velocities large enough to escape from the host galaxies, if no additional drag force is present. These outflows may thus contribute to the enrichment of the circumgalactic medium in dwarf galaxies.

If such AGN-driven outflows are also present in dwarf galaxies at high redshifts, they will increase the porosity of these dwarf galaxies and thus their contribution to the reionization of the universe [e.g. Silk, 2017]. They may also help explain the current core-cusp controversy regarding the dark matter distribution in dwarf galaxies [e.g. Macciò et al., 2020]. A proper treatment of such AGN feedback will need to be included in seed black hole formation models [e.g. Mezcua, 2019].

Chapter 5: Fast UV Outflows and Strong He II Emission in Dwarf Galaxies with AGN

5.1 Introduction

Stellar processes have long been considered the main source of feedback in dwarf galaxies [e.g. Larson, 1974, Veilleux et al., 2005a, Heckman and Thompson, 2017, Martín-Navarro and Mezcua, 2018]. However, it is still debated whether such stellar feedback is effective enough to reproduce all the related properties of the dwarf galaxies we see today [e.g. Garrison-Kimmel et al., 2013, McQuinn et al., 2019]. Recent studies have revealed hundreds of active galactic nuclei (AGN) in dwarf galaxies through multi-wavelength observations [see a recent review by Greene et al., 2019]. AGN activity can release tremendous amount of energy, and AGN feedback has been widely accepted as a critical mechanism to regulate the formation and evolution of massive galaxies [e.g., Di Matteo et al., 2005, Booth and Schaye, 2009, Fabian, 2012]. Therefore, it is interesting to also consider the possible impact of AGN feedback in dwarf galaxies. Moreover, low-z dwarf galaxies possess properties close to galaxies at early epochs. Similar AGN feedback may also regulate the growth of (super)massive black hole seeds and first galaxies [e.g. Silk, 2017].

Evidence of AGN feedback in dwarf galaxies is emerging. For example, hints of star formation quenching induced by AGN feedback [Penny et al., 2018] and lower-than-expectation global HI content [Bradford et al., 2018] have both been reported in dwarf galaxies with AGN. From the theoretical perspective, analytic analyses [e.g. Silk, 2017, Dashyan et al., 2018] and new simulations [Koudmani et al., 2019, 2020] have all pointed out the possibly significant effects of AGN feedback in dwarfs. In addition to the negative feedback discussed above that suppresses the star formation, AGN-driven outflows may also trigger star formation activities within dwarf galaxies [Schutte and Reines, 2022].

Recently, a sample of 29 dwarf galaxies with AGN (stellar mass $\log(M_\star/M_\odot) \lesssim 10.2$) was observed with Keck LRIS long-slit spectroscopy [Manzano-King et al., 2019, Manzano-King and Canalizo, 2020]. This sample was chosen from dwarf galaxies at $z<0.05$ in SDSS showing properties in the optical consistent with AGN activity [i.e., broad Balmer lines, Seyfert-like line ratios on the BPT/VO87 [Baldwin et al., 1981, Veilleux and Osterbrock, 1987] diagrams and/or highly-ionized He II line emission; Reines et al., 2013, Moran et al., 2014]. Follow-up integral field spectroscopy of 8 of the 29 dwarf galaxies confirmed the existence of rapid outflows in 7 of them [Liu et al., 2020, L20 hereafter]. These outflows are primarily driven by the AGN, and are powerful enough to impose feedback on their host galaxies in a way similar to those more luminous AGN with massive hosts.

While the results from the optical emission lines are tantalizing, they only probe the relatively denser part of the outflows as the emission line strength is proportional to n_e^2. Absorption lines, instead, depend on column densities linearly and are thus more sensitive probes of the full extent of outflows. Blueshifted absorption features are unambiguous signatures of the outward motion of gas located in front of the source of continuum radiation. Rest-frame far-ultraviolet (FUV) spectroscopy provides access to multiple strong absorption features spanning a broad range of ionization states, which is essential for obtaining better measurements or tighter upper limits on the physical conditions of outflows.

Such FUV spectroscopy has been used extensively to probe ionized and neutral outflows triggered by AGN [e.g. Crenshaw and Kraemer, 2012] and/or star formation [Heckman et al., 2015, Heckman and Borthakur, 2016], in galaxies with starbursts [e.g. Martin et al., 2015] or recently-quenched star formation [e.g. Tripp et al., 2011]. To evaluate the AGN feedback via fast outflows in dwarf galaxies with the same criterion, a sample of dwarf galaxies with primarily AGN-driven outflows needs to be examined similarly.

In this paper, we present the results from a pilot HST/COS FUV spectroscopic study of three dwarf galaxies with evidence of AGN-driven outflows from L20. In Section 5.2, the data sets, the physical properties of the sources measured from the HST/COS and ancillary data, and the data reduction procedures are described. The detection and characterization of absorption-line-traced outflows and thus AGN feedback within the sample are presented in Section 5.3. The analysis of He II λ1640 emission lines detected in the sample is described in Section 5.4. Throughout the paper, we assume a ΛCDM cosmology with H_0 = 69.3 km s^{-1} Mpc^{-1}, $\Omega_{\rm m}$ = 0.287, and $\Omega_\Lambda = 0.713$ [Hinshaw et al., 2013].

5.2 HST and Ancillary Data

5.2.1 HST/COS Observations

We observed the three FUV-brightest dwarf galaxies with AGN-driven outflows from the sample studied in L20. The targets were observed with HST/COS through cycle 27 program (PID 15915; PI: W. Liu). The spectra of our targets were obtained in TIME-TAG mode through the

PSA using the medium resolution FUV grating, G130M. Four focal plane offset positions were adopted to reduce the impact of fixed-pattern noise associated with the micro-channel plate. We got all four FP-POS settings for all targets, and the wavelength setting was adjusted according to the redshift of the target and was selected to cover major absorption line/emission line features including C II λ1335, C IV $\lambda\lambda$1548, 1550, Si II λ1526, and Si IV 1394,1403.

5.2.2 Data Reduction and Ancillary Data

The raw data were processed and combined by the CALCOS pipeline v3.3.10. CALCOS corrects the data for instrumental effects, assigns a vacuum wavelength scale, and extracts flux-calibrated spectra. It applies a heliocentric correction to the final x1d files for each exposure, and combines the individual exposures to a single spectra when possible.

In addition to the HST/COS data, we retrieve key physical properties of our sources from L20. Furthermore, the circular velocity of the objects, v_{circ} are derived base on their stellar mass, adopting the baryonic Tully-Fisher relation calibrated in Reyes et al. [2011] as $log(v_{cir}) = 0.278log(M_*) - 0.67$, with root-mean-square (RMS) residuals of 0.1 dex in v_{circ}. This relation was derived using spatially-resolved 2D gas kinematics in low-redshift emission-line galaxies $v_{cir} = \sqrt{2}(v_{rot}^2 + 2\sigma^2)^{1/2}$, where v_{rot} and σ are the rotation speed and mean value of the line-of-sight velocity dispersion, respectively. These results are summarized in Table 5.1.

Table 5.1. Properties of the Targets

Name (1)	Short Name (2)	Redshift (3)	$\log(M_{\rm stellar})$ (4)	$\log(v_{circ})$ (5)	R_{50} (6)	$\log(L_{[OIII]})$ (7)	$\log(L_{AGN,[OIII]})$ (8)	$\log(L_{AGN,FUV})$ (9)	SFR (10)
SDSS J090613.75+561015.5	J0906+56	0.0467	9.36	1.9±0.1	1.5	$41.15^{+0.01}_{-0.01}$	43.7	42.9	<0.3
SDSS J095418.16+471725.1	J0954+47	0.0327	9.12	1.9±0.1	2.0	$41.36^{+0.02}_{-0.02}$	43.9	42.8	<0.3
SDSS J100935.66+265648.9	J1009+26	0.0145	8.77	1.8±0.1	0.7	$40.48^{+0.01}_{-0.01}$	43.0	42.0	<0.1

Note. — Column (1): SDSS name of the target; Column (2): Short name of the target used in this paper; Column (3): Redshift of the target measured from the stellar fit to the spectrum integrated over the KCWI data cube; Column (4): Stellar mass in unit of solar mass and in logarithm from the NASA Sloan Altas (NSA)[1]; Column (5): Circular velocity in logarithm derived from stellar mass adopting calibration in Reyes et al. [2011]; Column (6): Half-light radius from the NSA, in unit of kpc; Column (7): Total [O III] λ5007 luminosity based on the observed total [O III] λ5007 fluxes within the field of view of the KCWI data without extinction correction, in units of erg s^{-1}; Column (8): Bolometric AGN luminosity, based on the extinction-corrected [O III] luminosity, in units of erg s^{-1}. Column (9): Bolometric AGN luminosity, based on the monochromatic continuum luminosity L_{1320} from HST/COS data and the CLOUDY AGN SED. See Appendix D.1 for more details; Column (10): Upper limit on the star formation rate based on the extinction-corrected [O II] $\lambda\lambda$3726, 3729 flux from the KCWI data, in units of $M_\odot$ yr^{-1}. Here we assume that $1/3$ of the [O II] $\lambda\lambda$3726, 3729 emission is from the star formation activity, following Ho [2005].

5.3 Outflows Traced by Blueshifted Absorption Features

5.3.1 Detection and Characterization of Outflows

Two sources in our sample, J0906+56 and J0954+47, show clear evidence of outflows traced by absorption features.

In J0906+56, only blueshifted C IV $\lambda\lambda$1548, 1550 absorption features are detected on top of broad, C IV emission (Fig. 5.1 and D.1). In J0954+47, blueshifted absorption features with similar profiles are seen in C II λ1335, C IV $\lambda\lambda$1548, 1550, Si II λ1526, and Si IV 1394,1403. Additionally, broader (reaching $\sim$5000 km s^{-1}) absorption troughs are seen in both C IV and Si IV doublets. These absorption troughs may be accompanied by redshifted broad emission line features (with peak S/N of $\sim$ 3), which is apparently consistent with P-Cygni profiles tracing spatially unresolved stellar wind or AGN wind in this object. If this broad, blueshifted trough is indeed a broad absorption line (BAL) like those seen in luminous quasars, it would be the first BAL ever discovered in a dwarf AGN.

As for J1009+26, only C II λ1335 and Si IV 1394,1403 absorption features at systemic velocities are unambiguously detected, broadly consistent with the relatively modest outflow velocity ($\sim$ 20 km s^{-1}) seen in [O III] λ5007 emission from L20. Zoom-in spectra for these absorption features are shown in Fig. D.3 in the Appendix D.2. The object shows an C IV doublet ratio $<$ 2 (i.e., less than the theoretical expectation), which may be explained by blueshifted C IV absorption features on top of the emission if the intrinsic C IV emission line shares the same velocity profile as He II. However, the Si IV doublet (likely tracing the same phase of ionized gas as C IV) in this object does not show similar blueshifted absorption features.

To measure the properties of the outflows in J0906+56 and J0954+47, we first fit the continuum/emission line profiles to obtain the normalized absorption line profiles in these objects. For the intrinsic C IV emission line doublet of J0906+56, we choose fitting windows with no absorption signatures and fit them with two Gaussian profiles with the same centroid velocity and velocity dispersions, and a fixed flux ratio of 2. For J0954+47, we focus on the C II $\lambda1335$, Si IV $\lambda1394$, and Si II $\lambda1526$. These absorption features are either not or only mildly contaminated by nearby emission and/or broad absorption features (See Fig. D.2) and the obtained normalized absorption line profiles are relatively more robust. Specifically, the continuum near C II $\lambda1335$ is fit with a linear function. The broad absorption trough in the vicinity of Si IV $\lambda1394$ and Si II $\lambda1526$ are both fit with 2nd-order polynomials. Additionally, for C IV $\lambda1550$ absorption, we aim to obtain an approximate profile of it as it is blended with the nearby C IV emission, C IV $\lambda1548$ absorption and broad C IV absorption trough. The intrinsic C IV $\lambda\lambda1548, 1550$ emission is fit with two Gaussian profiles with the same centroid velocity and velocity dispersion, and a fixed flux ratio of 2. The fitting window is chosen as the presumably pure emission-line wing of the C IV $\lambda1550$ emission, and the centroid velocity and velcity dispersion are fixed to those of the He II $\lambda1640$ emission line in this object. As we only care about the spectral range of $\gtrsim -500$ km s^{-1} of C IV $\lambda1550$ where the contribution from the broad C IV absorption trough should be trivial, the broad trough is thus not modeled in the fit. For C IV $\lambda1548$ and Si IV $\lambda1394$, the nearby emission/absorption features are more complex than those near C IV $\lambda1550$ and the attempt to constrain the intrinsic absorption line profiles results in huge uncertainties. These two features are thus not considered in the following analyses.

The normalized absorption features (excluding the C IV $\lambda1550$ in J0954+47 due to its large uncertainty as stated above) were fit with multiple Voigt profiles, which were convolved with HST/COS line-spread function (LSF)[2]. We adopted a customized software built on the non-linear least-squares fit implemented in LMFIT to search for the best-fit model. In our software, a velocity component is added to the model if the Bayesian Information Criterion (BIC) [Ivezić et al., 2019] decreases, and this process stops when the minimum BIC value is found. A total of 2 and 4 Voigt profile components are required by the best-fits of J0906+56 and J0954+47, respectively. The best-fit continuum/emission line profiles and the best-fit absorption line profiles of the two objects are shown in Fig. 5.1 and Fig. 5.2, respectively. Specifically, as shown in Fig. 5.2, the C II, Si II, and Si IV absorption features of J0954+47 are fit simultaneously where the centroid velocities and velocity dispersions of the same velocity components are tied together. The final results from the absorption line fits are listed in Table 5.2.

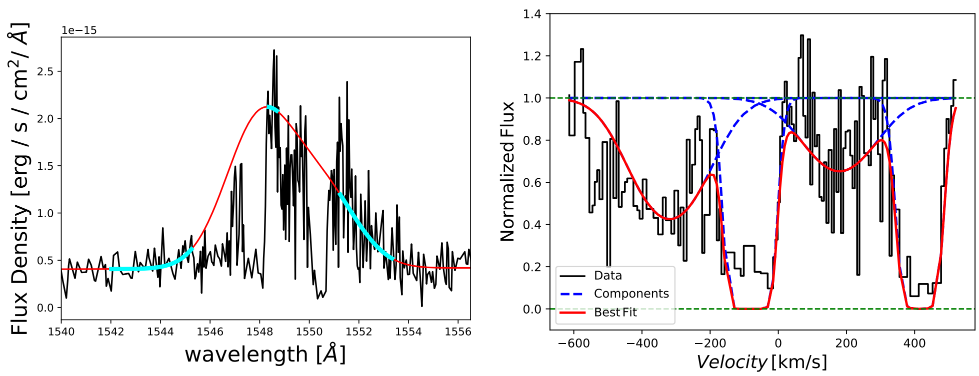

Figure 5.1: The fit to the C IV absorption feature in J0906+56. **Left:** The best-fit C IV emission line doublet model (red) with two Gaussian components to recover the unabsorbed emission line profile. The fitting windows are marked on the best-fit model in cyan; **Right:** The best-fit model (red) of the absorption features normalized to the best-fit emission line model shown in the left panel. The individual Voigt profile components are shown in blue dashed lines. The velocity is with respect to the systemic velocity.

[2]Tabulated on the HST/COS website https://www.stsci.edu/hst/instrumentation/cos/performance/spectral-resolution

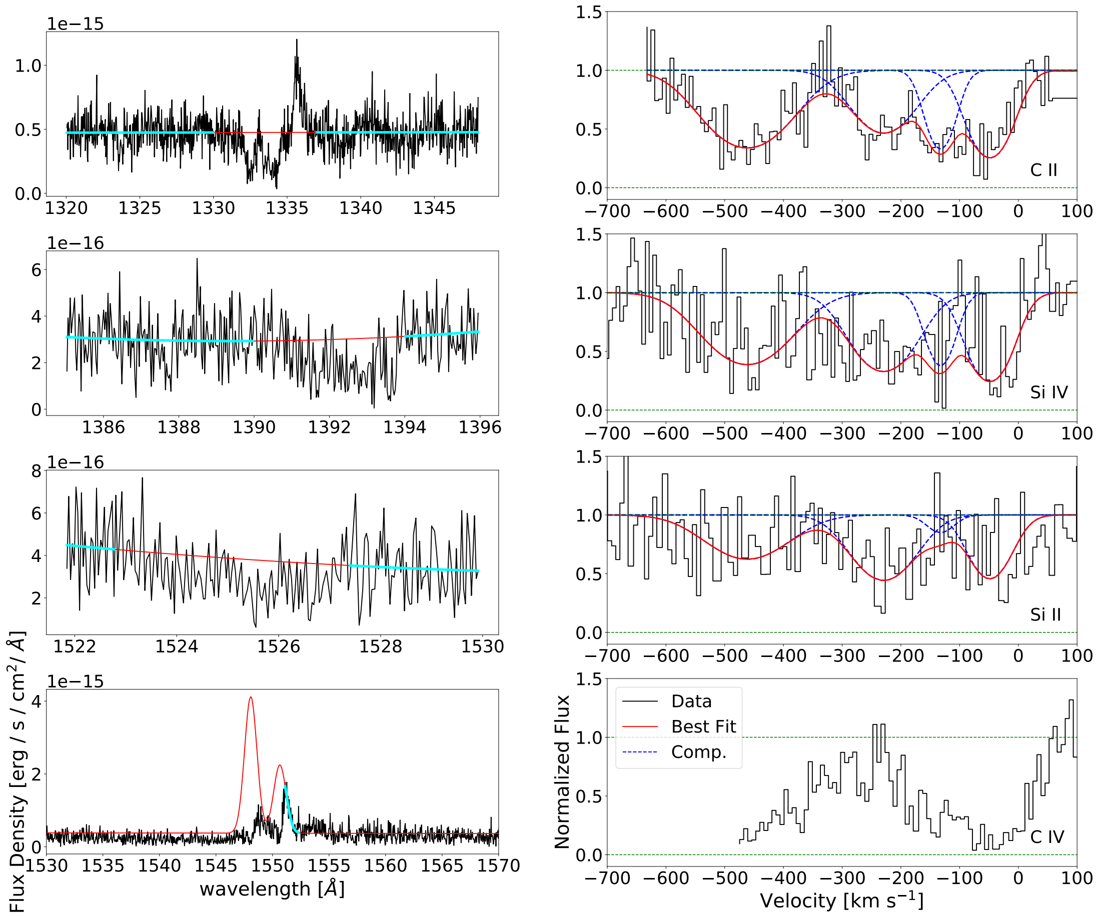

Figure 5.2: The C II λ1335, Si IV λ1394, Si II λ1526, and C IV λ1550 absorption features in J0954+47, from top to bottom. **Left:** The best-fit continuum/emission line model (red) in the vicinity of the absorption feature. The fitting windows are marked on the best-fit model in cyan. For C II, the continuum is fit with a linear function. For Si IV and Si II, the broad absorption trough in the vicinity of each absorption feature is fit with a 2nd-order polynomial. For C IV λ1550, the intrinsic C IV $\lambda\lambda$1548, 1550 emission is fit with two Gaussian profiles with the same centroid velocity and velocity dispersion, and a fixed flux ratio of 2. The centroid velocity and velocity dispersion are fixed to those of the He II λ1640 emission in this object. The UV continuum is fit with a linear function to featureless regions beyond the plotting range of the figure. Note that the blueshifted, broad C IV absorption trough and the possible, redshifted, broad C IV emission line wing are not considered in our fit due to large uncertainty. **Right:** The best-fit model (red) of the absorption features normalized by the best-fit continuum/emission line model shown in the left panel. The spectra are in the rest-frame of the corresponding absorption features. The individual Voigt profile components are shown in blue dashed lines. In the fit, the velocity and b parameter (line width) of individual components for all three lines (C II λ1335, Si IV λ1394, Si II λ1526) are tied together. The C IV λ1550 is excluded in the fit, but the normalized absorption line profile is shown for visual comparison with the other three absorption features.

5.3.2 The Outflow in J0954+47

Blueshifted absorption features of various ions in J0954+47 share similar velocity distributions (see Fig. 5.2), likely tracing the same outflow within this object. In the following, we derive the physical properties of the outflow in J0954+47 to evaluate the power source and impact of it. Note that we refer to the entire absorption feature as the entire outflow, and the most blueshifted velocity component in the best-fit model shown in Fig. 5.2 as the high-v outflow hereafter.

5.3.2.1 Photoionization Modeling

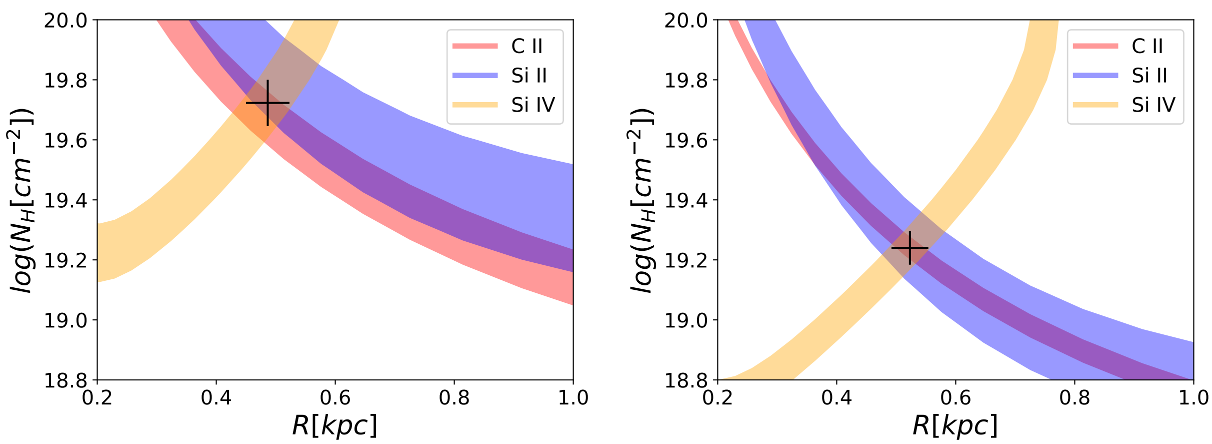

Figure 5.3: Phase plot showing the ionization solutions for the entire outflow (**left**) and the high-v outflow (**right**) of J0954+47. Each colored contour represents the locus of models (outflow radius R, hydrogen column density N_H) which predicts a ion column density consistent with the observed value of that ion. The width of the locus corresponds to the 1-σ uncertainty in the observed ion column density. The center of the black cross indicates the best solution based on the χ^2 minimization and the x and y sizes of the cross indicated the corresponding uncertainties. See Section 5.3.2.1 for more details.

We have adopted CLOUDY [Ferland et al., 1998] to model the properties of both the entire outflow and the high-v outflow adopting the measured column density of the outflow components of C II, Si II, and Si IV λ1394, assuming that they trace the same outflowing material.

Table 5.2. Properties of the Outflows

Object	Absorber	Comp.	v_{50} [km s^{-1}]	$log(N_{ion})$ [cm^{-2}]	$log(N_H)$ [cm^{-2}]	R [kpc]	$log(\dot{m}_{out})$ [M$_\odot$ yr^{-1}]	$log(\dot{p}_{out})$ [$dynes$]	$log(\dot{E}_{out})$ [$erg\ s^{-1}$]
(1)	(2)	(3)	(4)	(5)	(6)	(7)	(8)	(9)	(10)
J0906+56	C IV	average	-130 ± 40	15.3±0.1	...	...	... ...	...	
		high-v comp.	-320 ± 30	14.4 ± 0.1	...	...	...	...	...
J0954+47	C II			15.0 ± 0.1					
	Si IV	average	-260 ± 20	14.4 ± 0.1	19.7 ± 0.1	0.49 ± 0.04	-0.1 ± 0.2	33.2 ± 0.2	40.6 ± 0.2
	Si II			14.7 ± 0.2					
	C II			14.60 ± 0.04					
	Si IV	high-v comp.	-460 ± 10	13.90 ± 0.07	19.20 ± 0.06	0.52 ± 0.03	-0.3 ± 0.3	33.2 ± 0.3	40.9 ± 0.3
	Si II			14.10 ± 0.15					

Note. — Column (2): Transition considered; Column (3): Velocity component considered in the calculation. "average" indicates the mean values averaged over the entire absorption feature. "high-v comp." indicates the component with the highest outflow velocity in the best-fit model. Column (4): 50th-percentile velocity; Column (5): Ion column density in logarithm; Column (6): Hydrogen column density in logarithm derived from Section 5.3.2.1; Column (7): Outflow radius in kpc derived from Section 5.3.2.1; Column (8): Mass outflow rate in logarithm; Column (9): Momentum outflow rate in logarithm; Column (9): Kinetic energy outflow rate in logarithm.

We set up the modeling as follows: we assume that the ionizing spectrum is an typical AGN continuum described in the Section 6.2 of CLOUDY mannual[3], which gives $f_\nu = \nu^{\alpha_{uv}} exp(-h\nu/kT_{BB}) exp(-kT_{IR}/hv) + a\nu^{\alpha_x}$. T_{BB} is the temperature of the "Big Bump" component of the AGN, a rising power law with a high-energy exponential cut-off. α_{uv} is the low-energy slope of the "Big Bump" component. α_x is the slope of the X-ray component. The coefficient a is adjusted to produce the correct α_{OX}. We normalize this AGN continuum at 1320 Å to the observed flux density of the COS spectrum. We also set the X-ray to UV ratio, α_{OX}, to -1.9 as measured from Baldassare et al. [2017b]. We set the other three free parameters, T_{BB}, α_{uv}, and α_x to their default values (1.5×10^5 K, -0.5 and -1, respectively, which are typical for AGN) provided by CLOUDY. Two more parameters are needed for the modeling, the electron density n_e and metal abundance. Due to the absence of C II* λ1336 absorption, we obtain an upper limit of $\sim$ 10 cm^{-3} for n_e adopting the upper limit on the C* II/C II ratio[4]. On the other hand, we do not expect n_e to be much less than 10 cm^{-2}, given that the typical n_e for outflows in star-forming dwarf galaxies is $\gtrsim$ 10 cm^{-2} [e.g. Xu et al., 2022]. Therefore, we set n_e to 10 cm^{-2} in our following analysis. In addition, we set the metal abundance to solar values, the same values obtained from the photoionization modeling of the optical emission lines (L20).

With the model set-up above, the column density of each absorption feature (with its 1-σ uncertainty) defines a locus in the 2D diagram of total hydrogen column density N_H versus outflow radius R[5]. Following the same approach adopted in previous work [e.g. Borguet et al., 2012, Arav et al., 2013], the best-fit total hydrogen column density N_H and the outflow radius R is then obtained by minimizing the χ^2 :

[3] `https://gitlab.nublado.org/cloudy/cloudy/-/wikis/home`

[4] Adopting ChiantiPy, the Python interface to the CHIANTI atomic database for astronomical spectroscopy

[5] The default independent variable in CLOUDY is ionization parameter $U = \frac{Q}{4\pi c n_e R}$. With a given n_e, we convert U into R, the outflow radius.

$$\chi^2 = \sum_i \left(\frac{logN_{i,mod} - logN_{o,obs}}{logN_{i,obs} - log(N_{i,obs} \pm \sigma_i)}\right)^2 \tag{5.1}$$

where, for ion i, $N_{i,obs}$ and $N_{i,mod}$ are the observed and modeled column densities, and σ_i is the error in the measured column density.

The best-fit N_H and R are $19.7 \pm 0.1 cm^{-2}$ and 0.49 ± 0.04 kpc for the entire outflow and $19.20 \pm 0.06 cm^{-2}$ and 0.52 ± 0.03 kpc for the high-v outflow, respectively. The 1-σ errors are estimated as the full x and y extent of the overlapping region of the three loci. These results are listed in Table 5.2.

5.3.2.2 Energetics

With the N_H and R obtained above, the mass, momentum and kinetic energy outflow rate can then be calculated, following the equations:

$$\dot{m}_{out} = \Omega N_H \mu m_p R v \tag{5.2}$$

$$\dot{p}_{out} = \Omega N_H \mu m_p R v^2 \tag{5.3}$$

$$\dot{E}_{out} = \Omega N_H \mu m_p R v^3 \tag{5.4}$$

In the equations above, v is v_{50} of the best-fit absorption line profile. The hydrogen column density, N_H, and the outflow radius, R, are obtained from the photoionization modeling described in Section 5.3.2.1. Ω is the solid angle subtended by the outflow as seen from its origin. While

Ω cannot be measured directly from our data, the outflow likely has a wide opening angle: the outflow seen in the optical emission lines, which should be physically connected with the outflow seen in absorption, favors such geometry (L20). In addition, no evidence of partial covering is present based on the absorption line profiles. Therefore, we set $\Omega = 4\pi$ in our calculation. The final results are recorded in Table 5.2.

Furthermore, the spatial extent and energetics of the outflow traced by the absorption features are consistent with those derived from the blueshifted [O III] λ5007 emission line (L20) which has $R \lesssim 1.6$ kpc and $\dot{E}_{out} > 39.6$ erg s^{-1}. This suggests that the blueshifted absorption and emission features are likely tracing the same galactic outflow in this object.

5.3.2.3 Comparison with Starburst-driven Outflows

Star-formation-driven outflow is a popular feedback mechanism in dwarf galaxies. To understand the nature and impact of the fast outflow in J0954+47, we compare its properties with those of star-formation-driven outflows in low-z galaxies observed by *HST/COS*.

As shown in Fig. 5.4, we plot the outflow velocities as function of SFR[6] and circular velocities for both J0954+47 and those from Chisholm et al. [2015] or from Xu et al. [2022]. In Chisholm et al. [2015], the outflow velocity is measured as the velocity at half the equivalent width (i.e., the same as our v_{50} definition) of the overall best-fit Si II λ1260 profile. In Xu et al. [2022], the outflow velocity is measured as the median v_{50} of the blueshifted components in the best-fit model for all transitions detected, including O I λ1302, C II λ1335, Si II 1190, 1193,

[6] The upper limit on SFR for J0954+47 is derived from the [O II] $\lambda\lambda$3726, 3729 luminosity [based on Ho, 2005, see L20 for details], while the SFR of star-forming galaxies from Xu et al. [2022] are obtained from Berg et al. [2022], which are based on UV+optical spectral energy distribution (SED) fitting, and the SFR of star-forming galaxies from Chisholm et al. [2015] are obtained adopting both IR and UV data. There may be systematic inconsistency among these three types of SFR measurements, but we do not expect that such inconsistency is large enough to change our results qualitatively.

1260, 1304, 1526, Si III λ1206, and Si IV 1394,1403. To make decent comparisons, therefore, we show two outflow velocities for J0954+47: labeled in red is v_{50} of the overall absorption line profile as in Chisholm et al. [2015], and labeled in blue is v_{50} of the high-v outflow, similar to that defined in Xu et al. [2022].

It is clear that, with a SFR of <0.3 $M_\odot$ yr^{-1}, the outflow in J0954+47 is much faster than those in star-forming galaxies with similar SFR. Given a certain SFR, the presence of AGN boosts the outflow velocity in this dwarf galaxy. At the circular velocity (v_{circ}) of $\sim$ 70 km s^{-1} based on its stellar mass, the outflow in J0954+47 is also faster than those in star-formation-driven outflows from Chisholm et al. [2015] and is among the fastest outflow seen in the star-formation-driven ones from Xu et al. [2022]. This suggests that for a given gravitational potential, AGN can at least drive an outflow as fast as those seen in dwarf galaxies with extreme starbursts.

5.3.2.4 Energy Source of the Outflow

In this section, we show that the energetic outflow in J0954+47 is primarily driven by the AGN rather the star formation activity.

On the one hand, the AGN is powerful enough to drive the outflow, since the ratio of the kinetic energy outflow rate to AGN luminosity, $\dot{E}_{out}/L_{AGN}$, is $\sim$0.6% (the average for the entire outflow) or $\sim$1.2% (high-v outflow), comparable to low-z AGN with outflow measured with the same technique (Fig. 5.5; the L_{AGN} adopted here is derived based on the HST/COS data and the AGN template from CLOUDY. See Appendix D.1 for more details). On the other hand, the star formation activity seems not capable of providing enough momentum. The total momentum injection rate supplied by the star formation activity, $\dot{p}_{in} = 4.6 \times 10^{33} SFR[\mathrm{M}_\odot\ yr^{-1}]\ dynes$, which is the sum of the hot wind fluid driven by thermalized ejecta of massive stars [Chevalier and Clegg, 1985] and radiation pressure [Murray et al., 2005]. A SFR < 0.3 M$_\odot$ yr^{-1} translates into an upper limit on the momentum injection rate of $\sim 1.4 \times 10^{33}$ dynes, which is lower than the measured momentum outflow rate $\dot{p}_{out} \simeq 1.6 \times 10^{33}$ dynes. Apparently, the star formation activity has difficulty driving the observed outflow [with possible exception in extreme cases, e.g., see the discussion of the outflows in three star-forming galaxies with $\dot{p}_{out} > \dot{p}_{in}$ in Xu et al., 2022]. Note, however, that the measured momentum outflow rate may be overestimated if the solid angle of the outflow Omega is smaller than 4π.

5.3.2.5 The Impact of the Outflow

The outflow in J0954+47 may escape the galaxy due to its large velocity. We estimate the escape velocity as $v_{esc}^2 = 2v_{circ}^2[1 + ln(r_s/R)]$ where the mass distribution is modeled as a truncated isothermal sphere: r_s is the radius of the sphere, and R is the radius where the v_{esc} is calculated as $v_{esc} \simeq 3v_{circ}$ with $r_s/R \simeq 33$ as adopted in literature [e.g., see Veilleux et al., 2020, for a brief discussion]. The average velocity of the entire outflow (∼260 km s^{-1}) or the velocity of the high-v outflow (∼460 km s^{-1}) in J0954+47 is comparable to or significantly larger than v_{esc} of the system (∼220 km s^{-1}). A large portion (∼50% in terms of absorption line equivalent width or EW) of the ionized gas traced by the absorption may escape the system, which may help enrich the circumgalactic medium.

The outflow also carries significant amount of mass, momentum and kinetic energy. We obtain a mass loading factor (i.e., mass outflow rate over SFR) of $\gtrsim$3.4 ($\gtrsim$1.8) for the entire outflow (high-v outflow), suggesting that the outflowing gas can transport material out of the galaxy more efficiently than the gas consumption by star formation. The kinetic energy outflow rate to AGN luminosity, $\dot{E}_{out}/L_{AGN}$, is ∼0.6% (∼1.2%) for the average of the entire outflow (high-v outflow), which is comparable to (larger than) the expectations from some simulations of AGN feedback [e.g., Hopkins and Elvis, 2010] that only require ∼0.5% of AGN bolometric luminosity to be injected into the outflow for effective AGN feedback. This indicates that the outflow is powerful enough to provide AGN feedback to its dwarf host galaxy[7].

5.4 He II λ1640 Emission

5.4.1 Detection and Basic Properties

Strong He II λ1640 emission lines are detected in two objects, J0954+47 and J1009+26 (see Fig 5.6, D.2, and D.3), which is consistent with the AGN nature of these two objects, given the high ionization potential of He^{2+} (∼54.4 eV). The EW of He II are 2.71$\pm$0.14 Å and 7.00$\pm$0.29 Å, respectively, which are broadly consistent with the high EW seen in AGN [with a median He II EW of ∼8 Å; e.g. Hainline et al., 2011, Cassata et al., 2013]. The He II/C IV flux ratios of the two objects are ∼0.8 and ∼1.7, which fall in the range predicted by typical AGN photoionization models [e.g. Feltre et al., 2016]. In addition, the typical observed He II/C IV ratio of Type 2 quasar/AGN is ∼0.7 [e.g. McCarthy, 1993, Corbin and Boroson, 1996, Humphrey et al., 2008, Matsuoka et al., 2009].

The He II in these two sources are narrow, with FWHM of 120$\pm$10 km s^{-1} and 110$\pm$5 km

[7] Note that the prediction from simulations are usually the kinetic coupling efficiency, the fraction of the AGN bolometric luminosity coupled to gas near the black hole. This is always larger than the observed $\dot{E}_{out}/L_{AGN}$: Even for an energy-driven large-scale outflow, only a portion of the original nuclear wind power ends up in kinetic form, where the rest of the energy is may be used up in doing work against the gravitational potential and ambient pressure along the way [Harrison et al., 2018].

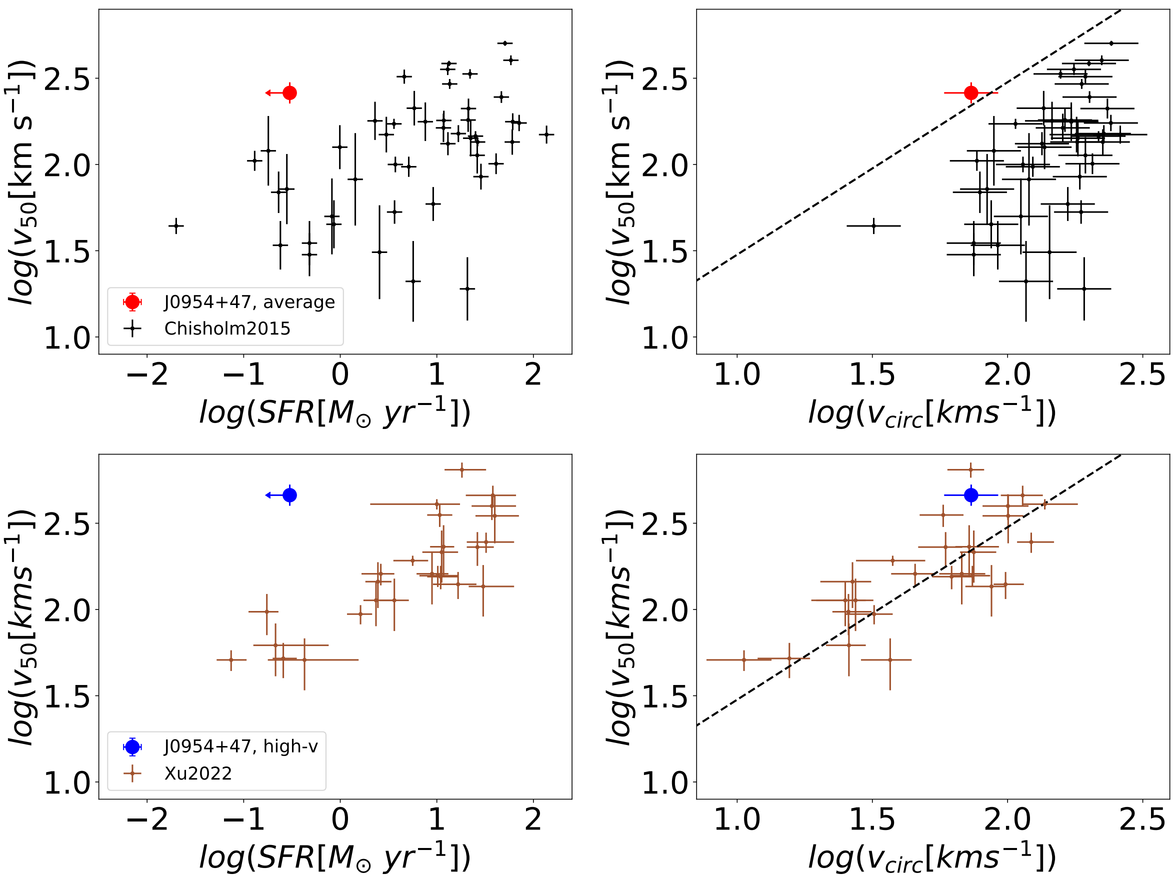

Figure 5.4: Outflow velocity (v_{50}) as function of star formation rate (left panels) and circular velocity (right panels) based on the overall absorption feature (entire outflow; red) and the highest velocity component in the best-fit (high-v outflow; blue) of J0954+47. In the upper panels, the black data points are the Si II outflows in star-forming galaxies from Chisholm et al. [2015]. In these two panels, the v_{50} are all measured from the overall absorption features; In the bottom panels, the outflows in the 45-source CLASSY sample from Xu et al. [2022] are shown in brown. For each object, v_{50} is the median value of all absorption features detected. In these two panels, the v_{50} are measured from the highest velocity component of the best-fit models. The black dashed lines in the two right panels indicate the expected escape velocity $v_{esc} \simeq 3v_{circ}$.

s^{-1} for J0954+47 and J1009+26, respectively. Therefore, these are not broad He II features as observed in Wolf-Rayet stars/galaxies [e.g. Abbott and Conti, 1987]. Meanwhile, to our knowledge, for star-forming galaxies in the nearby universe, relatively strong and narrow nebular He II emission has only been observed in metal-poor sources [e.g. Berg et al., 2016, Senchyna et al., 2017]. However, the EW of these He II lines (up to ∼1.7 Å as reported in these two references) are still lower than those of J0954+47 and J1009+26. Additionally, the metallicity of the latter two objects, based on the modeling of optical line ratios from L20, are also close to solar value.

Moreover, for J0906, the He II λ1640 line is not covered by the spectral range, but the detection of He II λ4686 emission line in this source implies the existence of He II λ1640.

Overall, the He II λ1640 emission lines detected in our sample are consistent with an AGN origin. A detailed ionization diagnosis adopting all FUV, optical, and Near-IR emission lines with various ionization potentials will be the subject of a future paper. The hard ionization spectra from the AGN in dwarf AGN like our objects may lead to high escape fractions of ionizing photons, which, if present in the early universe, may be an interesting contribution to cosmic reionization [e.g. Madau and Haardt, 2015, Robertson et al., 2015].

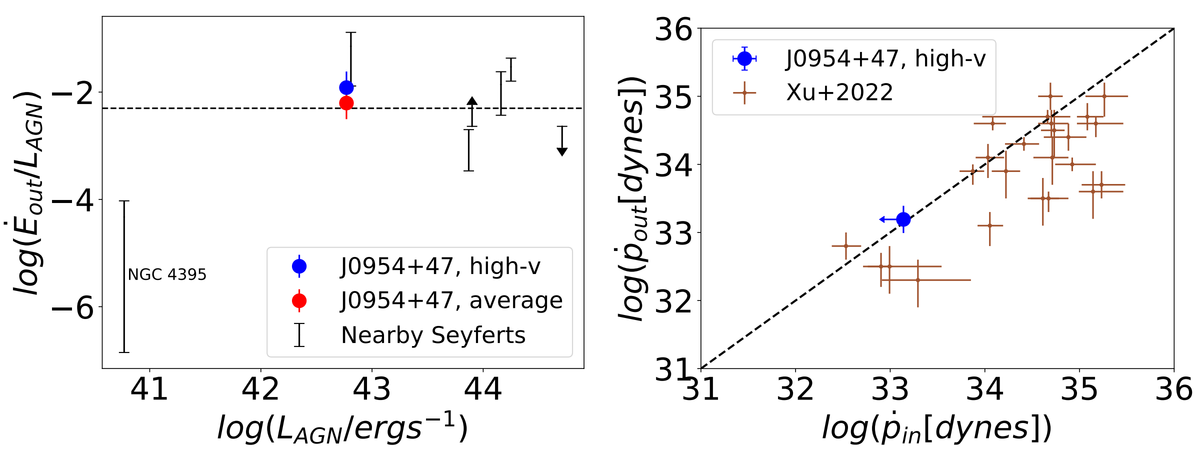

Figure 5.5: **Left:** Ratio of kinetic energy outflow rate to AGN luminosity as a function of AGN luminosity for the EW-weighted average of the entire outflow (red) and for the high-v outflow (blue) of J0954+47. Also shown in black are the X-ray and FUV absorber-traced outflows in nearby Seyferts from Crenshaw and Kraemer [2012]. Note that in the bottom left corner is the outflow in the archetype dwarf Seyfert 1, NGC 4395. The horizontal dashed line at 0.5% is the prediction for effective AGN feedback from Hopkins and Elvis [2010]. **Right:** Momentum outflow rate versus expected momentum injection rate from the star formation activity (see Section 5.3.2.4) for the high-v outflow in J0954+47 (blue) and those in low-z star-forming galaxies from Xu et al. [2022]. The dashed line indicates the 1:1 equality line.

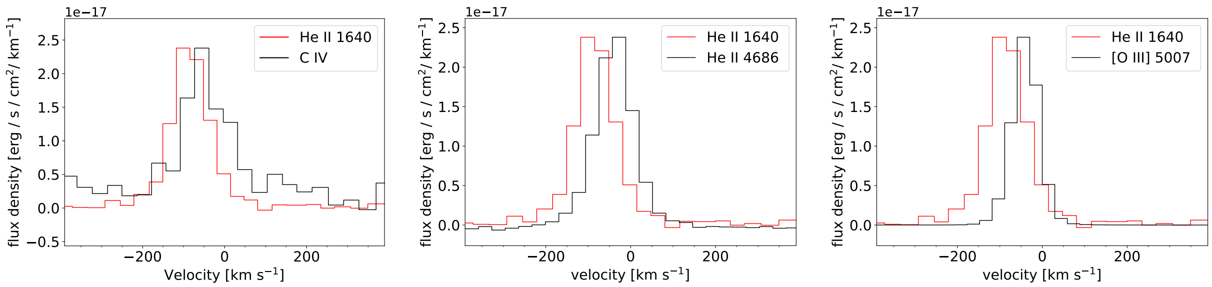

Figure 5.6: He II λ1640 emission line profile compared with C IV λ1550 (left), He II λ4686 (middle) and [O III] λ5007 (right) emission line profiles, respectively. All spectra are continuum subtracted. The He II λ1640 emission line is in its original flux scale while all other emission lines are re-scaled to have the same peak flux density as that of He II λ1640. The systemic velocity is determined from the stellar kinematics based on the IFS data from L20.

5.4.2 Blueshifted He II λ1640 Emission Tracing Highly-ionized Outflow in J1009+26?

An interesting characteristic of the He II emission line in J1009+26 is its blueshift. As shown in Fig. 5.6, v_{50} of He II λ1640 is ~ -90 km s^{-1} with respect to the systemic velocity based on the stellar kinematics measured in L20. As a comparison, v_{50} of C IV $\lambda\lambda$1548, 1550, He II λ4686, and [O III] λ5007 are ~ -50 km s^{-1}, ~ -20 km s^{-1}, and ~ -20 km s^{-1}, respectively. Among these emission lines, He II is the most blueshifted one.

One likely origin of the blueshifted He II λ1640 emission line is a highly-ionized AGN wind. As mentioned in Section 5.4.1, He II λ1640 is likely originating from the highly ionized gas near the central AGN. As a comparison, the C IV $\lambda\lambda$1548, 1550 and [O III] λ5007 may have a significant contribution from the ISM given their lower ionization potential. In addition, The line width of He II λ1640 is also larger than those of C IV $\lambda\lambda$1548, 1550 and [O III] λ5007. If these line widths reflect the virial motion of the gas, then the larger line width of He II λ1640 suggests that it is closer to the central engine of the AGN. Similar phenomenon has been seen in luminous

AGN [e.g. Fig. 14.10 in Osterbrock and Ferland, 2006]. The blueshifted He II λ1640 thus traces the highly-ionized AGN winds, while the $|v_{50}|$ of C IV $\lambda\lambda$1548, 1550 and [O III] λ5007 are smaller due to the contamination from the relatively more quiescent and static ISM.

The blueshift of He II λ1640 with respect to He II λ4686 might be caused by the heavier attenuation in the FUV than in the optical: The red emission line wing of He II λ1640 originating from the material on the far-side of the AGN is attenuated by gas/dust near the AGN more severely than that of He II λ4686. The He II λ1640 is thus more blueshifted due to the weaker red emission line wing. This is consistent with the fact that He II λ1640 is slightly narrower than He II λ4686, with 80-percentile line width W_{80} of 130 ± 30 and 160 ± 40, respectively.

5.5 Summary

In this paper, we present the results from a pilot HST/COS spectroscopy program to examine three dwarf galaxies with primarily AGN-driven outflows from the sample studied in Liu et al. [2020]. The main results are summarized as follows:

- Blueshifted absorption features tracing fast outflows are detected in two of the three objects. In object J0954+47, the outflow is detected in multiple transitions including C II, C IV, Si II, and Si IV. The outflow velocity is ~ -460 km s^{-1} for the high velocity component or ~ -230 km s^{-1} averaged over the entire absorption feature. This outflow is much faster than those in star-forming galaxies with similar star formation rates, and possesses a velocity comparable to those fastest outflows in star-forming galaxies with similar circular velocities.

- In J0954+47, the radius of the outflow, based on the results from photoionization modeling with CLOUDY, is estimated to be $\sim$0.5 kpc. The velocity of this outflow exceeds the escape velocity of the system, suggesting that a large fraction of the outflowing gas may escape the system. This outflow may help deposit energy into the circumgalactic medium and enrich it with metals.

- The outflow in J0954+47 carries significant amount of mass, momentum and kinetic energy. With a mass loading factor (i.e., mass outflow rate over SFR) of $\gtrsim$3.4 ($\gtrsim$1.8) averaged over the entire outflow (for the high-v outflow), the outflow can likely transport more material out of the galaxy than that ends up in stars.

- The kinetic energy outflow rate to AGN luminosity, $\dot{E}_{out}/L_{AGN}$, is $\sim$0.6% ($\sim$1.2%) averaged over the entire outflow (for the high-v outflow), which is comparable to (larger than) the expectations from some simulations of AGN feedback.

- Strong He II λ1640 emission lines are detected in two objects where the transition is covered by the observation. The EW and FWHM of the He II, and the C IV/He II ratios are consistent with an AGN origin. In one object J1009+26, the He II emission line is blueshifted with respect to the systemic velocity and is the most blueshifted line among all strong FUV and optical emission lines in this object. This blueshifted He II emission line is likely tracing a highly-ionized AGN wind in this object.

Chapter 6: Summary and Future Work

The focus of this thesis is AGN feedback via quasar/AGN-driven outflows in ULIRGs and dwarf galaxies.

6.1 AGN Feedback in ULIRGs

6.1.1 Summary

In the first half of the thesis, I have primarily investigated two aspects of AGN feedback via powerful outflows in nearby ULIRGs.

In Chapter 2, I focus on the blueshifted Lyα emission, and the highly-ionized, O VI and N V quasar winds in the ULIRGs. The main results are as follows:

- Lyα emission with blueshifted velocity centroids and/or wings is prevalent in our sample. The equivalent widths of the Lyα emission increase with increasing AGN luminosities and AGN bolometric fractions. The blueshift of the Lyα emission correlate positively with that of the [O III] λ5007 emission tracing ionized gas outflows, which suggests that the blueshifted Lyα emission likely traces the same outflows.

- The Lyα escape fractions tend to be slightly larger in objects with stronger AGN and larger outflow velocities.

- Blueshifted O VI and/or N V absorption features, indicative of quasar winds, are robustly detected in half of the sources with good continuum signal-to-noise ratios. Such outflows are more frequently detected in the X-ray weak or absorbed sources. The absorption equivalent widths, velocities and velocity dispersions of these outflows are also higher in the X-ray weak sources. These results suggest that these outflows are likely radiatively driven, since strong X-ray emission will over-ionize gas and reduce the radiative force greatly.

In Chapter 3, I turn to look at the giant, X-ray emitting halo of a nearby ULIRG Mrk 273, as well as the dual AGN activity and extended highly-ionized gas in it (Chapter 3). The main findings are as follows:

- The giant X-ray nebula extends on a scale of ~ 40 kpc $\times$ 40 kpc. The nebula has most likely been heated and enriched by multiple galactic outflows generated by the AGN and/or circumnuclear starburst in the past, on a time scale of $\lesssim 0.1$ Gyr.
- Dual AGN activity is strongly suggested by the X-ray data.
- Significant 1-3 keV emission is found along the ionization cones and/or outflowing gas detected in a previous study.

Overall, nuclear, highly-ionized quasar-driven outflows are present in many ULIRGs. The outflows in ULIRGs may reach several tens of kpc.

6.1.2 Future Work

While the projects presented in Chapter 2 and 3 have unveiled new information on the highly ionized, nuclear quasar winds and the spatial extent of outflowing gas in nearby ULIRGs, further investigations are needed for a better understanding of this phenomenon. This is crucial for drawing a comprehensive picture of how quasar-driven outflows are launched and propagate in ULIRGs, and thus provide feedback to the system. In the following, I list three future programs that will shed new light on these issues.

Probing Highly Ionized Quasar Wind through Near-infrared Coronal Lines: The highly-ionized quasar winds can also be traced by coronal emission lines in the near-infrared (NIR). I plan to propose for a JWST NIRSPEC/IFS program or an ground-based, AO-assisted, NIR IFS program, to examine the kinematics and dynamics of the highly-ionized gas through coronal emission lines. This may be more sensitive to the faint emission from the outflowing gas due to the smaller attenuation in the NIR.

Searching for UFO and/or WA with Future X-ray Telescopes: Due to the general X-ray faintness of ULIRGs, the current X-ray telescopes are not sensitive enough to detect potential ultra-fast outflows (UFOs) and warm absorbers (WAs) in ULIRGs tracing the nuclear quasar winds. Future X-ray telescopes like *XRISM* and *Athena* may finally enable such studies.

Examining X-ray Emitting Gaseous Halos with *Athena*/X-IFU: While the deep *Chandra* data presented in Chapter 3 reveal the overall temperature and metallicity of the giant gaseous nebula in Mrk 273, the spatially-resolved emission line properties are still largely unconstrained. The latter will reveal the spatially-resolved kinematics, dynamics, metallicity and ionization properties of the hot gas within the nebula, which are crucial for a more comprehensive understanding of the origin of the nebula. For example, the imprints from the outflows on the nebula include abrupt increase in velocity dispersions suggesting outflow-triggered shocks, metallicity patterns consistent with metal transport through the outflow, etc. The future X-IFU instrument onboard *Athena* will be suitable for such observations.

6.2 AGN Feedback in Dwarf Galaxies

6.2.1 Summary

In the second half of the thesis, I turn my attention to the low mass galaxies and explore the feasibility of AGN feedback in dwarf galaxies via fast outflows.

In Chapter 4, I report the results from a dedicated optical integral-field spectroscopic study of a sample of eight dwarf galaxies with known AGN and suspected outflows. The main results are as follows:

- The outflows detected are fast, with 50-percentile (median) velocity of up to $\sim$240 km s^{-1} and 80-percentile line width reaching $\sim$1200 km s^{-1}, in clear contrast with the more quiescent kinematics of the host gas and stellar components.
- The kinematics and energetics of these outflows suggest that they are primarily driven by the AGN.
- A small but non-negligible portion of the outflowing material likely escapes the main body of the host galaxy and contributes to the enrichment of the circumgalactic medium.
- Overall, the impact of these outflows on their host galaxies is similar to those taking place in the more luminous AGN with massive hosts in the low-redshift universe.

In Chapter 5, I have conducted a pilot *HST*/COS spectroscopy program to examine three dwarf galaxies with primarily AGN-driven outflows from the sample studied in Chapter 4. The main findings are as follows:

- Blueshifted absorption features tracing fast outflows are detected in two of the three objects. In object J0954+47, a large fraction of the outflowing gas may escape the system.

- The outflow in J0954+47 carries significant amount of mass, momentum and kinetic energy. With a mass loading factor larger than unity, the outflow may transport material out of the galaxy more efficiently than the gas consumption by star formation.

- The ratio of kinetic energy outflow rate to AGN luminosity of the outflow in J0954+47 is comparable to the expectations from some simulations of AGN feedback.

- Strong He II λ1640 emission lines are detected in two objects, which are consistent with an AGN origin. The blueshifted He II emission line in one object is likely tracing a highly-ionized outflow.

Overall, AGN-driven outflows may be a promising feedback mechanism in dwarf galaxies.

6.2.2 Future Work

The results presented in Chapter 4 and 5 show tantalizing evidence for AGN feedback in dwarf galaxies, but a more comprehensive understanding of this issue requires further investigation. In the following, I list three future projects that may give us a better insight.

Better Measurements of Outflow Energetics: A good evaluation of AGN feedback in dwarf galaxies through AGN-driven outflows relies on a robust measurement of the outflow energetics. The current observations presented in Chapter 4 still do not provide enough spatial resolution to firmly resolve the compact outflows in several sources, which makes the dynamics and energetics of these outflows uncertain. To achieve such high spatial resolution, I plan to propose for *HST* long-slit spectroscopy programs and/or AO-assisted optical IFS observations (like VLT/MUSE-AO) on the sample examined in Chapter 4 and 5.

Radio-mode AGN Feedback: In addition to the quasar-mode feedback, the radio-mode feedback should also be examined in dwarf galaxies. One of the object studied in Chapter 4 and 5, J0906+56, shows a $\sim$50 pc radio jet [Yang et al., 2020]. As a pilot study, I plan to propose for a VLA observation to look for evidence of radio jet/extended radio emission on larger spatial scale, and explore whether the radio emission is related to the fast outflows in this object. This will help me investigate whether the radio jet plays a role in driving the fast outflow or interacting with the ISM within this system.

A Larger Sample of Dwarf AGN for Better Statistics: The statistical power of the two studies presented above is very limited. The ongoing and future surveys including the Dark Energy Spectroscopic Instrument (DESI), the extended ROentgen Survey with an Imaging Telescope Array (eROSITA), the Vera-Rubin Telescope, the Prime Focus Spectrograph (PFS) and the Nancy Grace Roman Space Telescope will likely discover many more AGN in dwarf galaxies and may also discover those at higher redshifts. These larger samples of dwarf AGN will enable a statistically sound evaluation of the relationship between the AGN and their dwarf host galaxies, and allow for the identification of more AGN-driven outflows for further investigations.

Appendix A: Appendix for Chapter 2

A.1 Notes on Individual Objects

In this section, we summarize the detections of emission and absorption features in each ULIRG.

F01004−2237: Clearly broad, blueshifted wings are seen in both Lyα, and N V emission. An O VI BAL is present at the edge of the blue side of the spectrum.

Mrk 1014: There are broad Lyα, O VI, and N V emission. No associated O VI or N V absorption lines is visible.

F04103−2838: There is no Lyα emission at systemic velocity, while a narrow emission line is seen at $\sim$ -2000 km s^{-1} in the rest frame of Lyα. It may be a redshifted Si III 1206 emission ($\sim$ 150 km s^{-1}), or a narrow Lyα emission in the foreground. No associated N V absorption line is visible.

F07599+6508: The spectrum is dominated by a prominent N V BAL with a centroid velocity similar to the blueshifted Na I D $\lambda\lambda$5890, 5896 absorption line seen in the optical. There are also multiple blueshifted and redshifted, narrow N V absorption lines at lower velocities ($\lesssim -5000$ km s^{-1}).

F08572+3915_NW: No signal is detected.

F11119+3257: There is broad, blueshifted Lyα emission and a less blueshifted, narrower

Lyα absorption feature on top of it. Part of the blueshifted N V emission is also detected. No associated N V absorption line is visible.

Z11598$-$0112: There is broad, blueshifted Lyα emission, superimposed with narrower Lyα absorption line close to the systemic velocity. Associated O VI and N V absorption features are also detected.

F12072$-$0444: There are broad, blueshifted Lyα emission and narrower Lyα absorption line near the systemic velocity. No associated N V absorption line is visible.

3C 273: There is broad Lyα emission, superimposed by multiple narrow foreground absorption features. No associated O VI or N V absorption line is visible.

F13218+0552: There is broad O VI emission, superimposed by narrower O VI absorption line. Lyβ absorption line with velocity similar to the O VI absorption line may exist but can not be confirmed (S/N $\lesssim$2).

F13305$-$1739: The spectrum is dominated by broad Lyα and N V emission with blueshifted wings.

Mrk 273: No signal from the source is detected.

F14070+0525: No signal from the source is detected.

F15001+1433_E: No signal from the source is detected.

F15250+3608: The Lyα line shows a P-Cygni-like profile. N V emission is also detected. Emission and blueshifted absorption from the N V 1242 line is visible, whereas the N V 1239 transition overlaps with the strong geocoronal emission nearby so that no measurements of it can be made. As a result, the overall properties of the N V doublet is highly uncertain. Our estimates for the EW and centroid velocity of the N V 1242 absorber alone are $\sim$0.3 Å and -500 km s^{-1}, respectively, which has not taken into account the infilling from the N V 1238, 1242 emission.

There are several blueshifted absorption features from various low ionization species, including N II λ1084, N I λ1200, Si III λ1206, Si II $\lambda\lambda\lambda$1190, 1193, 1260, with $v_{wtavg} \simeq -$[300, 500] km s^{-1}.

F16156+0146_NW: The Lyα emission is peaked at $\sim$ +500 km s^{-1}, with a superimposed blueshifted, narrower absorption feature at ~ -300 km s^{-1}, and a broad emission wing extending to $\lesssim -2600$ km s^{-1}. There are also weak, broad N V emission and a potential detection of Si III λ1206 absorption line.

F21219$-$1757: There are broad, blueshifted Lyα, N V, and O VI emission. Highly blueshifted absorption features at ~ -4500 km s^{-1}are seen for both the N V doublets and O VI 1038 line.

F23060+0505: There are broad Lyα and N V emission lines with blueshifted wings. Lyα and N V absorption lines with similar velocities are also seen.

F23233+2817: There is a broad Lyα emission superimposed by a narrow Lyα absorption line at the systemic velocity. Broad N V emission, and possible broad O VI emission are also visible. The FUV continuum is virtually not detected and no associated O VI or N V absorption feature is visible.

Appendix B: Appendix for Chapter 3

B.1 Spectral Analysis of Mrk 273x

Mrk 273x is at a projected angular separation of only $1'.3$ from Mrk 273 and it is observed simultaneously in our *Chandra* program. Mrk 273x is optically classified as a z = 0.46 Type 2 AGN, but its X-ray properties [e.g., lack of obvious absorption at low energies, high hard X-ray luminosity, absence of Fe Kα; Xia et al., 2002] are typical for an unabsorbed Type 1 AGN. By comparing the X-ray spectrum from the 2000 and 2016 data, constraints can be obtained on the variability of this source in X-ray. The spectra of Mrk 273x from the 2000 data and the 2016 data are shown in Figure B.1. The two spectra are consistent with each other and no clear variability is seen.

The spectra were fitted well (reduced χ^2 = 1.2) using a model with a power-law component (Γ=$1.53^{+0.15}_{-0.06}$) without much absorption ($N_H \sim 1.0^{+0.2}_{-0.2}\times10^{21}$ cm^{-2}), plus a blackbody component (kT<0.26 keV). The blackbody component was used to model possible residuals at $\sim$ 0.4-0.8 keV when only a power-law component was fitted to the data, although the p-value of the F-test between the two fits is only 0.6. The current data are thus not conclusive on the existence of the blackbody component, which might be a soft X-ray excess usually seen in Type 1 AGN [e.g. Crummy et al., 2006]. Potential Fe Kα line was fitted and an upper limit of $\sim$56 eV on the equivalent width (EW) in the observer's frame was obtained. The X-ray spectra over 16 years agree with each other, which show typical features for unabsorbed Type 1 AGN. This suggests that the Type 2 optical spectrum of Mrk 273x is intrinsic, i.e. due to the lack of a broad line region. This type of sources, where the X-ray spectrum shows all the characteristics of an unabsorbed Type 1 AGN while the optical spectrum points to a Type 2 AGN, remains a challenge to the standard AGN unification model.

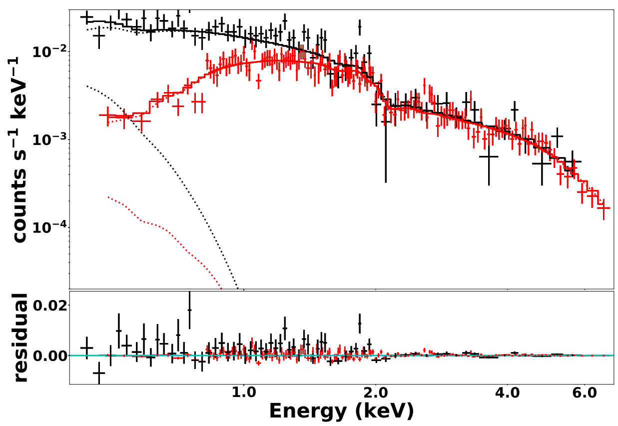

Figure B.1: Top: the spectra of Mrk 273x of 2000 data (black) and 2016 data (red) are shown separately. The apparent difference of the two spectra is mainly due to the drop of the instrument response in the soft X-ray from year 2000 to year 2016, but not a change in the flux of the source. Simultaneous fitting was applied to the data and the model was an absorbed power-law component plus a blackbody component with Galactic absorption. The model is shown in solid lines and the components of it are shown in dotted lines. Bottom: residuals (data minus model).

Appendix C: Appendix for Chapter 4

C.1 Results on Individual Objects

The detailed results from our analysis are presented in this Appendix. For each object, we show the maps of the [O III] λ5007 flux and kinematics, globally and for each velocity component, a map of the stellar kinematics, and the radial profiles of the line fluxes from individual velocity components. In addition, the line ratio maps and spatially resolved BPT and VO87 diagrams are also shown for J0906+56 and J0842+03. In all cases, the systematic velocities of our targets are determined from the stellar velocities measured from the spectra integrated over the whole data cubes. In the few objects where the broader velocity component shows kinematic characteristics that are apparently similar to those of a rotating gas disk, we have also attempted to fit the velocity field with *Kinemetry* [Krajnović et al., 2006], a software based on a generalized harmonic expansion method of the two-dimensional velocity field.

C.1.1 J0100−01

Fig. C.1–C.3 present the KCWI maps of the [O III] λ5007 flux and kinematics, the map of the stellar kinematics, and the [O III] λ5007 flux radial profiles of the individual velocity components of target J0100−01.

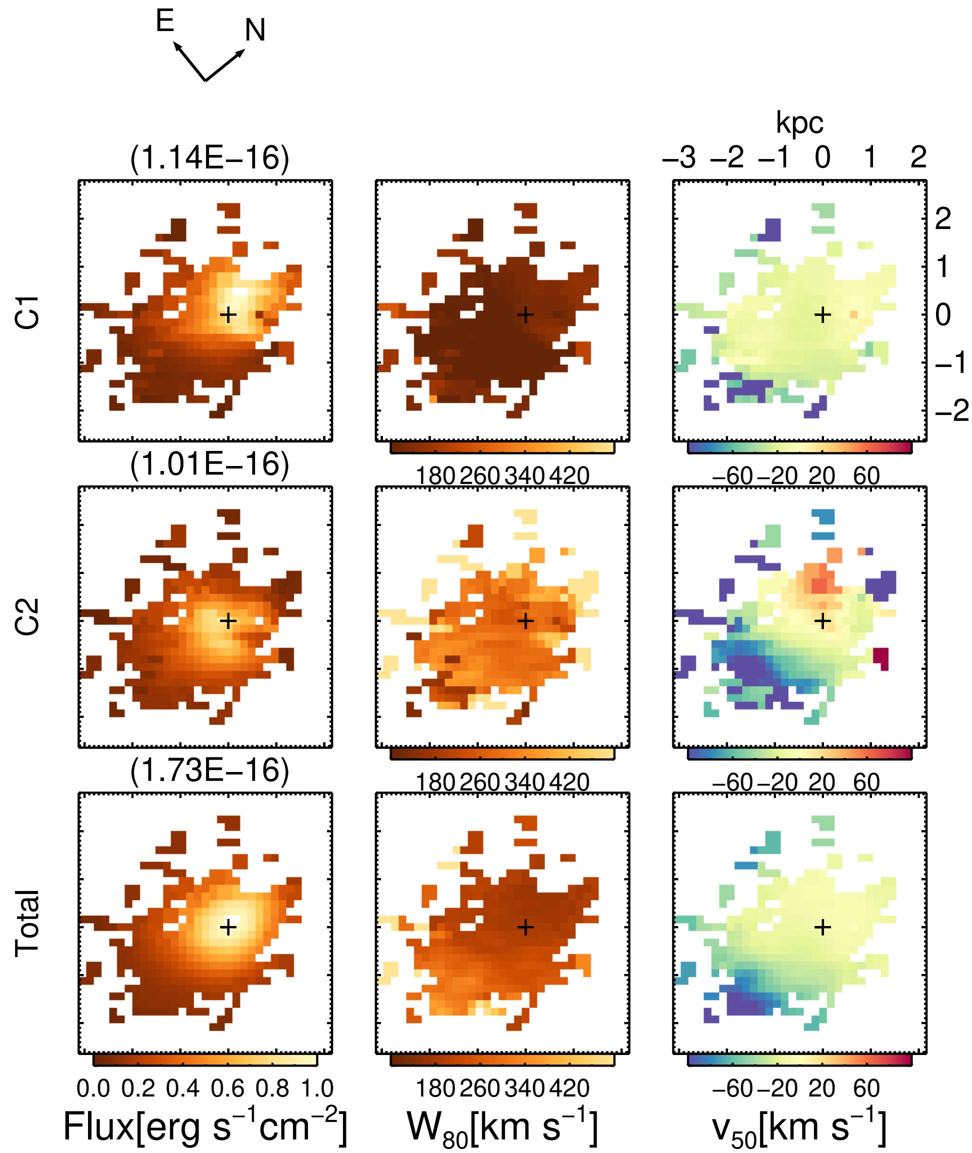

Figure C.1: Voronoi-binned maps of the [O III] λ5007 flux and kinematics in J0100−01 based on the KCWI data. The orientation of the maps is indicated by the compass at the top of the figure. Maps of the properties of the individual velocity components derived from the multi-Gaussian fits (C1, C2), and those of the overall emission profiles (Total), are shown from top to bottom. The flux maps are shown in the leftmost column, where each map is normalized to the maximum flux value in the map, which is listed in cgs units above each panel. The line widths W_{80} and velocities v_{50} are shown in the middle and rightmost columns, respectively. In each panel, the black cross indicates the spaxel where the peak of the total [O III] λ5007 emission line flux falls. The coordinates of the panels are in kpc.

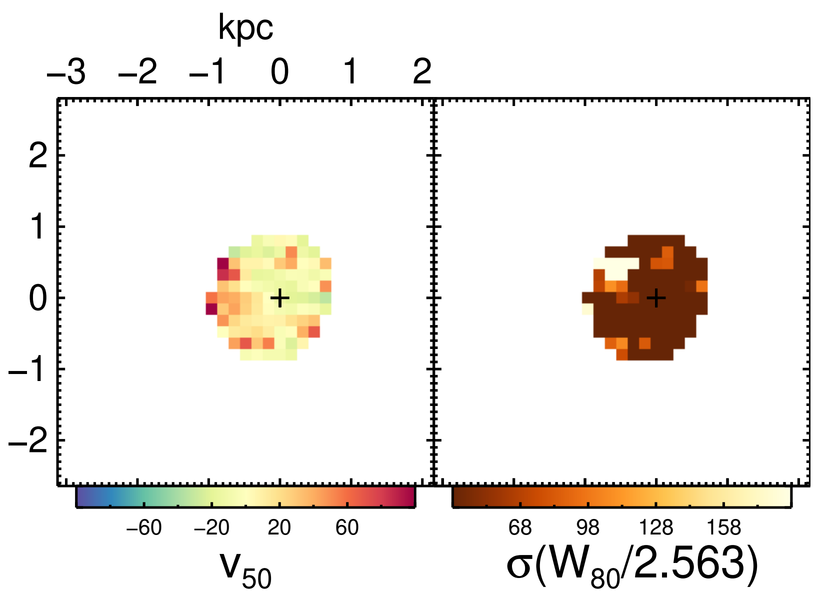

Figure C.2: Maps of the stellar median velocity (left) and velocity dispersion (right) in J0100−01 on the same spatial scale as Fig. C.1. The map of the median velocity is drawn on the same color scale as the v_{50} maps of [O III] λ5007 (Fig. C.1). The map of the velocity dispersion is also drawn on the same color scale as the W_{80} maps of [O III] λ5007, namely the same color represents the same line width in all maps. For a Gaussian profile, the conversion between W_{80} and velocity dispersion σ is $W_{80} = 2.563\ \sigma$. In each panel, the black cross indicates the spaxel where the peak of the total [O III] λ5007 emission line flux is located.

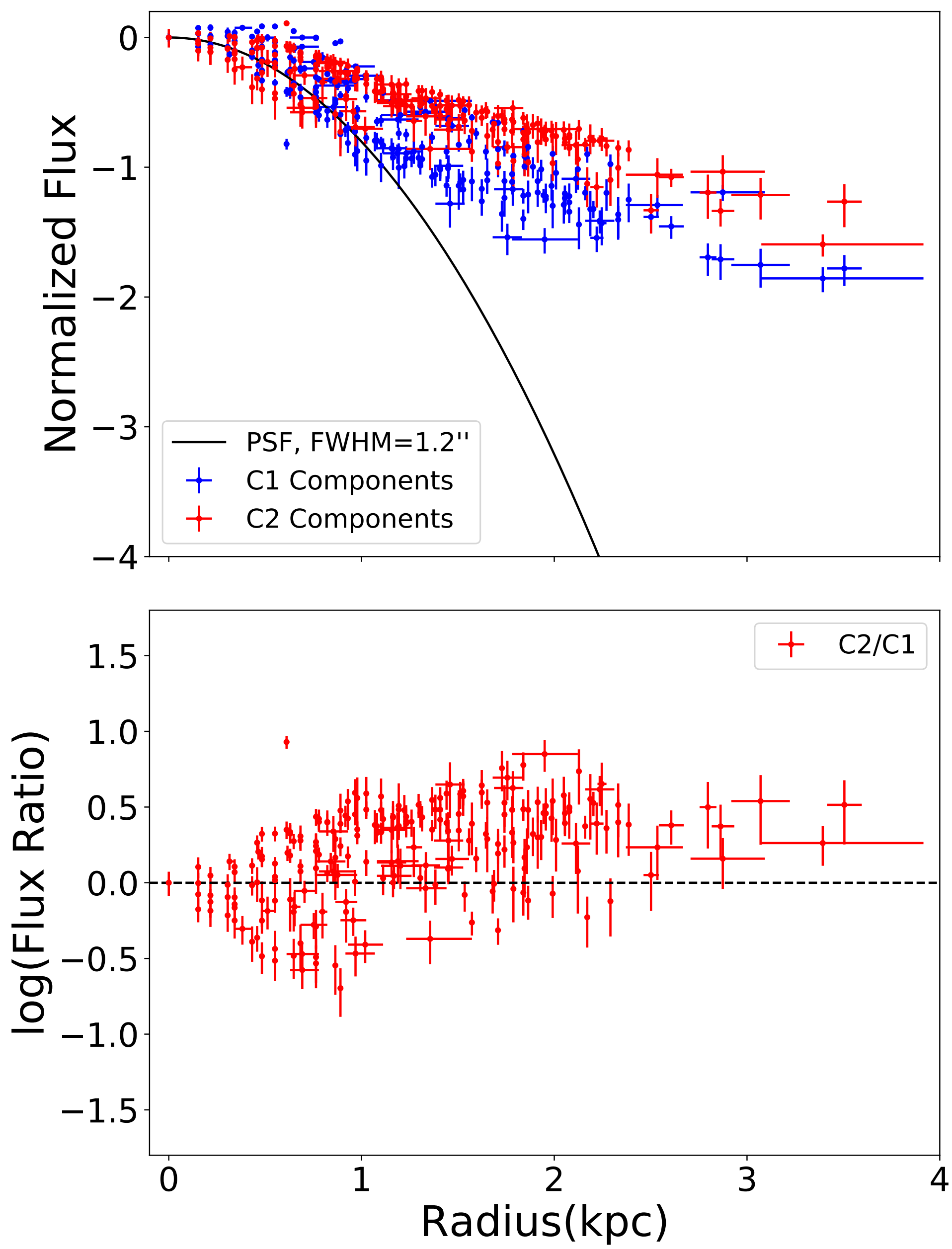

Figure C.3: Top panel: Radial profiles of the [O III] λ5007 fluxes from the two velocity components of J0100−01. For each component, the fluxes are normalized to those of the spaxel with peak emission line flux (i.e., the spaxel indicated by the black cross in Fig. C.1). The PSF profile is derived from fits to the spectrophotometric standard stars of the IFS observations using single Gaussian profiles (see Section 4.2.2 for more details). Bottom panel: C2/C1 flux ratios on a logarithmic scale as a function of distance from the spaxel with peak emission line flux. In both panels, the data points beyond the maximal spatial extent of the outflow component (C2 in this target) are omitted. In addition, the error bars in radius (x-axis) are set either to zero for single spaxels or to reflect the radial coverage of the spatial bin.

C.1.1.1 Maps of the [O III] λ5007 Flux and Kinematics

Two velocity components (C1 and C2) are sufficient to describe the [O III] λ5007 line profiles in this galaxy. The spatial distribution of the [O III] λ5007 flux is not symmetric with respect to the galaxy center (Fig. C.1). More flux is present in the southern portion of the galaxy than in the north. This is especially true when considering the C2 component (discussed in more detail below).

The [O III] λ5007 line profiles show a mild velocity gradient similar to that of the C1 component, and both of them appear to be systematically slightly blueshifted by $\sim$20 km s^{-1} with respect to the stellar velocities. Note, however, that the stellar velocities are only measured reliably in the inner kpc of this galaxy (Fig. C.2), so the amplitude and position angle of the stellar velocity gradient is uncertain. The line widths W_{80} of the [O III] λ5007 line profiles are generally narrow except in the southwestern portion of the galaxy, where W_{80} reach $\sim$440 km s^{-1}.

The C1 component shows a mild velocity gradient with v_{50} ranging from ~-60 km s^{-1} to 0 km s^{-1}and a median of ~-20 km s^{-1}. The C1 line widths are in general narrow (median W_{80} $\simeq$ 120 km s^{-1}), consistent with the idea that the C1 component is made of quiescent gas rotating in the galaxy.

The flux asymmetry is more apparent in the C2 component than in the C1 component. The C2 component is significantly blueshifted in the south portion of the galaxy, where v_{50} reach values of ~-240 km s^{-1}, well in excess of the stellar velocities measured on smaller scale. A clear gradient in v_{50} is seen along the N – S direction (PA$\simeq$10°), but the most redshifted velocities are $\sim+50$ km s^{-1}. The line widths of the C2 components are generally large, reaching a maximum value of $\sim$650 km s^{-1}. The kinematics of the C2 component may be interpreted as a tilted, biconical outflow, where the near (S) side of the outflow is blueshifted and the far (N) side is redshifted. The redshifted velocities are significantly smaller (in absolute terms) than the blueshifted ones, perhaps an indication that the far side of the outflow is largely blocked by the galaxy. However, without reliable stellar velocities on large scale, it is hard to exclude the possibility that the north portion of the C2 component consists of turbulent, rotating gas within the galaxy.

To further examine the origin of the v_{50} gradient seen in the C2 component, we have tested fitting the separate v_{50} maps of the C2 and C1 components with *Kinemetry* [Krajnović et al., 2006]. This software fits the two-dimensional map of the line-of-sight velocity distribution of a galaxy by determining the best-fit ellipses along which the profiles of the moments can be extracted and analyzed by means of harmonic expansion. As a product of the fit, the best-fit circular velocity field can be obtained. In practice, we carried out the fits in two steps: (i) we fitted the v_{50} map with the default setting in *Kinemetry* where the PA and flattening of each ellipse were allowed to vary freely; (2) a second and final fit was applied where the PA and flattening were fixed to the median values measured from step (i). Due to the asymmetry in the flux distribution of the C2 components, we applied the fits described above only to the region within r $\lesssim$ 1.2 kpc where relatively complete ellipses required for the fits can be drawn from the data, and extrapolate the best-fit circular velocity field to the south where the blueshifted emission are mostly seen. For the C1 component, the residual velocities (defined as the difference between the observed v_{50} and the circular velocities from the best-fit) are consistent with random noise as expected, suggesting that the kinematics of the C1 component can be described as a rotating disk. For the C2 component, on the contrary, we find that there are significant negative residual velocities in the southern portion of the galaxy. This is consistent with our earlier statement that the blueshifted emission on the south side is likely originating from the near side of a biconical outflow.

C.1.1.2 Flux Radial Profiles

The [O III] λ5007 flux radial profiles shown in Fig. C.3 confirm that the individual velocity components in J0100−01 are spatially resolved in the KCWI data. There is a weak trend for the C2/C1 flux ratios to increase radially, further indicating that these components have slightly different flux distributions as stated in Section C.1.1.1.

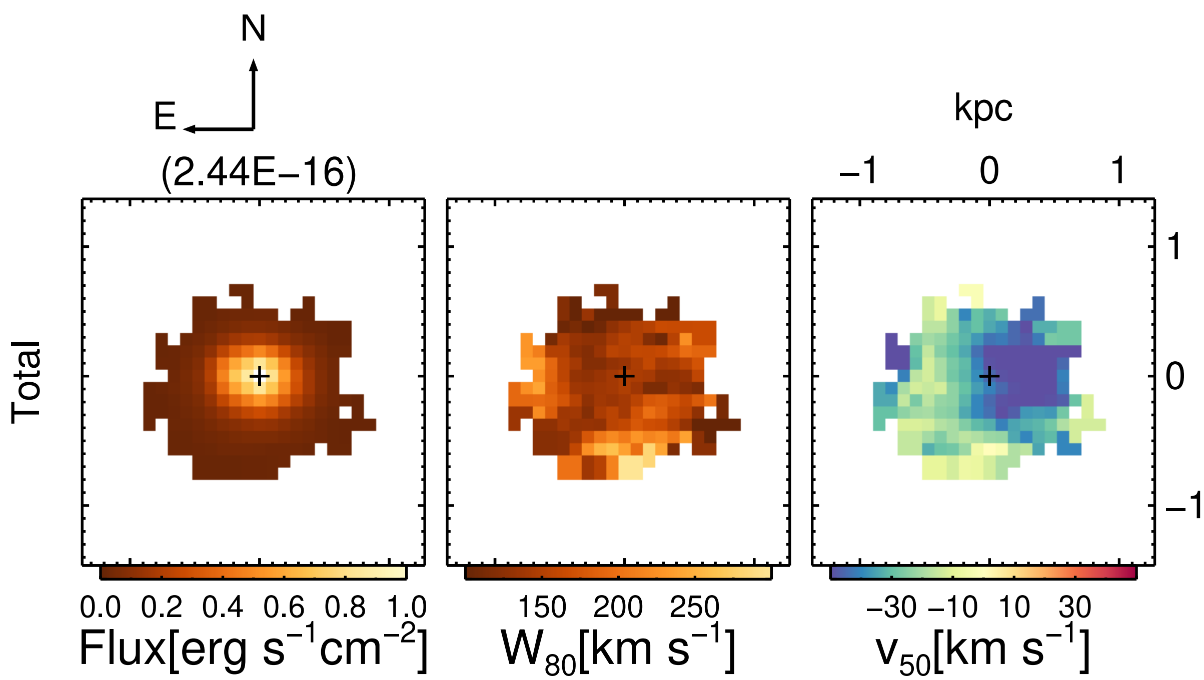

Figure C.4: Same as Fig. C.1 but for J0811+23, where a single Gaussian component is sufficient to fit the [O III] λ5007 line profiles.

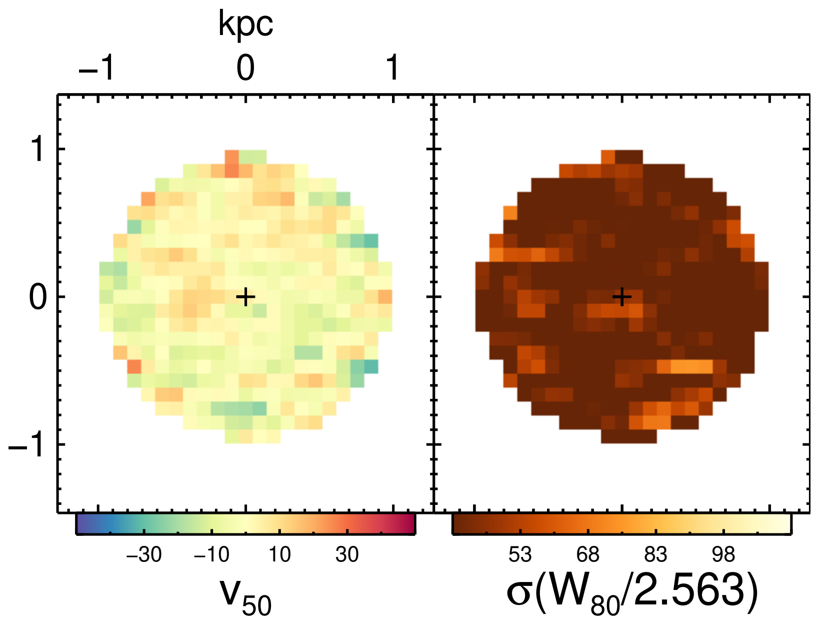

Figure C.5: Same as Fig. C.2 but for J0811+23.

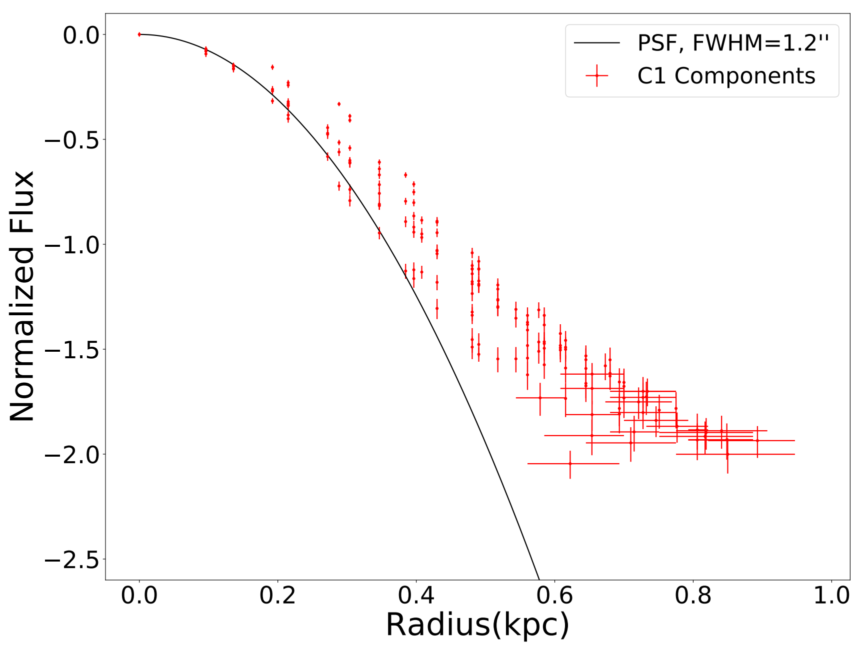

Figure C.6: Same as the top panel of Fig. C.3 but for J0811+23.

C.1.2 J0811+23

The results of our analysis of the KCWI data of J0811+23 are presented in Fig. C.4–C.6.

C.1.2.1 Maps of the [O III] λ5007 Flux and Kinematics

A single Gaussian component is sufficient to fit the [O III] λ5007 line profiles in this object. The values of v_{50} (Fig. C.4) are everywhere blueshifted with respect to those of the stellar component (Fig. C.5) and show a gradient from $\sim$−60 to $\sim$−20 km s^{-1} along PA $\simeq$ −80°, which is not seen in the stellar velocity field. The line widths of the emission lines are also on average larger than the velocity dispersions of the stellar components (median W_{80} $\sim$140 and 90 km s^{-1}, respectively).

These results show that the kinematics of the ionized gas cannot be described by pure rotation. The blueshifted ionized gas likely takes part in a bulk outflow. We speculate that the v_{50} gradient seen in [O III] λ5007 may be caused by geometrical effects and/or internal velocity gradient in the outflow itself, given that the stellar components show no obvious rotation.

C.1.2.2 Flux Radial Profiles

The [O III] λ5007 flux radial profile (Fig. C.6) is clearly more extended than the PSF, consistent with the presence of a clear, spatially resolved velocity gradient in the ionized gas.

C.1.3 J0840+18

Fig. C.7–C.9 display the results of our analysis of the KCWI data on J0840+18.

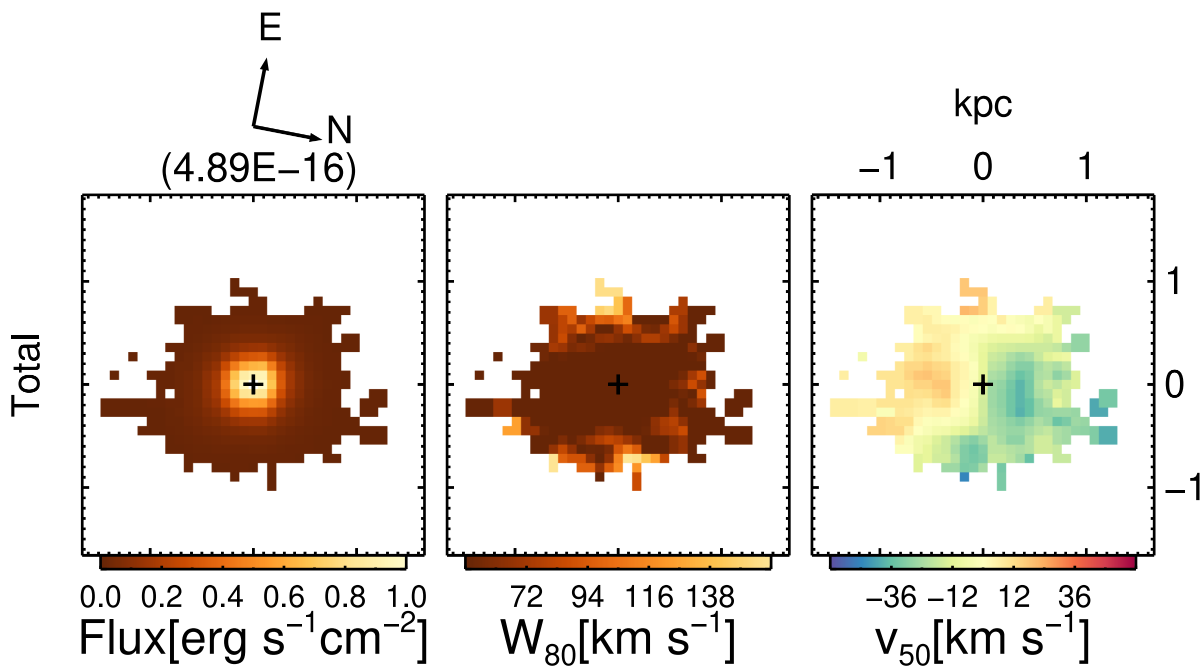

Figure C.7: Same as Fig. C.4 but for J0840+18, where a single Gaussian component is sufficient to fit the [O III] λ5007 line profiles. This is the only object in our sample without a clear sign of outflow.

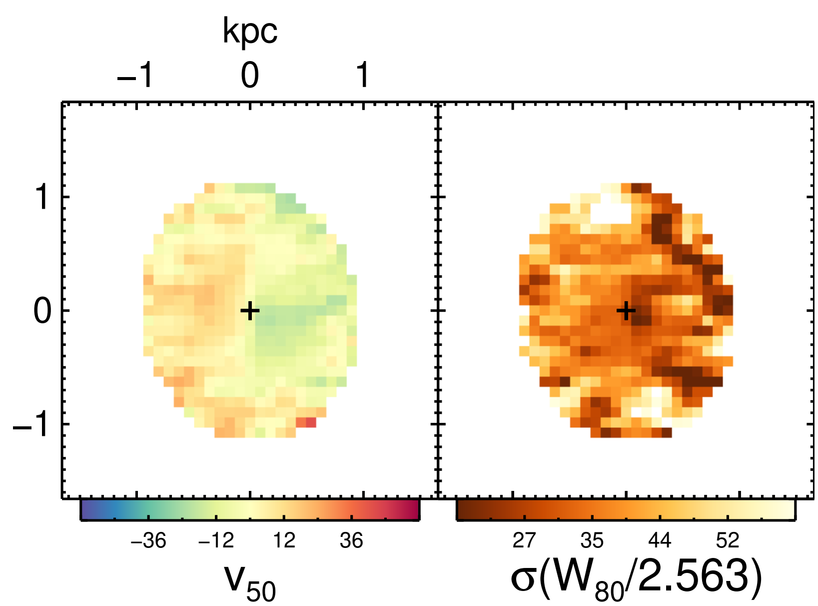

Figure C.8: Same as Fig. C.5 but for J0840+18.

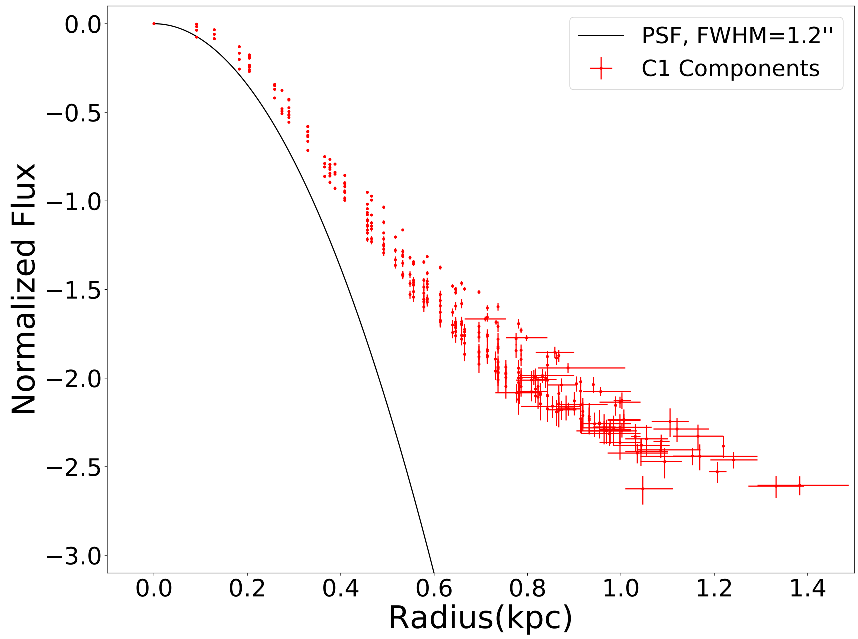

Figure C.9: Same as Fig. C.6 but for J0840+18.

C.1.3.1 Maps of the [O III] λ5007 Flux and Kinematics

A single Gaussian component is sufficient to fit the [O III] λ5007 line profiles. The map of [O III] λ5007 v_{50} (Fig. C.7) shows a clear gradient (-30 km s^{-1} to $+20$ km s^{-1}) similar to that of the stellar v_{50} (Fig. C.8). The line widths of the emission lines are smaller than the velocity dispersions of the stellar component. These results suggest that the ionized gas is simply rotating within the galaxy in the same direction as the stars. No clear evidence of outflow is seen in this object.

C.1.3.2 Flux Radial Profiles

The [O III] λ5007 flux radial profile (Fig. C.9) is clearly more extended than the PSF, which is consistent with the spatially resolved velocity gradients seen in both the ionized gas and underlying stellar population.

C.1.4 J0842+03

J0842+03 was observed with both GMOS and KCWI. The results derived from these two independent data sets agree well with each other. While the GMOS data trace the structures on small spatial scale better than the KCWI data, the KCWI data allow us to probe the fainter emission on the outskirts of the galaxy host.

Fig. C.10–C.12 present the maps of the [O III] λ5007 flux and kinematics, the map of the stellar kinematics, and the [O III] λ5007 flux radial profiles of the individual velocity components. The line ratio maps and spatially resolved BPT and VO87 diagrams are shown in Fig. C.13–C.14.

C.1.4.1 Maps of the [O III] λ5007 Flux and Kinematics

Two Gaussian components (C1 and C2) are enough to describe the [O III] λ5007 emission line profiles in this system (as already shown in Fig. 4.1). The projected distribution of the [O III] λ5007 emission, both velocity-integrated and in the individual velocity components, is largely symmetric with respect to the galaxy center.

The emission line profiles are in general blueshifted with respect to the systemic velocity (median $v_{50} \simeq -110$ km s^{-1} in the GMOS data and $\simeq -70$ km s^{-1}in the KCWI data) and show a clear velocity gradient (see the bottom rows in Fig. C.10). The line widths are also much broader than the stellar velocity dispersions (see Fig. C.11). This indicates that the kinematics of the ionized gas are dominated by non-rotational motion.

The C1 component is on average blueshifted by 80 km s^{-1} in the GMOS data and 30 km s^{-1} in the KCWI data, but shows a clear velocity gradient (with v_{50} ranging from $\sim$$-110$ km s^{-1} to $\sim$$-20$ km s^{-1} in the GMOS data, and from $\sim$$-60$ km s^{-1} to $\sim$$+10$ km s^{-1}in the KCWI data)

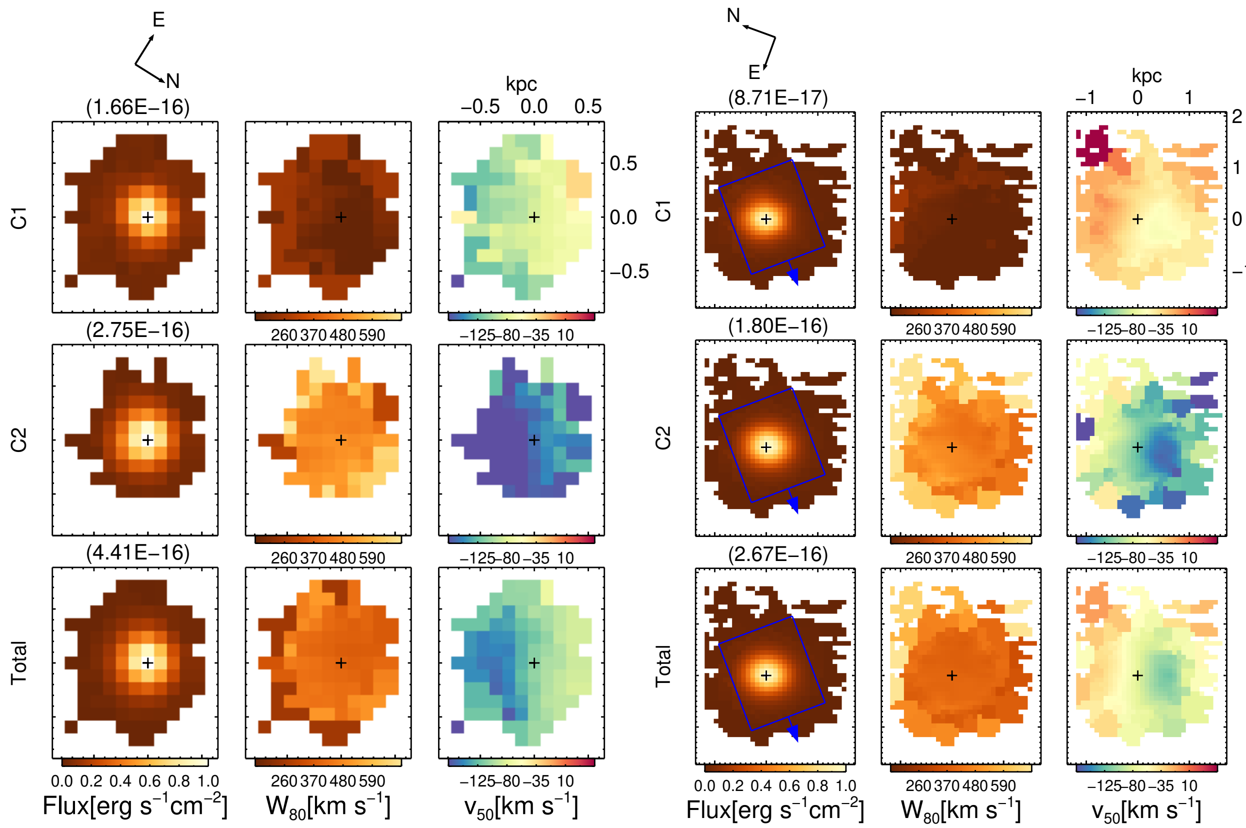

Figure C.10: Same as Fig. C.1 but for the GMOS data (left) and KCWI data (right) of J0842+03, where two velocity components C1 and C2 are needed to adequately fit the emission-line profiles. The orientation of the maps are noted at the top of each panel and are different from each other. In the left column of the right panel (KCWI data), the GMOS footprint is overplotted as a blue rectangle with the 0 o'clock direction noted by the blue arrow. Note that the color bars in the right column of each panel (v_{50}) are centered on a negative velocity for a better visualization of the velocity gradients in both the C1 and C2 components.

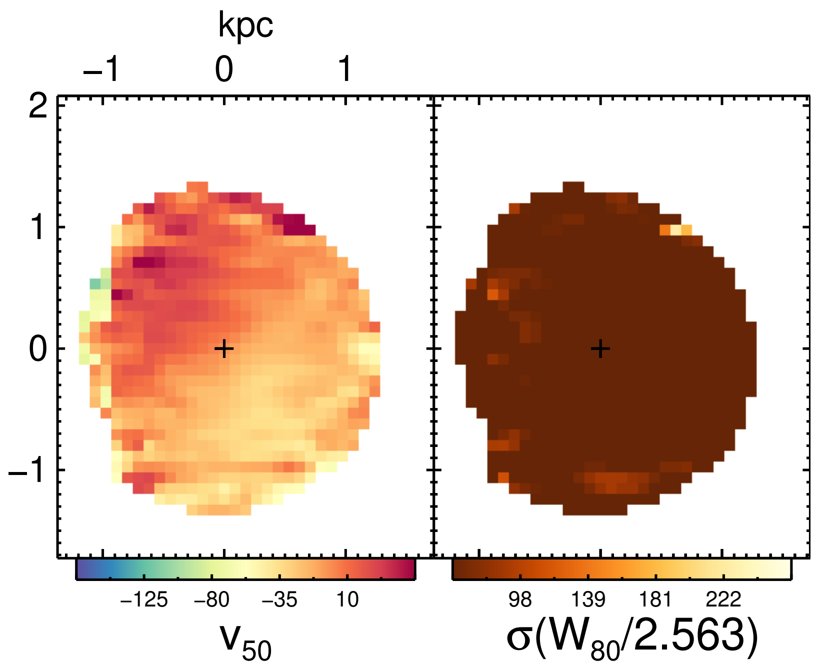

Figure C.11: Same as Fig. C.2 but for J0842+03.

with an orientation of the gradient (PA $\simeq$ 220°) that is similar to that of the stellar velocity field. The line widths of the C1 component are in general narrow (median $W_{80} \simeq 200$ km s^{-1}), similar to the stellar velocity dispersion. The C1 component likely represents a mixture of both rotating and outflowing gas.

The C2 component is in general significantly blueshifted with respect to the systemic velocity (v_{50} down to $\sim$−220 km s^{-1}in the GMOS data, and $\sim$−160 km s^{-1} in the KCWI data) and much broader (W_{80} up to ∼650 km s^{-1}in the GMOS data and ∼750 km s^{-1}in the KCWI data) than the C1 component. The C2 component is thus most likely associated with outflowing gas. A clear gradient is seen in the v_{50} of the C2 component, suggesting that the outflowing gas may have an intrinsic velocity structure and/or an asymmetrical geometry with respect to the line-of-sight. As the orientation of the velocity gradient of the C2 component is similar to that of the

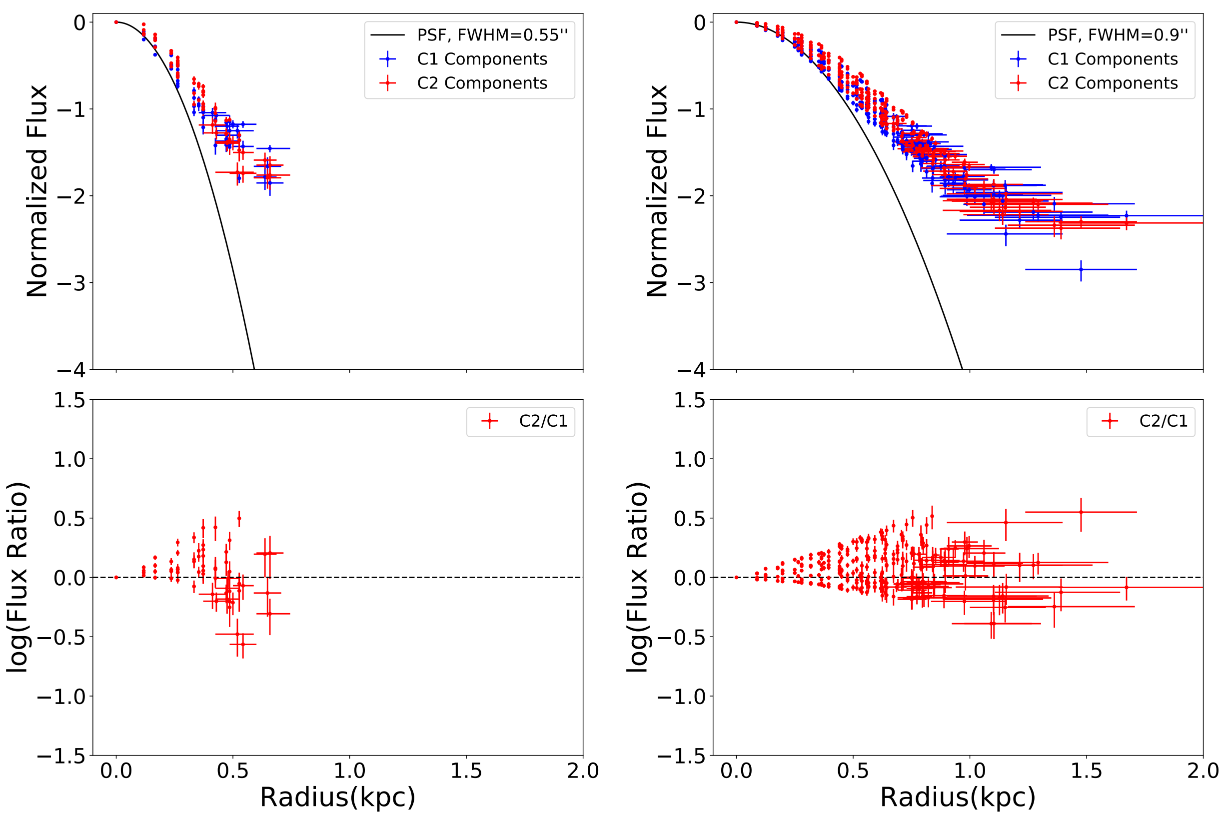

Figure C.12: Same as Fig. C.3 but for the GMOS data (left) and KCWI data (right) of J0842+03.

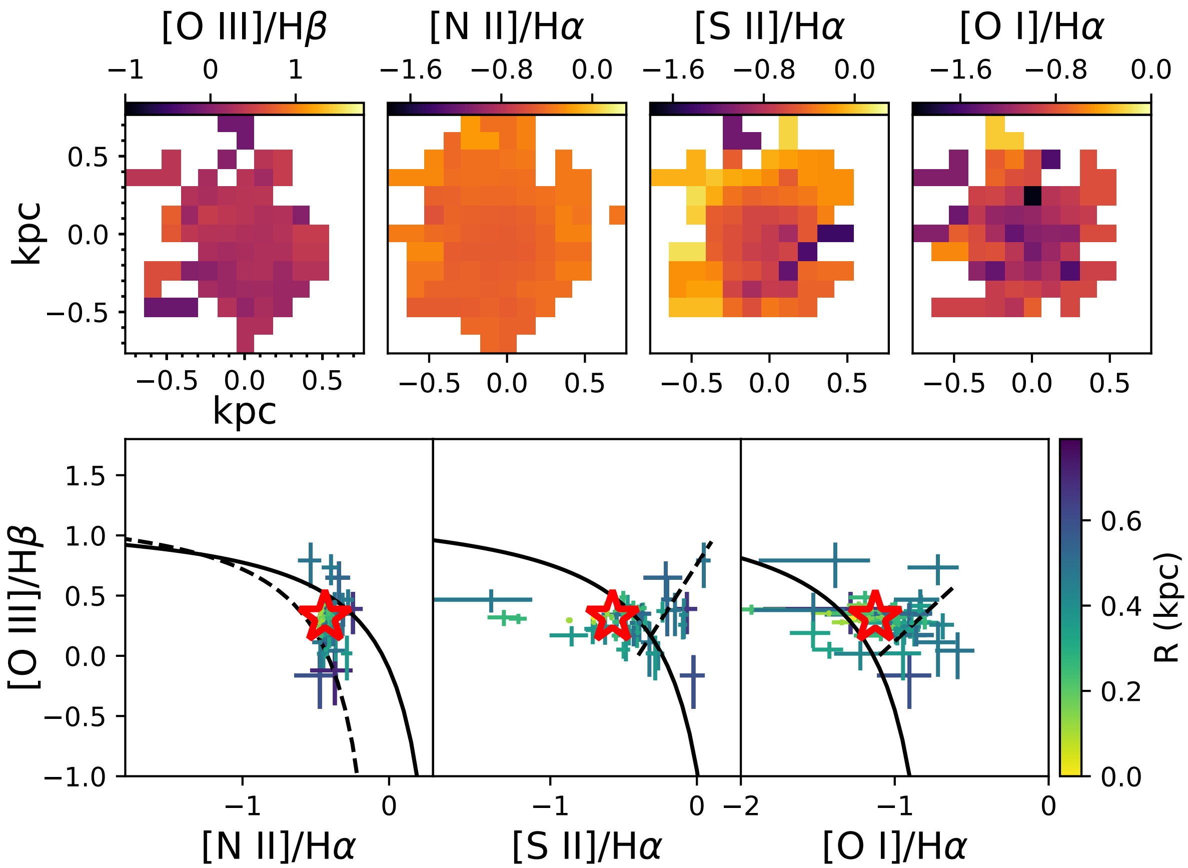

Figure C.13: Emission line diagnosis for the C1 component of J0842+03. Top row: Line ratio maps of [O III]/Hβ, [N II]/Hα, [S II]/Hα and [O I]/Hα, from left to right. Bottom row: Standard BPT and VO87 diagrams. The data points are color-coded according to their projected distance (in kpc) to the spaxel with peak emission line flux. The large red open star in each panel indicates the line ratios derived from the spatially-integrated spectrum. In all panels, the solid line is the theoretical line separating AGN (above right) and star-forming galaxies (below left) from Kewley et al. [2001]. In the left panel, the dashed line is the empirical line from Kauffmann et al. [2003] showing the same separation. Objects between the dotted and solid lines are classified as composites. In the middle and right panels, the diagonal dashed line is the theoretical line separating Seyferts (above left) and LINERs (below right) from Kewley et al. [2006].

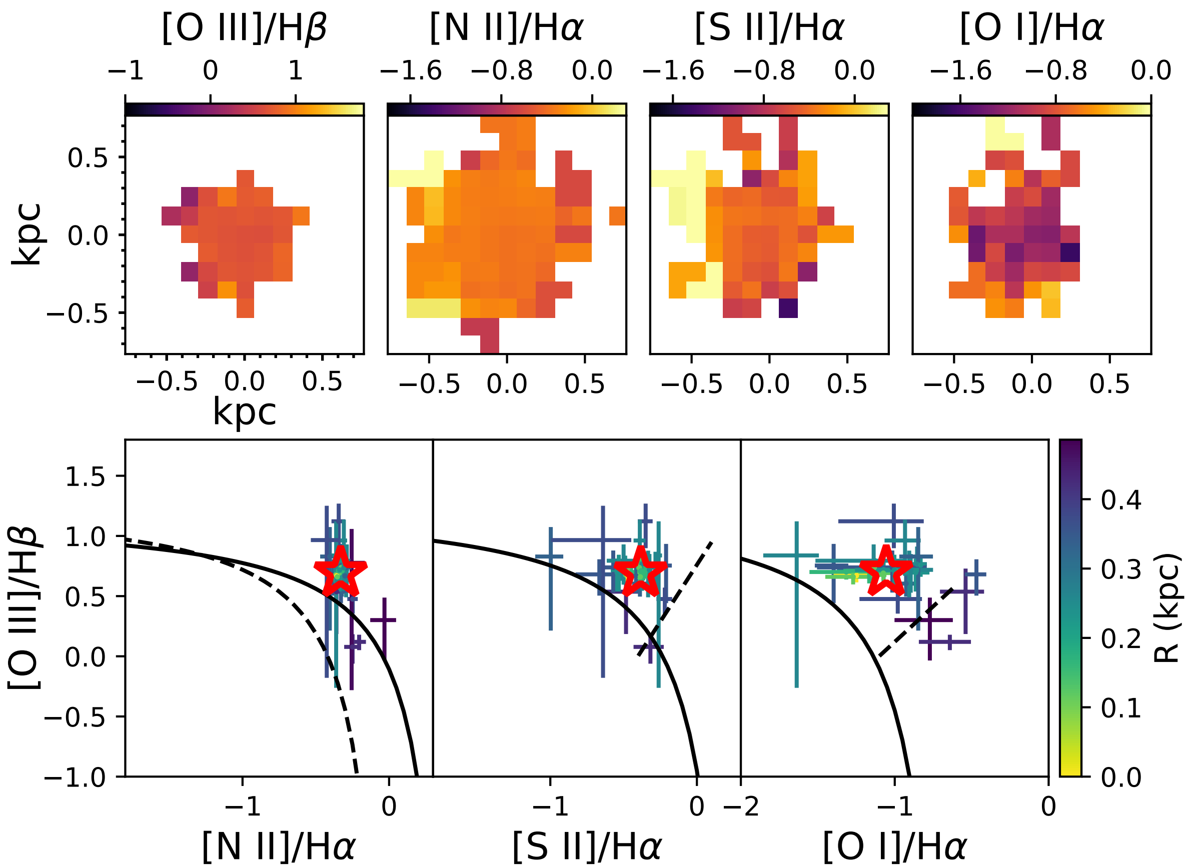

Figure C.14: Same as Fig. C.13 but for the component C2.

C1 component, an alternative explanation for this gradient is that the outflowing gas may have inherited a portion of the angular momentum from the galaxy.

C.1.4.2 Flux Radial Profiles

The fluxes from both velocity components are clearly more extended than the PSF (top panels in Fig. C.12), consistent with the resolved velocity structures seen in the kinematics maps (Fig. C.10). There is a slight trend for the C2/C1 flux ratio to increase radially outward in the KCWI data beyond radii of $\sim$0.5 kpc (bottom right panel in Fig. C.12); this trend is not detected in the GMOS data.

C.1.4.3 Ionization Diagnosis

Here we examine the ionization properties of individual velocity components based on the GMOS data with emphasis on the line ratios in the BPT and VO87 diagrams. The KCWI data are not discussed in this context because they do not cover Hα and the other important line diagnostics in the red.

The [O III]/Hβ ratios of both the C1 and C2 velocity components are roughly constant across the map. The other three line ratios, [N II]/Hα, [S II]/Hα, and [O I]/Hα, are also roughly constant or show only mild radial trends.

The spatially-integrated line ratios of the C2 component fall in the AGN region in all three BPT and VO87 diagrams, while for the C1 component, they lie in the AGN region only in the [O I]/Hα diagram. Instead, the spatially-integrated line ratios of C1 components are in the composite region of the [N II]/Hα diagram and in the star-forming region of the [S II]/Hα diagram.

For individual spaxels, the line ratios of the C2 component within r $\simeq$ 0.5 kpc are AGN-like in all three diagrams, while those of the C1 component suggest a significant contribution from star-forming activity, as the majority or a significant fraction of the spaxels are located in the composite regions of the [N II]/Hα diagram, and in the star-forming region of the [S II]/Hα diagram.

C.1.5 J0906+56

J0906+56 was observed with both GMOS and KCWI. While the KCWI data has a larger field of view, and detect emission lines out to a larger physical scale, the results from both data sets agree with each other in general, as in the case of J0842+03.

The maps of the [O III] λ5007 flux and kinematics, stellar kinematics, as well as [O III] λ5007 flux radial profiles of individual velocity components for this object are shown in Figs. C.15–C.17. The line ratio maps and spatially resolved BPT and VO87 diagrams are shown in Figs. C.18–C.19. The map of the stellar kinematics based on the GMOS data is significantly more uncertain than the map based on the KCWI data due to the lower S/N in the stellar continuum in the former. Therefore, only the stellar kinematics maps based on the KCWI data are shown in Figure C.16.

C.1.5.1 Maps of the [O III] λ5007 Flux and Kinematics

The emission line profiles in this object are generally broad, with W_{80} reaching ~650 km s^{-1} in the GMOS-based maps and ~670 km s^{-1} in KCWI-based maps. Up to three Gaussian components are needed to properly fit the [O III] λ5007 line emission. The stellar components

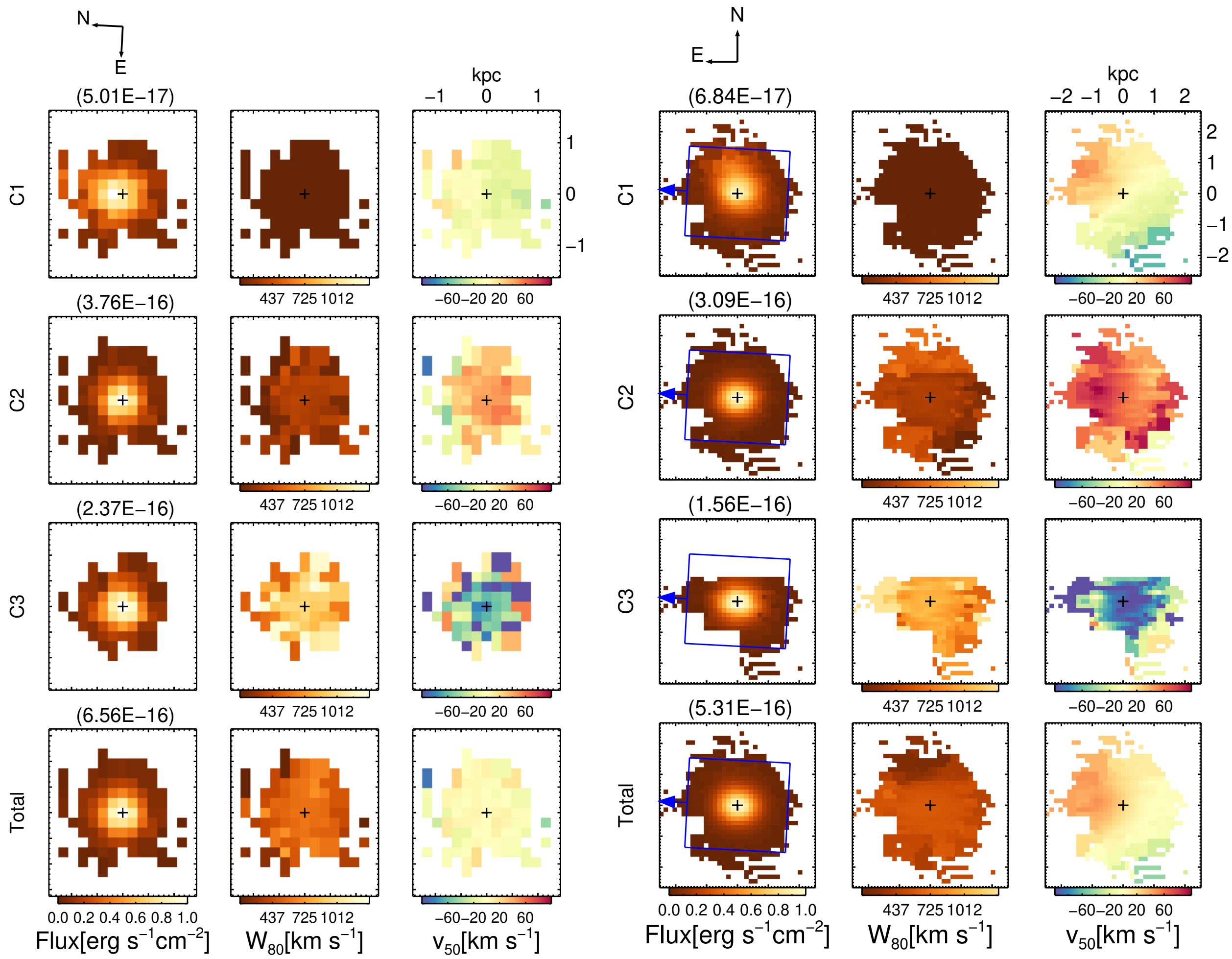

Figure C.15: Same as Fig. C.10 but for the GMOS data (left) and KCWI data (right) of J0906+56, where three velocity components C1, C2, and C3 are needed to adequately fit the emission-line profiles.

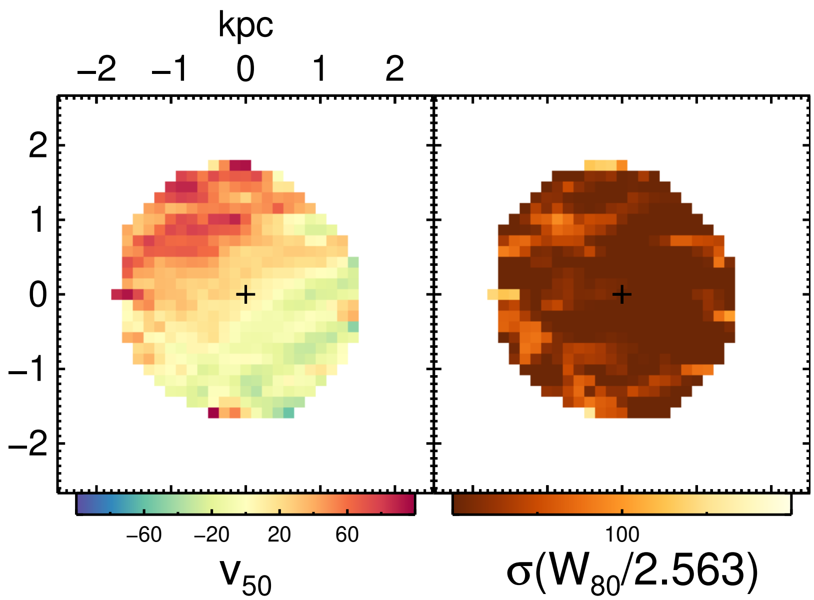

Figure C.16: Same as Fig. C.2 but for J0906+56.

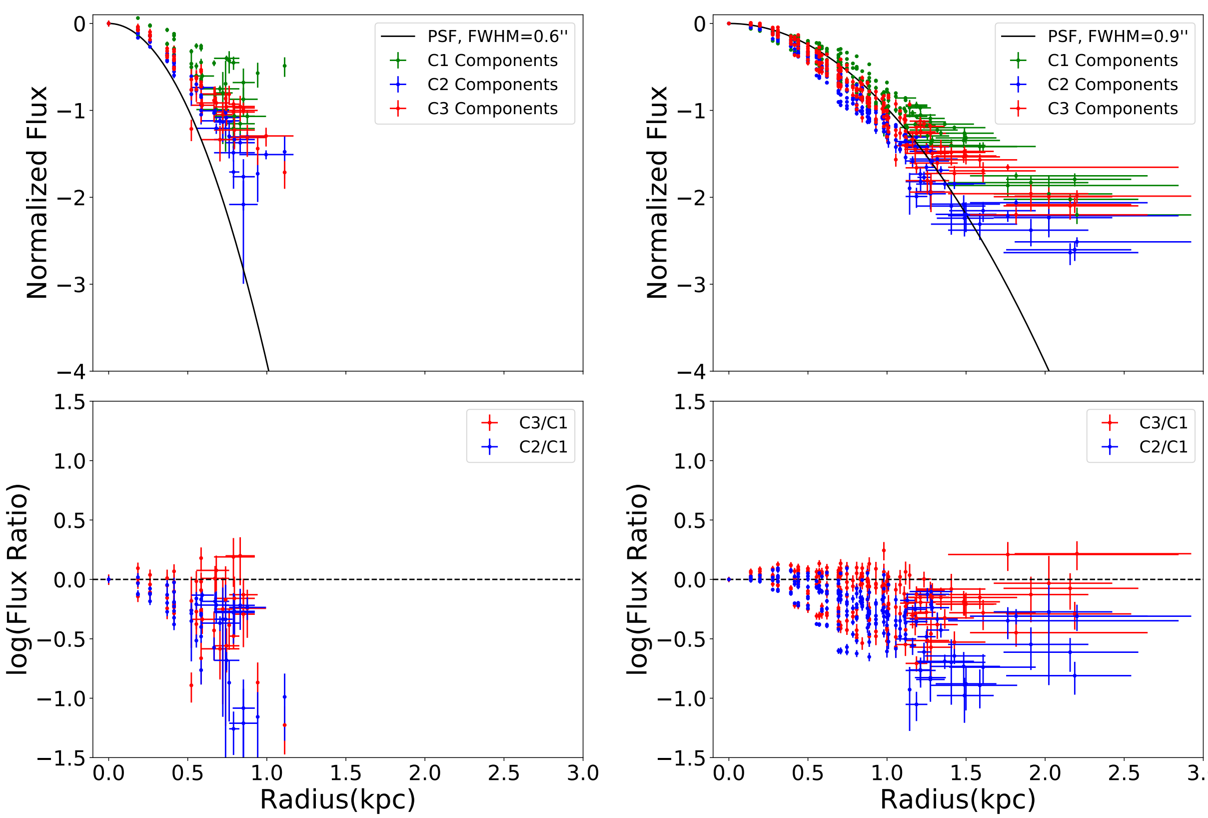

Figure C.17: Same as Fig. C.3 but for the GMOS data (left) and KCWI data (right) of J0906+56.

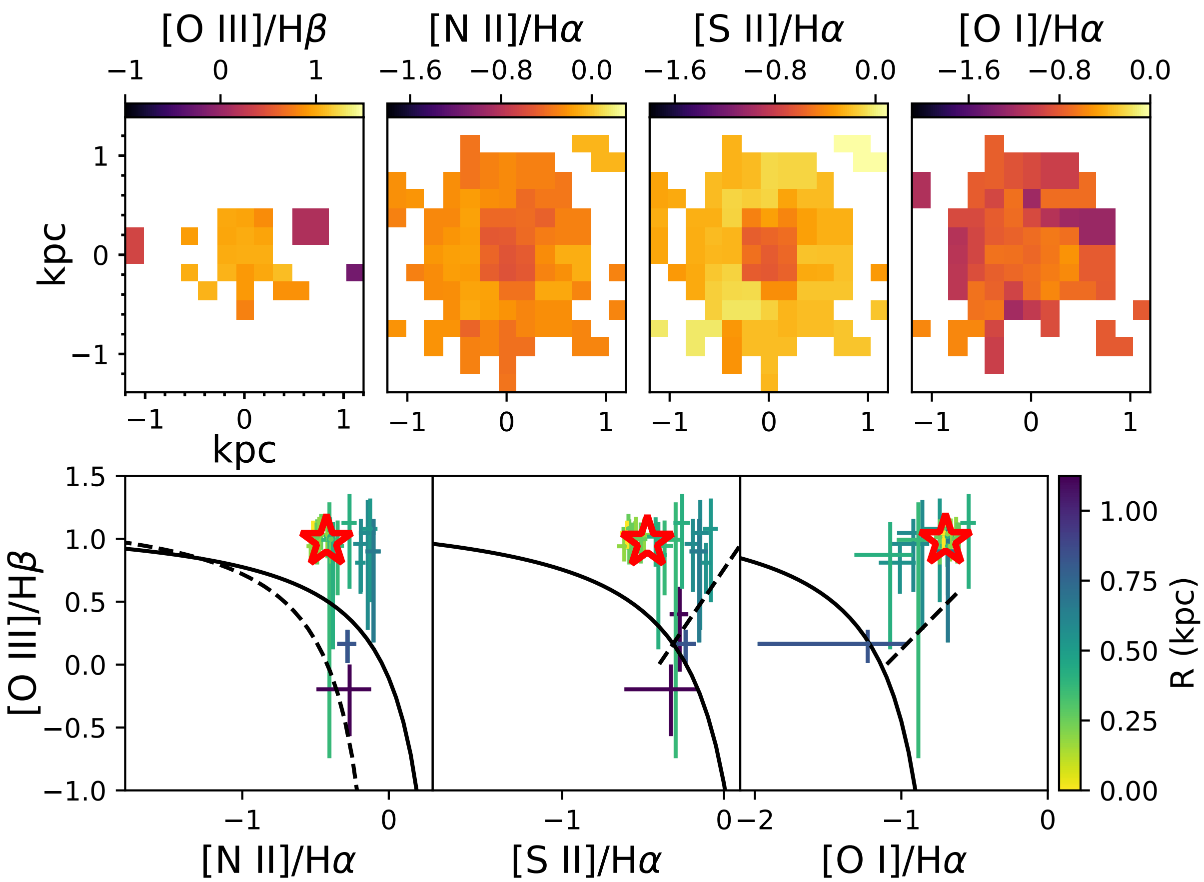

Figure C.18: Emission line diagnosis for the sum of the host component C1 + outflow component C2 of J0906+56. Top row: Line ratio maps of [O III]/Hβ, [N II]/Hα, [S II]/Hα and [O I]/Hα, from left to right. Bottom row: Standard BPT and VO87 diagrams. The data points are color-coded according to their projected distance (in kpc) to the center of the galaxies. The large red open star in each panel indicates the line ratios derived from the spatially-integrated spectrum. The presentation style and meaning of the symbols are the same as in Figs. C.13 and C.14.

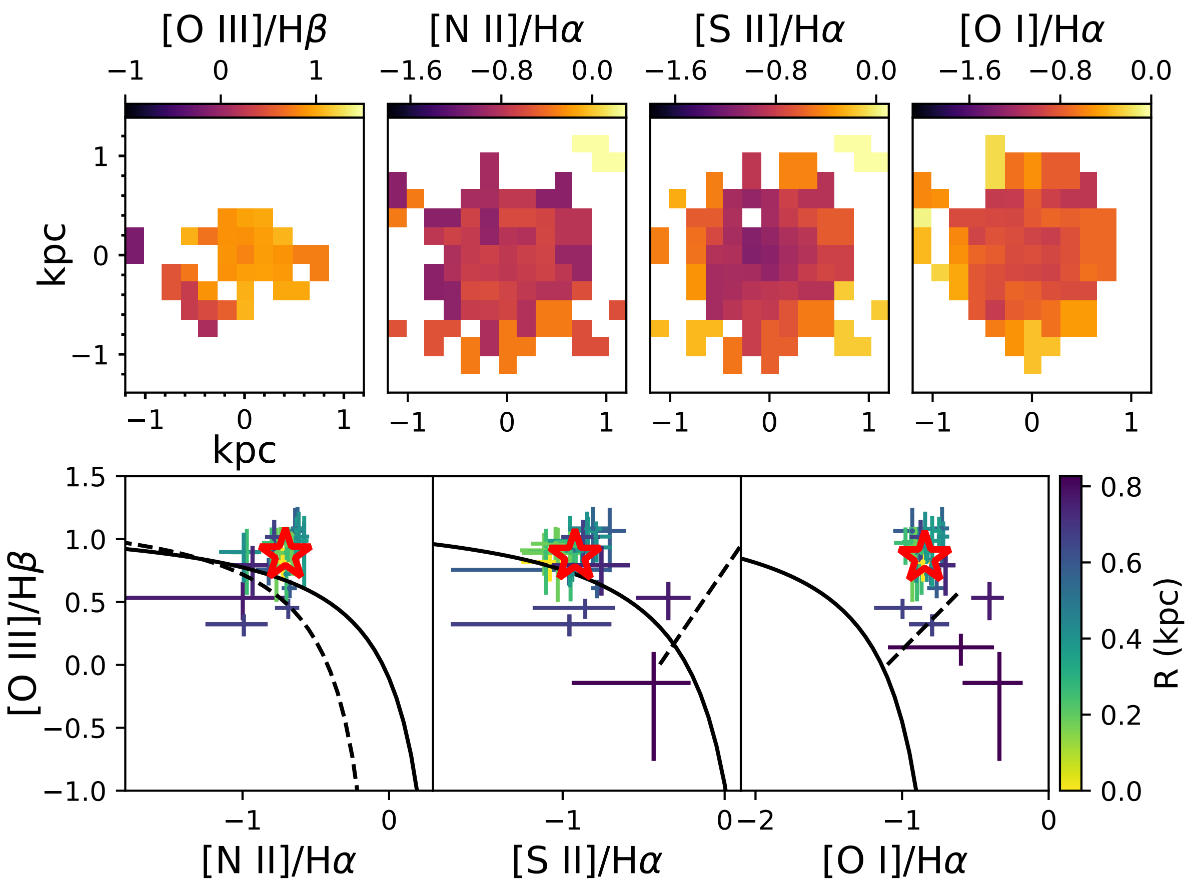

Figure C.19: Same as Fig. C.18 but for the outflow component C3.

show a clear velocity gradient with a PA $\simeq 30°$ and a velocity range from ~-40 km s^{-1} to $\sim+90$ km s^{-1}.

The maps of the velocity-integrated [O III] $\lambda5007$ flux and of the individual velocity components all show a roughly circular morphology. There are no clear offsets among the flux peaks of the global and flux individual components except for that of C1 components in the GMOS data, which is slightly offset to the east by $\sim$1 spaxel (0.2$''$) with respect to that of the global flux.

The C1 component shows a clear velocity gradient (with v_{50} varying from ~-30 km s^{-1} to $+30$ km s^{-1} in the GMOS data, stretching to $\sim\pm50$ km s^{-1} in the KCWI data). The orientation of the velocity gradient (PA $\simeq 30°$) is very similar to that of the stellar velocities, while the velocity range of the C1 gas component ($\sim\pm50$ km s^{-1}) is slightly smaller than that of the stars (~-40 to $\sim+90$ km s^{-1}) on the same spatial scale. The line width of the C1 component is generally narrow (median $W_{80} \simeq 110$ km s^{-1} in the KCWI data), comparable to the stellar velocity dispersions. The C1 component represents the quiescent rotating material within the host galaxy.

In contrast, the C3 component is generally blueshifted (with v_{50} down to -50 km s^{-1} in the GMOS data and -70 km s^{-1} in the KCWI data) with respect to the systemic velocity derived from the stellar velocity field, and the line widths are very large (with W_{80} reaching $\sim$1200 km s^{-1} in the GMOS data and $\sim$1250 km s^{-1} in the KCWI data). These characteristics are strong evidence of a fast outflow in this system.

The C2 component is in general redshifted with respect to the system velocity (with a median v_{50} of $\sim+30$ km s^{-1} in the GMOs data and $\sim+60$ km s^{-1} in the KCWI data), and the line widths are clearly broader (median $W_{80} \simeq 350$ km s^{-1} and $\simeq 430$km s^{-1}in the GMOS and KCWI data, respectively) than those of the C1 components and the stellar velocity dispersions. No clear spatial gradient is seen in either quantities. One possibility is that the C2 component represents the far side of the same outflow traced by the C3 component. The smaller absolute velocities and smaller line widths of the C2 component can be explained in this picture if only a portion of the redshifted gas is visible, where the broader, more redshifted portion of the outflow is blocked by the galaxy itself. Alternatively, the C2 component may represent non-outflowing ionized gas in the (extended) narrow-line region (NLR) of the AGN, similar in line widths to NLR gas in other Seyfert 2 Galaxies [e.g. Netzer, 1990].

Interestingly, a pc-scale ($\sim$47 pc) radio jet was recently reported in this target [Yang et al., 2020], which might be an important energy source for the outflowing ionized gas on kpc scale [e.g. Zakamska and Greene, 2014, Morganti et al., 2015, Ramos Almeida et al., 2017]. It is difficult to directlty connect this radio jet to the outflowing ionized gas revealed by our data, due to the large difference in physical scales between the two, and our data do not provide clear information on the orientation of the outflow in the sky plane. Nevertheless, it seems that the radio jet might have enough kinetic energy ($P_{jet} = 10^{42.6\pm0.7}$ erg s^{-1}) to drive the ionized gas outflow, assuming a simple scaling relation between radio luminosity and jet power [Yang et al., 2020].

C.1.5.2 Flux Radial Profiles

The radial profiles of the velocity components are all slightly more extended than the PSF based on the GMOS data, where the fluxes are on average larger than the corresponding PSF values at the $\sim$2-σ level at $r \simeq 0.8$ kpc in the GMOS data. For the KCWI data, the more extended PSF of the data makes the flux excesses less significant, although flux excesses are still seen for the C1 and C3 components at $r \simeq 1.3$ kpc (Fig. C.17). When comparing the fluxes of individual velocity components, the C3 component has a radial distribution that is very similar to that of the C1 component in both IFU data sets. Since C1 shows a clear, spatially resolved velocity gradient, the C3 component is also likely spatially resolved by our data, However, the C2 component is slightly more compact than the other two, where the C2/C1 flux ratios drops to ∼0.1–0.2 at r$\gtrsim$1 kpc in both GMOS and KCWI data.

C.1.5.3 Ionization Diagnosis

Here we examine the ionization properties of individual velocity components based on the GMOS data in the same manner as that for J0842+03. For the calculations of line ratios below, we combine the fluxes of the C1 and C2 components since i) we are interested in the difference, if any, between the pure, rapidly outflowing gas and the other gas components; ii) the C1 component is significantly fainter and less spectrally resolved, and thus has more uncertain line ratios than the other two components. For both the C3 and C1+C2 components, the [O III]/Hβ ratios are roughly constant across the map. The other three line ratios, [N II]/Hα, [S II]/Hα, and [O I]/Hα, are also roughly constant or show only rather mild radial trends.

Both the C3 and C1+C2 components show spatially-integrated line ratios consistent with AGN in all three BPT and VO87 diagrams. For both the C3 and C1+C2 components, the line ratios of individual spaxels are also dominated by AGN-like line ratios, at least within r $\simeq$ 0.7 kpc. The [N II]/Hα and [S II]/Hα ratios are in general smaller than those measured in the more luminous AGN with more massive host galaxies. This is consistent with the lower gas-phase metallicity expected from this dwarf galaxy (log $M_*/M_\odot$ = 9.36; Table 5.1).

For the C3 component, there is a possible trend that line ratios in spaxels at larger radii are closer to the dividing lines of AGN and star-forming activity in all three BPT and VO87 diagrams. This is perhaps a sign that the ionization parameter decreases with increasing radii, as is generally the case in AGN, and/or that the relative contribution to the ionization/excitation from possible star-forming activity increases at larger radii.

C.1.6 J0954+47

The maps of the [O III] λ5007 flux and kinematics, the map of stellar kinematics, and the [O III] λ5007 flux radial profiles of the individual velocity components in this object are presented in Fig. C.20–C.22.

C.1.6.1 Maps of the [O III] λ5007 Flux and Kinematics

Three velocity components (C1, C2, and C3) are needed to describe the [O III] λ5007 line profiles in this system. The flux maps of the total emission line and individual components show a circular morphology in general. The map of the median velocities v_{50} of the overall emission line profiles shows a gradient similar to that of the C1 component, although the C1 component is slightly more redshifted on average.

The C1 component shows a clear velocity gradient with v_{50} varying from $\sim$0 km s^{-1} to $\sim$+20 km s^{-1}, with a position angle similar to that of the stellar velocity field (PA $\simeq -45°$; Fig. C.21). The line widths are small in general (median $W_{80} \simeq 70$ km s^{-1}), similar to the velocity dispersion of the stellar component. These results suggest that the C1 component is largely rotating in the potential well of the galaxy, but with a smaller velocity amplitude (the values of v_{50} of the [O III] λ5007 C1 component are on average $\sim$10–20 km s^{-1} smaller in absolute terms

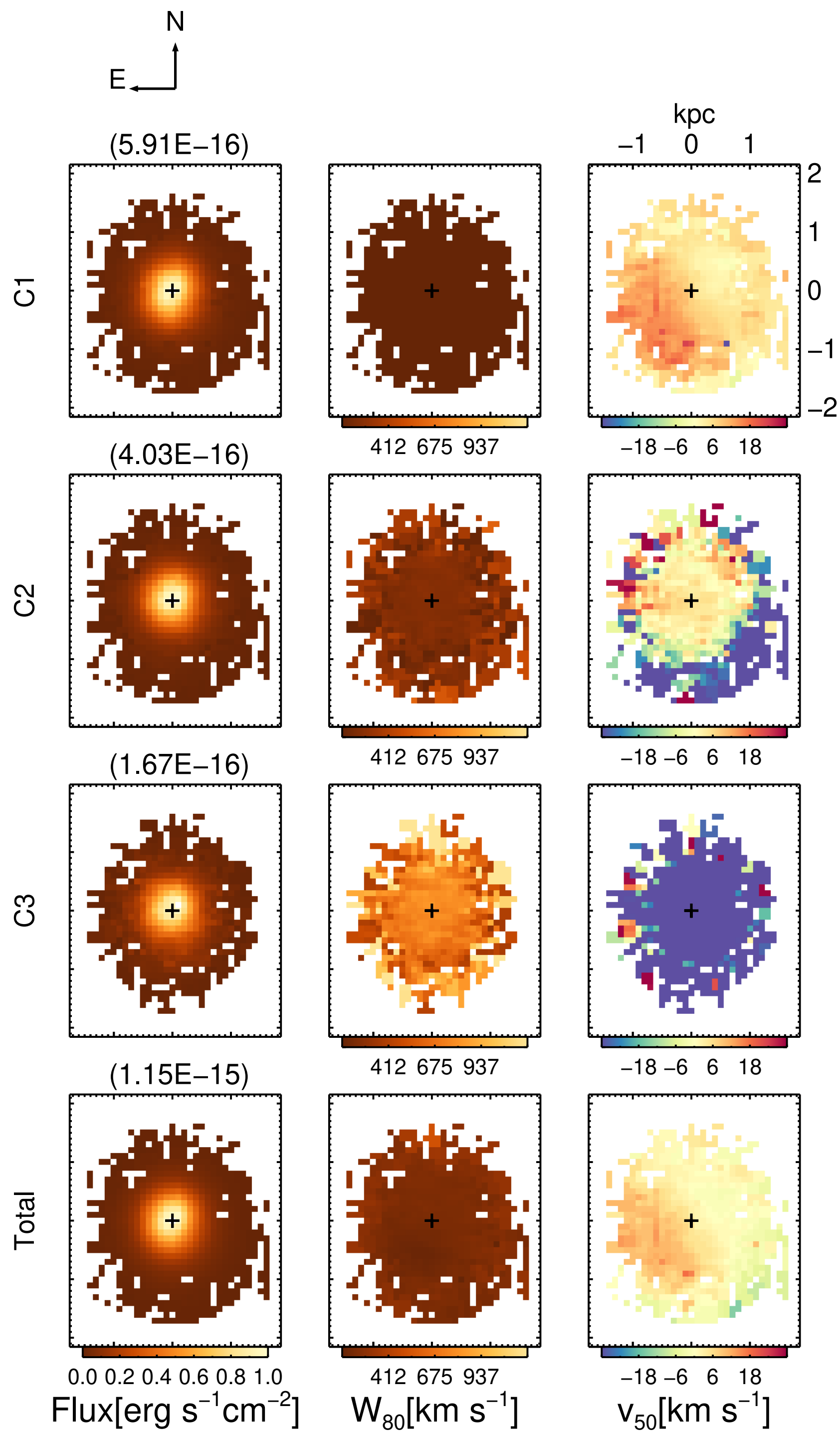

Figure C.20: Same as Fig. C.1 but for J0954+47 based on the KCWI data.

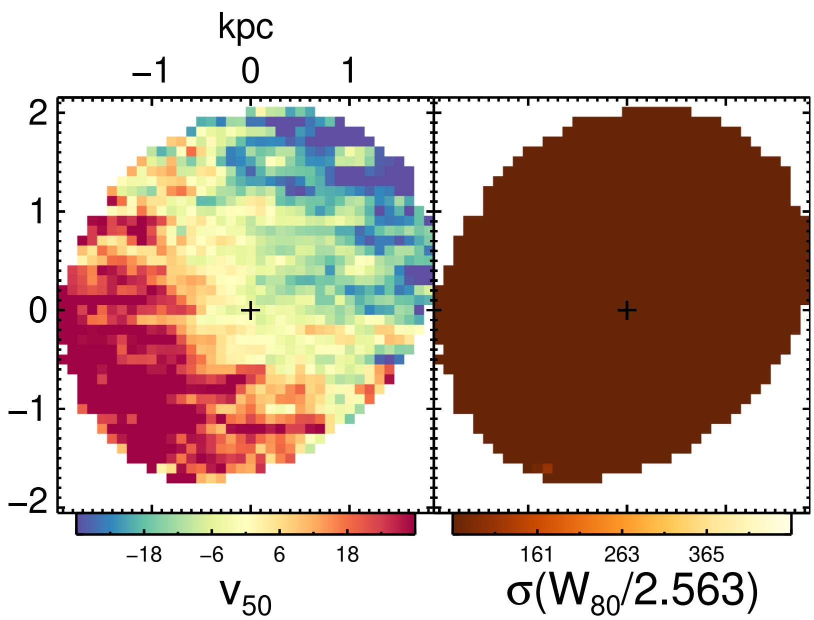

Figure C.21: Same as Fig. C.2 but for J0954+47.

than the stellar values),

The C2 component is generally close to the systemic velocity except in the southwestern region, where they are significantly blueshifted (by as much as $\sim$70 km s^{-1}) and slightly broader than in other parts of the galaxy. These blueshifted and broad velocity profiles may indicate the presence of outflowing and/or turbulent gas.

The C3 component is significantly blueshifted with respect to the systemic velocity (v_{50} down to $\sim$$-$80 km s^{-1}) and show large line width (W_{80} up to $\sim$1100 km s^{-1}). Mild radial gradients are seen in these quantities. The large line widths and clear blueshifts of the C3 component strongly suggest that they are associated with a fast outflow.

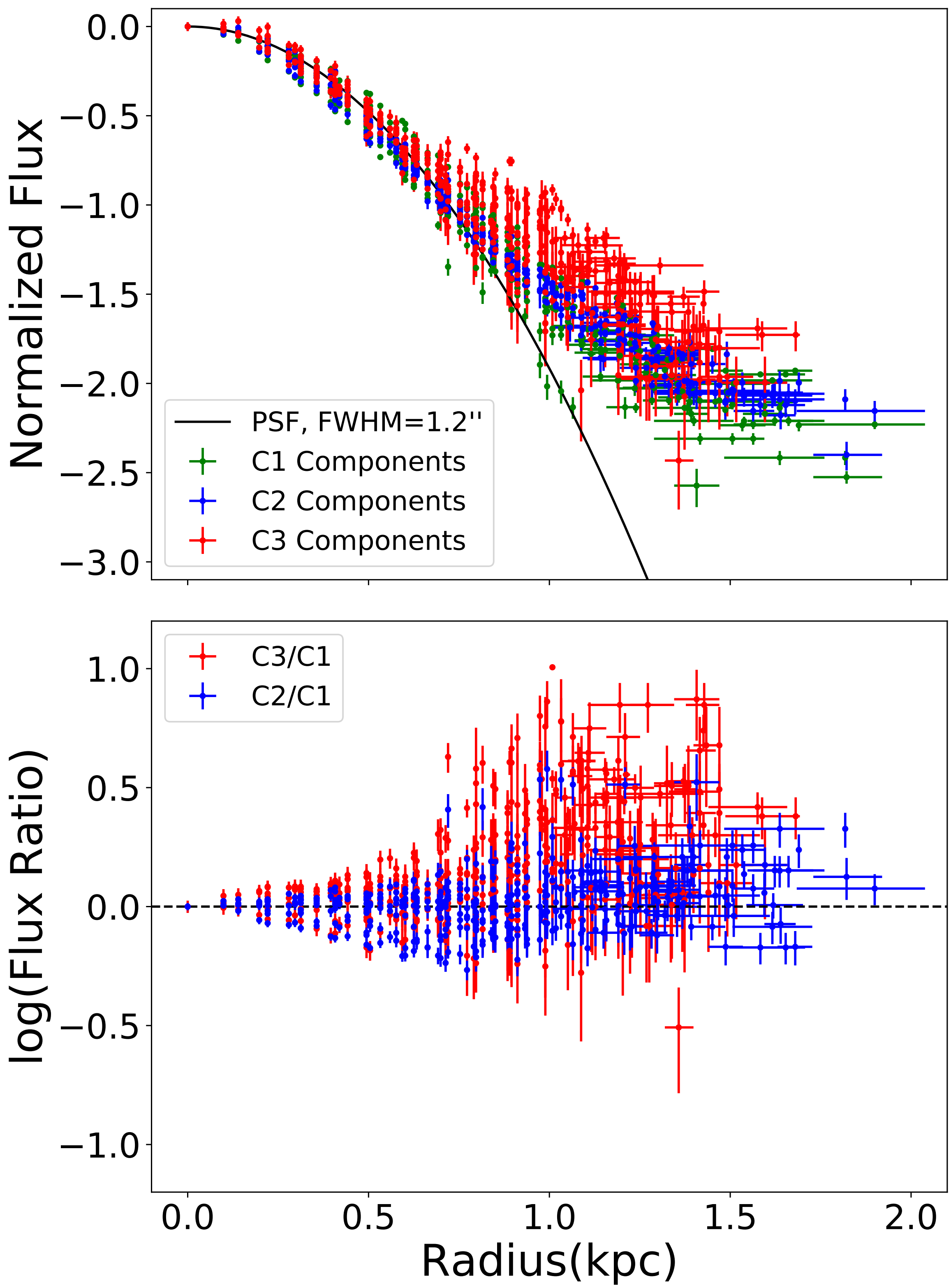

Figure C.22: Same as Fig. C.3 but for J0954+47.

C.1.6.2 Flux Radial Profiles

The [O III] λ5007 flux radial profiles of the individual velocity components are largely consistent with the PSF within 1 kpc, but all show excess emission (up to $\sim$4-σ level) beyond $\sim$1 kpc. The flux ratios of C2/C1 and C3/C1 scatter around unity in general, suggesting that they share a similar radial distribution. The C3 components might thus be spatially resolved by our data, as the C1 and C2 components are very likely so judging from the clear spatial velocity gradients/structures seen in the v_{50} maps.

C.1.7 J1005+12

The results on this object are presented in Fig. C.23–C.25, in the same format as that for J0954+47.

C.1.7.1 Maps of the [O III] λ5007 Flux and Kinematics

Three velocity components (C1, C2, and C3) are required to fit the [O III] λ5007 line profiles adequately in this object. The values of v_{50} of the overall emission line profiles are slightly blueshifted (~ -30 km s^{-1}), and show a gradient along PA $\simeq$ 30° that is very similar to that of the C1 component.

The C1 component shows a clear velocity gradient with v_{50} ranging from ~ -40 km s^{-1} to $\sim$10 km s^{-1}, but this gradient is not centered on the systemic velocity and is perpendicular (PA$\simeq$ 150°) to that seen on a slightly large spatial scale in the stellar velocity field (PA $\simeq$ 60°). The line widths of the C1 component are in general narrow (median $W_{80} \simeq$ 80 km s^{-1}), similar to the stellar velocity dispersions. If we interpret the velocity gradient of the C1 component as

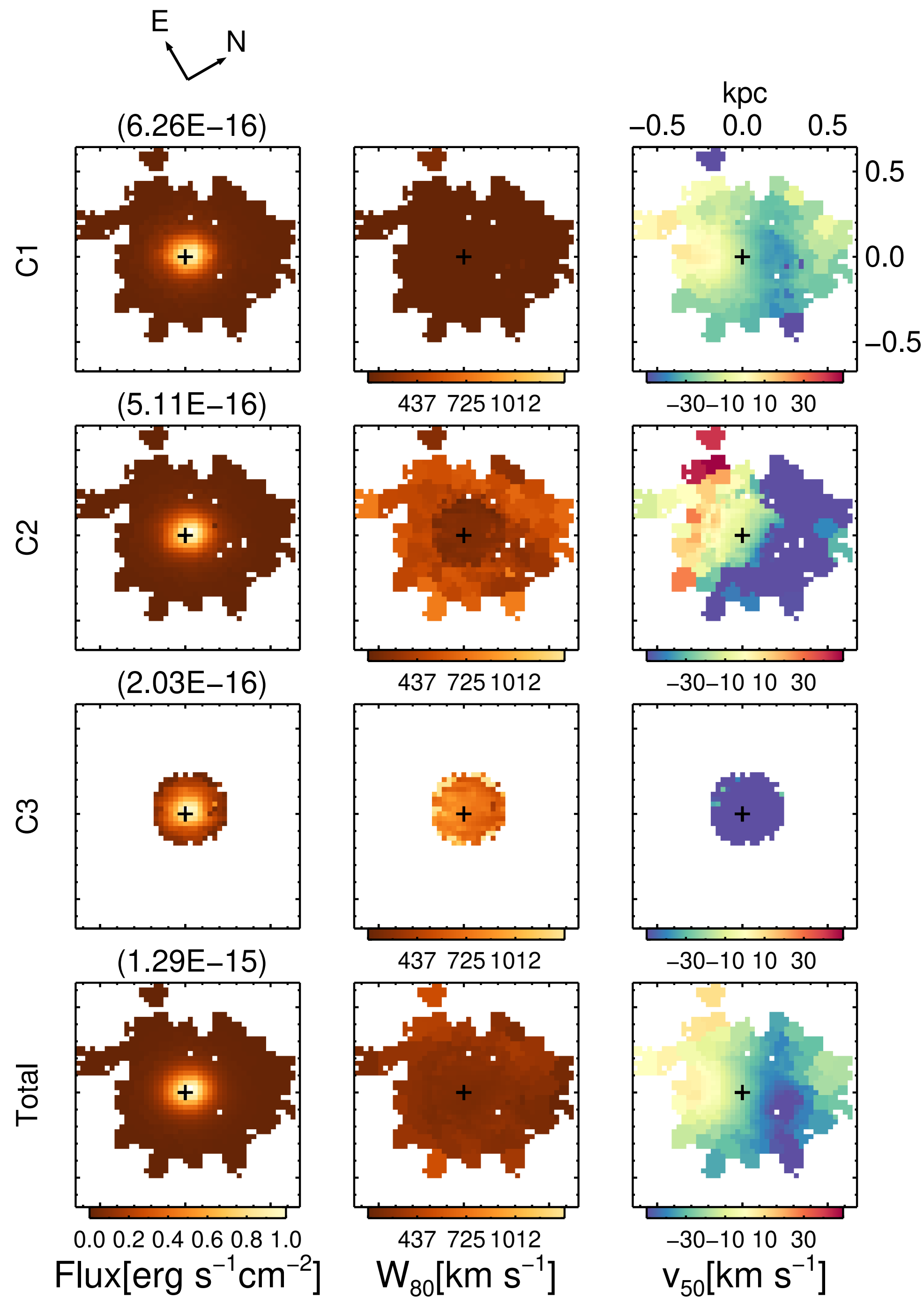

Figure C.23: Same as Fig. C.1 but for J1005+12.

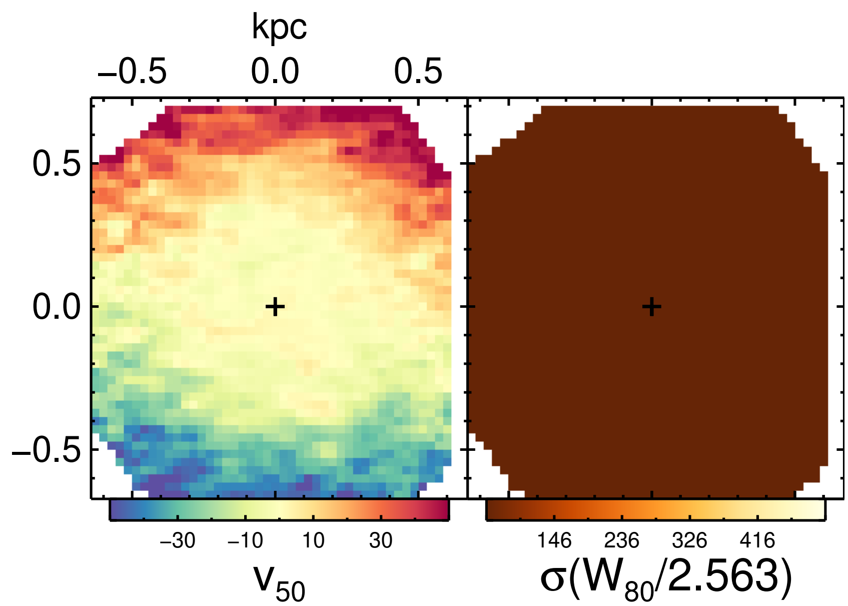

Figure C.24: Same as Fig. C.2 but for J1005+12.

a sign of rotation, the different angular momentum of the C1 component relative to that of the stellar component suggests that the C1 component consists of gas acquired externally after the stars in the galaxy were already in place [e.g. Chen et al., 2016]. The overall blueshift of the C1 component may also hint at the influence of an outflow (see below).

The C2 component shows a dramatic velocity gradient where v_{50} vary from $\sim$−100 km s^{-1} to 50 km s^{-1}. The kinematic major axis of the C2 component has a PA $\simeq$ 135°, offset from those of the C1 component and stellar velocity field. The line widths of the C2 component are also significantly larger (median $W_{80} \simeq$ 440 km s^{-1}) than those of the C1 component. The interpretation of the C2 component is unclear; it may represent a mixture of rotating, turbulent and outflowing gas in the galaxy.

The nature of the C2 component is further explored by fitting the v_{50} map of this component with *Kinemetry*, following the same procedure as in Appendix C.1.1.1. The residual velocities

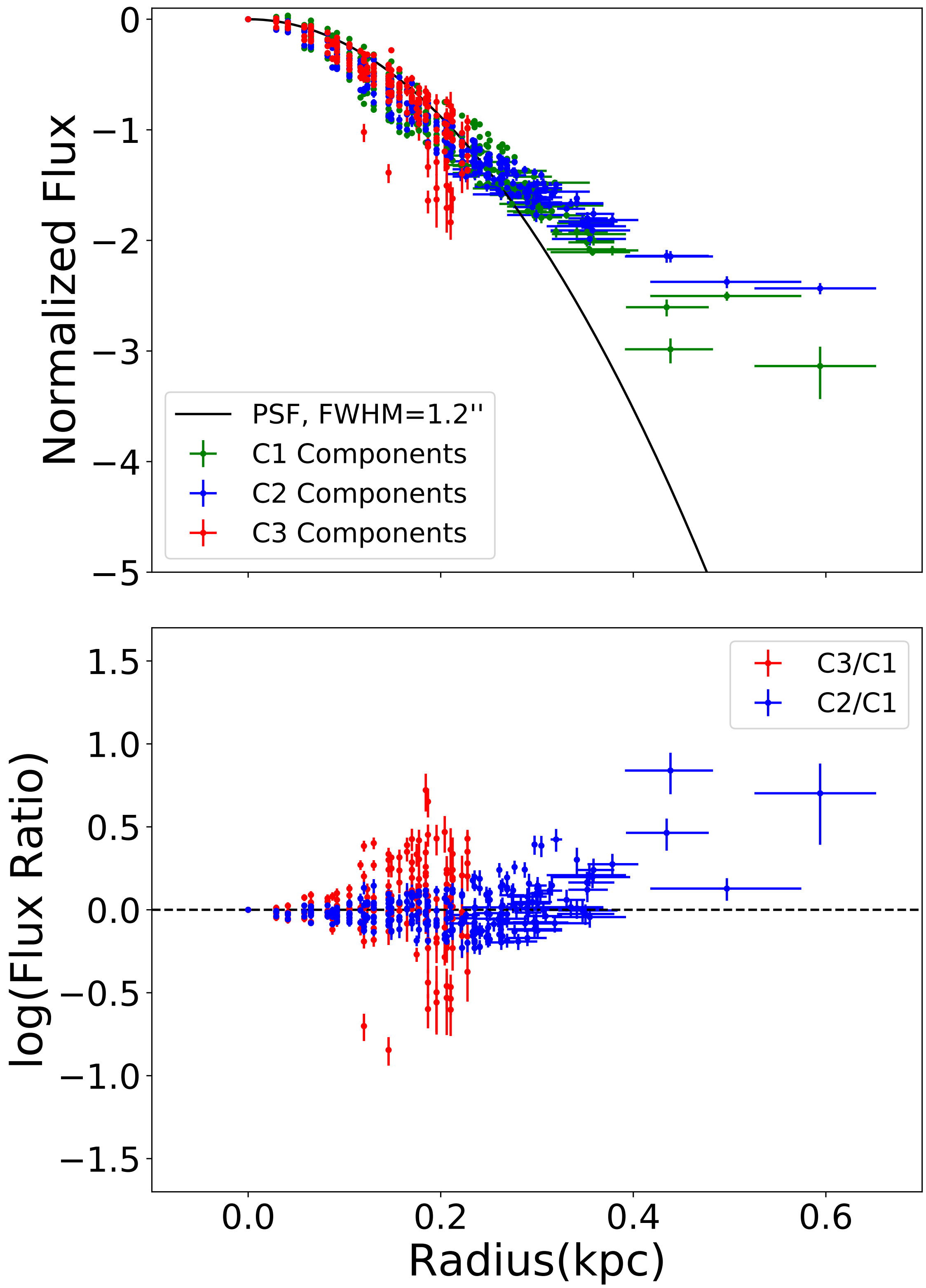

Figure C.25: Same as Fig. C.3 but for J1005+12. Contrary to Fig. C.3, the data points of C1 and C2 components beyond the maximal spatial extent of the C3 component are shown instead.

(observed v_{50} − best-fit circular velocities) show absolute amplitudes similar to those of the best-fit circular velocities. This suggests that a pure, rotating disk cannot explain the kinematics of the C2 component alone, which further supports our statement in the previous paragraph that it is partially affected by outflowing gas.

The C3 component is blueshifted (v_{50} down to ~ -200 km s^{-1}) and shows large line widths (W_{80} up to $\sim$1200 km s^{-1}). Mild radial gradients are seen in these quantities. The large line widths and clear blueshifts of the C3 component suggest that they are most likely due to a fast outflow.

C.1.7.2 Flux Radial Profiles

The [O III] λ5007 flux radial profiles of the individual velocity components are largely consistent with the PSF within $\sim$0.2 kpc, but excess flux is detected (at the $\sim$4-σ level on avaerage) beyond 0.2 kpc in C1 and C2 velocity components (Fig. C.25). The flux ratios among individual velocity components are in general scattered around unity within 0.2 kpc, suggesting no difference of radial flux distributions among the three velocity components. However, the C2 component may have slight flux excess compared to the C1 component beyond $\sim$0.3 kpc.

C.1.8 J1009+26

The results of our analysis of the KCWI data for J1009+26 are presented in Fig. C.26–C.28.

C.1.8.1 Maps of the [O III] λ5007 Flux and Kinematics

Two Gaussian components are sufficient to describe the [O III] λ5007 emission line profiles in this object. The maps of v_{50} and W_{80} of the overall line profiles show apparent gradients and structures that are very similar to those of the C1 component (Fig. C.26).

The values of v_{50} in the C1 component are on average slightly blueshifted (~ -10 km s^{-1}) compared with the stellar velocities (shown in Fig. C.27). The PA of the v_{50} gradient is $\sim 0°$, similar to that of the gradient of the stellar components. The line widths of the C1 components are once again narrow (median $W_{80} \simeq 80$ km s^{-1}), and similar to the stellar velocity dispersions. The C1 component appears to be associated with gas that is largely rotating within the galaxy, but the slight overall blueshift may be a sign of a small bulk outflow.

The flux peak of the C2 component is slightly offset from that of the C1 component by $\sim 0.15''$ (1 spaxel) to the southeast. The map of v_{50} of the C2 component shows a clear gradient along the SE-NW direction (PA $\simeq -40°$), much steeper (v_{50} varies from -60 km s^{-1} to 40 km s^{-1}) and offset in position angle with respect to that seen in the C1 component. The line widths of the C2 component are also much broader than those of the C1 component (with W_{80} reaching 480 km s^{-1}), and no clear spatial structure is seen. The C2 component may represent a tilted, biconical outflow, like that of J0100$-$01, where the near (NW) side of the outflow is blueshifted and the far (SE) side is redshifted. Alternatively, the apparent bisymmetry of the velocity field of the C2 component may be interpreted as a rotating structure, but the large line widths indicate that the gas is turbulent.

This result is confirmed using *Kinemetry*: while the residual velocities (observed v_{50} $-$ best-fit circular velocities) for the C2 component do not show clear patterns indicative of biconical outflowing gas, the best-fit circular velocity field of the C2 component has significantly larger amplitudes and a clearly different position angle when compared to those of the C1 component, as reported above from our visual examination of the observed kinematic maps.

C.1.8.2 Flux Radial Profiles

As shown in Fig. C.28, the flux radial profiles of both velocity components are clearly more extended than the PSF, which is consistent with the spatial gradient clearly seen in the v_{50} maps. The C2 component has excess flux relative to the C1 component beyond $\sim$0.3 kpc, where the flux ratios reach a maximum of $\sim$10 at around 0.7 kpc.

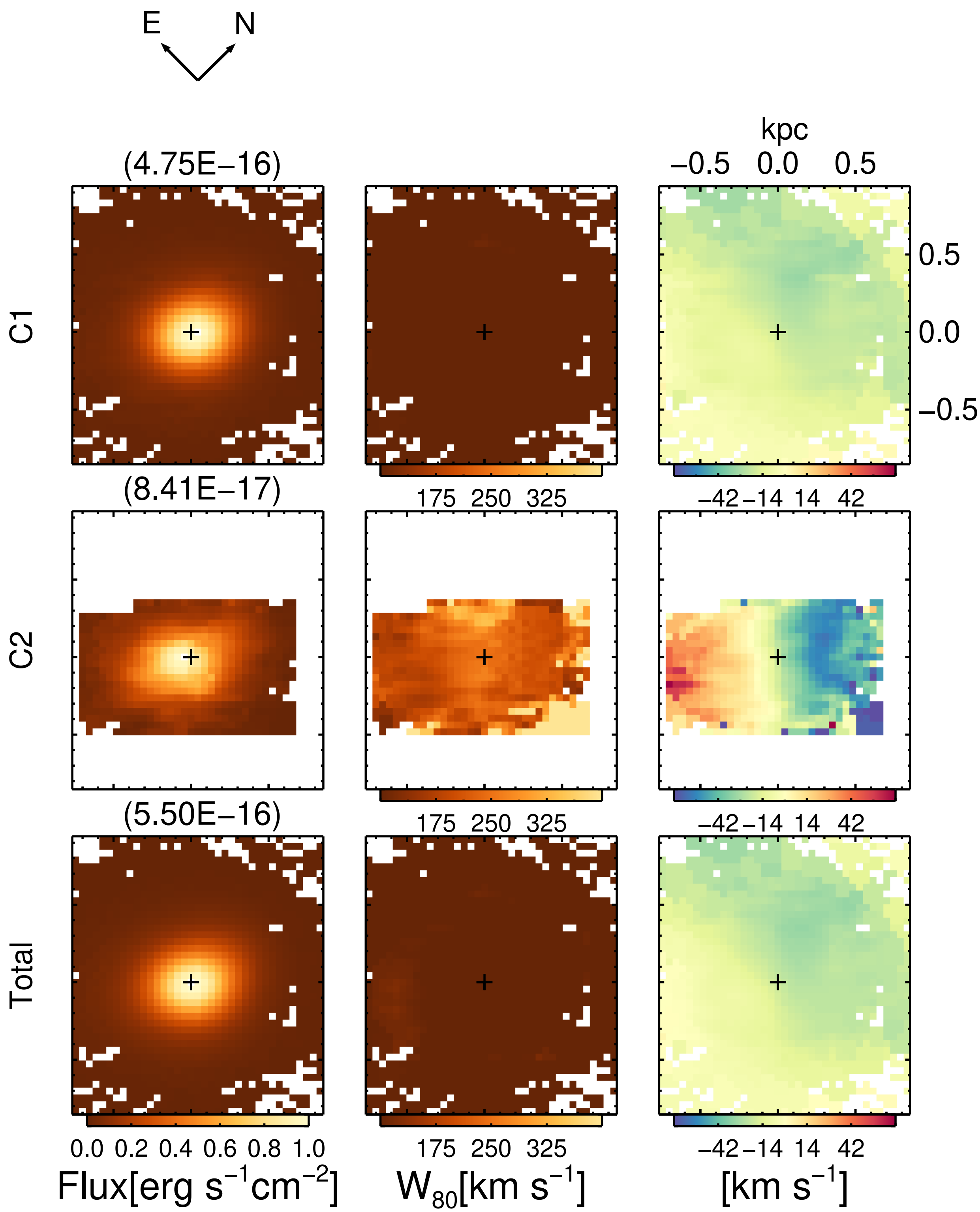

Figure C.26: Same as Fig. C.1 but for J1009+26.

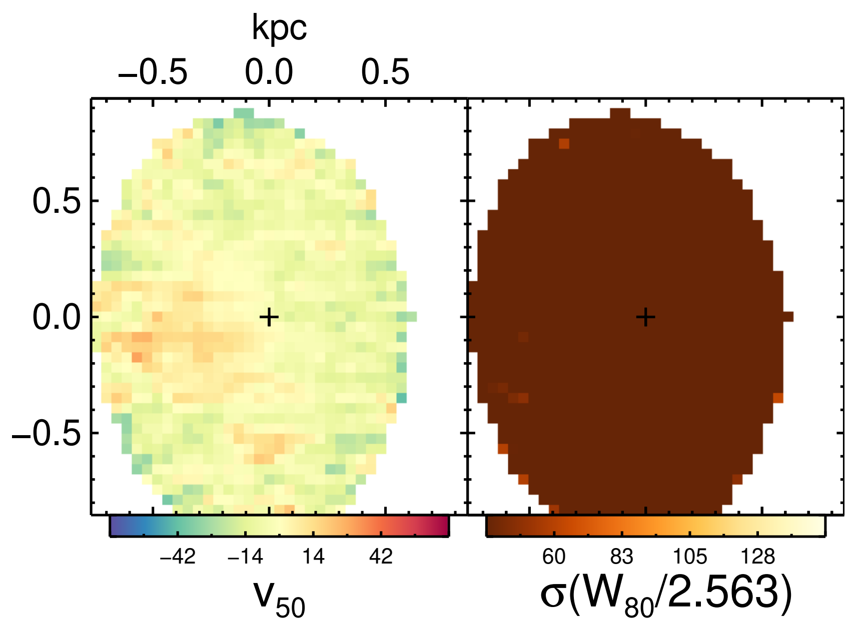

Figure C.27: Same as Fig. C.2 but for J1009+26.

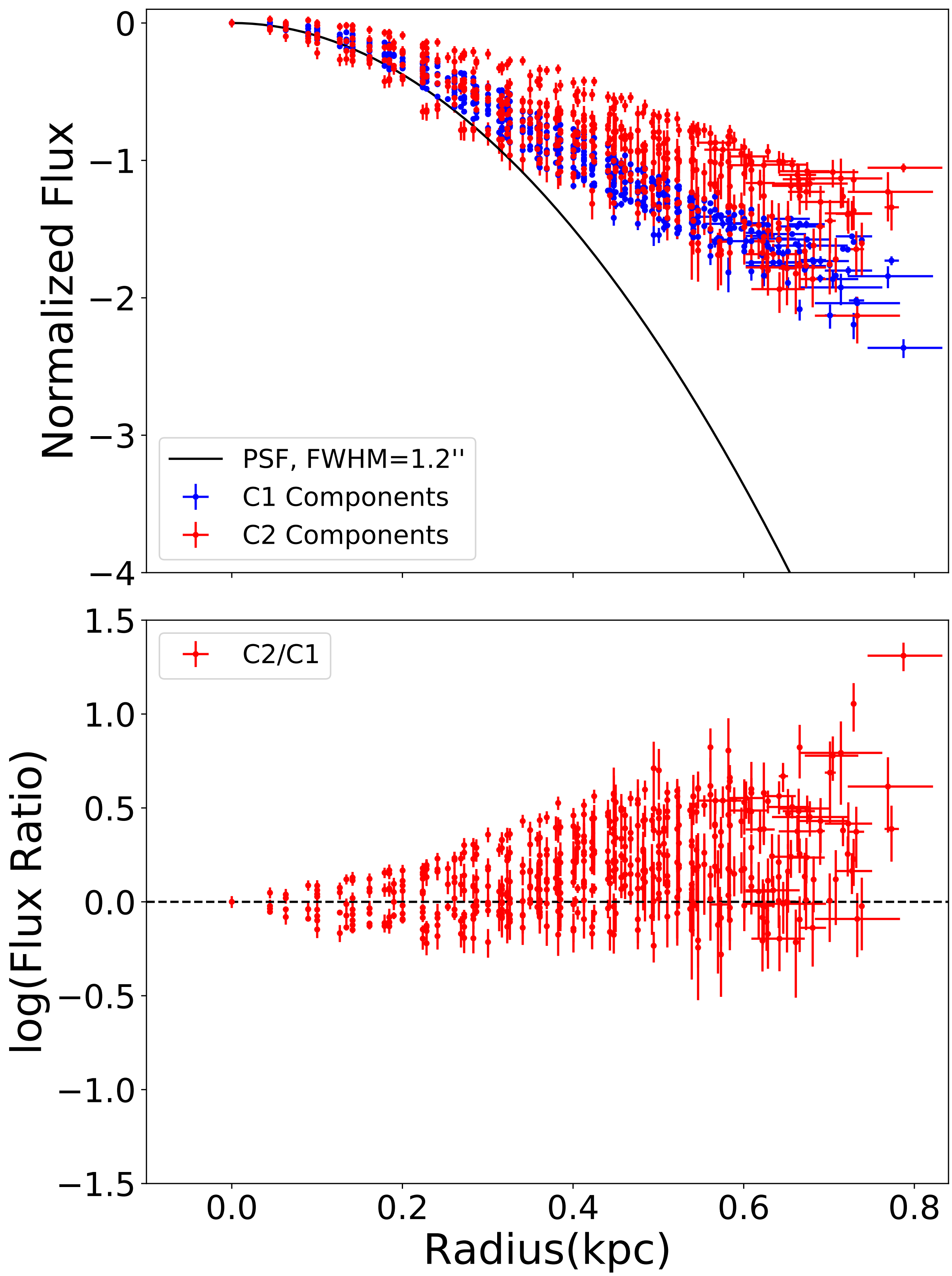

Figure C.28: Same as Fig. C.3 but for J1009+26.

Appendix D: Appendix for Chapter 5

D.1 AGN Luminosity and SFR of J0954+47

The AGN luminosity and SFR of J0954+47 are the two fundamental physical properties on which the discussions on the energy source and impact of the outflow are based. The AGN luminosity can also be obtained by integrating the AGN spectrum (scaled by the observed monochromatic continuum luminosity at 1320 Å) adopted for the photoionization modeling in Section 5.3.2.1, which gives log(L_{AGN}) $\simeq$ 42.8 erg s^{-1}. This is an order of magnitude smaller than the [O III] λ5007 based L_{AGN}. Each of the two estimates of L_{AGN} has its own caveat. For the FUV-based one, zero extinction is assumed and log(L_{AGN}) may be underestimated. The departure of the intrinsic AGN radiation from the adopted AGN spectrum is also not known. For the O III-based one, the uncertainty of the scaling factor is mainly due to the large scatter of the scaling relation Lamastra et al. [2009]. To make our analysis more self-consistent, we adopt the FUV-based L_{AGN} in our following discussion on the outflow detected through the FUV absorption features.

As for the SFR, the O II-based upper limit (<0.3 $M_\odot$ yr^{-1}), as reported in L20, is obtained by adopting the empirical relation calibrated for AGN only Ho [2005]. In addition, two more upper limits, based on the FUV luminosity (<0.08 $M_\odot$ yr^{-1}) and FUV+MIR luminosities (<1.9 $M_\odot$ yr^{-1}), are reported in Latimer et al. [2021]. Both values are deemed upper limits as the scaling relations adopted are calibrated based on star-forming galaxies and the AGN contamination to the FUV and MIR luminosities are not subtracted. The FUV-only one may be a bit low as it does not account for the dust-obscured star formation activity. The FUV+MIR-based one is too high: J0954+47 is classified as AGN in all popular *WISE*-based MIR diagnosis [e.g. Jarrett et al., 2011, Mateos et al., 2012][1]. The MIR luminosity is thus likely dominated by the AGN rather than the star formation, leading to a significant overestimate of SFR. In all, we adopt the O II-based upper limit on SFR in the following discussions.

D.2 Full G160M Spectra of Our Objects

The full HST/COS G160M spectra of J0906+56, J0954+47 and J1009+26 are shown in Fig. D.1, D.2 and D.3.

[1] As far as we are concerned, the only exception is the diagnosis proposed by Assef et al. [2010] adopting all 4 *WISE* band.

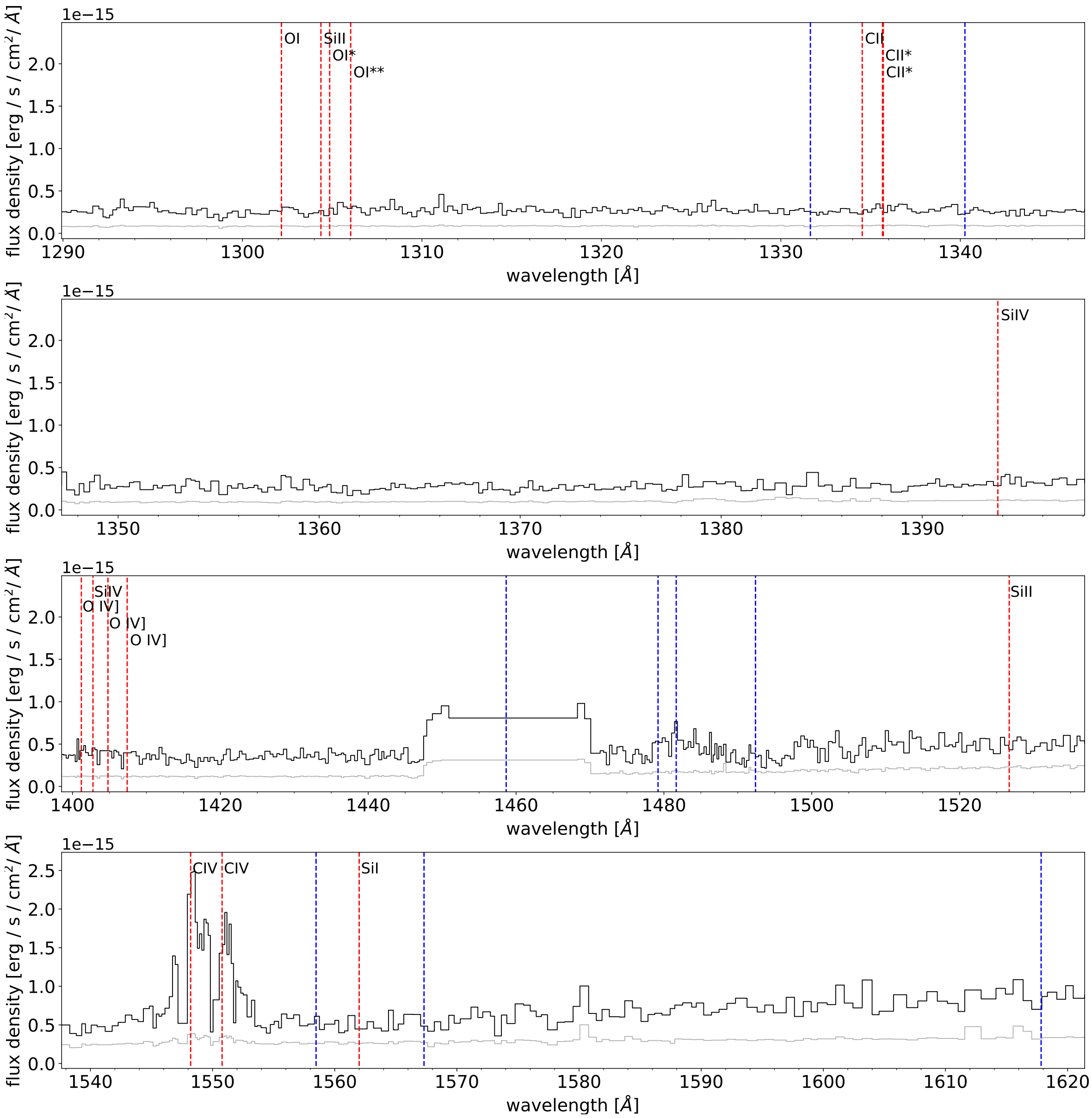

Figure D.1: Full G160M spectrum for J0906+56. The expected locations of strong transitions at the systemic velocity are marked in red dashed lines. The expected locations of strong z=0 foreground absorption features are marked in blue dashed lines.

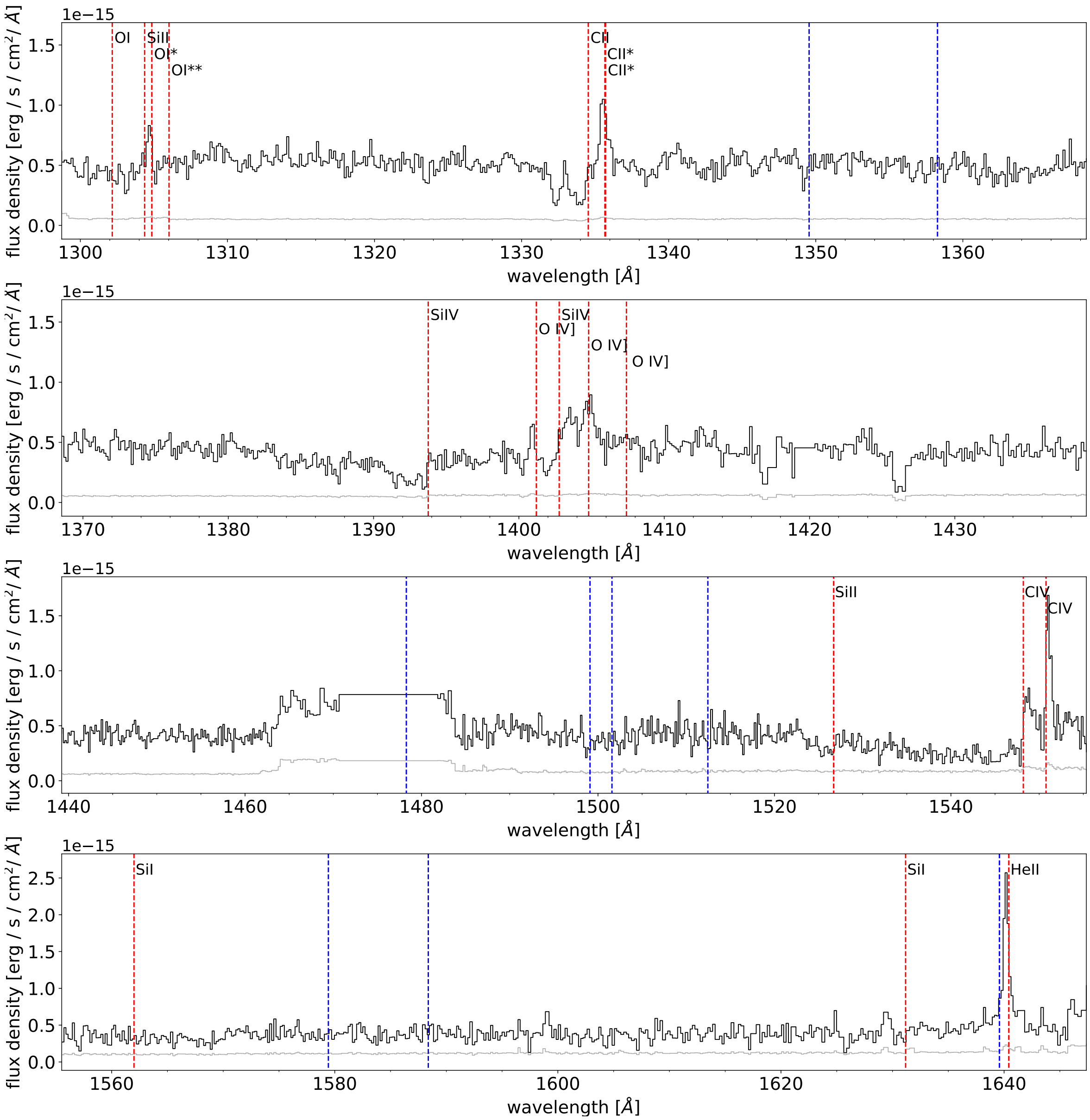

Figure D.2: Same as Fig. D.1 but for J0954+47.

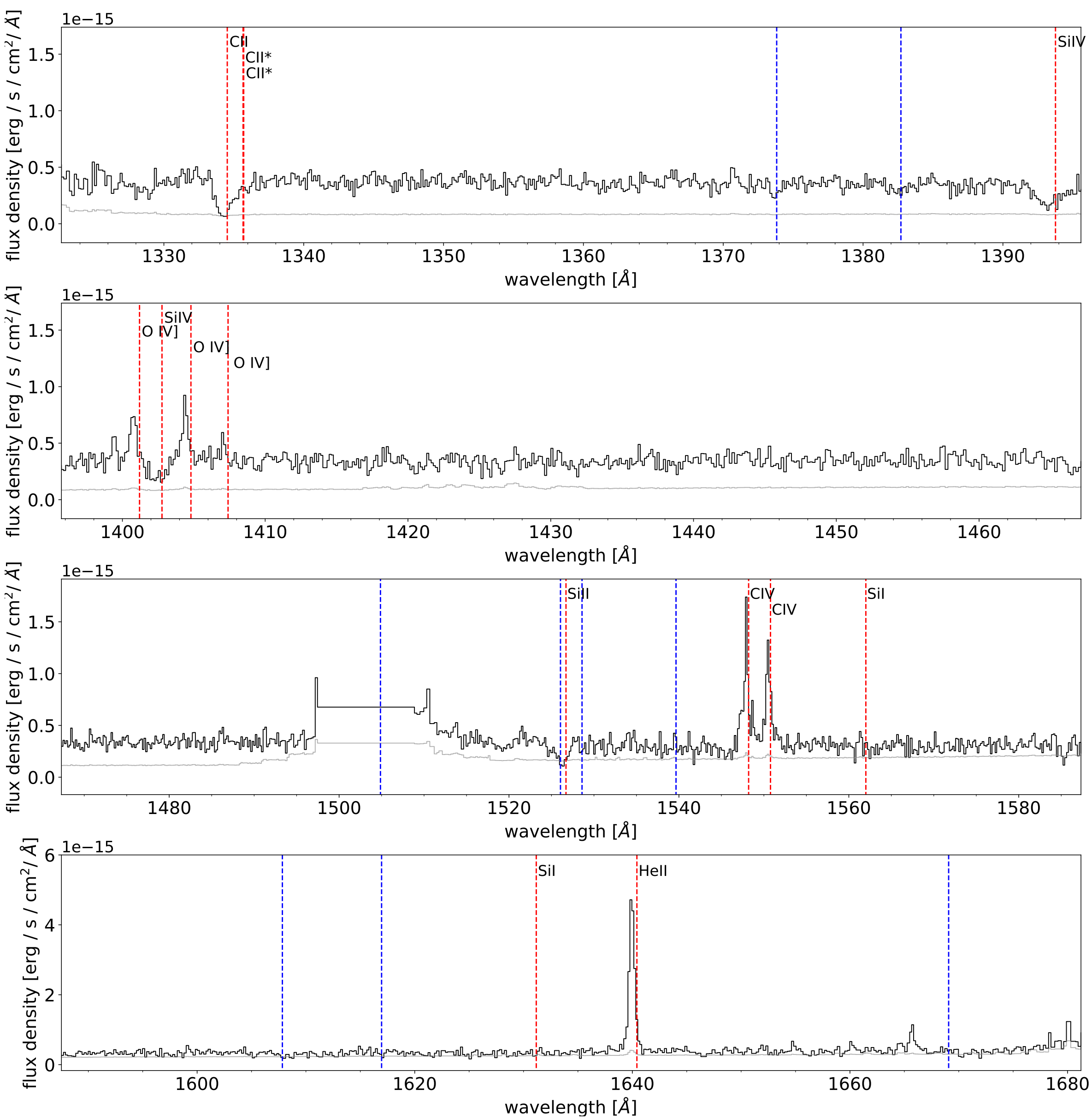

Figure D.3: Same as Fig. D.1 but for J1009+26.

Appendix E: Facilities and Software

E.1 Facilities

A summary of facilities used in this thesis is listed below:

- *Chandra*

  ACIS-S was used to obtain the X-ray images of Mrk 273 (Chapter 3).

- *Gemini Telescope*

  GMOS was utilized to obtain the IFS data of dwarf galaxies with AGN (Chapter 4).

- *Hubble Space Telescope*

  COS was used to obtain the FUV spectra of ULIRGs (Chapter 2) and dwarf galaxies with AGN (Chapter 5).

- *Keck Telescope*

  KCWI was utilized to obtain the IFS data of dwarf galaxies with AGN (Chapter 4).

E.2 Softwares

A summary of software used in this thesis is listed below:

- astropy [Astropy Collaboration et al., 2013, 2018]
- CALCOS (`https://github.com/spacetelescope/calcos`)
- CIAO [Fruscione et al., 2006]
- IFSFIT [Rupke, 2014a]
- IFSRED [Rupke, 2014b]
- LINMIX_ERR [Kelly, 2007]
- LMFIT [Newville et al., 2016]
- NumPy [Harris et al., 2020]
- pPXF [Cappellari, 2017],
- pymccorrelation [Privon et al., 2020]
- SciPy [Virtanen et al., 2020]

Bibliography

S. Aalto, S. Garcia-Burillo, S. Muller, J. M. Winters, E. Gonzalez-Alfonso, P. van der Werf, C. Henkel, F. Costagliola, and R. Neri. High resolution observations of HCN and HCO^+J = 3-2 in the disk and outflow of Mrk 231. Detection of vibrationally excited HCN in the warped nucleus. *A&A*, 574:A85, February 2015. doi: 10.1051/0004-6361/201423987.

David C. Abbott and Peter S. Conti. Wolf-rayet stars. *Annual Review of Astronomy and Astrophysics*, 25(1):113–150, 1987. doi: 10.1146/annurev.aa.25.090187.000553. URL `https://doi.org/10.1146/annurev.aa.25.090187.000553`.

R. Aladro, S. König, S. Aalto, E. González-Alfonso, N. Falstad, S. Martín, S. Muller, S. García-Burillo, C. Henkel, P. van der Werf, E. Mills, J. Fischer, F. Costagliola, M. Krips, and . Molecular gas in the northern nucleus of Mrk273: Physical and chemical properties of the disk and its outflow. *ArXiv e-prints*, May 2018.

James T. Allen, Paul C. Hewett, Natasha Maddox, Gordon T. Richards, and Vasily Belokurov. A strong redshift dependence of the broad absorption line quasar fraction. *MNRAS*, 410(2): 860–884, January 2011. doi: 10.1111/j.1365-2966.2010.17489.x.

Mark G. Allen, Michael A. Dopita, Zlatan I. Tsvetanov, and Ralph S. Sutherland. Physical Conditions in the Seyfert Galaxy NGC 2992. *ApJ*, 511(2):686–708, February 1999. doi: 10.1086/306718.

Mark G. Allen, Brent A. Groves, Michael A. Dopita, Ralph S. Sutherland, and Lisa J. Kewley. The MAPPINGS III Library of Fast Radiative Shock Models. *ApJS*, 178(1):20–55, Sep 2008. doi: 10.1086/589652.

Jeremy Allington-Smith, Graham Murray, Robert Content, George Dodsworth, Roger Davies, Bryan W. Miller, Inger Jorgensen, Isobel Hook, David Crampton, and Richard Murowinski. Integral Field Spectroscopy with the Gemini Multiobject Spectrograph. I. Design, Construction, and Testing. *PASP*, 114(798):892–912, August 2002. doi: 10.1086/341712.

M. E. Anderson, E. Churazov, and J. N. Bregman. A deep XMM-Newton study of the hot gaseous halo around NGC 1961. *MNRAS*, 455:227–243, January 2016. doi: 10.1093/mnras/stv2314.

Nahum Arav and Zhi-Yun Li. The Role of Radiative Acceleration in Outflows from Broad Absorption Line QSOs. I. Comparison with O Star Winds. *ApJ*, 427:700, June 1994. doi: 10.1086/174177.

Nahum Arav, Jelle Kaastra, Gerard A. Kriss, Kirk T. Korista, Jack Gabel, and Daniel Proga. X-Ray/Ultraviolet Campaign on the Mrk 279 AGN Outflow: Constraining Inhomogeneous Absorber Models. *ApJ*, 620(2):665–672, February 2005. doi: 10.1086/425560.

Nahum Arav, Maxwell Moe, Elisa Costantini, Kirk T. Korista, Chris Benn, and Sara Ellison. Measuring Column Densities in Quasar Outflows: VLT Observations of QSO 2359-1241. *ApJ*, 681(2):954–964, July 2008. doi: 10.1086/588651.

Nahum Arav, Benoit Borguet, Carter Chamberlain, Doug Edmonds, and Charles Danforth. Quasar outflows and AGN feedback in the extreme UV: HST/COS observations of HE 0238-1904. *MNRAS*, 436(4):3286–3305, Dec 2013. doi: 10.1093/mnras/stt1812.

Nahum Arav, Xinfeng Xu, Timothy Miller, Gerard A. Kriss, and Rachel Plesha. HST/COS Observations of Quasar Outflows in the 500-1050 Å Rest Frame. I. The Most Energetic Outflows in the Universe and Other Discoveries. *ApJS*, 247(2):37, April 2020. doi: 10.3847/1538-4365/ab66af.

L. Armus, J. M. Mazzarella, A. S. Evans, J. A. Surace, D. B. Sanders, K. Iwasawa, D. T. Frayer, J. H. Howell, B. Chan, A. Petric, T. Vavilkin, D. C. Kim, S. Haan, H. Inami, E. J. Murphy, P. N. Appleton, J. E. Barnes, G. Bothun, C. R. Bridge, V. Charmandaris, J. B. Jensen, L. J. Kewley, S. Lord, B. F. Madore, J. A. Marshall, J. E. Melbourne, J. Rich, S. Satyapal, B. Schulz, H. W. W. Spoon, E. Sturm, V. U, S. Veilleux, and K. Xu. GOALS: The Great Observatories All-Sky LIRG Survey. *PASP*, 121:559, June 2009. doi: 10.1086/600092.

Lee Armus, Timothy M. Heckman, and George K. Miley. The Optical Emission-Line Nebulae of Powerful Far-Infrared Galaxies. *ApJ*, 364:471, December 1990. doi: 10.1086/169431.

K. A. Arnaud. XSPEC: The First Ten Years. In G. H. Jacoby and J. Barnes, editors, *Astronomical Data Analysis Software and Systems V*, volume 101 of *Astronomical Society of the Pacific Conference Series*, page 17, 1996.

S. Arribas, L. Colina, E. Bellocchi, R. Maiolino, and M. Villar-Martín. Ionized gas outflows and global kinematics of low-z luminous star-forming galaxies. *A&A*, 568:A14, Aug 2014. doi: 10.1051/0004-6361/201323324.

R. J. Assef, C. S. Kochanek, M. Brodwin, R. Cool, W. Forman, A. H. Gonzalez, R. C. Hickox, C. Jones, E. Le Floc'h, J. Moustakas, S. S. Murray, and D. Stern. Low-Resolution Spectral Templates for Active Galactic Nuclei and Galaxies from 0.03 to 30 μm. *ApJ*, 713(2):970–985, April 2010. doi: 10.1088/0004-637X/713/2/970.

Astropy Collaboration, Thomas P. Robitaille, Erik J. Tollerud, Perry Greenfield, Michael Droettboom, Erik Bray, Tom Aldcroft, Matt Davis, Adam Ginsburg, Adrian M. Price-Whelan, Wolfgang E. Kerzendorf, Alexander Conley, Neil Crighton, Kyle Barbary, Demitri Muna, Henry Ferguson, Frédéric Grollier, Madhura M. Parikh, Prasanth H. Nair, Hans M. Unther, Christoph Deil, Julien Woillez, Simon Conseil, Roban Kramer, James E. H. Turner, Leo Singer, Ryan Fox, Benjamin A. Weaver, Victor Zabalza, Zachary I. Edwards, K. Azalee Bostroem, D. J. Burke, Andrew R. Casey, Steven M. Crawford, Nadia Dencheva, Justin Ely, Tim Jenness, Kathleen Labrie, Pey Lian Lim, Francesco Pierfederici, Andrew Pontzen, Andy Ptak, Brian Refsdal, Mathieu Servillat, and Ole Streicher. Astropy: A community Python package for astronomy. *A&A*, 558:A33, October 2013. doi: 10.1051/0004-6361/201322068.

Astropy Collaboration, A. M. Price-Whelan, B. M. Sipőcz, H. M. Günther, P. L. Lim, S. M. Crawford, S. Conseil, D. L. Shupe, M. W. Craig, N. Dencheva, A. Ginsburg, J. T. VanderPlas, L. D. Bradley, D. Pérez-Suárez, M. de Val-Borro, T. L. Aldcroft, K. L. Cruz, T. P. Robitaille, E. J. Tollerud, C. Ardelean, T. Babej, Y. P. Bach, M. Bachetti, A. V. Bakanov, S. P. Bamford, G. Barentsen, P. Barmby, A. Baumbach, K. L. Berry, F. Biscani, M. Boquien, K. A.

Bostroem, L. G. Bouma, G. B. Brammer, E. M. Bray, H. Breytenbach, H. Buddelmeijer, D. J. Burke, G. Calderone, J. L. Cano Rodríguez, M. Cara, J. V. M. Cardoso, S. Cheedella, Y. Copin, L. Corrales, D. Crichton, D. D'Avella, C. Deil, É. Depagne, J. P. Dietrich, A. Donath, M. Droettboom, N. Earl, T. Erben, S. Fabbro, L. A. Ferreira, T. Finethy, R. T. Fox, L. H. Garrison, S. L. J. Gibbons, D. A. Goldstein, R. Gommers, J. P. Greco, P. Greenfield, A. M. Groener, F. Grollier, A. Hagen, P. Hirst, D. Homeier, A. J. Horton, G. Hosseinzadeh, L. Hu, J. S. Hunkeler, Ž. Ivezić, A. Jain, T. Jenness, G. Kanarek, S. Kendrew, N. S. Kern, W. E. Kerzendorf, A. Khvalko, J. King, D. Kirkby, A. M. Kulkarni, A. Kumar, A. Lee, D. Lenz, S. P. Littlefair, Z. Ma, D. M. Macleod, M. Mastropietro, C. McCully, S. Montagnac, B. M. Morris, M. Mueller, S. J. Mumford, D. Muna, N. A. Murphy, S. Nelson, G. H. Nguyen, J. P. Ninan, M. Nöthe, S. Ogaz, S. Oh, J. K. Parejko, N. Parley, S. Pascual, R. Patil, A. A. Patil, A. L. Plunkett, J. X. Prochaska, T. Rastogi, V. Reddy Janga, J. Sabater, P. Sakurikar, M. Seifert, L. E. Sherbert, H. Sherwood-Taylor, A. Y. Shih, J. Sick, M. T. Silbiger, S. Singanamalla, L. P. Singer, P. H. Sladen, K. A. Sooley, S. Sornarajah, O. Streicher, P. Teuben, S. W. Thomas, G. R. Tremblay, J. E. H. Turner, V. Terrón, M. H. van Kerkwijk, A. de la Vega, L. L. Watkins, B. A. Weaver, J. B. Whitmore, J. Woillez, V. Zabalza, and Astropy Contributors. The Astropy Project: Building an Open-science Project and Status of the v2.0 Core Package. *AJ*, 156(3): 123, September 2018. doi: 10.3847/1538-3881/aabc4f.

H. Atek, D. Schaerer, and D. Kunth. Origin of Lyα absorption in nearby starbursts and implications for other galaxies. *A&A*, 502(3):791–801, August 2009. doi: 10.1051/0004-6361/200911856.

Hakim Atek, Daniel Kunth, Daniel Schaerer, J. Miguel Mas-Hesse, Matthew Hayes, Göran

Östlin, and Jean-Paul Kneib. Influence of physical galaxy properties on Lyα escape in star-forming galaxies. *A&A*, 561:A89, January 2014. doi: 10.1051/0004-6361/201321519.

W. Baade and R. Minkowski. Identification of the Radio Sources in Cassiopeia, Cygnus A, and Puppis A. *ApJ*, 119:206, January 1954. doi: 10.1086/145812.

Hyun-Jin Bae, Jong-Hak Woo, Marios Karouzos, Elena Gallo, Helene Flohic, Yue Shen, and Suk-Jin Yoon. The Limited Impact of Outflows: Integral-field Spectroscopy of 20 Local AGNs. *ApJ*, 837(1):91, March 2017. doi: 10.3847/1538-4357/aa5f5c.

Vivienne F. Baldassare, Amy E. Reines, Elena Gallo, and Jenny E. Greene. X-ray and Ultraviolet Properties of AGNs in Nearby Dwarf Galaxies. *ApJ*, 836(1):20, February 2017a. doi: 10.3847/1538-4357/836/1/20.

Vivienne F. Baldassare, Amy E. Reines, Elena Gallo, and Jenny E. Greene. X-ray and Ultraviolet Properties of AGNs in Nearby Dwarf Galaxies. *ApJ*, 836(1):20, February 2017b. doi: 10.3847/1538-4357/836/1/20.

Vivienne F. Baldassare, Marla Geha, and Jenny Greene. Identifying AGNs in Low-mass Galaxies via Long-term Optical Variability. *ApJ*, 868(2):152, Dec 2018. doi: 10.3847/1538-4357/aae6cf.

J. A. Baldwin, M. M. Phillips, and R. Terlevich. Classification parameters for the emission-line spectra of extragalactic objects. *PASP*, 93:5–19, Feb 1981. doi: 10.1086/130766.

C. L. Bennett, D. Larson, J. L. Weiland, and G. Hinshaw. The 1% Concordance Hubble Constant. *ApJ*, 794:135, October 2014. doi: 10.1088/0004-637X/794/2/135.

Misty C. Bentz, Kelly D. Denney, Catherine J. Grier, Aaron J. Barth, Bradley M. Peterson, Marianne Vestergaard, Vardha N. Bennert, Gabriela Canalizo, Gisella De Rosa, Alexei V. Filippenko, Elinor L. Gates, Jenny E. Greene, Weidong Li, Matthew A. Malkan, Richard W. Pogge, Daniel Stern, Tommaso Treu, and Jong-Hak Woo. The Low-luminosity End of the Radius-Luminosity Relationship for Active Galactic Nuclei. *ApJ*, 767(2):149, Apr 2013. doi: 10.1088/0004-637X/767/2/149.

Danielle A. Berg, Evan D. Skillman, Richard B. C. Henry, Dawn K. Erb, and Leticia Carigi. Carbon and Oxygen Abundances in Low Metallicity Dwarf Galaxies. *ApJ*, 827(2):126, August 2016. doi: 10.3847/0004-637X/827/2/126.

Danielle A. Berg, Bethan L. James, Teagan King, Meaghan Mcdonald, Zuyi Chen, John Chisholm, Timothy Heckman, Crystal L. Martin, Dan P. Stark, The Classy Team, :, Alessandra Aloisi, Ricardo O. AmorÍn, Karla Z. Arellano-CÓrdova, Matthew Bayliss, Rongmon Bordoloi, Jarle Brinchmann, StÉphane Charlot, Jacopo Chevallard, Ilyse Clark, Dawn K. Erb, Anna Feltre, Matthew Hayes, Alaina Henry, Svea Hernandez, Anne Jaskot, Tucker Jones, Lisa J. Kewley, Nimisha Kumari, Claus Leitherer, Mario Llerena, Michael Maseda, Matilde Mingozzi, Themiya Nanayakkara, Masami Ouchi, Adele Plat, Richard W. Pogge, Swara Ravindranath, Jane R. Rigby, Ryan Sanders, Claudia Scarlata, Peter Senchyna, Evan D. Skillman, Charles C. Steidel, Allison L. Strom, Yuma Sugahara, Stephen M. Wilkins, Aida Wofford, and Xinfeng Xu. The COS Legacy Archive Spectroscopy SurveY (CLASSY) Treasury Atlas. *arXiv e-prints*, art. arXiv:2203.07357, March 2022.

M. Bischetti, E. Piconcelli, G. Vietri, A. Bongiorno, F. Fiore, E. Sani, A. Marconi, F. Duras, L. Zappacosta, M. Brusa, A. Comastri, G. Cresci, C. Feruglio, E. Giallongo, F. La Franca,

V. Mainieri, F. Mannucci, S. Martocchia, F. Ricci, R. Schneider, V. Testa, and C. Vignali. The WISSH quasars project. I. Powerful ionised outflows in hyper-luminous quasars. *A&A*, 598: A122, February 2017. doi: 10.1051/0004-6361/201629301.

M. Bischetti, R. Maiolino, S. Carniani, F. Fiore, E. Piconcelli, and A. Fluetsch. Widespread QSO-driven outflows in the early Universe. *A&A*, 630:A59, October 2019. doi: 10.1051/0004-6361/201833557.

M. Bischetti, C. Feruglio, V. D'Odorico, N. Arav, E. Bañados, G. Becker, S. E. I. Bosman, S. Carniani, S. Cristiani, G. Cupani, R. Davies, A. C. Eilers, E. P. Farina, A. Ferrara, R. Maiolino, C. Mazzucchelli, A. Mesinger, R. A. Meyer, M. Onoue, E. Piconcelli, E. Ryan-Weber, J. T. Schindler, F. Wang, J. Yang, Y. Zhu, and F. Fiore. Suppression of black-hole growth by strong outflows at redshifts 5.8-6.6. *Nature*, 605(7909):244–247, May 2022. doi: 10.1038/s41586-022-04608-1.

J. K. Blackburn. FTOOLS: A FITS Data Processing and Analysis Software Package. In R. A. Shaw, H. E. Payne, and J. J. E. Hayes, editors, *Astronomical Data Analysis Software and Systems IV*, volume 77 of *Astronomical Society of the Pacific Conference Series*, page 367, 1995.

Á. Bogdán, H. Bourdin, W. R. Forman, R. P. Kraft, M. Vogelsberger, L. Hernquist, and V. Springel. Probing the Hot X-Ray Corona around the Massive Spiral Galaxy, NGC 6753, Using Deep XMM-Newton Observations. *ApJ*, 850:98, November 2017. doi: 10.3847/1538-4357/aa9523.

M. Bondi, M. A. Pérez-Torres, D. Dallacasa, and T. W. B. Muxlow. A supernova factory in Mrk 273? *MNRAS*, 361:748–752, August 2005. doi: 10.1111/j.1365-2966.2005.09206.x.

C. M. Booth and Joop Schaye. Cosmological simulations of the growth of supermassive black holes and feedback from active galactic nuclei: method and tests. *MNRAS*, 398(1):53–74, September 2009. doi: 10.1111/j.1365-2966.2009.15043.x.

R. Bordoloi, J. Tumlinson, J. K. Werk, B. D. Oppenheimer, M. S. Peeples, J. X. Prochaska, T. M. Tripp, N. Katz, R. Davé, A. J. Fox, C. Thom, A. B. Ford, D. H. Weinberg, J. N. Burchett, and J. A. Kollmeier. The COS-Dwarfs Survey: The Carbon Reservoir around Sub-L* Galaxies. *ApJ*, 796:136, December 2014. doi: 10.1088/0004-637X/796/2/136.

Benoit C. J. Borguet, Doug Edmonds, Nahum Arav, Jay Dunn, and Gerard A. Kriss. A 10 kpc Scale Seyfert Galaxy Outflow: HST/COS Observations of IRAS F22456-5125. *ApJ*, 751(2): 107, June 2012. doi: 10.1088/0004-637X/751/2/107.

J. D. Bradford, M. C. Geha, J. E. Greene, A. E. Reines, and C. M. Dickey. The Effect of AGNs on the Global H I Content of Isolated Low-mass Galaxies. *ApJ*, 861:50, July 2018. doi: 10.3847/1538-4357/aac88d.

J. Braine, E. Davoust, M. Zhu, U. Lisenfeld, C. Motch, and E. R. Seaquist. A molecular gas bridge between the Taffy galaxies. *A&A*, 408:L13–L16, September 2003. doi: 10.1051/0004-6361: 20031148.

W. N. Brandt, A. Laor, and Beverley J. Wills. On the Nature of Soft X-Ray Weak Quasi-stellar Objects. *ApJ*, 528(2):637–649, January 2000. doi: 10.1086/308207.

J. Brinchmann, S. Charlot, S. D. M. White, C. Tremonti, G. Kauffmann, T. Heckman, and J. Brinkmann. The physical properties of star-forming galaxies in the low-redshift Universe. *MNRAS*, 351(4):1151–1179, Jul 2004. doi: 10.1111/j.1365-2966.2004.07881.x.

M. Brusa, G. Cresci, E. Daddi, R. Paladino, M. Perna, A. Bongiorno, E. Lusso, M. T. Sargent, V. Casasola, C. Feruglio, F. Fraternali, I. Georgiev, V. Mainieri, S. Carniani, A. Comastri, F. Duras, F. Fiore, F. Mannucci, A. Marconi, E. Piconcelli, G. Zamorani, R. Gilli, F. La Franca, G. Lanzuisi, D. Lutz, P. Santini, N. Z. Scoville, C. Vignali, F. Vito, S. Rabien, L. Busoni, and M. Bonaglia. Molecular outflow and feedback in the obscured quasar XID2028 revealed by ALMA. *A&A*, 612:A29, April 2018. doi: 10.1051/0004-6361/201731641.

D. A. Buote, C. R. Canizares, and A. C. Fabian. X-ray emission lines and multiphase gas in elliptical galaxies and galaxy clusters. *MNRAS*, 310:483–510, December 1999. doi: 10.1046/j.1365-8711.1999.02969.x.

G. R. Burbidge, E. M. Burbidge, and A. R. Sandage. Evidence for the Occurrence of Violent Events in the Nuclei of Galaxies. *Reviews of Modern Physics*, 35(4):947–972, January 1963. doi: 10.1103/RevModPhys.35.947.

S. Buttiglione, A. Capetti, A. Celotti, D. J. Axon, M. Chiaberge, F. D. Macchetto, and W. B. Sparks. An optical spectroscopic survey of the 3CR sample of radio galaxies with z ¡ 0.3. I. Presentation of the data. *A&A*, 495(3):1033–1060, March 2009. doi: 10.1051/0004-6361:200811102.

Ewan Cameron. On the Estimation of Confidence Intervals for Binomial Population Proportions in Astronomy: The Simplicity and Superiority of the Bayesian Approach. *PASA*, 28(2):128–139, June 2011. doi: 10.1071/AS10046.

Michele Cappellari. Improving the full spectrum fitting method: accurate convolution with Gauss-Hermite functions. *MNRAS*, 466(1):798–811, Apr 2017. doi: 10.1093/mnras/stw3020.

Michele Cappellari and Yannick Copin. Adaptive spatial binning of integral-field spectroscopic data using Voronoi tessellations. *MNRAS*, 342(2):345–354, Jun 2003. doi: 10.1046/j.1365-8711.2003.06541.x.

Jason A. Cardelli, Geoffrey C. Clayton, and John S. Mathis. The Relationship between Infrared, Optical, and Ultraviolet Extinction. *ApJ*, 345:245, Oct 1989a. doi: 10.1086/167900.

Jason A. Cardelli, Geoffrey C. Clayton, and John S. Mathis. The Relationship between Infrared, Optical, and Ultraviolet Extinction. *ApJ*, 345:245, Oct 1989b. doi: 10.1086/167900.

C. L. Carilli and G. B. Taylor. The Extreme Compact Starburst in Markarian 273. *ApJL*, 532: L95–L99, April 2000. doi: 10.1086/312584.

S. Carniani, A. Marconi, R. Maiolino, B. Balmaverde, M. Brusa, M. Cano-Díaz, C. Cicone, A. Comastri, G. Cresci, F. Fiore, C. Feruglio, F. La Franca, V. Mainieri, F. Mannucci, T. Nagao, H. Netzer, E. Piconcelli, G. Risaliti, R. Schneider, and O. Shemmer. Ionised outflows in z ~2.4 quasar host galaxies. *A&A*, 580:A102, Aug 2015. doi: 10.1051/0004-6361/201526557.

W. Cash. Parameter estimation in astronomy through application of the likelihood ratio. *ApJ*, 228:939–947, March 1979. doi: 10.1086/156922.

P. Cassata, O. Le Fèvre, S. Charlot, T. Contini, O. Cucciati, B. Garilli, G. Zamorani, C. Adami,

S. Bardelli, V. Le Brun, B. Lemaux, D. Maccagni, A. Pollo, L. Pozzetti, L. Tresse, D. Vergani, A. Zanichelli, and E. Zucca. He II emitters in the VIMOS VLT Deep Survey: Population III star formation or peculiar stellar populations in galaxies at $2 < z < 4.6$? *A&A*, 556:A68, August 2013. doi: 10.1051/0004-6361/201220969.

Yan-Mei Chen, Yong Shi, Christy A. Tremonti, Matt Bershady, Michael Merrifield, Eric Emsellem, Yi-Fei Jin, Song Huang, Hai Fu, David A. Wake, Kevin Bundy, David Stark, Lihwai Lin, Maria Argudo-Fernandez, Thaisa Storchi Bergmann, Dmitry Bizyaev, Joel Brownstein, Martin Bureau, John Chisholm, Niv Drory, Qi Guo, Lei Hao, Jian Hu, Cheng Li, Ran Li, Alexandre Roman Lopes, Kai-Ke Pan, Rogemar A. Riffel, Daniel Thomas, Lan Wang, Kyle Westfall, and Ren-Bin Yan. The growth of the central region by acquisition of counterrotating gas in star-forming galaxies. *Nature Communications*, 7(1):13269, 2016. doi: 10.1038/ncomms13269. URL `https://doi.org/10.1038/ncomms13269`.

R. A. Chevalier and A. W. Clegg. Wind from a starburst galaxy nucleus. *Nature*, 317(6032): 44–45, September 1985. doi: 10.1038/317044a0.

John Chisholm, Christy A. Tremonti, Claus Leitherer, Yanmei Chen, Aida Wofford, and Britt Lundgren. Scaling Relations Between Warm Galactic Outflows and Their Host Galaxies. *ApJ*, 811(2):149, October 2015. doi: 10.1088/0004-637X/811/2/149.

C. Cicone, R. Maiolino, E. Sturm, J. Graciá-Carpio, C. Feruglio, R. Neri, S. Aalto, R. Davies, F. Fiore, J. Fischer, S. García-Burillo, E. González-Alfonso, S. Hailey-Dunsheath, E. Piconcelli, and S. Veilleux. Massive molecular outflows and evidence for AGN feedback from CO observations. *A&A*, 562:A21, February 2014. doi: 10.1051/0004-6361/201322464.

C. Cicone, R. Maiolino, S. Gallerani, R. Neri, A. Ferrara, E. Sturm, F. Fiore, E. Piconcelli, and C. Feruglio. Very extended cold gas, star formation and outflows in the halo of a bright quasar at z > 6. *A&A*, 574:A14, February 2015. doi: 10.1051/0004-6361/201424980.

L. Colina, S. Arribas, and K. D. Borne. Integral Field Spectroscopy of Markarian 273: Mapping High-Velocity Gas Flows and an Off-Nucleus Seyfert 2 Nebula. *ApJL*, 527:L13–L16, December 1999. doi: 10.1086/312389.

J. J. Condon, Z.-P. Huang, Q. F. Yin, and T. X. Thuan. Compact starbursts in ultraluminous infrared galaxies. *ApJ*, 378:65–76, September 1991. doi: 10.1086/170407.

C. Conroy, G. J. Graves, and P. G. van Dokkum. Early-type Galaxy Archeology: Ages, Abundance Ratios, and Effective Temperatures from Full-spectrum Fitting. *ApJ*, 780:33, January 2014. doi: 10.1088/0004-637X/780/1/33.

Michael R. Corbin and Todd A. Boroson. Combined Ultraviolet and Optical Spectra of 48 Low-Redshift QSOs and the Relation of the Continuum and Emission-Line Properties. *ApJS*, 107: 69, November 1996. doi: 10.1086/192355.

D. M. Crenshaw and S. B. Kraemer. Feedback from Mass Outflows in Nearby Active Galactic Nuclei. I. Ultraviolet and X-Ray Absorbers. *ApJ*, 753:75, July 2012. doi: 10.1088/0004-637X/753/1/75.

D. M. Crenshaw, H. R. Schmitt, S. B. Kraemer, R. F. Mushotzky, and J. P. Dunn. Radial Velocity Offsets Due to Mass Outflows and Extinction in Active Galactic Nuclei. *ApJ*, 708(1):419–426, January 2010. doi: 10.1088/0004-637X/708/1/419.

D. Michael Crenshaw and Steven B. Kraemer. Resolved Spectroscopy of the Narrow-Line Region in NGC 1068: Kinematics of the Ionized Gas. *ApJL*, 532(2):L101–L104, April 2000. doi: 10.1086/312581.

G. Cresci, F. Mannucci, M. Della Valle, and R. Maiolino. A NICMOS search for obscured supernovae in starburst galaxies. *A&A*, 462:927–931, February 2007. doi: 10.1051/0004-6361:20065364.

Darren J. Croton, Volker Springel, Simon D. M. White, G. De Lucia, C. S. Frenk, L. Gao, A. Jenkins, G. Kauffmann, J. F. Navarro, and N. Yoshida. The many lives of active galactic nuclei: cooling flows, black holes and the luminosities and colours of galaxies. *MNRAS*, 365(1):11–28, January 2006. doi: 10.1111/j.1365-2966.2005.09675.x.

J. Crummy, A. C. Fabian, L. Gallo, and R. R. Ross. An explanation for the soft X-ray excess in active galactic nuclei. *MNRAS*, 365:1067–1081, February 2006. doi: 10.1111/j.1365-2966.2005.09844.x.

P. A. Curran. Monte Carlo error analyses of Spearman's rank test. *arXiv e-prints*, art. arXiv:1411.3816, November 2014.

G. Dashyan, J. Silk, G. A. Mamon, Y. Dubois, and T. Hartwig. AGN feedback in dwarf galaxies? *MNRAS*, 473:5698–5703, February 2018. doi: 10.1093/mMNRAS/stx2716.

R. I. Davies, F. Müller Sánchez, R. Genzel, L. J. Tacconi, E. K. S. Hicks, S. Friedrich, and A. Sternberg. A Close Look at Star Formation around Active Galactic Nuclei. *ApJ*, 671(2):1388–1412, December 2007. doi: 10.1086/523032.

J. E. Davis, M. W. Bautz, D. Dewey, R. K. Heilmann, J. C. Houck, D. P. Huenemoerder, H. L. Marshall, M. A. Nowak, M. L. Schattenburg, N. S. Schulz, and R. K. Smith. Raytracing with MARX: x-ray observatory design, calibration, and support. In *Space Telescopes and Instrumentation 2012: Ultraviolet to Gamma Ray*, volume 8443 of *Proc. SPIE*, page 84431A, September 2012. doi: 10.1117/12.926937.

A. De Rosa, C. Vignali, B. Husemann, S. Bianchi, T. Bogdanović, M. Guainazzi, R. Herrero-Illana, S. Komossa, E. Kun, N. Loiseau, Z. Paragi, M. Perez-Torres, and E. Piconcelli. Disclosing the properties of low-redshift dual AGN through XMM-Newton and SDSS spectroscopy. *MNRAS*, 480:1639–1655, October 2018. doi: 10.1093/mnras/sty1867.

T. Di Matteo, V. Springel, and L. Hernquist. Energy input from quasars regulates the growth and activity of black holes and their host galaxies. *Nature*, 433:604–607, February 2005. doi: 10.1038/nature03335.

C. Dickey, M. Geha, A. Wetzel, and K. El-Badry. AGN All the Way Down? AGN-like Line Ratios are Common In the Lowest-Mass Isolated Quiescent Galaxies. *arXiv e-prints*, February 2019.

Mark Dijkstra. Saas-Fee Lecture Notes: Physics of Lyman Alpha Radiative Transfer. *arXiv e-prints*, art. arXiv:1704.03416, April 2017.

Jie Ding, Jane C. Charlton, Christopher W. Churchill, and Christopher Palma. The Multiphase Absorption Systems toward PG 1206+459. *ApJ*, 590(2):746–769, June 2003. doi: 10.1086/375028.

X.-B. Dong, L. C. Ho, W. Yuan, T.-G. Wang, X. Fan, H. Zhou, and N. Jiang. A Uniformly

Selected Sample of Low-mass Black Holes in Seyfert 1 Galaxies. *ApJ*, 755:167, August 2012. doi: 10.1088/0004-637X/755/2/167.

D. Downes and P. M. Solomon. Rotating Nuclear Rings and Extreme Starbursts in Ultraluminous Galaxies. *ApJ*, 507:615–654, November 1998. doi: 10.1086/306339.

Bruce T. Draine. *Physics of the Interstellar and Intergalactic Medium.* 2011.

Yohan Dubois, Sébastien Peirani, Christophe Pichon, Julien Devriendt, Raphaël Gavazzi, Charlotte Welker, and Marta Volonteri. The HORIZON-AGN simulation: morphological diversity of galaxies promoted by AGN feedback. *MNRAS*, 463(4):3948–3964, December 2016. doi: 10.1093/mnras/stw2265.

F. Duval, D. Schaerer, G. Östlin, and P. Laursen. Lyman α line and continuum radiative transfer in a clumpy interstellar medium. *A&A*, 562:A52, February 2014. doi: 10.1051/0004-6361/201220455.

D. J. Eisenstein, D. H. Weinberg, E. Agol, H. Aihara, C. Allende Prieto, S. F. Anderson, J. A. Arns, É. Aubourg, S. Bailey, E. Balbinot, and et al. SDSS-III: Massive Spectroscopic Surveys of the Distant Universe, the Milky Way, and Extra-Solar Planetary Systems. *AJ*, 142:72, September 2011. doi: 10.1088/0004-6256/142/3/72.

D. N. Esch, A. Connors, M. Karovska, and D. A. van Dyk. An Image Restoration Technique with Error Estimates. *ApJ*, 610:1213–1227, August 2004. doi: 10.1086/421761.

A. C. Fabian. Observational Evidence of Active Galactic Nuclei Feedback. *ARA&A*, 50:455–489, September 2012. doi: 10.1146/annurev-astro-081811-125521.

Claude-André Faucher-Giguère and Eliot Quataert. The physics of galactic winds driven by active galactic nuclei. *MNRAS*, 425(1):605–622, Sep 2012. doi: 10.1111/j.1365-2966.2012.21512.x.

A. Feltre, S. Charlot, and J. Gutkin. Nuclear activity versus star formation: emission-line diagnostics at ultraviolet and optical wavelengths. *MNRAS*, 456(3):3354–3374, March 2016. doi: 10.1093/mnras/stv2794.

G. J. Ferland, K. T. Korista, D. A. Verner, J. W. Ferguson, J. B. Kingdon, and E. M. Verner. CLOUDY 90: Numerical Simulation of Plasmas and Their Spectra. *PASP*, 110:761–778, July 1998. doi: 10.1086/316190.

L. Ferrarese and D. Merritt. A Fundamental Relation between Supermassive Black Holes and Their Host Galaxies. *ApJL*, 539:L9–L12, August 2000. doi: 10.1086/312838.

C. Feruglio, F. Fiore, S. Carniani, E. Piconcelli, L. Zappacosta, A. Bongiorno, C. Cicone, R. Maiolino, A. Marconi, N. Menci, S. Puccetti, and S. Veilleux. The multi-phase winds of Markarian 231: from the hot, nuclear, ultra-fast wind to the galaxy-scale, molecular outflow. *A&A*, 583:A99, November 2015. doi: 10.1051/0004-6361/201526020.

Steven L. Finkelstein, Seth H. Cohen, Sangeeta Malhotra, and James E. Rhoads. Evolution of Lyα Galaxies: Stellar Populations at z ~0.3. *ApJ*, 700(1):276–283, July 2009. doi: 10.1088/0004-637X/700/1/276.

Edward L. Fitzpatrick. Correcting for the Effects of Interstellar Extinction. *PASP*, 111(755):63–75, Jan 1999. doi: 10.1086/316293.

A. Fluetsch, R. Maiolino, S. Carniani, A. Marconi, C. Cicone, M. A. Bourne, T. Costa, A. C. Fabian, W. Ishibashi, and G. Venturi. Cold molecular outflows in the local Universe and their feedback effect on galaxies. *MNRAS*, 483(4):4586–4614, March 2019. doi: 10.1093/mnras/sty3449.

A. Fluetsch, R. Maiolino, S. Carniani, S. Arribas, F. Belfiore, E. Bellocchi, S. Cazzoli, C. Cicone, G. Cresci, A. C. Fabian, R. Gallagher, W. Ishibashi, F. Mannucci, A. Marconi, M. Perna, E. Sturm, and G. Venturi. Properties of the Multiphase Outflows in Local (Ultra)luminous Infrared Galaxies. *arXiv e-prints*, art. arXiv:2006.13232, June 2020.

Antonella Fruscione, Jonathan C. McDowell, Glenn E. Allen, Nancy S. Brickhouse, Douglas J. Burke, John E. Davis, Nick Durham, Martin Elvis, Elizabeth C. Galle, Daniel E. Harris, David P. Huenemoerder, John C. Houck, Bish Ishibashi, Margarita Karovska, Fabrizio Nicastro, Michael S. Noble, Michael A. Nowak, Frank A. Primini, Aneta Siemiginowska, Randall K. Smith, and Michael Wise. CIAO: Chandra's data analysis system. In David R. Silva and Rodger E. Doxsey, editors, *Society of Photo-Optical Instrumentation Engineers (SPIE) Conference Series*, volume 6270 of *Society of Photo-Optical Instrumentation Engineers (SPIE) Conference Series*, page 62701V, June 2006. doi: 10.1117/12.671760.

D. R. Garnett. Element Abundances in Magellanic Cloud H II Regions from Carbon to Argon. In Y. H. Chu, N. Suntzeff, J. Hesser, and D. Bohlender, editors, *New Views of the Magellanic Clouds*, volume 190 of *IAU Symposium*, page 266, January 1999.

S. Garrison-Kimmel, M. Rocha, M. Boylan-Kolchin, J. S. Bullock, and J. Lally. Can feedback solve the too-big-to-fail problem? *MNRAS*, 433:3539–3546, August 2013. doi: 10.1093/mMNRAS/stt984.

Pradip Gatkine, Sylvain Veilleux, and Antonino Cucchiara. The CGM-GRB Study. I. Uncovering the Circumgalactic Medium around GRB Hosts at Redshifts 2-6. *ApJ*, 884(1):66, October 2019. doi: 10.3847/1538-4357/ab31ae.

Karl Gebhardt, Ralf Bender, Gary Bower, Alan Dressler, S. M. Faber, Alexei V. Filippenko, Richard Green, Carl Grillmair, Luis C. Ho, John Kormendy, Tod R. Lauer, John Magorrian, Jason Pinkney, Douglas Richstone, and Scott Tremaine. A Relationship between Nuclear Black Hole Mass and Galaxy Velocity Dispersion. *ApJL*, 539(1):L13–L16, August 2000. doi: 10.1086/312840.

R. Genzel, D. Lutz, E. Sturm, E. Egami, D. Kunze, A. F. M. Moorwood, D. Rigopoulou, H. W. W. Spoon, A. Sternberg, L. E. Tacconi-Garman, L. Tacconi, and N. Thatte. What Powers Ultraluminous IRAS Galaxies? *ApJ*, 498:579–605, May 1998. doi: 10.1086/305576.

Robert R. Gibson, Linhua Jiang, W. N. Brandt, Patrick B. Hall, Yue Shen, Jianfeng Wu, Scott F. Anderson, Donald P. Schneider, Daniel Vanden Berk, S. C. Gallagher, Xiaohui Fan, and Donald G. York. A Catalog of Broad Absorption Line Quasars in Sloan Digital Sky Survey Data Release 5. *ApJ*, 692(1):758–777, February 2009. doi: 10.1088/0004-637X/692/1/758.

German Gimeno, Katherine Roth, Kristin Chiboucas, Pascale Hibon, Luc Boucher, John White, Matthew Rippa, Kathleen Labrie, James Turner, Kevin Hanna, Manuel Lazo, Gabriel Pérez, Rolando Rogers, Roberto Rojas, Vinicius Placco, and Richard Murowinski. On-sky commissioning of Hamamatsu CCDs in GMOS-S. In Christopher J. Evans, Luc Simard, and

Hideki Takami, editors, *Ground-based and Airborne Instrumentation for Astronomy VI*, volume 9908, pages 872 – 885. International Society for Optics and Photonics, SPIE, 2016. doi: 10.1117/12.2233883. URL `https://doi.org/10.1117/12.2233883`.

E. González-Alfonso, J. Fischer, J. Graciá-Carpio, N. Falstad, E. Sturm, M. Meléndez, H. W. W. Spoon, A. Verma, R. I. Davies, D. Lutz, S. Aalto, E. Polisensky, A. Poglitsch, S. Veilleux, and A. Contursi. The Mrk 231 molecular outflow as seen in OH. *A&A*, 561:A27, January 2014. doi: 10.1051/0004-6361/201321709.

R. M. González Delgado, M. Cerviño, L. P. Martins, C. Leitherer, and P. H. Hauschildt. Evolutionary stellar population synthesis at high spectral resolution: optical wavelengths. *MNRAS*, 357(3):945–960, March 2005. doi: 10.1111/j.1365-2966.2005.08692.x.

O. González-Martín, J. Masegosa, I. Márquez, M. A. Guerrero, and D. Dultzin-Hacyan. X-ray nature of the LINER nuclear sources. *A&A*, 460:45–57, December 2006. doi: 10.1051/0004-6361:20054756.

A. D. Goulding, J. E. Greene, C.-P. Ma, M. Veale, A. Bogdan, K. Nyland, J. P. Blakeslee, N. J. McConnell, and J. Thomas. The MASSIVE Survey. IV. The X-ray Halos of the Most Massive Early-type Galaxies in the Nearby Universe. *ApJ*, 826:167, August 2016. doi: 10.3847/0004-637X/826/2/167.

G. J. Graves, S. M. Faber, and R. P. Schiavon. Dissecting the Red Sequence. IV. The Role of Truncation in the Two-dimensional Family of Early-type Galaxy Star Formation Histories. *ApJ*, 721:278–296, September 2010. doi: 10.1088/0004-637X/721/1/278.

Gravity Collaboration, E. Sturm, J. Dexter, O. Pfuhl, M. R. Stock, R. I. Davies, D. Lutz, Y. Clénet,

A. Eckart, F. Eisenhauer, R. Genzel, D. Gratadour, S. F. Hönig, M. Kishimoto, S. Lacour, F. Millour, H. Netzer, G. Perrin, B. M. Peterson, P. O. Petrucci, D. Rouan, I. Waisberg, J. Woillez, A. Amorim, W. Brandner, N. M. Förster Schreiber, P. J. V. Garcia, S. Gillessen, T. Ott, T. Paumard, K. Perraut, S. Scheithauer, C. Straubmeier, L. J. Tacconi, and F. Widmann. Spatially resolved rotation of the broad-line region of a quasar at sub-parsec scale. *Nature*, 563 (7733):657–660, November 2018. doi: 10.1038/s41586-018-0731-9.

J. E. Greene and L. C. Ho. A New Sample of Low-Mass Black Holes in Active Galaxies. *ApJ*, 670:92–104, November 2007. doi: 10.1086/522082.

Jenny E. Greene, Jay Strader, and Luis C. Ho. Intermediate-Mass Black Holes. *arXiv e-prints*, art. arXiv:1911.09678, Nov 2019.

J. P. Grimes, T. Heckman, D. Strickland, and A. Ptak. A Chandra X-Ray Investigation of the Violent Interstellar Medium: From Dwarf Starbursts to Ultraluminous Infrared Galaxies. *ApJ*, 628:187–204, July 2005. doi: 10.1086/430692.

Brent Groves and Mark Allen. ITERA: IDL Tool for Emission-line Ratio Analysis. *arXiv e-prints*, art. arXiv:1002.3372, Feb 2010.

Brent A. Groves, Michael A. Dopita, and Ralph S. Sutherland. Dusty, Radiation Pressure-Dominated Photoionization. I. Model Description, Structure, and Grids. *ApJS*, 153(1):9–73, Jul 2004. doi: 10.1086/421113.

Kayhan Gültekin, Douglas O. Richstone, Karl Gebhardt, Tod R. Lauer, Scott Tremaine, M. C. Aller, Ralf Bender, Alan Dressler, S. M. Faber, Alexei V. Filippenko, Richard Green, Luis C.

Ho, John Kormendy, John Magorrian, Jason Pinkney, and Christos Siopis. The M-σ and M-L Relations in Galactic Bulges, and Determinations of Their Intrinsic Scatter. *ApJ*, 698(1): 198–221, June 2009. doi: 10.1088/0004-637X/698/1/198.

Kevin N. Hainline, Alice E. Shapley, Jenny E. Greene, and Charles C. Steidel. The Rest-frame Ultraviolet Spectra of UV-selected Active Galactic Nuclei at z ~2-3. *ApJ*, 733(1):31, May 2011. doi: 10.1088/0004-637X/733/1/31.

Karl J. Haislmaier, Todd M. Tripp, Neal Katz, J. Xavier Prochaska, Joseph N. Burchett, John M. O'Meara, and Jessica K. Werk. The COS Absorption Survey of Baryon Harbors: unveiling the physical conditions of circumgalactic gas through multiphase Bayesian ionization modelling. *MNRAS*, 502(4):4993–5037, April 2021. doi: 10.1093/mnras/staa3544.

F. Hamann, N. Kanekar, J. X. Prochaska, M. T. Murphy, S. Ellison, A. L. Malec, N. Milutinovic, and W. Ubachs. A high-velocity narrow absorption line outflow in the quasar J212329.46 - 005052.9. *MNRAS*, 410(3):1957–1974, January 2011. doi: 10.1111/j.1365-2966.2010.17575.x.

F. Hamann, G. Chartas, S. McGraw, P. Rodriguez Hidalgo, J. Shields, D. Capellupo, J. Charlton, and M. Eracleous. Extreme-velocity quasar outflows and the role of X-ray shielding. *MNRAS*, 435(1):133–148, October 2013. doi: 10.1093/mnras/stt1231.

Fred Hamann, Thomas A. Barlow, Vesa Junkkarinen, and E. M. Burbidge. High-Resolution Spectra of Intrinsic Absorption Lines in the Quasi-stellar Object UM 675. *ApJ*, 478(1):80–86, Mar 1997a. doi: 10.1086/303781.

Fred Hamann, E. A. Beaver, Ross D. Cohen, Vesa Junkkarinen, R. W. Lyons, and E. M. Burbidge.

The Nature and Origin of z_a ~z_e Absorption Lines in the Redshift 0.20 Quasar, PKS 2135-147. *ApJ*, 488(1):155–163, Oct 1997b. doi: 10.1086/304698.

Fred Hamann, K. T. Korista, G. J. Ferland, Craig Warner, and Jack Baldwin. Metallicities and Abundance Ratios from Quasar Broad Emission Lines. *ApJ*, 564(2):592–603, January 2002. doi: 10.1086/324289.

Fred Hamann, Todd M. Tripp, David Rupke, and Sylvain Veilleux. On the emergence of THOUSANDS of absorption lines in the quasar PG 1411+442: a clumpy high-column density outflow from the broad emission-line region? *MNRAS*, 487(4):5041–5061, August 2019. doi: 10.1093/mnras/stz1408.

Nadine Häring and Hans-Walter Rix. On the Black Hole Mass-Bulge Mass Relation. *ApJL*, 604 (2):L89–L92, April 2004. doi: 10.1086/383567.

Charles R. Harris, K. Jarrod Millman, Stéfan J. van der Walt, Ralf Gommers, Pauli Virtanen, David Cournapeau, Eric Wieser, Julian Taylor, Sebastian Berg, Nathaniel J. Smith, Robert Kern, Matti Picus, Stephan Hoyer, Marten H. van Kerkwijk, Matthew Brett, Allan Haldane, Jaime Fernández del Río, Mark Wiebe, Pearu Peterson, Pierre Gérard-Marchant, Kevin Sheppard, Tyler Reddy, Warren Weckesser, Hameer Abbasi, Christoph Gohlke, and Travis E. Oliphant. Array programming with NumPy. *Nature*, 585(7825):357–362, September 2020. doi: 10.1038/s41586-020-2649-2. URL `https://doi.org/10.1038/s41586-020-2649-2`.

C. M. Harrison. Impact of supermassive black hole growth on star formation. *Nature Astronomy*, 1:0165, July 2017. doi: 10.1038/s41550-017-0165.

C. M. Harrison, D. M. Alexander, A. M. Swinbank, Ian Smail, S. Alaghband-Zadeh, F. E. Bauer, S. C. Chapman, A. Del Moro, R. C. Hickox, R. J. Ivison, Karín. Menéndez-Delmestre, J. R. Mullaney, and N. P. H. Nesvadba. Energetic galaxy-wide outflows in high-redshift ultraluminous infrared galaxies hosting AGN activity. *MNRAS*, 426(2):1073–1096, October 2012. doi: 10.1111/j.1365-2966.2012.21723.x.

C. M. Harrison, D. M. Alexander, J. R. Mullaney, and A. M. Swinbank. Kiloparsec-scale outflows are prevalent among luminous AGN: outflows and feedback in the context of the overall AGN population. *MNRAS*, 441:3306–3347, July 2014. doi: 10.1093/mnras/stu515.

C. M. Harrison, T. Costa, C. N. Tadhunter, A. Flütsch, D. Kakkad, M. Perna, and G. Vietri. AGN outflows and feedback twenty years on. *Nature Astronomy*, 2:198–205, February 2018. doi: 10.1038/s41550-018-0403-6.

Matthew Hayes, Göran Östlin, Florent Duval, Andreas Sandberg, Lucia Guaita, Jens Melinder, Angela Adamo, Daniel Schaerer, Anne Verhamme, Ivana Orlitová, J. Miguel Mas-Hesse, John M. Cannon, Hakim Atek, Daniel Kunth, Peter Laursen, Héctor Otí-Floranes, Stephen Pardy, Thøger Rivera-Thorsen, and E. Christian Herenz. The Lyman Alpha Reference Sample. II. Hubble Space Telescope Imaging Results, Integrated Properties, and Trends. *ApJ*, 782 (1):6, February 2014. doi: 10.1088/0004-637X/782/1/6.

T. M. Heckman and S. Borthakur. The Implications of Extreme Outflows from Extreme Starbursts. *ApJ*, 822:9, May 2016. doi: 10.3847/0004-637X/822/1/9.

T. M. Heckman and T. A. Thompson. A Brief Review of Galactic Winds. *ArXiv e-prints*, January 2017.

T. M. Heckman, R. M. Alexandroff, S. Borthakur, R. Overzier, and C. Leitherer. The Systematic Properties of the Warm Phase of Starburst-Driven Galactic Winds. *ApJ*, 809:147, August 2015. doi: 10.1088/0004-637X/809/2/147.

A. Heger and S. E. Woosley. Nucleosynthesis and Evolution of Massive Metal-free Stars. *ApJ*, 724:341–373, November 2010. doi: 10.1088/0004-637X/724/1/341.

Ryan C. Hickox and David M. Alexander. Obscured Active Galactic Nuclei. *ARA&A*, 56:625–671, September 2018. doi: 10.1146/annurev-astro-081817-051803.

Jason T. Hinkle, Sylvain Veilleux, and David S. N. Rupke. Ionization Mechanisms in Quasar Outflows. *ApJ*, 881(1):31, Aug 2019. doi: 10.3847/1538-4357/ab2bfa.

G. Hinshaw, D. Larson, E. Komatsu, D. N. Spergel, C. L. Bennett, J. Dunkley, M. R. Nolta, M. Halpern, R. S. Hill, N. Odegard, L. Page, K. M. Smith, J. L. Weiland, B. Gold, N. Jarosik, A. Kogut, M. Limon, S. S. Meyer, G. S. Tucker, E. Wollack, and E. L. Wright. Nine-year Wilkinson Microwave Anisotropy Probe (WMAP) Observations: Cosmological Parameter Results. *ApJS*, 208(2):19, October 2013. doi: 10.1088/0067-0049/208/2/19.

I. Ting Ho, Lisa J. Kewley, Michael A. Dopita, Anne M. Medling, J. T. Allen, Joss Bland-Hawthorn, Jessica V. Bloom, Julia J. Bryant, Scott M. Croom, L. M. R. Fogarty, Michael Goodwin, Andy W. Green, Iraklis S. Konstantopoulos, Jon S. Lawrence, Á. R. López-Sánchez, Matt S. Owers, Samuel Richards, and Rob Sharp. The SAMI Galaxy Survey: shocks and outflows in a normal star-forming galaxy. *MNRAS*, 444(4):3894–3910, Nov 2014. doi: 10.1093/mnras/stu1653.

Luis C. Ho. [O II] Emission in Quasar Host Galaxies: Evidence for a Suppressed Star Formation Efficiency. *ApJ*, 629(2):680–685, Aug 2005. doi: 10.1086/431643.

C. E. Hood, A. J. Barth, L. C. Ho, and J. E. Greene. A Spitzer Spectral Atlas of Low-mass Active Galactic Nuclei. *ApJ*, 838:26, March 2017. doi: 10.3847/1538-4357/aa60c9.

P. F. Hopkins, K. Bundy, N. Murray, E. Quataert, T. R. Lauer, and C.-P. Ma. Compact high-redshift galaxies are the cores of the most massive present-day spheroids. *MNRAS*, 398:898–910, September 2009. doi: 10.1111/j.1365-2966.2009.15062.x.

Philip F. Hopkins and Martin Elvis. Quasar feedback: more bang for your buck. *MNRAS*, 401 (1):7–14, January 2010. doi: 10.1111/j.1365-2966.2009.15643.x.

Philip F. Hopkins, Lars Hernquist, Thomas J. Cox, Tiziana Di Matteo, Brant Robertson, and Volker Springel. A Unified, Merger-driven Model of the Origin of Starbursts, Quasars, the Cosmic X-Ray Background, Supermassive Black Holes, and Galaxy Spheroids. *ApJS*, 163(1): 1–49, March 2006. doi: 10.1086/499298.

Philip F. Hopkins, Paul Torrey, Claude-André Faucher-Giguère, Eliot Quataert, and Norman Murray. Stellar and quasar feedback in concert: effects on AGN accretion, obscuration, and outflows. *MNRAS*, 458(1):816–831, May 2016. doi: 10.1093/mnras/stw289.

D. G. Hummer and P. J. Storey. Recombination-line intensities for hydrogenic ions - I. Case B calculations for H I and He II. *MNRAS*, 224:801–820, February 1987. doi: 10.1093/mnras/224.3.801.

A. Humphrey, M. Villar-Martín, J. Vernet, R. Fosbury, S. di Serego Alighieri, and L. Binette. Deep spectroscopy of the FUV-optical emission lines from a sample of radio galaxies at z ~2.5:

metallicity and ionization. *MNRAS*, 383(1):11–40, January 2008. doi: 10.1111/j.1365-2966.2007.12506.x.

P. J. Humphrey, D. A. Buote, F. Gastaldello, L. Zappacosta, J. S. Bullock, F. Brighenti, and W. G. Mathews. A Chandra View of Dark Matter in Early-Type Galaxies. *ApJ*, 646:899–918, August 2006. doi: 10.1086/505019.

B. Husemann, L. Wisotzki, S. F. Sánchez, and K. Jahnke. The properties of the extended warm ionised gas around low-redshift QSOs and the lack of extended high-velocity outflows. *A&A*, 549:A43, January 2013. doi: 10.1051/0004-6361/201220076.

B. Husemann, J. Scharwächter, V. N. Bennert, V. Mainieri, J. H. Woo, and D. Kakkad. Large-scale outflows in luminous QSOs revisited. The impact of beam smearing on AGN feedback efficiencies. *A&A*, 594:A44, October 2016. doi: 10.1051/0004-6361/201527992.

W. Ishibashi and T. J.-L. Courvoisier. X-ray power law spectra in active galactic nuclei. *A&A*, 512:A58, March 2010. doi: 10.1051/0004-6361/200913587.

W. Ishibashi, A. C. Fabian, and R. Maiolino. The energetics of AGN radiation pressure-driven outflows. *MNRAS*, 476(1):512–519, May 2018. doi: 10.1093/mnras/sty236.

T. Isobe, E. D. Feigelson, and P. I. Nelson. Statistical Methods for Astronomical Data with Upper Limits. II. Correlation and Regression. *ApJ*, 306:490, July 1986. doi: 10.1086/164359.

Željko Ivezić, Andrew J. Connelly, Jacob T. Vanderplas, and Alexander Gray. *Statistics, Data Mining, and Machine Learning in Astronomy*. 2019.

K. Iwasawa, J. M. Mazzarella, J. A. Surace, D. B. Sanders, L. Armus, A. S. Evans, J. H. Howell,

S. Komossa, A. Petric, S. H. Teng, V. U, and S. Veilleux. The location of an active nucleus and a shadow of a tidal tail in the ULIRG Mrk 273. *A&A*, 528:A137, April 2011a. doi: 10.1051/0004-6361/201015872.

K. Iwasawa, D. B. Sanders, S. H. Teng, V. U, L. Armus, A. S. Evans, J. H. Howell, S. Komossa, J. M. Mazzarella, A. O. Petric, J. A. Surace, T. Vavilkin, S. Veilleux, and N. Trentham. C-GOALS: Chandra observations of a complete sample of luminous infrared galaxies from the IRAS Revised Bright Galaxy Survey. *A&A*, 529:A106, May 2011b. doi: 10.1051/0004-6361/201015264.

K. Iwasawa, V. U, J. M. Mazzarella, A. M. Medling, D. B. Sanders, and A. S. Evans. Testing a double AGN hypothesis for Mrk 273. *A&A*, 611:A71, April 2018. doi: 10.1051/0004-6361/201731662.

T. H. Jarrett, M. Cohen, F. Masci, E. Wright, D. Stern, D. Benford, A. Blain, S. Carey, R. M. Cutri, P. Eisenhardt, C. Lonsdale, A. Mainzer, K. Marsh, D. Padgett, S. Petty, M. Ressler, M. Skrutskie, S. Stanford, J. Surace, C. W. Tsai, S. Wheelock, and D. L. Yan. The Spitzer-WISE Survey of the Ecliptic Poles. *ApJ*, 735(2):112, July 2011. doi: 10.1088/0004-637X/735/2/112.

P. M. W. Kalberla, W. B. Burton, D. Hartmann, E. M. Arnal, E. Bajaja, R. Morras, and W. G. L. Pöppel. The Leiden/Argentine/Bonn (LAB) Survey of Galactic HI. Final data release of the combined LDS and IAR surveys with improved stray-radiation corrections. *A&A*, 440:775–782, September 2005. doi: 10.1051/0004-6361:20041864.

Marios Karouzos, Jong-Hak Woo, and Hyun-Jin Bae. Unraveling the Complex Structure of

AGN-driven Outflows. I. Kinematics and Sizes. *ApJ*, 819(2):148, March 2016. doi: 10.3847/0004-637X/819/2/148.

M. Karovska, E. Schlegel, W. Hack, J. C. Raymond, and B. E. Wood. A Large X-Ray Outburst in Mira A. *ApJL*, 623:L137–L140, April 2005. doi: 10.1086/430111.

Shai Kaspi, Dan Maoz, Hagai Netzer, Bradley M. Peterson, Marianne Vestergaard, and Buell T. Jannuzi. The Relationship between Luminosity and Broad-Line Region Size in Active Galactic Nuclei. *ApJ*, 629(1):61–71, August 2005. doi: 10.1086/431275.

Shai Kaspi, W. N. Brandt, Dan Maoz, Hagai Netzer, Donald P. Schneider, and Ohad Shemmer. Reverberation Mapping of High-Luminosity Quasars: First Results. *ApJ*, 659(2):997–1007, April 2007. doi: 10.1086/512094.

Guinevere Kauffmann, Timothy M. Heckman, Christy Tremonti, Jarle Brinchmann, Stéphane Charlot, Simon D. M. White, Susan E. Ridgway, Jon Brinkmann, Masataka Fukugita, Patrick B. Hall, Željko Ivezić, Gordon T. Richards, and Donald P. Schneider. The host galaxies of active galactic nuclei. *MNRAS*, 346(4):1055–1077, December 2003. doi: 10.1111/j.1365-2966.2003.07154.x.

Brandon C. Kelly. Some Aspects of Measurement Error in Linear Regression of Astronomical Data. *ApJ*, 665(2):1489–1506, August 2007. doi: 10.1086/519947.

L. J. Kewley, M. A. Dopita, R. S. Sutherland, C. A. Heisler, and J. Trevena. Theoretical Modeling of Starburst Galaxies. *ApJ*, 556:121–140, July 2001. doi: 10.1086/321545.

Lisa J. Kewley, Margaret J. Geller, and Rolf A. Jansen. [O II] as a Star Formation Rate Indicator. *AJ*, 127(4):2002–2030, Apr 2004. doi: 10.1086/382723.

Lisa J. Kewley, Brent Groves, Guinevere Kauffmann, and Tim Heckman. The host galaxies and classification of active galactic nuclei. *MNRAS*, 372(3):961–976, November 2006. doi: 10.1111/j.1365-2966.2006.10859.x.

D. C. Kim and D. B. Sanders. The IRAS 1 Jy Survey of Ultraluminous Infrared Galaxies. I. The Sample and Luminosity Function. *ApJS*, 119(1):41–58, November 1998a. doi: 10.1086/313148.

D. C. Kim and D. B. Sanders. The IRAS 1 Jy Survey of Ultraluminous Infrared Galaxies. I. The Sample and Luminosity Function. *ApJS*, 119(1):41–58, Nov 1998b. doi: 10.1086/313148.

D. C. Kim, S. Veilleux, and D. B. Sanders. Optical and Near-Infrared Imaging of the IRAS 1 Jy Sample of Ultraluminous Infrared Galaxies. I. The Atlas. *ApJS*, 143(2):277–314, December 2002. doi: 10.1086/343843.

D. C. Kim, A. S. Evans, T. Vavilkin, L. Armus, J. M. Mazzarella, K. Sheth, J. A. Surace, S. Haan, J. H. Howell, T. Díaz-Santos, A. Petric, K. Iwasawa, G. C. Privon, and D. B. Sanders. Hubble Space Telescope ACS Imaging of the GOALS Sample: Quantitative Structural Properties of Nearby Luminous Infrared Galaxies with L ¡SUB¿IR¡/SUB¿ > 10¡SUP¿11.4¡/SUP¿ L ¡SUB¿?¡/SUB¿. *ApJ*, 768:102, May 2013. doi: 10.1088/0004-637X/768/2/102.

D.-W. Kim and G. Fabbiano. X-Ray Scaling Relations of 'Core' and 'Coreless' E and S0 Galaxies. *ApJ*, 812:127, October 2015. doi: 10.1088/0004-637X/812/2/127.

D.-W. Kim, G. Fabbiano, and A. Pipino. X-Ray Properties of Young Early-type Galaxies. II. Abundance Ratio in the Hot Interstellar Matter. *ApJ*, 751:38, May 2012. doi: 10.1088/0004-637X/751/1/38.

Andrew King and Ken Pounds. Powerful Outflows and Feedback from Active Galactic Nuclei. *ARA&A*, 53:115–154, August 2015. doi: 10.1146/annurev-astro-082214-122316.

Christian Knigge, Simone Scaringi, Michael R. Goad, and Christopher E. Cottis. The intrinsic fraction of broad-absorption line quasars. *MNRAS*, 386(3):1426–1435, May 2008. doi: 10.1111/j.1365-2966.2008.13081.x.

S. Komossa, V. Burwitz, G. Hasinger, P. Predehl, J. S. Kaastra, and Y. Ikebe. Discovery of a Binary Active Galactic Nucleus in the Ultraluminous Infrared Galaxy NGC 6240 Using Chandra. *ApJL*, 582:L15–L19, January 2003. doi: 10.1086/346145.

S. Konami, K. Matsushita, T. G. Tsuru, P. Gandhi, and T. Tamagawa. Suzaku Metal Abundance Patterns in the Outflow Region of M82 and the Importance of Charge Exchange. *PASJ*, 63: S913–S924, November 2011. doi: 10.1093/pasj/63.sp3.S913.

J. Kormendy and L. C. Ho. Coevolution (Or Not) of Supermassive Black Holes and Host Galaxies. *ARA&A*, 51:511–653, August 2013a. doi: 10.1146/annurev-astro-082708-101811.

John Kormendy and Luis C. Ho. Coevolution (Or Not) of Supermassive Black Holes and Host Galaxies. *ARA&A*, 51(1):511–653, Aug 2013b. doi: 10.1146/annurev-astro-082708-101811.

M. Koss, R. Mushotzky, E. Treister, S. Veilleux, R. Vasudevan, N. Miller, D. B. Sanders, K. Schawinski, and M. Trippe. Chandra Discovery of a Binary Active Galactic Nucleus in Mrk 739. *ApJL*, 735:L42, July 2011. doi: 10.1088/2041-8205/735/2/L42.

S. Koudmani, D. Sijacki, M. A. Bourne, and M. C. Smith. Fast and energetic AGN-driven outflows in simulated dwarf galaxies. *MNRAS*, 484:2047–2066, April 2019. doi: 10.1093/mMNRAS/stz097.

Sophie Koudmani, Nicholas A. Henden, and Debora Sijacki. A little FABLE: exploring AGN feedback in dwarf galaxies with cosmological simulations. *arXiv e-prints*, art. arXiv:2007.10342, July 2020.

Davor Krajnović, Michele Cappellari, P. Tim de Zeeuw, and Yannick Copin. Kinemetry: a generalization of photometry to the higher moments of the line-of-sight velocity distribution. *MNRAS*, 366(3):787–802, March 2006. doi: 10.1111/j.1365-2966.2005.09902.x.

M. Kriek, C. Conroy, P. G. van Dokkum, A. E. Shapley, J. Choi, N. A. Reddy, B. Siana, F. van de Voort, A. L. Coil, and B. Mobasher. A massive, quiescent, population II galaxy at a redshift of 2.1. *Nature*, 540:248–251, December 2016. doi: 10.1038/nature20570.

A. Lamastra, S. Bianchi, G. Matt, G. C. Perola, X. Barcons, and F. J. Carrera. The bolometric luminosity of type 2 AGN from extinction-corrected [OIII]. No evidence of Eddington-limited sources. *A&A*, 504(1):73–79, Sep 2009. doi: 10.1051/0004-6361/200912023.

R. B. Larson. Effects of supernovae on the early evolution of galaxies. *MNRAS*, 169:229–246, November 1974. doi: 10.1093/mMNRAS/169.2.229.

Lilikoi J. Latimer, Amy E. Reines, Kevin N. Hainline, Jenny E. Greene, and Daniel Stern. A Chandra and HST View of WISE-selected AGN Candidates in Dwarf Galaxies. *ApJ*, 914(2): 133, June 2021. doi: 10.3847/1538-4357/abfe0c.

Peter Laursen, Florent Duval, and Göran Östlin. On the (Non-)Enhancement of the Lyα Equivalent Width by a Multiphase Interstellar Medium. *ApJ*, 766(2):124, April 2013. doi: 10.1088/0004-637X/766/2/124.

N. Lehner, J. X. Prochaska, H. A. Kobulnicky, K. L. Cooksey, J. C. Howk, G. M. Williger, and S. L. Cales. The Connection Between a Lyman Limit System, a Very Strong O VI Absorber, and Galaxies at z ~0.203. *ApJ*, 694(2):734–750, April 2009. doi: 10.1088/0004-637X/694/2/734.

Emily M. Levesque, Lisa J. Kewley, and Kirsten L. Larson. Theoretical Modeling of Star-Forming Galaxies. I. Emission-Line Diagnostic Grids for Local and Low-Metallicity Galaxies. *AJ*, 139(2):712–727, February 2010. doi: 10.1088/0004-6256/139/2/712.

J.-T. Li and Q. D. Wang. Chandra survey of nearby highly inclined disc galaxies - I. X-ray measurements of galactic coronae. *MNRAS*, 428:2085–2108, January 2013a. doi: 10.1093/mnras/sts183.

J.-T. Li and Q. D. Wang. Chandra survey of nearby highly inclined disc galaxies - II. Correlation analysis of galactic coronal properties. *MNRAS*, 435:3071–3084, November 2013b. doi: 10.1093/mnras/stt1501.

J.-T. Li, R. A. Crain, and Q. D. Wang. Chandra survey of nearby highly inclined disc galaxies - III. Comparison with hydrodynamical simulations of circumgalactic coronae. *MNRAS*, 440:859–869, May 2014. doi: 10.1093/mnras/stu329.

J.-T. Li, J. N. Bregman, Q. D. Wang, R. A. Crain, M. E. Anderson, and S. Zhang. The Circum-Galactic Medium of Massive Spirals. II. Probing the Nature of Hot Gaseous Halo around the Most Massive Isolated Spiral Galaxies. *ApJS*, 233:20, December 2017. doi: 10.3847/1538-4365/aa96fc.

D. A. Liedahl, A. L. Osterheld, and W. H. Goldstein. New calculations of Fe L-shell X-ray spectra in high-temperature plasmas. *ApJL*, 438:L115–L118, January 1995. doi: 10.1086/187729.

Guilin Liu, Nadia L. Zakamska, Jenny E. Greene, Nicole P. H. Nesvadba, and Xin Liu. Observations of feedback from radio-quiet quasars - I. Extents and morphologies of ionized gas nebulae. *MNRAS*, 430(3):2327–2345, Apr 2013a. doi: 10.1093/mnras/stt051.

Guilin Liu, Nadia L. Zakamska, Jenny E. Greene, Nicole P. H. Nesvadba, and Xin Liu. Observations of feedback from radio-quiet quasars - II. Kinematics of ionized gas nebulae. *MNRAS*, 436(3):2576–2597, Dec 2013b. doi: 10.1093/mnras/stt1755.

Weizhe Liu, Sylvain Veilleux, Kazushi Iwasawa, David S. N. Rupke, Stacy Teng, Vivian U, Francesco Tombesi, David Sanders, Claire E. Max, and Marcio Meléndez. Elliptical Galaxy in the Making: The Dual Active Galactic Nuclei and Metal-enriched Halo of Mrk 273. *ApJ*, 872(1):39, Feb 2019. doi: 10.3847/1538-4357/aafdfc.

Weizhe Liu, Sylvain Veilleux, Gabriela Canalizo, David S. N. Rupke, Christina M. Manzano-King, Thomas Bohn, and Vivian U. Integral Field Spectroscopy of Fast Outflows in Dwarf Galaxies with AGNs. *ApJ*, 905(2):166, December 2020. doi: 10.3847/1538-4357/abc269.

Weizhe Liu, Sylvain Veilleux, David S. N. Rupke, Todd M. Tripp, Frederick Hamann, and Crystal Martin. Galactic Winds across the Gas-Rich Merger Sequence II. Lyman Alpha Emission and Highly Ionized O VI and N V Outflows in Ultraluminous Infrared Galaxies. *arXiv e-prints*, art. arXiv:2206.09015, June 2022.

Ewa L. Łokas and Gary A. Mamon. Properties of spherical galaxies and clusters with an NFW density profile. *MNRAS*, 321(1):155–166, Feb 2001. doi: 10.1046/j.1365-8711.2001.04007.x.

L. B. Lucy. An iterative technique for the rectification of observed distributions. *AJ*, 79:745, June 1974. doi: 10.1086/111605.

B. Luo, W. N. Brandt, D. M. Alexander, F. A. Harrison, D. Stern, F. E. Bauer, S. E. Boggs, F. E. Christensen, A. Comastri, W. W. Craig, A. C. Fabian, D. Farrah, F. Fiore, F. Fuerst, B. W. Grefenstette, C. J. Hailey, R. Hickox, K. K. Madsen, G. Matt, P. Ogle, G. Risaliti, C. Saez, S. H. Teng, D. J. Walton, and W. W. Zhang. Weak Hard X-Ray Emission from Two Broad Absorption Line Quasars Observed with NuSTAR: Compton-thick Absorption or Intrinsic X-Ray Weakness? *ApJ*, 772(2):153, August 2013. doi: 10.1088/0004-637X/772/2/153.

B. Luo, W. N. Brandt, D. M. Alexander, D. Stern, S. H. Teng, P. Arévalo, F. E. Bauer, S. E. Boggs, F. E. Christensen, A. Comastri, W. W. Craig, D. Farrah, P. Gandhi, C. J. Hailey, F. A. Harrison, M. Koss, P. Ogle, S. Puccetti, C. Saez, A. E. Scott, D. J. Walton, and W. W. Zhang. Weak Hard X-Ray Emission from Broad Absorption Line Quasars: Evidence for Intrinsic X-Ray Weakness. *ApJ*, 794(1):70, October 2014. doi: 10.1088/0004-637X/794/1/70.

B. Luo, W. N. Brandt, P. B. Hall, Jianfeng Wu, S. F. Anderson, G. P. Garmire, R. R. Gibson, R. M. Plotkin, G. T. Richards, D. P. Schneider, O. Shemmer, and Yue Shen. X-ray Insights into the Nature of PHL 1811 Analogs and Weak Emission-line Quasars: Unification with a Geometrically Thick Accretion Disk? *ApJ*, 805(2):122, June 2015. doi: 10.1088/0004-637X/805/2/122.

D. Lutz, E. Sturm, A. Janssen, S. Veilleux, S. Aalto, C. Cicone, A. Contursi, R. I. Davies, C. Feruglio, J. Fischer, A. Fluetsch, S. Garcia-Burillo, R. Genzel, E. González-Alfonso, J. Graciá-Carpio, R. Herrera-Camus, R. Maiolino, A. Schruba, T. Shimizu, A. Sternberg, L. J. Tacconi, and A. Weiß. Molecular outflows in local galaxies: Method comparison and a role of intermittent AGN driving. *A&A*, 633:A134, January 2020. doi: 10.1051/0004-6361/201936803.

Andrea V. Macciò, Samuele Crespi, Marvin Blank, and Xi Kang. NIHAO-XXIII: Dark Matter density shaped by Black Hole feedback. *MNRAS*, April 2020. doi: 10.1093/mnrasl/slaa058.

Piero Madau and Francesco Haardt. Cosmic Reionization after Planck: Could Quasars Do It All? *ApJL*, 813(1):L8, November 2015. doi: 10.1088/2041-8205/813/1/L8.

R. Maiolino, S. Gallerani, R. Neri, C. Cicone, A. Ferrara, R. Genzel, D. Lutz, E. Sturm, L. J. Tacconi, F. Walter, C. Feruglio, F. Fiore, and E. Piconcelli. Evidence of strong quasar feedback in the early Universe. *MNRAS*, 425(1):L66–L70, September 2012. doi: 10.1111/j.1745-3933.2012.01303.x.

Christina M. Manzano-King and Gabriela Canalizo. Active galactic nucleus and dwarf galaxy gas kinematics. *MNRAS*, 498(3):4562–4576, September 2020. doi: 10.1093/mnras/staa2654.

Christina M. Manzano-King, Gabriela Canalizo, and Laura V. Sales. AGN-Driven Outflows in Dwarf Galaxies. *ApJ*, 884(1):54, Oct 2019. doi: 10.3847/1538-4357/ab4197.

Craig Markwardt. MPFIT: Robust non-linear least squares curve fitting, Aug 2012.

C. L. Martin, M. Dijkstra, A. Henry, K. T. Soto, C. W. Danforth, and J. Wong. The Lyα Line Profiles of Ultraluminous Infrared Galaxies: Fast Winds and Lyman Continuum Leakage. *ApJ*, 803:6, April 2015. doi: 10.1088/0004-637X/803/1/6.

Crystal L. Martin. Mapping Large-Scale Gaseous Outflows in Ultraluminous Galaxies with Keck

II ESI Spectra: Variations in Outflow Velocity with Galactic Mass. *ApJ*, 621(1):227–245, March 2005. doi: 10.1086/427277.

Crystal L. Martin. Mapping Large-Scale Gaseous Outflows in Ultraluminous Infrared Galaxies with Keck II ESI Spectra: Spatial Extent of the Outflow. *ApJ*, 647(1):222–243, August 2006. doi: 10.1086/504886.

Crystal L. Martin and Nicolas Bouché. Physical Conditions in the Low-ionization Component of Starburst Outflows: The Shape of Near-Ultraviolet and Optical Absorption-line Troughs in Keck Spectra of ULIRGs. *ApJ*, 703(2):1394–1415, October 2009. doi: 10.1088/0004-637X/703/2/1394.

D. Christopher Martin, James Fanson, David Schiminovich, Patrick Morrissey, Peter G. Friedman, Tom A. Barlow, Tim Conrow, Robert Grange, Patrick N. Jelinsky, Bruno Milliard, Oswald H. W. Siegmund, Luciana Bianchi, Yong-Ik Byun, Jose Donas, Karl Forster, Timothy M. Heckman, Young-Wook Lee, Barry F. Madore, Roger F. Malina, Susan G. Neff, R. Michael Rich, Todd Small, Frank Surber, Alex S. Szalay, Barry Welsh, and Ted K. Wyder. The Galaxy Evolution Explorer: A Space Ultraviolet Survey Mission. *ApJL*, 619(1):L1–L6, January 2005. doi: 10.1086/426387.

I. Martín-Navarro and M. Mezcua. Exploring the Limits of AGN Feedback: Black Holes and the Star Formation Histories of Low-mass Galaxies. *ApJL*, 855(2):L20, March 2018. doi: 10.3847/2041-8213/aab103.

S. Mateos, A. Alonso-Herrero, F. J. Carrera, A. Blain, M. G. Watson, X. Barcons, V. Braito, P. Severgnini, J. L. Donley, and D. Stern. Using the Bright Ultrahard XMM-Newton survey to define an IR selection of luminous AGN based on WISE colours. *MNRAS*, 426(4):3271–3281, November 2012. doi: 10.1111/j.1365-2966.2012.21843.x.

K. Matsuoka, T. Nagao, R. Maiolino, A. Marconi, and Y. Taniguchi. Chemical evolution of high-redshift radio galaxies. *A&A*, 503(3):721–730, September 2009. doi: 10.1051/0004-6361/200811478.

Thomas A. Matthews and Allan R. Sandage. Optical Identification of 3C 48, 3C 196, and 3C 286 with Stellar Objects. *ApJ*, 138:30, July 1963. doi: 10.1086/147615.

Patrick J. McCarthy. High redshift radio galaxies. *ARA&A*, 31:639–688, January 1993. doi: 10.1146/annurev.aa.31.090193.003231.

P. J. McMillan. Mass models of the Milky Way. *MNRAS*, 414:2446–2457, July 2011. doi: 10.1111/j.1365-2966.2011.18564.x.

Kristen. B. W. McQuinn, Liese van Zee, and Evan D. Skillman. Galactic Winds in Low-mass Galaxies. *ApJ*, 886(1):74, November 2019. doi: 10.3847/1538-4357/ab4c37.

David Merritt and Laura Ferrarese. The M-σ Relation for Supermassive Black Holes. *ApJ*, 547(1):140–145, January 2001. doi: 10.1086/318372.

M. Mezcua and H. Domínguez Sánchez. Hidden AGN in dwarf galaxies revealed by MaNGA: light echoes, off-nuclear wanderers, and a new broad-line AGN. *arXiv e-prints*, art. arXiv:2007.08527, July 2020.

M. Mezcua, F. Civano, S. Marchesi, H. Suh, G. Fabbiano, and M. Volonteri. Intermediate-mass black holes in dwarf galaxies out to redshift $\sim$2.4 in the Chandra COSMOS-Legacy Survey. *MNRAS*, 478:2576–2591, August 2018. doi: 10.1093/mMNRAS/sty1163.

M. Mezcua, H. Suh, and F. Civano. Radio jets from AGNs in dwarf galaxies in the COSMOS survey: mechanical feedback out to redshift $\sim$3.4. *MNRAS*, 488(1):685–695, September 2019. doi: 10.1093/mnras/stz1760.

Mar Mezcua. Dwarf galaxies might not be the birth sites of supermassive black holes. *Nature Astronomy*, 3:6–7, January 2019. doi: 10.1038/s41550-018-0662-2.

H. J. Mo and S. D. M. White. The abundance and clustering of dark haloes in the standard ΛCDM cosmogony. *MNRAS*, 336:112–118, October 2002. doi: 10.1046/j.1365-8711.2002.05723.x.

Maxwell Moe, Nahum Arav, Manuel A. Bautista, and Kirk T. Korista. Quasar Outflow Contribution to AGN Feedback: Observations of QSO SDSS J0838+2955. *ApJ*, 706(1):525–534, November 2009. doi: 10.1088/0004-637X/706/1/525.

E. C. Moran, K. Shahinyan, H. R. Sugarman, D. O. Vélez, and M. Eracleous. Black Holes At the Centers of Nearby Dwarf Galaxies. *AJ*, 148:136, December 2014. doi: 10.1088/0004-6256/148/6/136.

Raffaella Morganti, Tom Oosterloo, J. B. Raymond Oonk, Wilfred Frieswijk, and Clive Tadhunter. The fast molecular outflow in the Seyfert galaxy IC 5063 as seen by ALMA. *A&A*, 580:A1, August 2015. doi: 10.1051/0004-6361/201525860.

Raffaella Morganti, Sylvain Veilleux, Tom Oosterloo, Stacy H. Teng, and David Rupke. Another piece of the puzzle: The fast H I outflow in Mrk 231. *A&A*, 593:A30, September 2016. doi: 10.1051/0004-6361/201628978.

Patrick Morrissey, Matuesz Matuszewski, D. Christopher Martin, James D. Neill, Harland Epps, Jason Fucik, Bob Weber, Behnam Darvish, Sean Adkins, Steve Allen, Randy Bartos, Justin Belicki, Jerry Cabak, Shawn Callahan, Dave Cowley, Marty Crabill, Willian Deich, Alex Delecroix, Greg Doppman, David Hilyard, Ean James, Steve Kaye, Michael Kokorowski, Shui Kwok, Kyle Lanclos, Steve Milner, Anna Moore, Donal O'Sullivan, Prachi Parihar, Sam Park, Andrew Phillips, Luca Rizzi, Constance Rockosi, Hector Rodriguez, Yves Salaun, Kirk Seaman, David Sheikh, Jason Weiss, and Ray Zarzaca. The Keck Cosmic Web Imager Integral Field Spectrograph. *ApJ*, 864(1):93, September 2018. doi: 10.3847/1538-4357/aad597.

Donald C. Morton. Atomic Data for Resonance Absorption Lines. III. Wavelengths Longward of the Lyman Limit for the Elements Hydrogen to Gallium. *ApJS*, 149(1):205–238, Nov 2003. doi: 10.1086/377639.

Benjamin P. Moster, Thorsten Naab, and Simon D. M. White. Galactic star formation and accretion histories from matching galaxies to dark matter haloes. *MNRAS*, 428(4):3121–3138, Feb 2013. doi: 10.1093/mnras/sts261.

N. Murray, J. Chiang, S. A. Grossman, and G. M. Voit. Accretion Disk Winds from Active Galactic Nuclei. *ApJ*, 451:498, October 1995. doi: 10.1086/176238.

Norman Murray, Eliot Quataert, and Todd A. Thompson. On the Maximum Luminosity of Galaxies and Their Central Black Holes: Feedback from Momentum-driven Winds. *ApJ*, 618(2): 569–585, January 2005. doi: 10.1086/426067.

Sowgat Muzahid, Glenn G. Kacprzak, Christopher W. Churchill, Jane C. Charlton, Nikole M. Nielsen, Nigel L. Mathes, and Sebastian Trujillo-Gomez. An Extreme Metallicity, Large-scale Outflow from a Star-forming Galaxy at z ~0.4. *ApJ*, 811(2):132, October 2015. doi: 10.1088/0004-637X/811/2/132.

S. Nagataki and K. Sato. Contribution of Type IA and Type II Supernovae to Intracluster Medium Enrichment. *ApJ*, 504:629–635, September 1998. doi: 10.1086/306097.

E. Nardini, J. Wang, G. Fabbiano, M. Elvis, S. Pellegrini, G. Risaliti, M. Karovska, and A. Zezas. The Exceptional Soft X-Ray Halo of the Galaxy Merger NGC 6240. *ApJ*, 765:141, March 2013. doi: 10.1088/0004-637X/765/2/141.

E. Nardini, J. N. Reeves, J. Gofford, F. A. Harrison, G. Risaliti, V. Braito, M. T. Costa, G. A. Matzeu, D. J. Walton, E. Behar, S. E. Boggs, F. E. Christensen, W. W. Craig, C. J. Hailey, G. Matt, J. M. Miller, P. T. O'Brien, D. Stern, T. J. Turner, and M. J. Ward. Black hole feedback in the luminous quasar PDS 456. *Science*, 347(6224):860–863, February 2015. doi: 10.1126/science.1259202.

J. F. Navarro, C. S. Frenk, and S. D. M. White. A Universal Density Profile from Hierarchical Clustering. *ApJ*, 490:493–508, December 1997. doi: 10.1086/304888.

Dylan Nelson, Annalisa Pillepich, Volker Springel, Rüdiger Pakmor, Rainer Weinberger, Shy Genel, Paul Torrey, Mark Vogelsberger, Federico Marinacci, and Lars Hernquist. First results from the TNG50 simulation: galactic outflows driven by supernovae and black hole feedback. *MNRAS*, 490(3):3234–3261, December 2019. doi: 10.1093/mnras/stz2306.

H. Netzer. AGN emission lines. In R. D. Blandford, H. Netzer, L. Woltjer, T. J. L. Courvoisier, and M. Mayor, editors, *Active Galactic Nuclei*, pages 57–160, January 1990.

Hagai Netzer, Dieter Lutz, Mario Schweitzer, Alessandra Contursi, Eckhard Sturm, Linda J. Tacconi, Sylvain Veilleux, D. C. Kim, David Rupke, Andrew J. Baker, Kalliopi Dasyra, Joseph Mazzarella, and Steven Lord. Spitzer Quasar and ULIRG Evolution Study (QUEST). II. The Spectral Energy Distributions of Palomar-Green Quasars. *ApJ*, 666(2):806–816, Sep 2007. doi: 10.1086/520716.

David A. Neufeld. The Escape of Lyman-Alpha Radiation from a Multiphase Interstellar Medium. *ApJL*, 370:L85, April 1991. doi: 10.1086/185983.

Matthew Newville, Till Stensitzki, Daniel B. Allen, Michal Rawlik, Antonino Ingargiola, and Andrew Nelson. Lmfit: Non-Linear Least-Square Minimization and Curve-Fitting for Python, June 2016.

Dieu D. Nguyen, Anil C. Seth, Nadine Neumayer, Sebastian Kamann, Karina T. Voggel, Michele Cappellari, Arianna Picotti, Phuong M. Nguyen, Torsten Böker, Victor Debattista, Nelson Caldwell, Richard McDermid, Nathan Bastian, Christopher C. Ahn, and Renuka Pechetti. Nearby Early-type Galactic Nuclei at High Resolution: Dynamical Black Hole and Nuclear Star Cluster Mass Measurements. *ApJ*, 858(2):118, May 2018. doi: 10.3847/1538-4357/aabe28.

Dieu D. Nguyen, Anil C. Seth, Nadine Neumayer, Satoru Iguchi, Michelle Cappellari, Jay Strader, Laura Chomiuk, Evangelia Tremou, Fabio Pacucci, Kouichiro Nakanishi, Arash Bahramian, Phuong M. Nguyen, Mark den Brok, Christopher C. Ahn, Karina T. Voggel, Nikolay Kacharov, Takafumi Tsukui, Cuc K. Ly, Antoine Dumont, and Renuka Pechetti. Improved Dynamical Constraints on the Masses of the Central Black Holes in Nearby Low-mass Early-type Galactic Nuclei and the First Black Hole Determination for NGC 205. *ApJ*, 872(1):104, February 2019. doi: 10.3847/1538-4357/aafe7a.

K. Nomoto, N. Tominaga, H. Umeda, C. Kobayashi, and K. Maeda. Nucleosynthesis yields of core-collapse supernovae and hypernovae, and galactic chemical evolution. *Nuclear Physics A*, 777:424–458, October 2006. doi: 10.1016/j.nuclphysa.2006.05.008.

K. Nomoto, C. Kobayashi, and N. Tominaga. Nucleosynthesis in Stars and the Chemical Enrichment of Galaxies. *ARA&A*, 51:457–509, August 2013. doi: 10.1146/annurev-astro-082812-140956.

Mladen Novak, Bram P. Venemans, Fabian Walter, Marcel Neeleman, Melanie Kaasinen, Lichen Liang, Robert Feldmann, Eduardo Bañados, Chris Carilli, Roberto Decarli, Alyssa B. Drake, Xiaohui Fan, Emanuele P. Farina, Chiara Mazzucchelli, Hans-Walter Rix, and Ran Wang. No Evidence for [C II] Halos or High-velocity Outflows in z $\gtrsim$ 6 Quasar Host Galaxies. *ApJ*, 904 (2):131, December 2020. doi: 10.3847/1538-4357/abc33f.

Donald E. Osterbrock and Gary J. Ferland. *Astrophysics of gaseous nebulae and active galactic nuclei*. 2006.

K. Pardo, A. D. Goulding, J. E. Greene, R. S. Somerville, E. Gallo, R. C. Hickox, B. P. Miller, A. E. Reines, and J. D. Silverman. X-Ray Detected Active Galactic Nuclei in Dwarf Galaxies at $0 < z < 1$. *ApJ*, 831:203, November 2016. doi: 10.3847/0004-637X/831/2/203.

M. Peeples, J. Tumlinson, A. Fox, A. Aloisi, S. Fleming, R. Jedrzejewski, C. Oliveira, T. Ayres, C. Danforth, B. Keeney, and E. Jenkins. The Hubble Spectroscopic Legacy Archive. Instrument Science Report COS 2017-4, April 2017.

S. J. Penny, K. L. Masters, R. Smethurst, R. C. Nichol, C. M. Krawczyk, D. Bizyaev, O. Greene, C. Liu, M. Marinelli, S. B. Rembold, R. A. Riffel, G. d. S. Ilha, D. Wylezalek, B. H. Andrews, K. Bundy, N. Drory, D. Oravetz, and K. Pan. SDSS-IV MaNGA: evidence of the importance of AGN feedback in low-mass galaxies. *MNRAS*, 476:979–998, May 2018. doi: 10.1093/mMNRAS/sty202.

E. Piconcelli, E. Jimenez-Bailón, M. Guainazzi, N. Schartel, P. M. Rodríguez-Pascual, and M. Santos-Lleó. The XMM-Newton view of PG quasars. I. X-ray continuum and absorption. *A&A*, 432:15–30, March 2005. doi: 10.1051/0004-6361:20041621.

G. C. Privon, C. Ricci, S. Aalto, S. Viti, L. Armus, T. Díaz-Santos, E. González-Alfonso, K. Iwasawa, D. L. Jeff, E. Treister, F. Bauer, A. S. Evans, P. Garg, R. Herrero-Illana, J. M. Mazzarella, K. Larson, L. Blecha, L. Barcos-Muñoz, V. Charmandaris, S. Stierwalt, and M. A. Pérez-Torres. A Hard X-Ray Test of HCN Enhancements As a Tracer of Embedded Black Hole Growth. *ApJ*, 893(2):149, April 2020. doi: 10.3847/1538-4357/ab8015.

Daniel Proga. Dynamics of Accretion Flows Irradiated by a Quasar. *ApJ*, 661(2):693–702, June 2007. doi: 10.1086/515389.

Daniel Proga and Timothy R. Kallman. Dynamics of Line-driven Disk Winds in Active Galactic Nuclei. II. Effects of Disk Radiation. *ApJ*, 616(2):688–695, December 2004. doi: 10.1086/425117.

A. Ptak, T. Heckman, N. A. Levenson, K. Weaver, and D. Strickland. A Chandra Survey of the Nearest Ultraluminous Infrared Galaxies: Obscured Active Galactic Nuclei or Superstarbursts? *ApJ*, 592:782–803, August 2003. doi: 10.1086/375766.

D. Raimann, T. Storchi-Bergmann, R. M. González Delgado, R. Cid Fernandes, T. Heckman, C. Leitherer, and H. Schmitt. Stellar population gradients in Seyfert 2 galaxies: northern sample. *MNRAS*, 339:772–792, March 2003. doi: 10.1046/j.1365-8711.2003.06222.x.

C. Ramos Almeida, J. Piqueras López, M. Villar-Martín, and P. S. Bessiere. An infrared view of AGN feedback in a type-2 quasar: the case of the Teacup galaxy. *MNRAS*, 470(1):964–976, September 2017. doi: 10.1093/mnras/stx1287.

C. Ramos Almeida, J. A. Acosta-Pulido, C. N. Tadhunter, C. González-Fernández, C. Cicone, and M. Fernández-Torreiro. A near-infrared study of the multiphase outflow in the type-2 quasar J1509+0434. *MNRAS*, 487(1):L18–L23, July 2019. doi: 10.1093/mnrasl/slz072.

P. Ranalli, A. Comastri, L. Origlia, and R. Maiolino. A deep X-ray observation of M82 with XMM-Newton. *MNRAS*, 386:1464–1480, May 2008. doi: 10.1111/j.1365-2966.2008.13128.x.

Martin J. Rees. Black Hole Models for Active Galactic Nuclei. *ARA&A*, 22:471–506, January 1984. doi: 10.1146/annurev.aa.22.090184.002351.

A. E. Reines, J. E. Greene, and M. Geha. Dwarf Galaxies with Optical Signatures of Active Massive Black Holes. *ApJ*, 775:116, October 2013. doi: 10.1088/0004-637X/775/2/116.

R. Reyes, R. Mandelbaum, J. E. Gunn, J. Pizagno, and C. N. Lackner. Calibrated Tully-Fisher relations for improved estimates of disc rotation velocities. *MNRAS*, 417(3):2347–2386, November 2011. doi: 10.1111/j.1365-2966.2011.19415.x.

C. Ricci, B. Trakhtenbrot, M. J. Koss, Y. Ueda, I. Del Vecchio, E. Treister, K. Schawinski, S. Paltani, K. Oh, I. Lamperti, S. Berney, P. Gandhi, K. Ichikawa, F. E. Bauer, L. C. Ho,

D. Asmus, V. Beckmann, S. Soldi, M. Baloković, N. Gehrels, and C. B. Markwardt. BAT AGN Spectroscopic Survey. V. X-Ray Properties of the Swift/BAT 70-month AGN Catalog. *ApJS*, 233(2):17, December 2017. doi: 10.3847/1538-4365/aa96ad.

J. A. Rich, L. J. Kewley, and M. A. Dopita. Galaxy-wide Shocks in Late-merger Stage Luminous Infrared Galaxies. *ApJ*, 734(2):87, June 2011. doi: 10.1088/0004-637X/734/2/87.

J. A. Rich, P. Torrey, L. J. Kewley, M. A. Dopita, and D. S. N. Rupke. An Integral Field Study of Abundance Gradients in nearby Luminous Infrared Galaxies. *ApJ*, 753(1):5, July 2012. doi: 10.1088/0004-637X/753/1/5.

J. A. Rich, L. J. Kewley, and M. A. Dopita. Composite Spectra in Merging U/LIRGs Caused by Shocks. *ApJL*, 781(1):L12, January 2014. doi: 10.1088/2041-8205/781/1/L12.

G. T. Richards, N. E. Kruczek, S. C. Gallagher, P. B. Hall, P. C. Hewett, K. M. Leighly, R. P. Deo, R. M. Kratzer, and Y. Shen. Unification of Luminous Type 1 Quasars through C IV Emission. *AJ*, 141:167, May 2011. doi: 10.1088/0004-6256/141/5/167.

Alexander J. Richings and Claude-André Faucher-Giguère. The origin of fast molecular outflows in quasars: molecule formation in AGN-driven galactic winds. *MNRAS*, 474(3):3673–3699, Mar 2018a. doi: 10.1093/mnras/stx3014.

Alexander J. Richings and Claude-André Faucher-Giguère. Radiative cooling of swept-up gas in AGN-driven galactic winds and its implications for molecular outflows. *MNRAS*, 478(3): 3100–3119, Aug 2018b. doi: 10.1093/mnras/sty1285.

Rogemar A. Riffel. Evidence for an accreting massive black hole in He 2-10 from adaptive optics integral field spectroscopy. *arXiv e-prints*, art. arXiv:2003.13375, March 2020.

G. W. Roberts-Borsani, A. Saintonge, K. L. Masters, and D. V. Stark. Outflows in star-forming galaxies: Stacking analyses of resolved winds and the relation to their hosts' properties. *MNRAS*, 493(3):3081–3097, April 2020. doi: 10.1093/mnras/staa464.

Brant E. Robertson, Richard S. Ellis, Steven R. Furlanetto, and James S. Dunlop. Cosmic Reionization and Early Star-forming Galaxies: A Joint Analysis of New Constraints from Planck and the Hubble Space Telescope. *ApJL*, 802(2):L19, April 2015. doi: 10.1088/2041-8205/802/2/L19.

J. Rodríguez Zaurín, C. N. Tadhunter, and R. M. González Delgado. The properties of the stellar populations in ULIRGs - I. Sample, data and spectral synthesis modelling. *MNRAS*, 400: 1139–1180, December 2009. doi: 10.1111/j.1365-2966.2009.15444.x.

J. Rodríguez Zaurín, C. N. Tadhunter, M. Rose, , C. N. Tadhunter, M. Rose, and J. Holt. The importance of warm, AGN-driven outflows in the nuclear regions of nearby ULIRGs. *MNRAS*, 432(1):138–166, Jun 2013. doi: 10.1093/mnras/stt423.

J. Rodríguez Zaurín, C. N. Tadhunter, D. S. N. Rupke, S. Veilleux, H. W. W. Spoon, M. Chiaberge, C. Ramos Almeida, D. Batcheldor, and W. B. Sparks. Extended warm gas in the ULIRG Mrk273: Galactic outflows and tidal debris. *A&A*, 571:A57, November 2014. doi: 10.1051/0004-6361/201423540.

Marvin Rose, Clive Tadhunter, Cristina Ramos Almeida, Javier Rodríguez Zaurín, Francesco Santoro, and Robert Spence. Quantifying the AGN-driven outflows in ULIRGs (QUADROS) - I: VLT/Xshooter observations of nine nearby objects. *MNRAS*, 474(1):128–156, February 2018. doi: 10.1093/mnras/stx2590.

B. Rosenwasser, S. Muzahid, J. C. Charlton, G. G. Kacprzak, B. P. Wakker, and C. W. Churchill. Understanding the strong intervening O VI absorber at $z_{abs} \sim 0.93$ towards PG1206+459. *MNRAS*, 476(2):2258–2277, May 2018. doi: 10.1093/mnras/sty211.

D. S. Rupke, S. Veilleux, and D. B. Sanders. Outflows in Infrared-Luminous Starbursts at z < 0.5. I. Sample, Na I D Spectra, and Profile Fitting. *ApJS*, 160:87–114, September 2005a. doi: 10.1086/432886.

D. S. N. Rupke and S. Veilleux. Integral Field Spectroscopy of Massive, Kiloparsec-scale Outflows in the Infrared-luminous QSO Mrk 231. *ApJL*, 729:L27, March 2011. doi: 10.1088/2041-8205/729/2/L27.

D. S. N. Rupke and S. Veilleux. Breaking the Obscuring Screen: A Resolved Molecular Outflow in a Buried QSO. *ApJL*, 775:L15, September 2013a. doi: 10.1088/2041-8205/775/1/L15.

D. S. N. Rupke and S. Veilleux. The Multiphase Structure and Power Sources of Galactic Winds in Major Mergers. *ApJ*, 768:75, May 2013b. doi: 10.1088/0004-637X/768/1/75.

D. S. N. Rupke and S. Veilleux. Spatially Extended Na I D Resonant Emission and Absorption in the Galactic Wind of the Nearby Infrared-Luminous Quasar F05189-2524. *ApJ*, 801:126, March 2015. doi: 10.1088/0004-637X/801/2/126.

D. S. N. Rupke, K. Gültekin, and S. Veilleux. Quasar-mode Feedback in Nearby Type 1 Quasars: Ubiquitous Kiloparsec-scale Outflows and Correlations with Black Hole Properties. *ApJ*, 850:40, November 2017. doi: 10.3847/1538-4357/aa94d1.

David S. Rupke, Sylvain Veilleux, and D. B. Sanders. Outflows in Infrared-Luminous Starbursts at z < 0.5. II. Analysis and Discussion. *ApJS*, 160(1):115–148, Sep 2005b. doi: 10.1086/432889.

David S. Rupke, Sylvain Veilleux, and D. B. Sanders. Outflows in Active Galactic Nucleus/Starburst-Composite Ultraluminous Infrared Galaxies1,. *ApJ*, 632(2):751–780, Oct 2005c. doi: 10.1086/444451.

David S. N. Rupke. IFSFIT: Spectral Fitting for Integral Field Spectrographs, Sep 2014a.

David S. N. Rupke. IFSRED: Data Reduction for Integral Field Spectrographs, Sep 2014b.

D. B. Sanders and I. F. Mirabel. Luminous Infrared Galaxies. *ARA&A*, 34:749, 1996. doi: 10.1146/annurev.astro.34.1.749.

D. B. Sanders, B. T. Soifer, J. H. Elias, G. Neugebauer, and K. Matthews. Warm ultraluminous galaxies in the IRAS survey - The transition from galaxy to quasar? *ApJL*, 328:L35–L39, May 1988. doi: 10.1086/185155.

Ryan L. Sanders, Alice E. Shapley, Mariska Kriek, Naveen A. Reddy, William R. Freeman, Alison L. Coil, Brian Siana, Bahram Mobasher, Irene Shivaei, Sedona H. Price, and Laura de Groot. The MOSDEF Survey: Electron Density and Ionization Parameter at z ~2.3. *ApJ*, 816(1):23, Jan 2016. doi: 10.3847/0004-637X/816/1/23.

Lia F. Sartori, Kevin Schawinski, Ezequiel Treister, Benny Trakhtenbrot, Michael Koss, Maryam Shirazi, and Kyuseok Oh. The search for active black holes in nearby low-mass galaxies using optical and mid-IR data. *MNRAS*, 454(4):3722–3742, Dec 2015. doi: 10.1093/mnras/stv2238.

B. D. Savage, A. Narayanan, B. P. Wakker, J. T. Stocke, B. A. Keeney, J. M. Shull, K. R. Sembach, Y. Yao, and J. C. Green. O VI Absorbers Tracing Hot Gas Associated with a Pair of Galaxies at z = 0.167. *ApJ*, 719(2):1526–1545, August 2010. doi: 10.1088/0004-637X/719/2/1526.

C. Scarlata, J. Colbert, H. I. Teplitz, N. Panagia, M. Hayes, B. Siana, A. Rau, P. Francis, A. Caon, A. Pizzella, and C. Bridge. The Effect of Dust Geometry on the Lyα Output of Galaxies. *ApJL*, 704(2):L98–L102, October 2009. doi: 10.1088/0004-637X/704/2/L98.

Joop Schaye, Robert A. Crain, Richard G. Bower, Michelle Furlong, Matthieu Schaller, Tom Theuns, Claudio Dalla Vecchia, Carlos S. Frenk, I. G. McCarthy, John C. Helly, Adrian Jenkins, Y. M. Rosas-Guevara, Simon D. M. White, Maarten Baes, C. M. Booth, Peter Camps, Julio F. Navarro, Yan Qu, Alireza Rahmati, Till Sawala, Peter A. Thomas, and James Trayford. The EAGLE project: simulating the evolution and assembly of galaxies and their environments. *MNRAS*, 446(1):521–554, January 2015. doi: 10.1093/mnras/stu2058.

Edward F. Schlafly and Douglas P. Finkbeiner. Measuring Reddening with Sloan Digital Sky Survey Stellar Spectra and Recalibrating SFD. *ApJ*, 737(2):103, August 2011. doi: 10.1088/0004-637X/737/2/103.

Zachary Schutte and Amy E. Reines. Black-hole-triggered star formation in the dwarf galaxy Henize 2-10. *Nature*, 601(7893):329–333, January 2022. doi: 10.1038/s41586-021-04215-6.

N. Z. Scoville, A. S. Evans, R. Thompson, M. Rieke, D. C. Hines, F. J. Low, N. Dinshaw, J. A. Surace, and L. Armus. NICMOS Imaging of Infrared-Luminous Galaxies. *AJ*, 119:991–1061, March 2000. doi: 10.1086/301248.

I. R. Seitenzahl, F. Ciaraldi-Schoolmann, F. K. Röpke, M. Fink, W. Hillebrandt, M. Kromer, R. Pakmor, A. J. Ruiter, S. A. Sim, and S. Taubenberger. Three-dimensional delayed-detonation models with nucleosynthesis for Type Ia supernovae. *MNRAS*, 429:1156–1172, February 2013. doi: 10.1093/mnras/sts402.

Peter Senchyna, Daniel P. Stark, Alba Vidal-García, Jacopo Chevallard, Stéphane Charlot, Ramesh Mainali, Tucker Jones, Aida Wofford, Anna Feltre, and Julia Gutkin. Ultraviolet spectra of extreme nearby star-forming regions - approaching a local reference sample for JWST. *MNRAS*, 472(3):2608–2632, December 2017. doi: 10.1093/mnras/stx2059.

R. G. Sharp and J. Bland-Hawthorn. Three-Dimensional Integral Field Observations of 10 Galactic Winds. I. Extended Phase (gsim10 Myr) of Mass/Energy Injection Before the Wind Blows. *ApJ*, 711(2):818–852, March 2010. doi: 10.1088/0004-637X/711/2/818.

Hsin-Yi Shih and David S. N. Rupke. The Complex Structure of the Multi-phase Galactic Wind in a Starburst Merger. *ApJ*, 724(2):1430–1440, December 2010. doi: 10.1088/0004-637X/724/2/1430.

J. M. Shull, M. Stevans, and C. W. Danforth. HST-COS Observations of AGNs. I. Ultraviolet Composite Spectra of the Ionizing Continuum and Emission Lines. *ApJ*, 752:162, June 2012. doi: 10.1088/0004-637X/752/2/162.

Debora Sijacki, Volker Springel, Tiziana Di Matteo, and Lars Hernquist. A unified model for AGN feedback in cosmological simulations of structure formation. *MNRAS*, 380(3):877–900, September 2007. doi: 10.1111/j.1365-2966.2007.12153.x.

J. Silk. Feedback by Massive Black Holes in Gas-rich Dwarf Galaxies. *ApJl*, 839:L13, April 2017. doi: 10.3847/2041-8213/aa67da.

Joseph Silk and Martin J. Rees. Quasars and galaxy formation. *A&A*, 331:L1–L4, March 1998.

S. A. Sim, D. Proga, L. Miller, K. S. Long, and T. J. Turner. Multidimensional modelling of X-ray spectra for AGN accretion disc outflows - III. Application to a hydrodynamical simulation. *MNRAS*, 408(3):1396–1408, November 2010. doi: 10.1111/j.1365-2966.2010.17215.x.

M. F. Skrutskie, R. M. Cutri, R. Stiening, M. D. Weinberg, S. Schneider, J. M. Carpenter, C. Beichman, R. Capps, T. Chester, J. Elias, J. Huchra, J. Liebert, C. Lonsdale, D. G. Monet, S. Price, P. Seitzer, T. Jarrett, J. D. Kirkpatrick, J. E. Gizis, E. Howard, T. Evans, J. Fowler, L. Fullmer, R. Hurt, R. Light, E. L. Kopan, K. A. Marsh, H. L. McCallon, R. Tam, S. Van Dyk, and S. Wheelock. The Two Micron All Sky Survey (2MASS). *AJ*, 131(2):1163–1183, February 2006. doi: 10.1086/498708.

H. E. Smith, C. J. Lonsdale, and C. J. Lonsdale. The Starburst-AGN Connection. II. The Nature of Luminous Infrared Galaxies as Revealed by VLBI, VLA, Infrared, and Optical Observations. *ApJ*, 492:137–172, January 1998. doi: 10.1086/305020.

B. T. Soifer, G. Neugebauer, K. Matthews, E. Egami, E. E. Becklin, A. J. Weinberger, M. Ressler, M. W. Werner, A. S. Evans, N. Z. Scoville, J. A. Surace, and J. J. Condon. High Resolution Mid-Infrared Imaging of Ultraluminous Infrared Galaxies. *AJ*, 119:509–523, February 2000. doi: 10.1086/301233.

Rachel S. Somerville, Philip F. Hopkins, Thomas J. Cox, Brant E. Robertson, and Lars Hernquist.

A semi-analytic model for the co-evolution of galaxies, black holes and active galactic nuclei. *MNRAS*, 391(2):481–506, December 2008. doi: 10.1111/j.1365-2966.2008.13805.x.

R. A. W. Spence, J. R. Zaurín, C. N. Tadhunter, M. Rose, A. Cabrera-Lavers, H. Spoon, and C. Muñoz-Tuñón. No evidence for large-scale outflows in the extended ionized halo of ULIRG Mrk273. *MNRAS*, 459:L16–L20, June 2016. doi: 10.1093/mnrasl/slw033.

H. W. W. Spoon, D. Farrah, V. Lebouteiller, E. González-Alfonso, J. Bernard-Salas, T. Urrutia, D. Rigopoulou, M. S. Westmoquette, H. A. Smith, J. Afonso, C. Pearson, D. Cormier, A. Efstathiou, C. Borys, A. Verma, M. Etxaluze, and D. L. Clements. Diagnostics of AGN-Driven Molecular Outflows in ULIRGs from Herschel-PACS Observations of OH at 119 μm. *ApJ*, 775:127, October 2013. doi: 10.1088/0004-637X/775/2/127.

M. Stone, S. Veilleux, M. Meléndez, E. Sturm, J. Graciá-Carpio, and E. González-Alfonso. The Search for Molecular Outflows in Local Volume AGNs with Herschel-PACS. *ApJ*, 826(2):111, August 2016. doi: 10.3847/0004-637X/826/2/111.

E. Sturm, E. González-Alfonso, S. Veilleux, J. Fischer, J. Graciá-Carpio, S. Hailey-Dunsheath, A. Contursi, A. Poglitsch, A. Sternberg, R. Davies, R. Genzel, D. Lutz, L. Tacconi, A. Verma, R. Maiolino, and J. A. de Jong. Massive Molecular Outflows and Negative Feedback in ULIRGs Observed by Herschel-PACS. *ApJL*, 733(1):L16, May 2011. doi: 10.1088/2041-8205/733/1/L16.

J. A. Surace, D. B. Sanders, W. D. Vacca, S. Veilleux, and J. M. Mazzarella. HST/WFPC2 Observations of Warm Ultraluminous Infrared Galaxies. *ApJ*, 492:116–136, January 1998. doi: 10.1086/305028.

Jason A. Surace, D. B. Sanders, and A. S. Evans. High-Resolution Optical/Near-Infrared Imaging of Cool Ultraluminous Infrared Galaxies. *ApJ*, 529:170–188, January 2000. doi: 10.1086/308247.

L. J. Tacconi, R. Genzel, D. Lutz, D. Rigopoulou, A. J. Baker, C. Iserlohe, and M. Tecza. Ultraluminous Infrared Galaxies: QSOs in Formation? *ApJ*, 580:73–87, November 2002. doi: 10.1086/343075.

M. Tecza, R. Genzel, L. J. Tacconi, S. Anders, L. E. Tacconi-Garman, and N. Thatte. Stellar Dynamics and the Implications on the Merger Evolution in NGC 6240. *ApJ*, 537:178–190, July 2000. doi: 10.1086/309021.

S. H. Teng, S. Veilleux, N. Anabuki, C. D. Dermer, L. C. Gallo, T. Nakagawa, C. S. Reynolds, D. B. Sanders, Y. Terashima, and A. S. Wilson. Suzaku Observations of Local Ultraluminous Infrared Galaxies. *ApJ*, 691:261–276, January 2009. doi: 10.1088/0004-637X/691/1/261.

Stacy H. Teng and Sylvain Veilleux. X-QUEST: A Comprehensive X-ray Study of Local ULIRGS and QSOs. *ApJ*, 725(2):1848–1876, December 2010. doi: 10.1088/0004-637X/725/2/1848.

Stacy H. Teng, A. S. Wilson, S. Veilleux, A. J. Young, D. B. Sanders, and N. M. Nagar. A Chandra X-Ray Survey of Ultraluminous Infrared Galaxies. *ApJ*, 633(2):664–679, November 2005. doi: 10.1086/491595.

Stacy H. Teng, W. N. Brandt, F. A. Harrison, B. Luo, D. M. Alexander, F. E. Bauer, S. E. Boggs, F. E. Christensen, A. Comastri, W. W. Craig, A. C. Fabian, D. Farrah, F. Fiore, P. Gandhi, B. W. Grefenstette, C. J. Hailey, R. C. Hickox, K. K. Madsen, A. F. Ptak, J. R. Rigby, G. Risaliti,

C. Saez, D. Stern, S. Veilleux, D. J. Walton, D. R. Wik, and W. W. Zhang. NuSTAR Reveals an Intrinsically X-Ray Weak Broad Absorption Line Quasar in the Ultraluminous Infrared Galaxy Markarian 231. *ApJ*, 785(1):19, April 2014. doi: 10.1088/0004-637X/785/1/19.

Stacy H. Teng, Jane R. Rigby, Daniel Stern, Andrew Ptak, D. M. Alexander, Franz E. Bauer, Stephen E. Boggs, W. Niel Brandt, Finn E. Christensen, Andrea Comastri, William W. Craig, Duncan Farrah, Poshak Gandhi, Charles J. Hailey, Fiona A. Harrison, Ryan C. Hickox, Michael Koss, Bin Luo, Ezequiel Treister, and William W. Zhang. A NuSTAR Survey of Nearby Ultraluminous Infrared Galaxies. *ApJ*, 814(1):56, November 2015. doi: 10.1088/0004-637X/814/1/56.

Todd A. Thompson, Eliot Quataert, Dong Zhang, and David H. Weinberg. An origin for multiphase gas in galactic winds and haloes. *MNRAS*, 455(2):1830–1844, January 2016. doi: 10.1093/mnras/stv2428.

F. Tombesi, M. Cappi, J. N. Reeves, G. G. C. Palumbo, T. Yaqoob, V. Braito, and M. Dadina. Evidence for ultra-fast outflows in radio-quiet AGNs. I. Detection and statistical incidence of Fe K-shell absorption lines. *A&A*, 521:A57, October 2010. doi: 10.1051/0004-6361/200913440.

F. Tombesi, M. Meléndez, S. Veilleux, J. N. Reeves, E. González-Alfonso, and C. S. Reynolds. Wind from the black-hole accretion disk driving a molecular outflow in an active galaxy. *Nature*, 519(7544):436–438, Mar 2015. doi: 10.1038/nature14261.

F. Tombesi, J. N. Reeves, T. Kallman, C. S. Reynolds, R. F. Mushotzky, V. Braito, E. Behar, M. A. Leutenegger, and M. Cappi. The Complex Circumnuclear Environment of the Broad-line Radio Galaxy 3C 390.3 Revealed by Chandra HETG. *ApJ*, 830:98, October 2016. doi: 10.3847/0004-637X/830/2/98.

F. Tombesi, R. F. Mushotzky, C. S. Reynolds, T. Kallman, J. N. Reeves, V. Braito, Y. Ueda, M. A. Leutenegger, B. J. Williams, Ł. Stawarz, and M. Cappi. Feeding and Feedback in the Powerful Radio Galaxy 3C 120. *ApJ*, 838:16, March 2017. doi: 10.3847/1538-4357/aa6342.

Christy A. Tremonti, John Moustakas, and Aleksandar M. Diamond-Stanic. The Discovery of 1000 km s^{-1} Outflows in Massive Poststarburst Galaxies at z=0.6. *ApJL*, 663(2):L77–L80, July 2007. doi: 10.1086/520083.

T. M. Tripp, K. R. Sembach, D. V. Bowen, B. D. Savage, E. B. Jenkins, N. Lehner, and P. Richter. A High-Resolution Survey of Low-Redshift QSO Absorption Lines: Statistics and Physical Conditions of O VI Absorbers. *ApJs*, 177:39–102, July 2008. doi: 10.1086/587486.

T. M. Tripp, J. D. Meiring, J. X. Prochaska, C. N. A. Willmer, J. C. Howk, J. K. Werk, E. B. Jenkins, D. V. Bowen, N. Lehner, K. R. Sembach, C. Thom, and J. Tumlinson. The Hidden Mass and Large Spatial Extent of a Post-Starburst Galaxy Outflow. *Science*, 334:952, November 2011. doi: 10.1126/science.1209850.

Todd M. Tripp and Blair D. Savage. O VI and Multicomponent H I Absorption Associated with a Galaxy Group in the Direction of PG 0953+415: Physical Conditions and Baryonic Content. *ApJ*, 542(1):42–56, October 2000. doi: 10.1086/309506.

Jonathan R. Trump, Patrick B. Hall, Timothy A. Reichard, Gordon T. Richards, Donald P. Schneider, Daniel E. Vanden Berk, Gillian R. Knapp, Scott F. Anderson, Xiaohui Fan, J. Brinkman,

S. J. Kleinman, and Atsuko Nitta. A Catalog of Broad Absorption Line Quasars from the Sloan Digital Sky Survey Third Data Release. *ApJS*, 165(1):1–18, July 2006. doi: 10.1086/503834.

T. G. Tsuru, M. Ozawa, Y. Hyodo, H. Matsumoto, K. Koyama, H. Awaki, R. Fujimoto, R. Griffiths, C. Kilbourne, K. Matsushita, K. Mitsuda, A. Ptak, P. Ranalli, and N. Y. Yamasaki. X-Ray Spectral Study of the Extended Emission, 'the Cap', Located 11.6kpc above the Disk of M82. *PASJ*, 59:269–282, January 2007. doi: 10.1093/pasj/59.sp1.S269.

Jason Tumlinson, Molly S. Peeples, and Jessica K. Werk. The Circumgalactic Medium. *ARA&A*, 55(1):389–432, August 2017. doi: 10.1146/annurev-astro-091916-055240.

V. U, D. B. Sanders, J. M. Mazzarella, A. S. Evans, J. H. Howell, J. A. Surace, L. Armus, K. Iwasawa, D.-C. Kim, C. M. Casey, T. Vavilkin, M. Dufault, K. L. Larson, J. E. Barnes, B. H. P. Chan, D. T. Frayer, S. Haan, H. Inami, C. M. Ishida, J. S. Kartaltepe, J. L. Melbourne, and A. O. Petric. Spectral Energy Distributions of Local Luminous and Ultraluminous Infrared Galaxies. *ApJS*, 203:9, November 2012. doi: 10.1088/0067-0049/203/1/9.

V. U, A. Medling, D. Sanders, C. Max, L. Armus, K. Iwasawa, A. Evans, L. Kewley, and G. Fazio. The Inner Kiloparsec of Mrk 273 with Keck Adaptive Optics. *ApJ*, 775:115, October 2013. doi: 10.1088/0004-637X/775/2/115.

Y. Ueda, M. Akiyama, G. Hasinger, T. Miyaji, and M. G. Watson. Toward the Standard Population Synthesis Model of the X-Ray Background: Evolution of X-Ray Luminosity and Absorption Functions of Active Galactic Nuclei Including Compton-thick Populations. *ApJ*, 786:104, May 2014. doi: 10.1088/0004-637X/786/2/104.

S. Veilleux, D. C. Kim, D. B. Sanders, J. M. Mazzarella, and B. T. Soifer. Optical Spectroscopy of Luminous Infrared Galaxies. II. Analysis of the Nuclear and Long-Slit Data. *ApJS*, 98:171, May 1995. doi: 10.1086/192158.

S. Veilleux, D.-C. Kim, and D. B. Sanders. Optical and Near-Infrared Imaging of the IRAS 1 Jy Sample of Ultraluminous Infrared Galaxies. II. The Analysis. *ApJS*, 143:315–376, December 2002. doi: 10.1086/343844.

S. Veilleux, G. Cecil, and J. Bland-Hawthorn. Galactic Winds. *ARA&A*, 43:769–826, September 2005a. doi: 10.1146/annurev.astro.43.072103.150610.

S. Veilleux, G. Cecil, and J. Bland-Hawthorn. Galactic Winds. *ARA&A*, 43:769–826, September 2005b. doi: 10.1146/annurev.astro.43.072103.150610.

S. Veilleux, D. C. Kim, C. Y. Peng, L. C. Ho, L. J. Tacconi, K. M. Dasyra, R. Genzel, D. Lutz, and D. B. Sanders. A Deep Hubble Space Telescope H-Band Imaging Survey of Massive Gas-rich Mergers. *ApJ*, 643(2):707–723, June 2006. doi: 10.1086/503188.

S. Veilleux, D. C. Kim, D. S. N. Rupke, C. Y. Peng, L. J. Tacconi, R. Genzel, D. Lutz, E. Sturm, A. Contursi, M. Schweitzer, K. M. Dasyra, L. C. Ho, D. B. Sanders, and A. Burkert. A Deep Hubble Space Telescope H-Band Imaging Survey of Massive Gas-Rich Mergers. II. The QUEST QSOs. *ApJ*, 701(1):587–606, August 2009a. doi: 10.1088/0004-637X/701/1/587.

S. Veilleux, D. S. N. Rupke, D. C. Kim, R. Genzel, E. Sturm, D. Lutz, A. Contursi, M. Schweitzer, L. J. Tacconi, H. Netzer, A. Sternberg, J. C. Mihos, A. J. Baker, J. M. Mazzarella, S. Lord, D. B. Sanders, A. Stockton, R. D. Joseph, and J. E. Barnes. Spitzer Quasar and Ulirg Evolution Study (QUEST). IV. Comparison of 1 Jy Ultraluminous Infrared Galaxies with Palomar-Green Quasars. *ApJS*, 182(2):628–666, Jun 2009b. doi: 10.1088/0067-0049/182/2/628.

S. Veilleux, M. Meléndez, E. Sturm, J. Gracia-Carpio, J. Fischer, E. González-Alfonso, A. Contursi, D. Lutz, A. Poglitsch, R. Davies, R. Genzel, L. Tacconi, J. A. de Jong, A. Sternberg, H. Netzer, S. Hailey-Dunsheath, A. Verma, D. S. N. Rupke, R. Maiolino, S. H. Teng, and E. Polisensky. Fast Molecular Outflows in Luminous Galaxy Mergers: Evidence for Quasar Feedback from Herschel. *ApJ*, 776(1):27, October 2013a. doi: 10.1088/0004-637X/776/1/27.

S. Veilleux, M. Meléndez, E. Sturm, J. Gracia-Carpio, J. Fischer, E. González-Alfonso, A. Contursi, D. Lutz, A. Poglitsch, R. Davies, R. Genzel, L. Tacconi, J. A. de Jong, A. Sternberg, H. Netzer, S. Hailey-Dunsheath, A. Verma, D. S. N. Rupke, R. Maiolino, S. H. Teng, and E. Polisensky. Fast Molecular Outflows in Luminous Galaxy Mergers: Evidence for Quasar Feedback from Herschel. *ApJ*, 776:27, October 2013b. doi: 10.1088/0004-637X/776/1/27.

S. Veilleux, M. Trippe, F. Hamann, D. S. N. Rupke, T. M. Tripp, H. Netzer, D. Lutz, K. R. Sembach, H. Krug, S. H. Teng, R. Genzel, R. Maiolino, E. Sturm, and L. Tacconi. The Surprising Absence of Absorption in the Far-ultraviolet Spectrum of Mrk 231. *ApJ*, 764(1):15, Feb 2013c. doi: 10.1088/0004-637X/764/1/15.

S. Veilleux, S. H. Teng, D. S. N. Rupke, R. Maiolino, and E. Sturm. Half-megasecond Chandra Spectral Imaging of the Hot Circumgalactic Nebula around Quasar Mrk 231. *ApJ*, 790:116, August 2014. doi: 10.1088/0004-637X/790/2/116.

S. Veilleux, M. Meléndez, T. M. Tripp, F. Hamann, and D. S. N. Rupke. The Complete Ultraviolet Spectrum of the Archetypal "Wind-dominated" Quasar Mrk 231: Absorption and Emission from a High-speed Dusty Nuclear Outflow. *ApJ*, 825:42, July 2016. doi: 10.3847/0004-637X/825/1/42.

S. Veilleux, A. Bolatto, F. Tombesi, M. Meléndez, E. Sturm, E. González-Alfonso, J. Fischer, and D. S. N. Rupke. Quasar Feedback in the Ultraluminous Infrared Galaxy F11119+3257: Connecting the Accretion Disk Wind with the Large-scale Molecular Outflow. *ApJ*, 843:18, July 2017. doi: 10.3847/1538-4357/aa767d.

Sylvain Veilleux. A Study of the Structure and Kinematics of the Narrow-Line Region in Seyfert Galaxies. III. Individual Objects. *ApJ*, 369:331, March 1991. doi: 10.1086/169765.

Sylvain Veilleux and Donald E. Osterbrock. Spectral Classification of Emission-Line Galaxies. *ApJS*, 63:295, Feb 1987. doi: 10.1086/191166.

Sylvain Veilleux and David S. Rupke. Identification of Galactic Wind Candidates Using Excitation Maps: Tunable-Filter Discovery of a Shock-excited Wind in the Galaxy NGC 1482. *ApJL*, 565(1):L63–L66, January 2002. doi: 10.1086/339226.

Sylvain Veilleux, D. C. Kim, and D. B. Sanders. Optical Spectroscopy of the IRAS 1 JY Sample of Ultraluminous Infrared Galaxies. *ApJ*, 522(1):113–138, Sep 1999. doi: 10.1086/307634.

Sylvain Veilleux, Roberto Maiolino, Alberto D. Bolatto, and Susanne Aalto. Cool outflows in galaxies and their implications. *A&A Rv*, 28(1):2, April 2020. doi: 10.1007/s00159-019-0121-9.

Sylvain Veilleux, David S. N. Rupke, Weizhe Liu, Anthony To, Margaret Trippe, Todd M. Tripp, Fred Hamann, Reinhard Genzel, Dieter Lutz, Roberto Maiolino, Hagai Netzer, Kenneth R. Sembach, Eckhard Sturm, Linda Tacconi, and Stacy H. Teng. Galactic Winds across the Gas-rich Merger Sequence. I. Highly Ionized N V and O VI Outflows in the QUEST Quasars. *ApJ*, 926(1):60, February 2022. doi: 10.3847/1538-4357/ac3cbb.

M. Villar-Martín, S. Arribas, B. Emonts, A. Humphrey, C. Tadhunter, P. Bessiere, A. Cabrera Lavers, and C. Ramos Almeida. Ionized outflows in luminous type 2 AGNs at z ¡ 0.6: no evidence for significant impact on the host galaxies. *MNRAS*, 460(1):130–162, July 2016. doi: 10.1093/mnras/stw901.

Pauli Virtanen, Ralf Gommers, Travis E. Oliphant, Matt Haberland, Tyler Reddy, David Cournapeau, Evgeni Burovski, Pearu Peterson, Warren Weckesser, Jonathan Bright, Stéfan J. van der Walt, Matthew Brett, Joshua Wilson, K. Jarrod Millman, Nikolay Mayorov, Andrew R. J. Nelson, Eric Jones, Robert Kern, Eric Larson, C J Carey, İlhan Polat, Yu Feng, Eric W. Moore, Jake VanderPlas, Denis Laxalde, Josef Perktold, Robert Cimrman, Ian Henriksen, E. A. Quintero, Charles R. Harris, Anne M. Archibald, Antônio H. Ribeiro, Fabian Pedregosa, Paul van Mulbregt, and SciPy 1.0 Contributors. SciPy 1.0: Fundamental Algorithms for Scientific Computing in Python. *Nature Methods*, 17:261–272, 2020. doi: 10.1038/s41592-019-0686-2.

M. Volonteri, Y. Dubois, C. Pichon, and J. Devriendt. The cosmic evolution of massive black holes in the Horizon-AGN simulation. *MNRAS*, 460(3):2979–2996, August 2016. doi: 10.1093/mnras/stw1123.

J. Wang, E. Nardini, G. Fabbiano, M. Karovska, M. Elvis, S. Pellegrini, C. Max, G. Risaliti, V. U, and A. Zezas. Fast and Furious: Shock Heated Gas as the Origin of Spatially Resolved Hard X-Ray Emission in the Central 5 kpc of the Galaxy Merger NGC 6240. *ApJ*, 781:55, January 2014. doi: 10.1088/0004-637X/781/1/55.

Rainer Weinberger, Volker Springel, Lars Hernquist, Annalisa Pillepich, Federico Marinacci, Rüdiger Pakmor, Dylan Nelson, Shy Genel, Mark Vogelsberger, Jill Naiman, and Paul Torrey.

Simulating galaxy formation with black hole driven thermal and kinetic feedback. *MNRAS*, 465(3):3291–3308, March 2017. doi: 10.1093/mnras/stw2944.

Jessica K. Werk, J. Xavier Prochaska, Sebastiano Cantalupo, Andrew J. Fox, Benjamin Oppenheimer, Jason Tumlinson, Todd M. Tripp, Nicolas Lehner, and Matthew McQuinn. The COS-Halos Survey: Origins of the Highly Ionized Circumgalactic Medium of Star-Forming Galaxies. *ApJ*, 833(1):54, December 2016. doi: 10.3847/1538-4357/833/1/54.

M. S. Westmoquette, J. E. Dale, B. Ercolano, and L. J. Smith. Optical IFU observations of gas pillars surrounding the super star cluster NGC 3603. *MNRAS*, 435(1):30–44, Oct 2013. doi: 10.1093/mnras/stt1172.

Aida Wofford, Claus Leitherer, and John Salzer. Lyα Escape from z ~0.03 Star-forming Galaxies: The Dominant Role of Outflows. *ApJ*, 765(2):118, Mar 2013. doi: 10.1088/0004-637X/765/2/118.

G. Worthey. Abundance Ratio Trends and Nucleosynthesis in Elliptical Galaxies and Spheroids. *PASP*, 110:888–899, August 1998. doi: 10.1086/316203.

Jianfeng Wu, W. N. Brandt, Patrick B. Hall, Robert R. Gibson, Gordon T. Richards, Donald P. Schneider, Ohad Shemmer, Dennis W. Just, and Sarah J. Schmidt. A Population of X-Ray Weak Quasars: PHL 1811 Analogs at High Redshift. *ApJ*, 736(1):28, July 2011. doi: 10.1088/0004-637X/736/1/28.

Dominika Wylezalek, Anthony M. Flores, Nadia L. Zakamska, Jenny E. Greene, and Rogemar A. Riffel. Ionized gas outflow signatures in SDSS-IV MaNGA active galactic nuclei. *MNRAS*, 492(4):4680–4696, March 2020. doi: 10.1093/mnras/staa062.

X. Y. Xia, S. J. Xue, S. Mao, T. Boller, Z. G. Deng, and H. Wu. Chandra Observations of Markarian 273: Unveiling the Central Active Galactic Nucleus and the Extended Hot Gas Halo. *ApJ*, 564:196–208, January 2002. doi: 10.1086/324187.

Xinfeng Xu, Timothy Heckman, Alaina Henry, Danielle A. Berg, John Chisholm, Bethan L. James, Crystal L. Martin, Daniel P. Stark, Alessandra Aloisi, Ricardo O. Amorín, Karla Z. Arellano-Córdova, Rongmon Bordoloi, Stéphane Charlot, Zuyi Chen, Matthew Hayes, Matilde Mingozzi, Yuma Sugahara, Lisa J. Kewley, Masami Ouchi, Claudia Scarlata, and Charles C. Steidel. CLASSY III: The Properties of Starburst-Driven Warm Ionized Outflows. *arXiv e-prints*, art. arXiv:2204.09181, April 2022.

Jun Yang, Leonid I. Gurvits, Zsolt Paragi, Sándor Frey, John E. Conway, Xiang Liu, and Lang Cui. A parsec-scale radio jet launched by the central intermediate-mass black hole in the dwarf galaxy SDSS J090613.77+561015.2. *MNRAS*, 495(1):L71–L75, April 2020. doi: 10.1093/mnrasl/slaa052.

Q. Yuan, R. F. Green, M. Brotherton, T. M. Tripp, M. E. Kaiser, and G. A. Kriss. Associated Absorption Lines in the Radio-loud Quasar 3C 351: Far-Ultraviolet Echelle Spectroscopy from the Hubble Space Telescope. *ApJ*, 575(2):687–696, August 2002. doi: 10.1086/341339.

Fakhri S. Zahedy, Hsiao-Wen Chen, Erin Boettcher, Michael Rauch, K. Decker French, and Ann I. Zabludoff. Evidence for Late-time Feedback from the Discovery of Multiphase Gas in a Massive Elliptical at z = 0.4. *ApJL*, 904(1):L10, November 2020. doi: 10.3847/2041-8213/abc48d.

N. L. Zakamska, F. Hamann, I. Pâris, W. N. Brandt, J. E. Greene, M. A. Strauss, C. Villforth,

D. Wylezalek, R. M. Alexandroff, and N. P. Ross. Discovery of extreme [O III] λ5007 Å outflows in high-redshift red quasars. *MNRAS*, 459:3144–3160, July 2016a. doi: 10.1093/mnras/stw718.

Nadia L. Zakamska and Jenny E. Greene. Quasar feedback and the origin of radio emission in radio-quiet quasars. *MNRAS*, 442(1):784–804, July 2014. doi: 10.1093/mnras/stu842.

Nadia L. Zakamska, Fred Hamann, Isabelle Pâris, W. N. Brandt, Jenny E. Greene, Michael A. Strauss, Carolin Villforth, Dominika Wylezalek, Rachael M. Alexandroff, and Nicholas P. Ross. Discovery of extreme [O III] λ5007 Å outflows in high-redshift red quasars. *MNRAS*, 459(3):3144–3160, July 2016b. doi: 10.1093/mnras/stw718.

Kastytis Zubovas and Andrew King. Clearing Out a Galaxy. *ApJL*, 745(2):L34, Feb 2012. doi: 10.1088/2041-8205/745/2/L34.

Kastytis Zubovas and Andrew R. King. Galaxy-wide outflows: cold gas and star formation at high speeds. *MNRAS*, 439(1):400–406, Mar 2014. doi: 10.1093/mnras/stt2472.